SYNTHESIS AND CHARACTERIZATION OF 4D AND 5D CYANOMETALLATE COMPOUNDS FOR MOLECULAR MAGNETISM

A Dissertation

by

FRANCISCO JAVIER BIRK

Submitted to the Office of Graduate and Professional Studies of
Texas A&M University
in partial fulfillment of the requirements for the degree of

DOCTOR OF PHILOSOPHY

Chair of Committee,	Kim Renée Dunbar
Committee Members,	Michael Hall
	Timothy Hughbanks
	Oleg Ozerov
	Winfried Teizer
Head of Department,	Simon North

August 2019

Major Subject: Chemistry

ABSTRACT

This research describes the synthesis and characterization of cyanometallate compounds based on 4d and 5d transition metal ions. Since the discovery of $[Mn_{12}(CH_3COO)_{16}(H2O)_4O_{12}]$ ($Mn_{12}OAc$) displaying magnetic hysteresis, the pursuit of Single Molecule Magnets (SMMs) has been an active field of research owing to their potential applications in high-density storage, spintronics, quantum computing, and molecular refrigeration technologies. SMM applications are limited by their low operating temperatures, however, and strategies for meeting this challenge are being vigorously pursued. One approach is to take advantage of strong anisotropic coupling between metal ions which can be achieved by using metal ions with large spin-orbit coupling constants and electronic orbital degeneracies. In order to expand on this hypothesis from previous work with $K_4[Mo^{III}(CN)_7]$, the synthesis of the $[W^{III}(CN)_7]^{4-}$ was targeted. Synthetic routes towards isolating this moiety were explored, culminating with the synthesis of the previously unknown heptacyanotungstate anion in $(Bu_4N)_3[W^{IV}(CN)_7]$. This seven-coordinate homoleptic species, and its molybdenum analogue $(Bu_4N)_3[Mo^{IV}(CN)_7]$ which was also prepared, constitute the first examples of S = 1 heptacyanometallates in the literature. Attempts to incorporate the heptacyanometallate(IV) moieties into polynuclear cyanide-bridged structures were undertaken to assess the magnetic exchange interactions with other metal spin centers, reactions that inevitably resulted in the decomposition of $[M^{IV}(CN)_7]^{3-}$ to the diamagnetic $[M^{IV}(CN)_8]^{4-}$ anion. Incorporation of the S = 1/2 $[M^{V}(CN)_8]^{3-}$ anion into discrete complexes was also investigated in order to compare the

results with the chemistry of $[M^{IV}(CN)_7]^{4-}$. The paramagnetic complexes containing $[M^{V}(CN)_8]^{3-}$, indeed, exhibit magnetic exchange coupling. In an effort to further exploit the spin-orbit coupling of the heavier transition elements, the incorporation of trigonal symmetry into 4d and 5d metal complexes with the tris(3,5-dimethylpyrazoyl)borate capping ligand was explored, and starting materials that can be used to prepare cyanometallates are reported.

DEDICATION

To my mother

ACKNOWLEDGEMENTS

I would like to thank my advisor, Professor Kim Dunbar, for her mentorship and support during my time at Texas A&M. I am grateful that she gave me a difficult project and the opportunity to take it in my own direction. Her patience to allow me to try my ideas and learn from them was invaluable towards becoming the chemist I am today, as were her efforts at teaching me how to think about solving problems and communicating ideas and results. I am well prepared for my future career because of her.

I would also like to thank my committee members: Professor Michael Hall, Professor Timothy Hughbanks, Professor Oleg Ozerov, and Professor Winfried Teizer. Your support and discussions were helpful during my studies.

I am especially fortunate to have had the opportunity to work closely with Dr. Dawid Pinkowicz. From the beginning of my graduate studies, he was instrumental in showing me how to handle and work with cyanide compounds, including the synthesis of many of my starting materials. I also appreciate the kindness of David and Dr. Barbara Sieklucka for hosting me at Jagiellonian University in Krakow, Poland for three months. It was stimulating culturally and scientifically, and I hope to visit again soon. Na zdrowie!

I would like to thank all of the past and current members of the Dunbar group who helped me both inside and outside of the lab: Dr. Hanhua Zhao, Dr. Helen Chifotides, Dr. Maria Fernanda Ballesteros Rivas, Dr. Silvia Gómez-Coca, Dr. Mohamed Saber, Dr. Heather Southerland, Dr. Brian Dolinar, Dr. Dimitrios Alexandropoulos, Dr. Vignesh Radhakrishnan, Dr. Yuan-Zhu Zhang, Dr. Zhongyue Zhang, Dr. Bruno Pena, Dr.

Zhangyong Li, Dr. Amanda David, Dr. Andrew Brown, Dr. Jill Ellenbarger, Dr. Codi Sanders, Dr. Toby Woods, Dr. Kelsey Schulte, Dr. David Kempe, Sayan Saha, Haomiao Xie, Carolyn Gunthardt, Agustin Millet, Ryan Coll, Ellen Song, An Vu, and Junjie Huang. It has been an absolute pleasure working and growing with you all.

I would also like to express thanks to the department staff for their help throughout my time at Texas A&M. Julie Zercher was very helpful in handling much of the paperwork associated with my fellowships and making sure I got paid. I would also like to thank Valerie McLaughlin for having fun discussions, especially related to graduate life. I would also like to thank the Dunbar assistants throughout the years: Mayela Canales, Angie Wilson, and Andrezza Antonio for all of their help. Most importantly, I would like to thank Sandy Manning for all of her help in handling degree requirements and offering advice and support when needed.

I am grateful to Dr. Tom Cundari from the University of North Texas who hosted me as an undergraduate for the NSF-REU program at UNT. It was a great experience and reinforced my desire to go to graduate school.

I am indebted to my undergraduate mentor, Dr. Philip Brucat, who offered guidance and support during my time at the University of Florida. I am especially grateful that he was willing to take me on so early and let me figure it out. I am also appreciative of my undergraduate professors, in particular Dr. Alexander Angerhofer, Dr. Daniel Talham, Dr. Adam Veige, Dr. Leslie Murray, Dr. William Dolbier, and Dr. Benjamin Smith for all of their guidance and support. Go Gators!

I would also like to express gratitude to Dr, Joseph Schlenoff and Dr. Kenneth Goldsby from Florida State University. Dr. Schlenoff allowed me to spend two summers working in his laboratory and it was a wonderful opportunity to get some experience at the bench. Dr. Goldsby has been a wonderful mentor over the years and has provided ample advice on graduate school and chemistry in general.

I would also like to acknowledge all of my elementary, middle school, and high school teachers; they provided a strong foundation upon which I was able to build. In particular I'd like to thank my science teachers: Mrs. Haggerty, Mrs. Wheeler, Mrs. Ouimete, Mr. McHenry, and Mr. Aley; they challenged me and helped me to discover a love of science.

I would also like to thank all of my fellow graduate students with whom I served with both the Graduate Student Association for Chemistry and the Graduate and Professional Student Council. It was an absolute pleasure to work with all of you on improving graduate student life at Texas A&M.

I would like to extend a heartfelt thanks to my friends for supporting and encouraging me throughout my time at Texas A&M. The camaraderie and shared experiences of graduate school helped to make it some of the best years of my life, and I will cherish the memories we have (and look forward to many more). I would like to thank my roommate Zac Perry and his dog Charlie for being there to listen and occasionally offer free dinner. I would also like to thank my Dungeons and Dragons friends for some wonderful memories and crazy situations, and my kickball and softball friends. A special shout-out to Dr. Jeremy Jarrett, my best friend since elementary school.

I would also like to thank my hockey friends over the past four years. They helped me to get out of the lab and relieve stress. In particular, I would like to thank some of the referees I have had the pleasure to work with: Paul Wilkinson, Kyle Kuskie, and Eric Kirn. Their feedback and advice helped me to improve not only as a referee but also as a person.

I would also like to thank my family for their support throughout my life. My parents Dennis and Nitza for instilling valuable life lessons and being there; Antonio and Ivelisse for being amazing siblings.

Finally, I would like to especially thank my best friend and partner, Courtney Dickie, for all of her support and encouragement over the past four years. She made graduate school much more bearable, and the journey through was much brighter because of her. I would also like to thank our cat, Washburne, for making our days brighter through his various antics.

In short, thank you to everyone who helped me throughout the past seven years of graduate school and even before that. It has been a pleasure and I am blessed to have such amazing friends and coworkers!

CONTRIBUTORS AND FUNDING SOURCES

Contributors

This work was supervised by a dissertation committee consisting of Professor Kim Dunbar, Professor Michael Hall, Professor Timothy Hughbanks, and Professor Oleg Ozerov of the Department of Chemistry and Professor Winfried Teizer of the Department of Physics & Astronomy.

The magnetic properties of **2** were analyzed by Dr. David Pinkowicz of Jagiellonian University.

The results from Chapter 2 in this dissertation have been published in Birk, F. J.; Pinkowicz, D.; Dunbar, K. R. *Angew. Chem. Int. Ed.* **2016**, *55*, 11368.

All other work conducted for the dissertation was completed by the student independently.

Funding Sources

Graduate study was supported by fellowships from the National Science Foundation Louis Stoke Bridge to the Doctorate Program and the Texas A&M Diversity fellowship.

This work was made possible through funds from the US Department of Energy under Grant Number DE-SC0012582 and the Robert A. Welch Foundation under Grant Number A-1449. Its contents are solely the responsibility of the authors and do not necessarily represent the official views of the US Department of Energy or the Welch Foundation.

NOMENCLATURE

(2.2.2)cryptand	4,7,13,16,21,24-Hexaoxa-1,10-diazabicyclo[8.8.8]hexacosane
AC	Alternating current
Bu_4N^+	Tetrabutylammonium cation
CH_3CN	Acetonitrile
$DAPBH_2$	2,6-diacetylppyridinebis(benzoylhydrazone)
DC	Direct current
DMF	N,N-dimethylformamide
Et_4N^+	Tetraethylammonium cation
Et_2O	Diethyl ether
MeOH	Methanol
$PY5Me_2$	2,6-bis(1,1-bis(2-pyridyl)ethyl)pyridine
SMM	Single Molecule Magnet
THF	Tetrahydrofuran
tmphen	3,4,7,8-tetramethylphenanthroline
Tp*	Tris(3,5-dimethylpyrazoyl)borate
ZFS	Zero-field splitting
μ_B	Bohr magneton

TABLE OF CONTENTS

Page

LIST OF FIGURES

Page

LIST OF TABLES

Page

CHAPTER I

INTRODUCTION

Humans first observed magnetism in the 6th century B.C. when the Greeks noted the interaction of iron fillings with loadstones.[2] Further developments were made in the twelfth century with the development of the compass to use the Earth's magnetic field for navigation. A more scientific understanding of magnetism began in the 17th century, with Gilbert's experiments determining that the Earth itself is a magnet.[2] The principles of magnetism were finally understood in the 20th century when experiments by Ørsted, Ampére, Maxwell, and Faraday led to a determination of the relationship between electricity and magnetism, and Maxwell's laws merged the fields of electricity and magnetism into a unified quantitative field. With the advent of quantum mechanics in the 20th century, Van Vleck and Dirac were able to explain magnetism at the molecular level. Today, magnets are prevalent throughout society, being used in medical imaging and devices, electrical motors, automobiles, computers and other electronics, telecommunications, and data storage devices.[3] Researchers also have discovered that magnetism plays a pivotal role in nature; birds, sea animals, and even bacteria have been found to use nanoparticles of magnetite, Fe_3O_4, to assist with navigation.[4-6] Many animals produce magnetite, including humans, but the role magnetite plays in the human brain is not yet fully understood. Clearly, magnetism plays a crucial role in our lives and there are still many new horizons for harnessing this force.

Magnetism is a quantum property arising from the electron spin and orbital angular momentum.[1] When the electrons are paired, there is a diamagnetic response wherein the electrons are repelled by a magnetic field, χ_D; unpaired electrons are attracted to a magnetic field, and are broadly termed paramagnetic, χ_P. When a material is placed in a magnetic field, the field within the material will deviate from the homogeneous field value (depending on whether it is paramagnetic or diamagnetic):

$$B = H_0 + 4\pi M \qquad \text{Equation 1}$$

Where B is the magnetic induction (the field within the material), M is the intensity of the magnetization, and H_0 is the homogenous magnetic field applied. Dividing equation 1 by H_0 yields the volume susceptibility, χ_V, which is a unitless quantity and has components of both the paramagnetic susceptibility and diamagnetic susceptibility:

$$\chi_V = \frac{M}{H_0} = \chi_P + \chi_D \qquad \text{Equation 2}$$

The χ_V can be converted to a mass susceptibility (units cm^3/g or emu/g), χ_g, which is more easily measured for materials, by dividing by the density, ρ (g/cm^3), of the material:

$$\chi_g = \frac{\chi_V}{\rho} \qquad \text{Equation 3}$$

Finally, the mass susceptibility can be converted to a molar susceptibility, χ_M, by multiplying the χ_g by the molecular weight of the compound (M_W); it has units of cm^3/mol or emu/mol.

$$\chi_M = \chi_g(M_W) \qquad \text{Equation 4}$$

The molar susceptibility, χ_M, is independent of the mass or field and should be the same for every measurement of the same material; as a result, it makes it easier for comparing

magnetic properties of different molecules. Unless otherwise noted, all magnetic susceptibilities will be denoted as molar susceptibilities. In 1932, Van Vleck derived a general equation for modeling χ_M and fitting magnetic susceptibility data for molecular materials under a variety of conditions[7]:

$$\chi_M = \frac{N_A \sum_n \left(\frac{E_n^{(1)2}}{k_B T} - 2E_n^{(2)}\right) exp\left(\frac{-E_n^0}{k_B T}\right)}{\sum_n exp\left(\frac{-E_n^0}{k_B T}\right)} \qquad \text{Equation 5}$$

where N_A is Avogardro's number, k_B is Boltzmann's constant, T is temperature, E_n^0 is the energy of a particular level n in zero field, and $E_n^{(1)}$ and $E_n^{(2)}$ are the first-order and second-order Zeeman coefficients.

Molecular Magnetism

Molecular magnetism is an interdisciplinary field encompassing research from chemistry, physics, and materials science. Molecular magnets have many potential applications, including spintronics,[8-9] quantum computing,[10-13] high density information storage,[14-15] and magnetic refrigeration.[16-19] The nascence of the field traces back to 1952 with the seminal study of the exchange interaction between copper(II) metal centers in the dimer $[Cu_2(OAc)_4(H_2O)_2]$.[20] Since this time, significant efforts have been made to explore the magnetic properties of molecular materials which have yielded interesting results such as multifunctional materials, where the magnetic properties depend on an external stimulus such as light or temperature.

In general, magnets are composed of domains which consist of spins that are aligned in the same direction (Figure 1). In the absence of a magnetic field the domains will be randomly oriented such that there is no net magnetic moment. The domains are

separated by domain walls, or Bloch walls, where the individual spins begin to vary and are not aligned with the spins in the domain.[21] The width of the domain wall depends upon the exchange interaction that keeps the spins aligned; a larger exchange interaction will lead to wider domain walls. When a magnetic field is applied, the domains aligned with the magnetic field will grow through the domain walls, which begin to align with the field, and the result is a net magnetic moment. Typical domain sizes are 10^{-4} to 10^{-6} m in size, but if the particle shrinks in size, eventually the size of the domain is comparable to the size of the Bloch walls, and the particle becomes a single domain. Further reduction of the size of the particles leads to decreased magnetic anisotropy (A) of the particle; it depends on the decreasing volume (V) of the particle by the formula $A = KV$, where K is an anisotropy constant specific to the material.[22] Such particles are termed superparamagnets, and the particles can reverse their spin on a short time-scale due to the small amount of thermal energy needed (fast paramagnetic relaxation), and application of a magnetic field will magnetize the individual magnetic molecules similar to a paramagnet, but produce a much larger magnetic susceptibility.[22] Superparamagnetism represents the finite limit for the bulk magnetic response of a material.

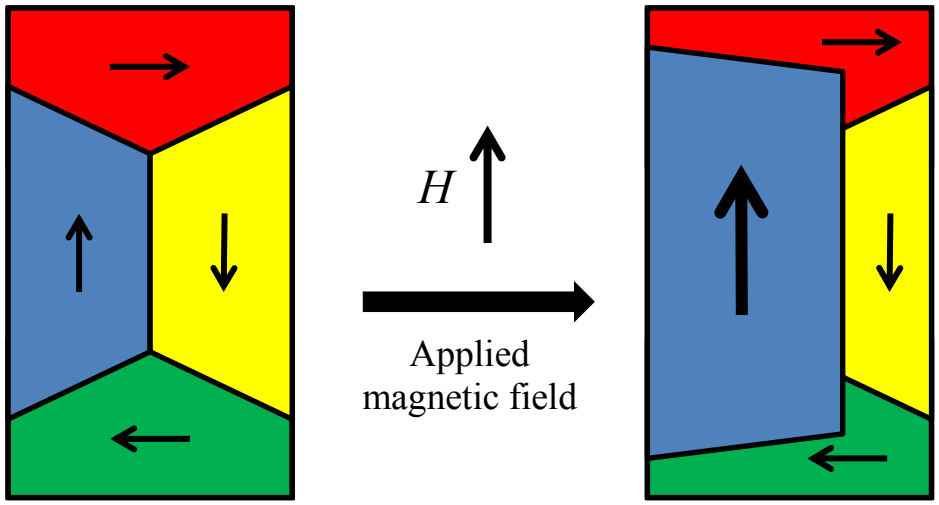

Figure 1: Magnetic domains in a simple paramagnet; application of a magnetic field results in domains aligned with the field growing and domains not aligned with the applied field shrinking as they begin to align with the field.

Another property of magnets is the ability to exhibit hysteresis in which application of an increasing magnitude of a magnetic field leads to saturation of the magnetization, M_S. Upon removal of the magnetic field, the magnet maintains its magnetization at zero field (remnant magnetization, M_R) and only the application of a magnetic field in the reverse direction will return the magnetization to zero, referred to as the coercive field (H_C) (Figure 2).[3] Magnets can be classified based on the basis of their hysteresis loops: a hard magnet requires a large coercive field and results in a 'fat' hysteresis loop and a soft magnet has a small coercive field and appears as a 'skinny' hysteresis loop. A strong magnet will reach the saturation point, M_S, quickly, while a weak magnet will not saturate well or does not saturate or requires very high fields to saturate. Soft magnets are used in generators, transformers, and electromagnets due to the enhanced flux that can be

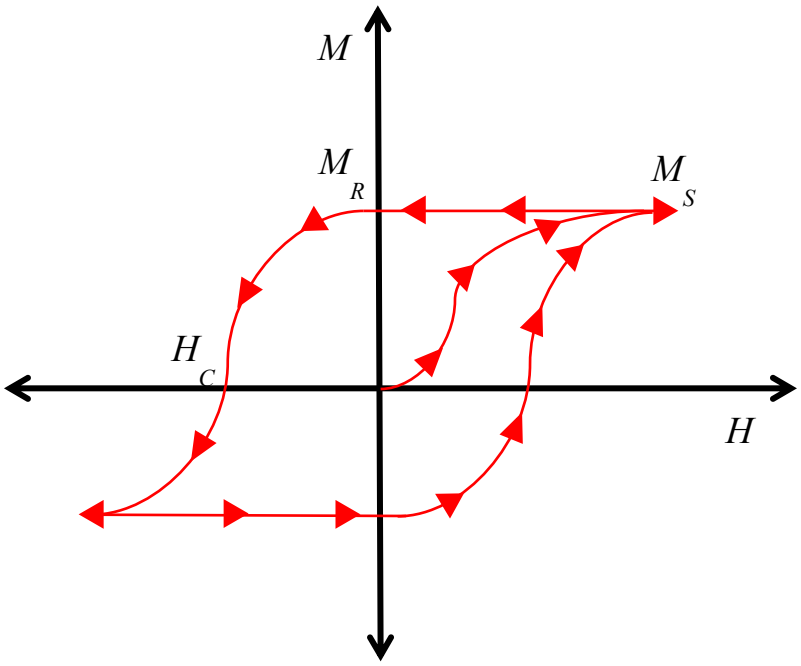

Figure 2: Hysteresis loop of a magnet; red arrows indicate direction of field sweep.

produced by electrical currents, while hard magnets have a wide variety of uses, including device controllers, directing beams (i.e. in televisions), and permanent magnets, which includes electronics and recording devices (computers, data storage, audio devices, etc.).[3] For a bulk sample composed of atoms or molecules with non-interacting magnetic spins, the magnetic moments will align with an applied magnetic field, and upon removal of the magnetic field, the magnetic moments will thermally relax back to random orientations such that there is no net magnetic moment; such materials are referred to as paramagnets. Paramagnets have a temperature-dependence to their susceptibility, which follows the Curie-Weiss law, represented by the equation:

$$\chi = \frac{C}{T - \theta}$$ Equation 06

$$C = \frac{N_A g^2 \beta^2 S(S+1)}{3k_B}$$ Equation 07

where g is the Landé g-factor, β is the Bohr magneton constant, and S is the spin of the system.[23] As the temperature decreases, there is a linear decrease in χ^{-1} with an intercept of $\theta = 0$ (Figure 3) and χT equals the constant C (Figure 4). For interacting magnetic spin systems within a molecule or material, there are several types of exchange interactions that dictate how the metal centers interact. The three main types are ferromagnetic, antiferromagnetic, and ferrimagnetic coupling (Figure 5). Ferromagnetism involves spins aligning in a parallel fashion which leads to a positive θ in the χ^{-1} versus T Curie-Weiss plot (Figure 3) while χT will increase with decreasing temperature (Figure 4).

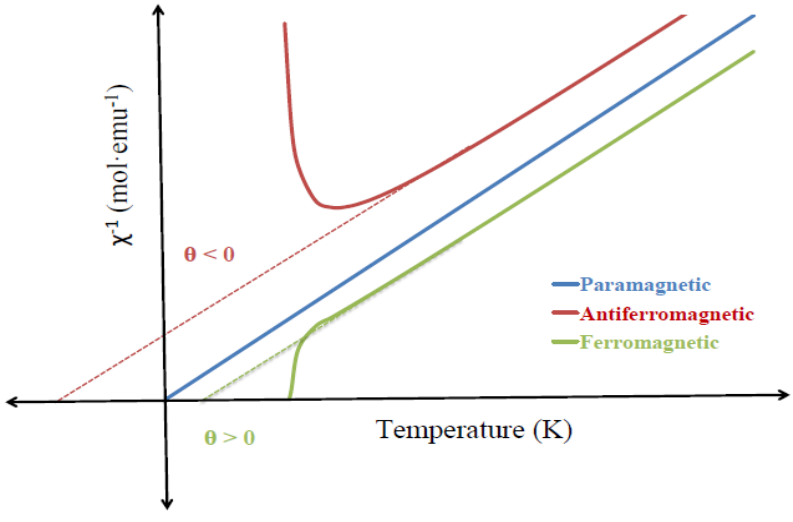

Figure 3: χ^{-1} vs temperature for different coupling schemes.

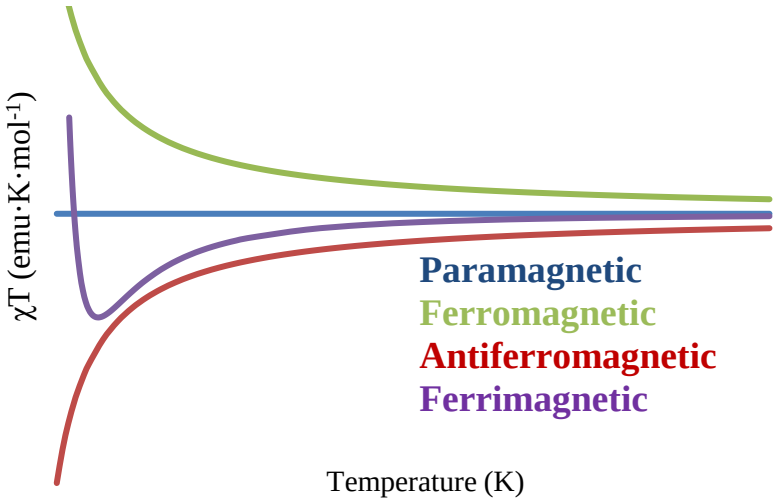

Figure 4: χT vs temperature for different magnetic behaviors.[1]

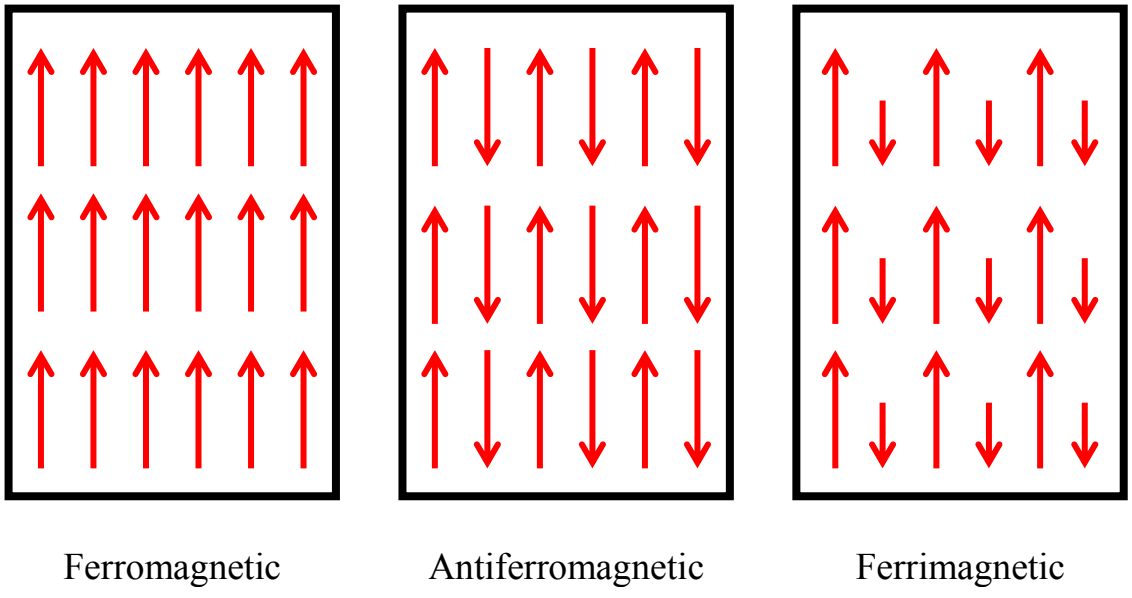

Figure 5: Types of magnetic behaviors: a) ferromagnetic b) antiferromagnetic c) ferrimagnetic

Antiferromagnetism involves spins aligning in an anti-parallel manner so that there is a cancellation and $S = 0$, and there will be a negative θ in the χ^{-1} Curie-Weiss plot (Figure 3) while χT will decrease with decreasing temperature (Figure 4). Finally, ferrimagnetism is a special case of antiferromagnetic coupling where the spins are of unequal magnitude such that there is still a net magnetic moment.

Intermolecular interactions are also possible between nearest neighbors in molecular materials, which can result in long-range magnetic ordering and can be maintained even after removal of the magnetic field below a critical temperature. When the long-range order is a result of spin parallel alignment, the material is a ferromagnet, and below the critical temperature, known as the Curie temperature (T_C), thermal fluctuations are unable to overcome the ordering interaction; above the Curie temperature the thermal motions dominate and the material will behave as a paramagnet. When the long-range ordering results in an antiparallel spin alignment of equal magnitude, the material is described as an antiferromagnet, and when the alignment is of unequal magnitude, the material is a ferrimagnet. In both cases, as with ferromagnets, below a critical temperature the long-range order dominates over thermal activity; this critical temperature is termed the Neel temperature, T_N, and above it both antiferromagnets and ferrimagnets behave as paramagnets.

Single Molecule Magnets (SMMs)

A single molecule magnet (SMM) is an individual molecule that behaves as a magnet, and represents the superparamagnetic limit. In the case of canonical SMMs, the bistable spin states are separated by a double-well potential (Figure 6), and the magnitude

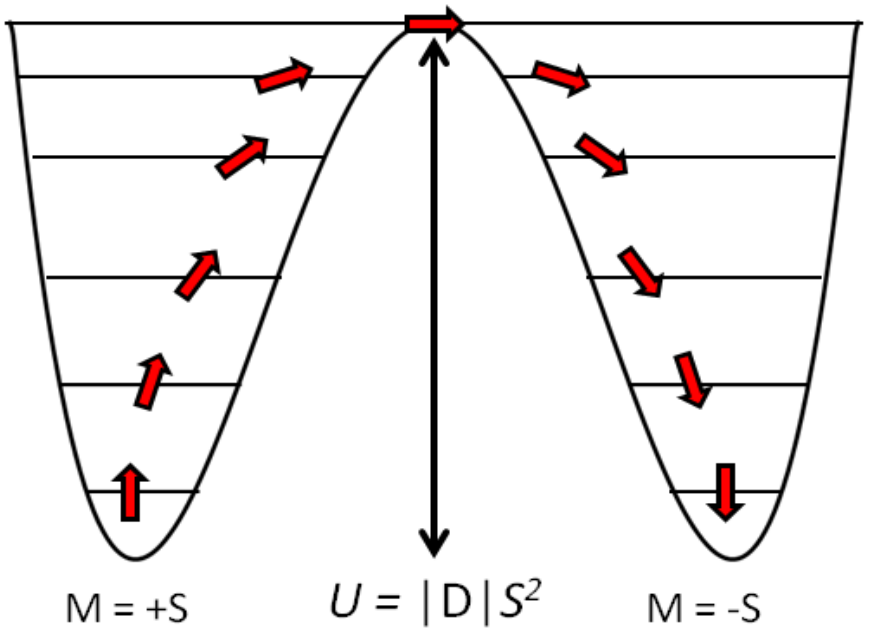

Figure 6: Double well potential for a SMM with a negative D, integer spin system S, and barrier U; each well would correspond to the ground spin state, and the red arrows correspond to the spins in each well.

of the energy barrier for the reversal of magnetization (*U*) between these two spin states is related to the ground state electron spin (*S*) and magnetic anisotropy arising from the negative zero field splitting (*D*), represented by the equations

$$U = |D|S^2 \qquad \text{Equation 08}$$

$$U = |D|\left(S^2 - \tfrac{1}{4}\right) \qquad \text{Equation 09}$$

for integer spin systems (equation 4) and for non-integer spin systems (equation 5), respectively.[22] These equations follow from the Crystal Field Hamiltonian for spin states, which is represented by the equations

$$H_{CF} = DS_z^2 + E\left(S_x^2 - S_y^2\right) \qquad \text{Equation 10}$$

$$D = D_{zz} - \frac{1}{2}D_{xx} - \frac{1}{2}D_{yy} \quad \text{Equation 11}$$

$$E = \frac{1}{2}\left(D_{xx} - D_{yy}\right) \quad \text{Equation 12}$$

where *D* refers to the axial splitting parameter and *E* is the rhombic field parameter. *D* will be zero only under cubic symmetry conditions ($D_{xx} = D_{yy} = D_{zz}$), and, in an axial symmetry, *E* will be zero ($D_{xx} = D_{yy}$).[22] It is in this axial symmetry that the spin state energies can be expressed by the *D* parameter, even in the absence of a magnetic field, and this *D* is referred to as the zero-field splitting (ZFS) parameter. While *U* represents the thermal barrier that must be overcome to switch the spin state, the actual measured barrier, U_{eff}, will be lower as a result of relaxation mechanisms such as quantum tunneling through the barrier and Raman relaxation. The blocking temperature, T_B, has several definitions, but a common one is the temperature at which the magnetization relaxation time equals the characteristic time of the experiment, or where hysteresis is maintained.[24] The characteristic time can be calculated, assuming thermal activation, as an Arrhenius plot and can be represented by the equation

$$\tau = \tau_0 exp\left(\frac{U}{k_B T}\right) \quad \text{Equation 13}$$

where τ_0 is the attempt frequency and *U* is the barrier energy.

The first molecule found to behave as an SMM is $[Mn_{12}O_{12}(CH_3COO)_{16}(H_2O)_4]\cdot 2CH_3COOH\cdot 4H_2O$, or Mn_{12} acetate, isolated and crystallographically characterized by Lis in 1980 and later studied by Sessoli and Gatteschi in 1993 and Christou and Hendrickson in 1998 (Figure 7).[25-28] The molecule consist of eight Mn^{III} outer ions coupled antiferromagnetically to four Mn^{IV} ions in the cubane core

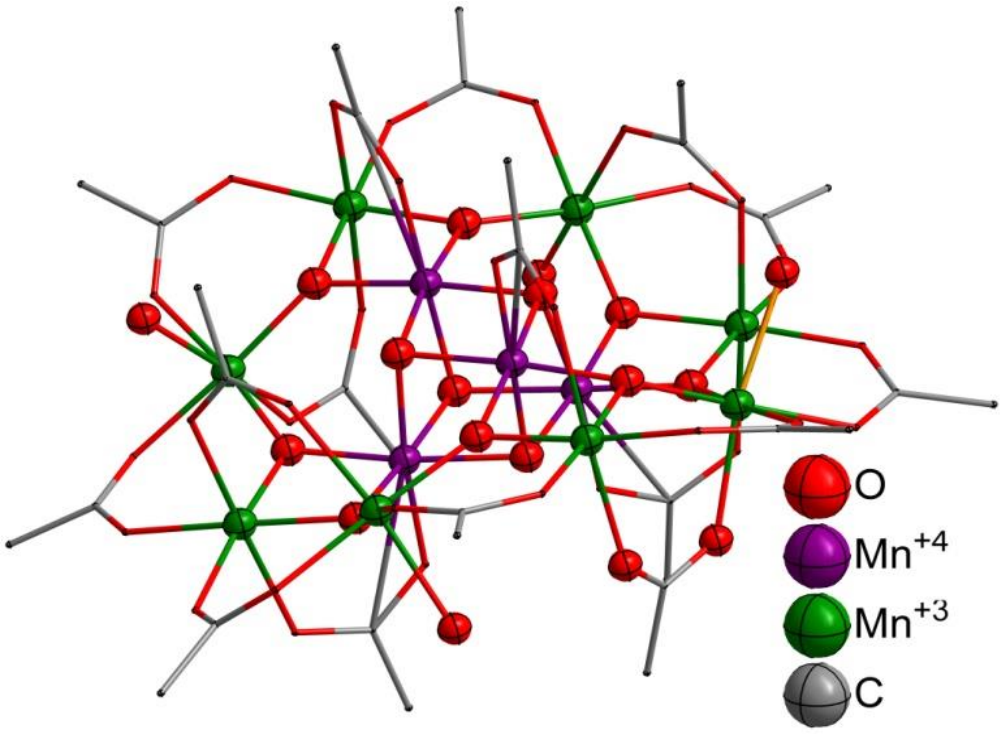

Figure 7: Molecular structure of Mn_{12}(acetate); green ions correspond to Mn^{III} while purple ions correspond to Mn^{IV} ions; hydrogens atoms are omitted for clarity.

to give a ground state of S = 10. The molecule exhibits hysteresis below 3.2 K with a barrier of 45 cm^{-1}. Since this time, a number of research groups have focused on trying to increase the spin, *S*, of molecular systems in the expectation of achieving higher blocking temperatures, particularly by exploration of manganese-based oxides,[29-34] which culminated with an *S* = 83/2 system that exhibits hysteresis below only 1 K (Figure 8).[35]

In 2007, Waldmann pointed out that the zero field splitting term, *D*, includes an S^{-2} term that effectively cancels out the spin component for the barrier height.[36] He also noted that increasing the spin of the system results in dipolar interactions and that larger molecules tend to have local anisotropies pointing in different directions, both of which

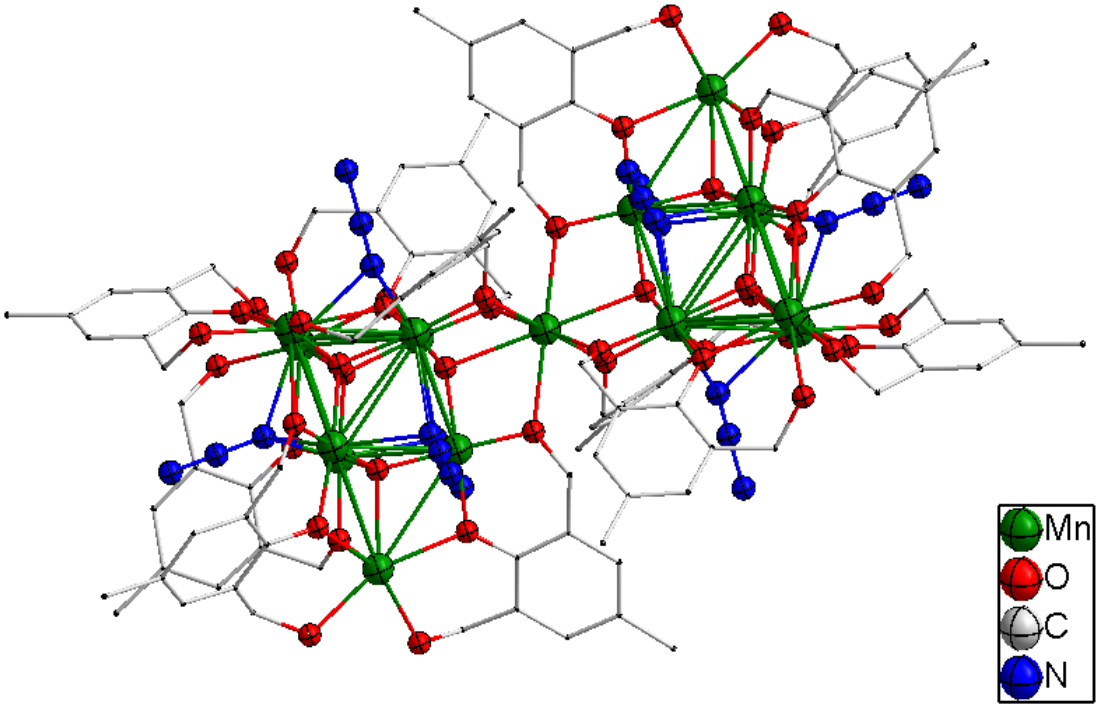

Figure 8: Molecular structure of the Mn_{19} molecule with an S = 83/2 ground state.

are detrimental to SMM behavior. As a result, recent efforts have focused on increasing the anisotropy of the molecules to try to achieve better SMMs,[37] and there have been a number of different approaches to this end. In particular, initial efforts at increasing anisotropy have focused on lanthanide ions, owing to the unquenched orbital angular momentum of the 4f shell and large spin-orbit coupling constants. The first isolated lanthanide SMMs are the double decker compounds $(Bu_4N)[Ln(Pc)_2]$ (Pc = phthalocyanine), where Ln is Dy or Tb; the Dy compound has an effective barrier of 28 cm^{-1} while the Tb has an effective barrier of 230 cm^{-1} (measurements were made with the Tb diluted to minimize quantum tunneling).[38] Since then, a number of research groups

have assembled various lanthanide SMMs in different coordination geometries,[39-45] with the dysprosium(III) ion being particularly effective for engendering SMM behavior.[46-52] Theoretical studies have also been undertaken to predict coordination geometries and lanthanide ions that are expected to yield better SMMs.[43, 53-56] An interesting result by Long and Evans in 2011 is the report of divalent lanthanide compounds bridged by a dinitrogen radical, $[K(18\text{-crown-6})(THF)_2][(Ln(N(SiMe_3)_2)(THF))_2(\mu\text{-}\eta^2\text{:}\eta^2\text{-}N_2)]$ (Ln = Tb, Ho, Er). The Tb compound exhibits hysteresis up to 14 K;[57] this result opened up a new area of radical-bridged lanthanide molecules. While lanthanide-based SMMs have been found to have barriers up to 1815 cm^{-1},[48] many do not exhibit hysteresis as a result of quantum tunneling of the magnetization. Recent work has led to the current record for an SMM, namely $[Dy(Cp^{ttt}_2)][B(C_6F_5)_4]$ (Cp^{ttt} =1,2,4-tri(*tert*-butyl)cyclopentadienide) with a barrier of 1277 cm^{-1} and hysteresis up to 60 K.[49-50]

In addition to lanthanide ions, research has also focused on 3d transition metal mononuclear SMMs that take advantage of large anisotropies as a result of ligand fields and unquenched orbital angular moments. The first mononuclear 3d transition metal SMM was reported by Freedman and Long in 2010 as $[Fe^{II}(tpa^{Mes})]^-$ (tpa^{Mes} = tris(2-mesityl-pyrrolyl-α-methyl)amine). The molecule exhibits a trigonal pyramidal geometry that leads to an unquenched orbitally degenerate ground state and results in a *D* value of -39.6 cm^{-1} and an energy barrier of 42 cm^{-1} under an applied field.[58] Since then a number of mononuclear SMMs have been reported that feature 3d metal ions,[59] predominantly with Fe,[60-64] Ni,[65-66] and Co[66-69]. Theoretical calculations have also led to predictions as to which coordination geometries and electronic geometries are expected to yield SMMs,[70-

[72] work that has resulted in the isolation of unusual geometries for 3d metal compounds, including linear,[60-62, 65-66] trigonal planar,[71] trigonal pyramidal,[58, 63, 73] trigonal prismatic,[67, 69] and pentagonal bipyramidal[64, 68]. The current record for a 3d transition metal single ion magnet is a two-coordinate cobalt imido complex, [Co^{II}(sIPr)(NDmp)] (sIPr = 1,3-bis(2,6-diisopropylphenyl)-4,5-dihydro-imidizole-2-ylidene and Dmp = 2,6-dimesitylphenyl), that was reported in 2017 to have an effective barrier of 413 cm^{-1}.[74]

The recent focus on increasing the anisotropy of transition metal SMMs has led to the identification of three sources of anisotropy: (1) axial zero-field splitting of the magnetic centers (2) exchange anisotropy between metal centers, and (3) dipole-dipole interactions. Dipole-dipole interactions are insignificant for achieving larger anisotropies (although some complexes utilizing Mn^{II} ions have invoked it as an explanation for the anisotropy),[75] and initial efforts focused on the first source, the ZFS of magnetic centers with little success. Recent studies have been directed at using exchange coupling anisotropy to increase the anisotropy of SMMs, as outlined later.

Exchange Coupling

The ability of transition metals form polynuclear complexes results in a superexchange interaction between the metal centers through a bridging ligand. The methods of exchange interaction can be classified into four mechanisms: direct exchange, indirect exchange, superexchange, and double exchange.[22] Direct exchange occurs between metal centers that in proximity such that their spins can directly through overlapping orbitals which results in antiferromagnetic coupling. Superexchange involves magnetic coupling between two metal centers through a diamagnetic ligand (Figure 9),

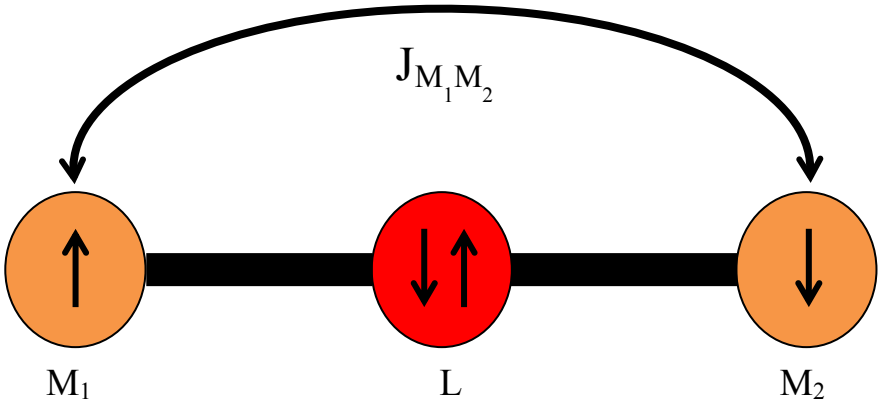

Figure 9: Superexchange coupling scheme through a diamagnetic ligand.

and the exchange interaction depends on the angle between the metal-ligand-metal bond: a linear angle results in antiferromagnetic interaction (non-orthogonal overlap), while a 90° can result in a ferromagnetic interaction as a result of orthogonal orbitals.[23] Finally, double exchange is a special case of superexchange in which both metal centers are the same but in different oxidation states, and thus one spin center has more spin(s) than the other.[22] The superexchange mechanism is described by Hesienberg, Dirac, Van Vleck (HDVV) Hamiltonian,

$$\hat{H} = -2JS_1S_2 \qquad \text{Equation 21}$$

where S_1 and S_2 are the two interacting spin centers and J is the exchange interaction that describes the coupling interaction between the spin centers (in this dissertation, a negative J corresponds to antiferromagnetic coupling, while a positive J corresponds to ferromagnetic coupling between S_1 and S_2).

The Heisenberg Hamiltonian (equation 21) assumes isotropic coupling; that is, the coupling is the same in the x, y, and z directions. Isotropic coupling leads to S being a

good quantum number, and it allows for SMMs to be defined in terms of an isotropic *S* as outlined in equations 8 and 9 above.[23]

In contrast, anisotropic exchange involves directionality, and can be divided into two classes: XY and Ising. The Heisenberg exchange equation 21 is

$$H = -2\left[J_{xy}\left(S_{ix}S_{jx} + S_{iy}S_{jy}\right) + J_z S_{iz}S_{jz}\right] \quad \text{Equation 22}$$

when $J_{xy} = J_z$, the isotropic Heisenberg equation, eq. 21, is obtained. When $J_{xy} = 0$, the Ising limit is obtained and the Hamiltonian collapses to

$$H = -2J_z S_{iz}S_{jz} \quad \text{Equation 23}$$

and when $J_z = 0$ the XY limit is obtained and the Hamiltonian becomes

$$H = -2J_{xy}\left(S_{ix}S_{jx} + S_{iy}S_{jy}\right) \quad \text{Equation 24}$$

An excellent example demonstrating this concept was published by Wang and Dunbar, in which three trinuclear isomers exhibit XY or Ising exchange depending on the coordination mode adopted by $Mn(SB)Cl_2$ (SB = Schiff base) with $K_4[Mo^{III}(CN)_7]$ (Figure 10).[76] The structure of one the compounds, $[Mn(L_{N5Me})]_2[Mo^{III}(CN)_7]$ (L_{N5Me} = 2,6-bis[1,2-(N-methylamino)ethylimino)ethyl]-pyridine) (Figure 10a) involves coordination of the Mn capping group with the axial cyanides of the heptacyanomolybdate(III) anion. This molecule engages in Ising coupling with J_z = -34 cm^{-1} and J_{xy} = -11 cm^{-1} and exhibits SMM behavior with an effective barrier of 40.5 cm^{-1} and hysteresis to 3.2 K. This is the highest barrier for a cyanide based SMM. The other two compounds, $[Mn(L_{N3O2})]_2[Mo^{III}(CN)_7]$ (L_{N3O2} = 2,13-dimetyl-6,9-dioxa-3,12,18-triazabicyclo[12.3.1]octadeca-1(18),2,12,14,16-pentaene) (Figure 10b) and $[Mn(L_{DAPSC})]_2[Mo^{III}(CN)_7]$ (L_{DAPSC} =2,6-diacetylpyridine bis(semicarbazone))) (Figure

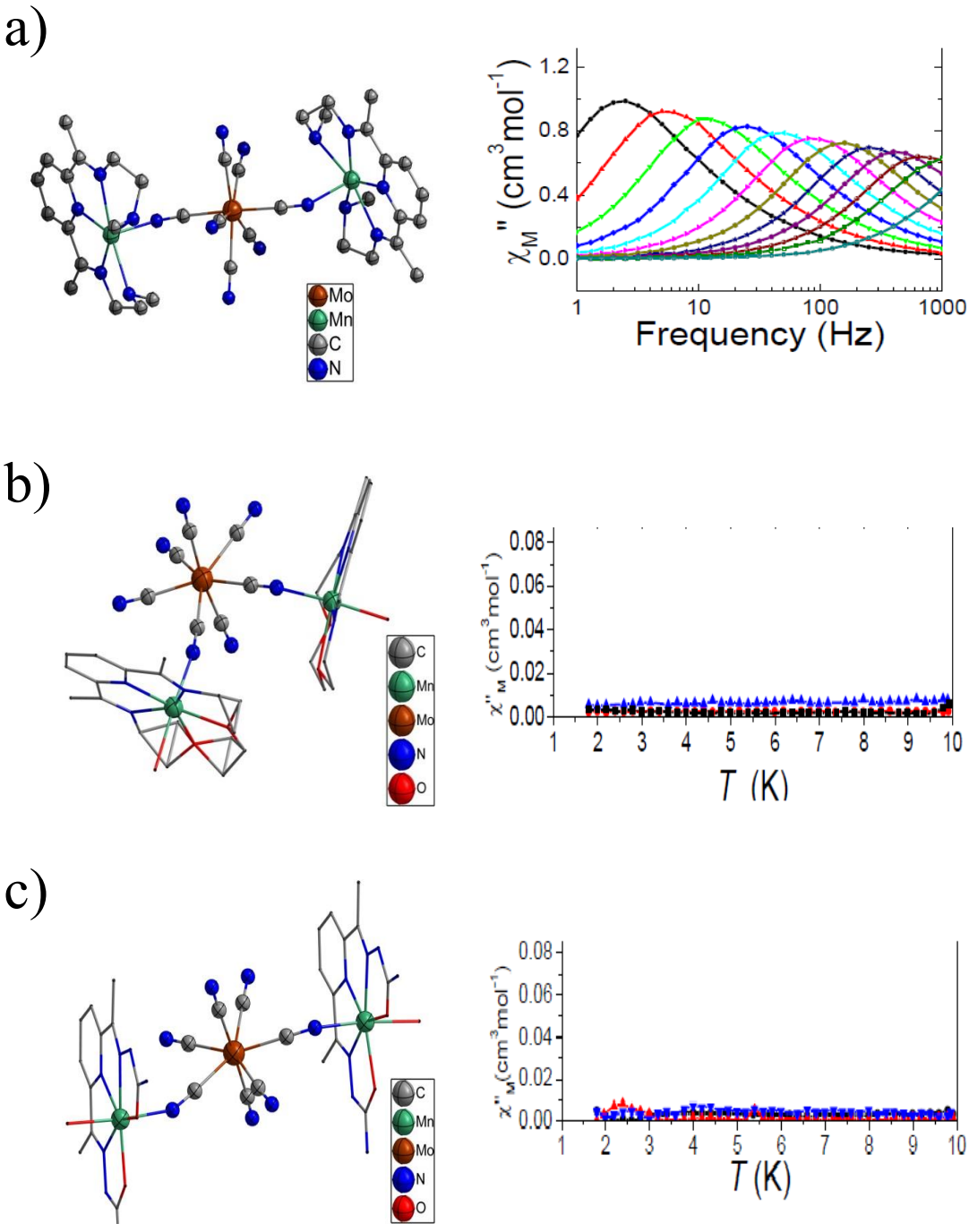

Figure 10: Crystal structures and out-of-phase AC susceptibilities for three Mn_2Mo trinuclear molecules: a) $[Mn(N_{5Me})]_2[Mo(CN)_7]$, b) $[Mn(N_3O_2)]_2[Mo(CN)_7]$, c) $[Mn(DAPSC)]_2[Mo(CN)_7]$. Used with permission, copyright American Chemical Society.

10c), involve coordination of the Mn and Mo metal centers through the 1, 2 and 1, 3 cyanide positions in the equatorial plane, respectively, of the heptacyanomolybdate anion. These compounds exhibit J_{xy} of -9 cm^{-1} and -4 cm^{-1} and J_z values of -7.5 cm^{-1} and 0 cm^{-1}, respectively. Both compounds are simple paramagnets with no slow paramagnetic relaxation or hysteresis as a result of the XY exchange.[77]

Theory supports the experimental results, as Mironov performed several theoretical calculations supporting the idea that Ising anisotropic coupling between certain metal centers should yield a large magnetic anisotropy and result in higher T_B SMMs.[75, 78-81] Mironov's work indicates that U_{eff} is a result of the energy difference between the ground and first excited spin levels, and that, for 3d metal centers, the maximum U_{eff} would not exceed 20 cm^{-1} and would usually be less than 1 cm^{-1}, which would lead to a maximum T_B of about 3-5 K.[75] The reason for the dependence of U_{eff} on the energy difference between the ground and first excited spin energies is that the quantum tunneling rate increases significantly as the excited spin state increases, and thus quantum tunneling relaxation occurs before the barrier top is reached. The U_{eff} based on the difference in energy of the spin states is an intrinsic property of the 3d metal center, so increasing the size of the compound will not increase U_{eff}. However, Mironov has suggested that using 4d or 5d metal centers with orbitally degenerate ground states will result in S no longer being a good quantum number (therefore equations 8 and 9 would no longer apply) due to spin-orbit coupling. This situation also results in anisotropic coupling which must be described by the Ising Hamiltonian instead of the Heisenberg isotropic Hamiltonian. The orbitally degenerate magnetic center will yield a spin energy level that is different from

the 3d metal ion, including a degenerate ground state and a large energy difference between the ground and first excited spin state, which is determined by the J_z of the anisotropic exchange coupling. Mironov predicted that the J coupling values for 5d-3d metal ion anisotropic exchange should be on the order of tens or hundreds of wavenumbers, which would lead to much larger blocking temperatures. In order to calculate the spin energy levels for select polynuclear complexes to estimate the U_{eff} and T_B, the Hamiltonian was numerically diagonalized using the full basis set of spin wavefunctions. The Hamiltonian *I* is based on having superexchange via a cyanide ligand between the 4d or 5d metal center with an orbitally degenerate ground state and a 3d metal ion; the superexchange allows one to use the microscopic kinetic exchange theory developed by Anderson, although Mironov adjusted for having an orbitally degenerate ground state and anisotropic exchange, which were unaccounted for in the original theory.[80, 82] In particular, charge transfer configurations were used to extract transfer parameters, which could then be used to calculate the J values. In one case, the exchange between Mn—Mo was analyzed, and the J values were found to be

$$J_z = \frac{1}{5}\left[\frac{-t_\pi^2}{U_1(1-\frac{I}{U1})} - \frac{t_\pi^2}{U_2(1-\frac{2I}{U_2})} + \frac{2t_\sigma 2I}{U_2^2}\right] \qquad \text{Equation 25}$$

$$J_{xy} = \frac{t_\pi^2}{5}\left(\frac{1}{U_2} - \frac{I}{U_1^2}\right) \qquad \text{Equation 26}$$

where t_π and t_σ are the transfer parameters for π and σ-bonding, U_1 is the Mo→Mn CT energy, *I* is the Hund intraatomic exchange energy between the low and high spin states of Mo after charge transfer. Mironov examined the anisotropic coupling using $[Os^{III}(CN)_6]^{3-}$, $[Mo^{III}(CN)_7]^{4-}$, and $[Re^{IV}(CN)_7]^{3-}$ anions with 3d metal ions.[75, 79] One

benefit is that the 4d and 5d orbitals lead to better overlap and thus greater anisotropic exchange. Mironov also examined how distortions affect the *J* values, and, while distortions from ideal geometries lead to lower *J* values, the large spin-orbit coupling offsets the decrease as long as the distortions are not severe. For $[Mo^{III}(CN)_7]^{3-}$, Chibotaru calculated that the g tensor of the pentagonal bipyramidal geometry should be very anisotropic as a result of the five-fold symmetry and large crystal field gap between the ground state and excited orbitals.[83] In particular, the ground state e''^3 (d_{xz} and d_{yz} orbitals) is split via spin-orbit coupling to yield two Kramers doublets which cannot be mixed by Zeeman interactions, and so there is no magnetic moment in the equatorial plane. The choice of 3d metal ion also affects the J_z and J_{xy} coupling values; in particular Mironov predicted that a 5d-3d anisotropic exchange value of 300-400 cm^{-1} could be obtained by using a 3d metal with a low spin of $S = 1/2$ or $S = 1$, which would lead to a blocking temperature of 70 to 100 K.[78]

Transition Metals and Cyanide Ligand

Based on Mironov's predictions that anisotropic coupling leads to higher-temperature SMMs, transition metal cyanide compounds are ideal for testing his theoretical predictions, and, in fact, in his work he proposed several cyanometallate compounds that should be ideal for anisotropic exchange. Additionally, cyanide compounds have a rich history: the first cyanide compound, Prussian Blue, was discovered over three centuries ago by the artist Diesbach and used as a pigment. It was also one of the first coordination compounds studied, and since then cyanide compounds have been synthesized for almost all the metals of the periodic table. While Prussian Blue was

initially used as a dye and pigment, it has also been studied for its structural, optical, and magnetic properties; the original compound's formula is $Fe^{III}_4[Fe^{II}(CN)_6]_3 \cdot 14\text{-}16H_2O$ (Figure 11), although it is possible to substitute the Fe^{III} cation with other metals which can lead to high temperature magnets. The Prussian Blue compound itself was found to show ferromagnetic ordering at 5.6 K,[84] and this result spawned the field of cyanide-based molecular magnetism. Cyanide compounds have also recently found uses for heavy metal and radioactive poisoning antidotes, molecular sieves,[85-86] hydrogen storage materials,[87-88] gas adsorption,[86, 89-90] and as conducting or battery materials,[91-94] in addition to previously mentioned uses as pigments and magnetic materials.

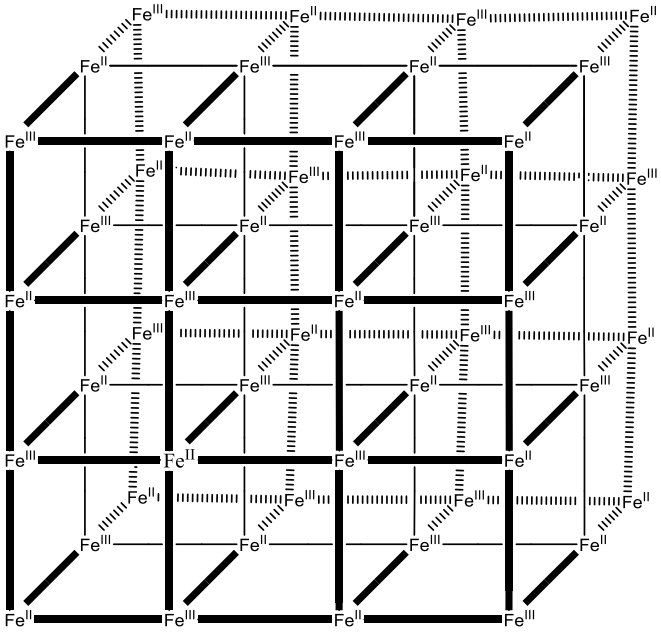

Figure 11: Prussian Blue structure; alternating octahedral sites of Fe^{II} and Fe^{III} ions; vacant sites are possible and interstitial sites can be occupied by metal ions or cations.

The cyanide ligand, CN^-, offers several benefits for bridging transition metals. As a diamagnetic ligand, it results in superexchange mechanism; it is also linear, which results in predictable coordination geometries, unlike other ligands, such as O^{2-}, that adopt varying degrees of bent or linear coordination mode based on the electronic configuration. A benefit to this situation is that the exchange interaction between metal centers is predictable: orbitals with the same symmetry result in antiferromagnetic coupling, while orbitals with orthogonal symmetry yield ferromagnetic coupling (Figure 12), and these interactions can be predicted based on the electronic configurations of the metal ions.[95] In contrast, the exchange coupling for oxo-bridged complexes depends on the bonding angle between the metal centers and the oxo bridge, and thus is less controllable. Additionally, the cyanide ligand can be monitored by infrared (IR) spectroscopy because of the characteristic $\nu(C\equiv N)$ stretching frequency which changes with reference to the free cyanide ligand stretching frequency ($\nu(C\equiv N) = 2080\ cm^{-1}$) depending on several factors. For transition metal cyanide compounds, the carbon-end of the cyanide ligand binds to the metal center first and acts as a σ-donor due to the highest occupied MO being a σ orbital with predominantly carbon character. The transition metal can donate electron density into π* orbitals, of predominantly N character, as a result of d—π backbonding. The σ-bonding results in an increase in the IR stretching mode frequency, while π-backbonding results in the stretching frequency shifting to lower frequencies. The cyanide ligand is a much better π-acceptor than a σ-donor.[96] The stretching frequency also changes as a result of the oxidation state, number of cyanides, and metal center electronegativity: a lower

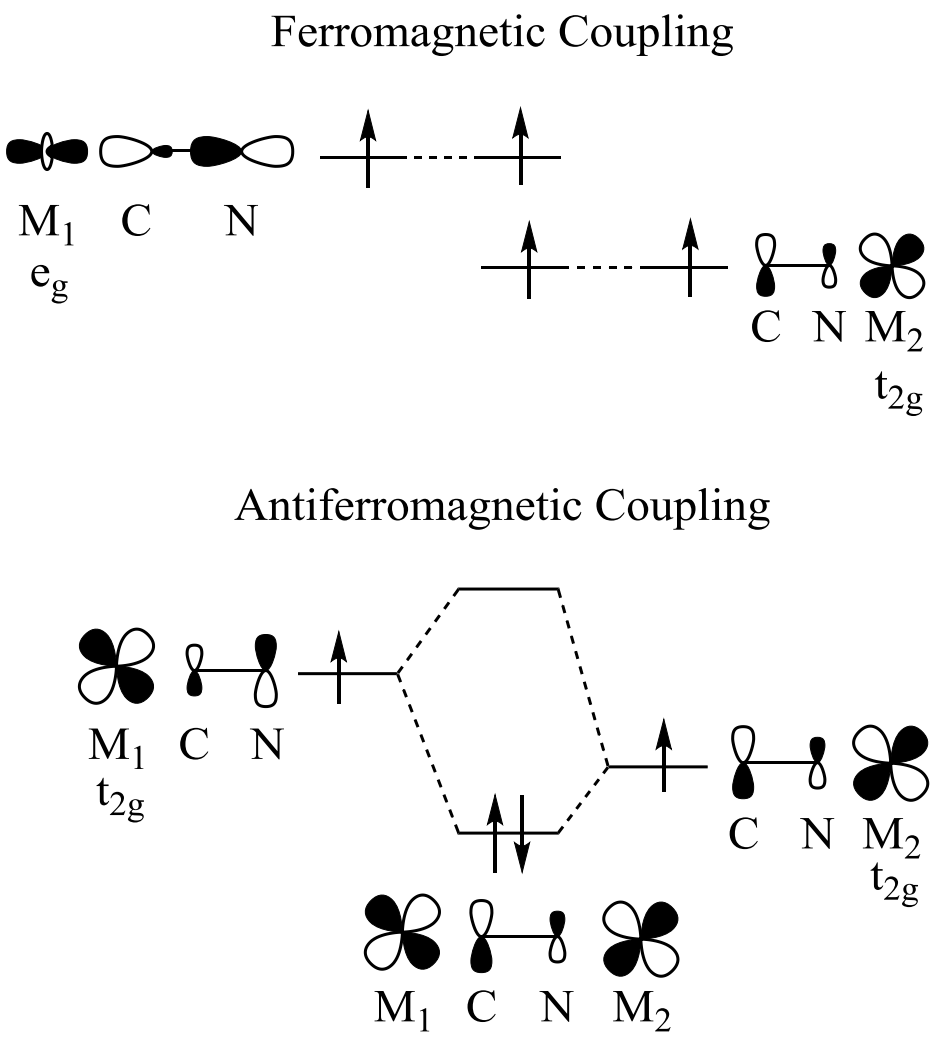

Figure 12: Exchange coupling between transition metal ions bridged by a cyanide ligand.

oxidation state leads to a lower frequency as a result of stronger π-backbonding, a decrease in the number of cyanides results in a shift to higher frequencies due to an increase in the positive charge on the metal center which strengthens σ-bonding, and increasing the electronegativity on the metal ion results in a higher frequency from greater σ-donation

from the cyanides.[97] Finally, when the cyanide ligand bridges two transition metals, as in superexchange coupling, the IR stretching frequencies will shift to higher frequencies compared to terminal cyanide ligands.

A major advantage of using transition metal cyanide compounds is the ability to use a building block approach, namely the transition metal cyanide compounds are combined with other metal-ligand systems in certain ratios to synthesize polynuclear complexes with a desired geometry (Figure 13).[98-99] For example, a hexacyanometallate anion reacted with a metal ion that has a pentadentate capping ligand and only one open site in a 1:2 ratio should yield a linear trinuclear complex; in contrast, a hexacyanometallate anion reacted with a metal ion that two open sites that are *cis* to each other as a result of the capping ligands and in a 2:3 ratio should yield a trigonal bipyramidal geometry, while a 1:1 ratio would yield a square geometry (Figure 13). The ability to combine cyanometallates having certain geometries and electronic configurations with other metal centers with tailored ligands to enforce desired polynuclear geometries can dictate the magnetic properties, and represents a powerful tool for testing theoretical predictions of magnetism by design as opposed to serendipity.

Another advantage to the building block approach is the variety of cyanometallate geometries and electronic configurations available. Among homoleptic transition metals, the possible geometries include trigonal bipyramidal (5 cyanides), octahedral (6 cyanides), pentagonal bipyramidal (7 cyanides), and dodecahedral/square prismatic (8 cyanides). The 3d cyanometallates commonly have octahedral geometries, while the 4d metals can have six, seven, or eight cyanides, and the 5d metals are often seven or eight coordinate. [98]

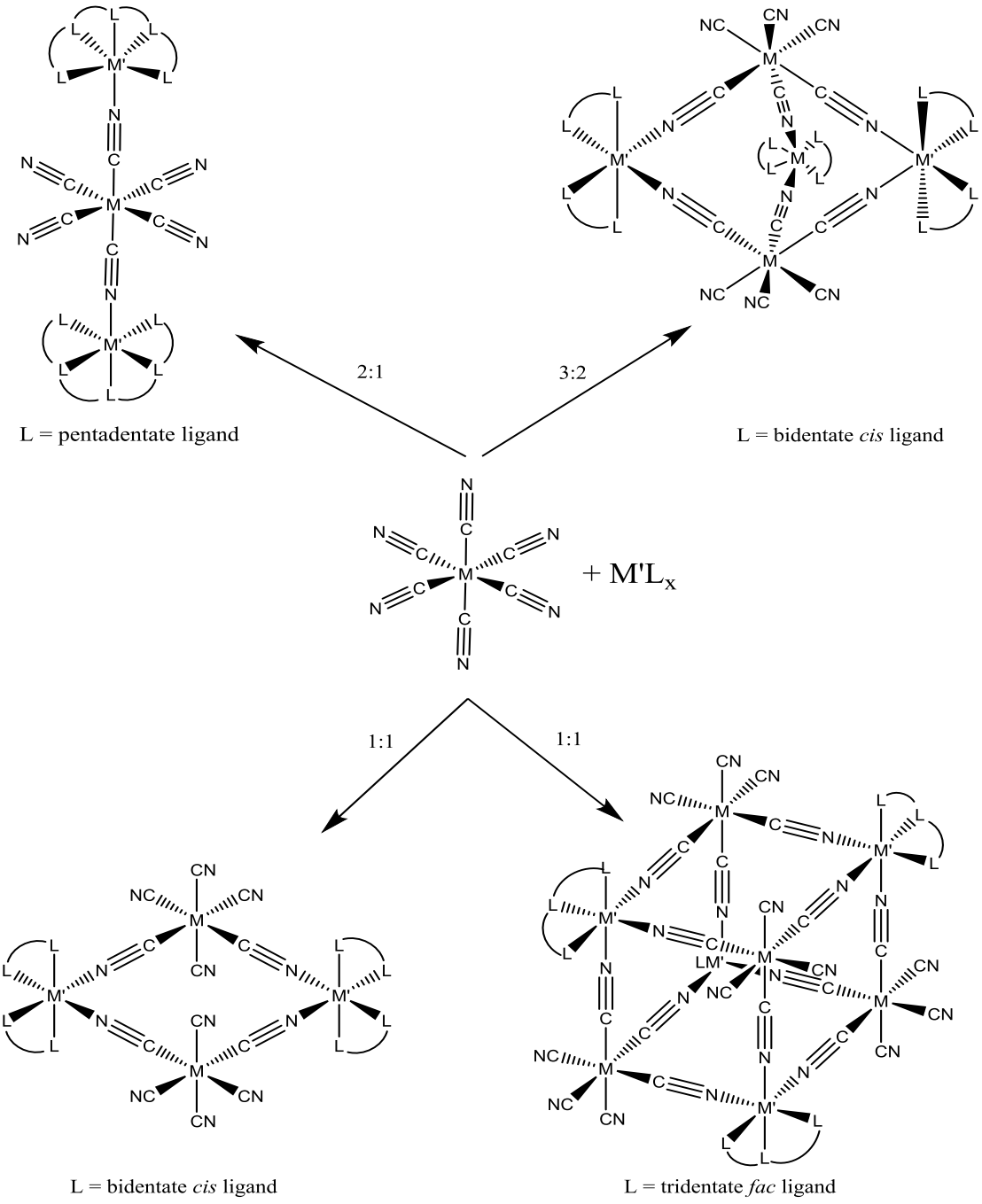

Figure 13: Building block approach for cyanide-based molecules. The geometry of the cyanometallate, geometry of the bridging metal, and the ratio between the two lead to different structures.

Thus, careful design can lead to the design of cyanometallate compounds with specific electronic configurations in order to obtain a desired exchange coupling. For example, Ruiz used density functional calculations to predict which Prussian Blue analogues would have higher Curie temperatures for ferromagnetic ordering; in particular, they calculated theoretical Curie temperatures of 552 K for $V^{II}_3[Mo^{III}(CN)_6]_2$, 355 K for $Mo^{II}_3[Cr^{III}(CN)_6]_2$, 480 K for $V^{II}_3[Mn^{III}(CN)_6]_2$, and 344 K for $V^{II}_3[V^{III}(CN)_6]_2$.[95] Mironov based his calculations on the same principle of predicting the exchange interaction based on the geometry and electronic configuration.

4d and 5d Cyanometallate Compounds

As outlined above, anisotropic coupling between metal centers is predicted to give rise to higher-barrier SMMs, and one method to accomplish this is to use heavier transition metals, notably 4d and 5d ions. The larger covalent radii of 4d and 5d metals should result in better overlap with the cyanide ligands, leading to stronger superexchange and larger *J* coupling values. Additionally, 4d and 5d metal ions exhibit greater anisotropy as a result of g-factor anisotropy and significantly larger spin-orbit coupling compared to the 3d ions. The spin-orbit coupling increases with Z_{eff}^4, which is the effective atomic number, resulting in much larger effects for 4d and 5d ions compared to 3d ions, which leads to a mixing of excited states with ground states which increases the anisotropy. The most common geometries for six, seven, and eight coordinate geometries of cyanometallates are octahedral, pentagonal bipyramidal, and dodecahedral or square antiprismatic, respectively.

With regards to cyanide-based compounds, there are a limited number of 4d/5d anions available, but the recent rise in molecular magnetism has also sparked a renaissance in transition metal cyanide chemistry, with much focus on the synthesis of novel cyanometallates.[100] Early work by the Long group resulted in the synthesis of the $Li_3[Mo^{III}(CN)_6]$[101] and $(Bu_4N)_3[Re^{IV}(CN)_7]$[102] paramagnetic precursors, both of which are d^3 systems. Additionally, the use of octacyanometallates, with d^1 isotropic electron configurations have also been used particularly of the Nb^{IV}, Mo^{V}, and W^{V} ions. Recent work in the Dunbar group has focused on the use of the $K_4[Mo^{III}(CN)_7]$ species, which provides a means to test Mironov's theoretical predictions as an S = 3/2 ion with an orbitally degenerate ground state as well. Several groups have used the $[Os^{III}(CN)_6]^{3-}$ moiety, which is an S = 1/2 with a t_{2g}^5 electron configuration.

The $(Bu_4N)_3[Re^{IV}(CN)_7]$ compound was first isolated by Bennet and Long in 2003, and it adopts a pentagonal bipyramidal geometry, resulting in an S = 1/2 orbitally degenerate ground state.[102] The anion forms star-like clusters with $[M^{II}(PY5Me_2)(CH_3CN)](PF_6)_2$ (M^{II} = Mn, Ni, Co, Cu; $PY5Me_2$ = 2,6-bis(1,1-bis(2-pyridyl)ethyl)pyridine), with the $[Mn^{II}(PY5Me_2)]_4[Re^{IV}(CN)_7]$ compound with an effective barrier of 33 cm^{-1} being the first redox-switchable SMM (Figure 14),[103] while the $[Co^{II}(PY5Me_2)]_4[Re^{IV}(CN)_7]$ exhibits charge transfer properties.[104] Attempts to incorporate the $[Re^{IV}(CN)_7]^{3-}$ anion into complexes with Mn^{II}(SB) (SB = Schiff base) resulted in three-dimensional networks with complicated magnetic properties but no hysteresis was observed.[105-106] Apart from these few examples with the $[Re^{IV}(CN)_7]^{3-}$ anion, the Re^{IV} ion has also been incorporated into heteroleptic building blocks, namely

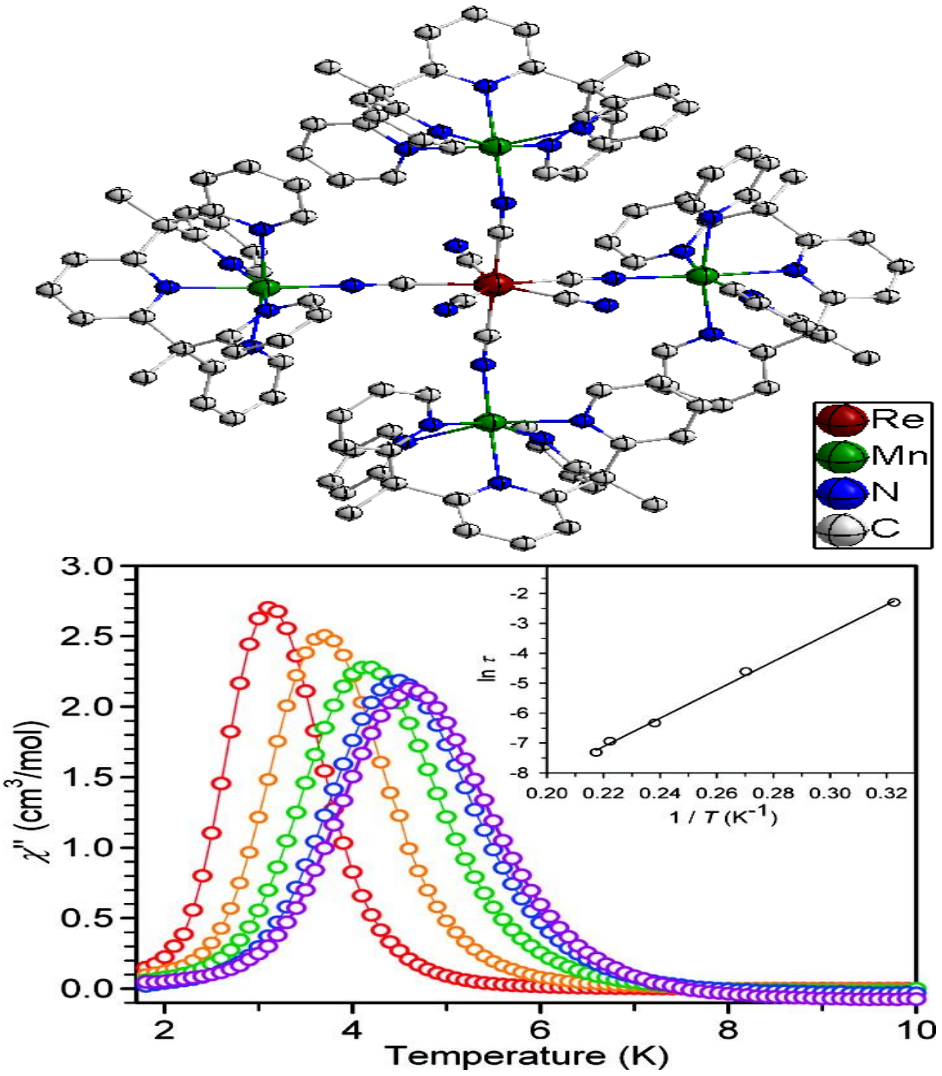

Figure 14: Molecular structure and out-of-phase signal for $[(Mn^{II}PY5Me_2)_4Re^{IV}(CN)_7]$. Used with permission, copyright American Chemical Society.

$[Re^{IV}Cl_4(CN)_2]^{2-}$, which has been used to synthesize several chain magnets, including a $Mn^{II}Re^{IV}(CN)_2$ single chain magnet with U_{eff} = 31 cm^{-1},[107] and a $Cu^{II}Re^{IV}(CN)_2$ zigzag chain with the largest ferromagnetic exchange coupling reported for a cyanide ligand, with J = +29 cm^{-1}.[108]

The $[Os^{III}(CN)_6]^{3-}$ anion has been used in several cases as an anisotropic building block with its S =1/2 degenerate ground state. The first examples were from the Dunbar group, which involved synthesizing Prussian Blue analogues of the formula $[M^{II}(tmphen)_2]_3[Os^{III}(CN)_6]_2$ (M^{II} = Ni and Fe, tmphen = 3,4,7,8-tetramethylphenanthroline); the Ni complex exhibits ferromagnetic coupling and behaves as a ferromagnet with T_C = 6.2 K,[109-110] while the Fe compound displays interesting photomagnetism via a charge-transfer-induced spin transition (CTIST).[111] A Prussian Blue analog, $Co^{II}_3[Os^{III}(CN)_6]_2$, was also reported to show CTIST and Temperature Induced Excited Spin State Trapping (TIESST) and magnetic ordering below 37 K.[112] A few linear molecules have also been reported: the first was the trinuclear complex $(Et_4N)[Mn^{III}(5\text{-Brsalen})(CH_3OH)]_2[Os^{III}(CN)_6]$ (5-Brsalen = *N,N'*-ethylenebis(5-bromomsalicylideneiminato)), the first reported osmium based SMM with Ising ferromagnetic exchange coupling between the Mn^{III} and Os^{III} ions (J = +30.6 cm^{-1}) and antiferromagnetic coupling between trimers; the compound exhibits an effective barrier of 13 cm^{-1}.[113] A comparison to the Fe analogue, which exhibits weaker ferromagnetic exchange (J = +5.8 cm^{-1}) and an effective barrier of 1.2 cm^{-1}, supports the hypothesis that the spin-orbit coupling and greater overlap from diffuse orbitals of the Os ion results in a larger Ising exchange that leads to the higher blocking temperature. Dunbar *et al.*, also synthesized a series of linear trinuclear complexes with the formula $(PPN)[Mn^{III}(salphen)(CH_3OH)]_2[M^{III}(CN)_6]$ (PPN = bis(triphenylphosphoranylidene) ammonium, salphen = N,N'-bis(salicylidene)1,2-diaminobenzene, and M^{III} = Fe, Ru, Os); all compounds show SMM behavior that can be turned on or off depending on whether

there is interstitial methanol or not (desolvation of methanol leads to SMM behavior and an open hysteresis loop), and this solvation/desolvation is reversible.[114] All three compounds exhibit ferromagnetic coupling, with J_{MnOs} = + 7.7 cm^{-1}, J_{MnRu} = +4.0cm^{-1}, and J_{MnFe} = +4.5cm^{-1} for the desolvated complexes; the solvated compounds exhibit increased coupling as compared to the desolvated compounds. The AC susceptibility measurements revealed increasing effective barriers for the desolvated compounds of 15.4 cm^{-1} for Fe, 17.0 cm^{-1} for Ru, and 29.2 cm^{-1} for Os, which have higher barriers as compared to the solvated compounds. Another example is a heptanuclear complex where six Mn^{III} ions are bonded to the $[M^{III}(CN)_6]^{3-}$ (M^{III} = Fe, Os) cyanometallate and the exchange coupling is much stronger for osmium than for iron and there is SMM slow relaxation for the osmium complex.[115] A single chain magnet was reported by Vostrikova and co-workers with the formula $[Mn^{III}(acacen)Os^{III}(CN)_6]_\infty$ (acacen = N,N'-ethylenebis(acetylacetonylideneaminato)); the molecule has a calculated barrier of 11 cm^{-1}.[116] Finally, the crystal structure of $[Os^{IV}(CN)_7]^{3-}$ was recently reported, but the compound is diamagnetic and no further studies have been reported for this anion.[117]

The $[Mo^{III}(CN)_7]^{4-}$ anion was first synthesized in the 1930s,[118] but, until recently, it was only studied from a structural and spectroscopic perspective. Kahn was the first to report magnetic materials based on this anion in the 1990s with a series of 2D and 3D magnets with antiferromagnetic coupling to the $Mn^{II}(H_2O)_x$ units.[119-123] The Mn^{II}—Mo^{III} coupling was initially thought to be ferromagnetic, although it was later found to be antiferromagnetic on the basis of neutron diffraction studies and DFT calculations; the non-cancellation of spins results in ferrimagnetic ordering, explaining the initial magnetic

observations.[124] The materials also contain multiple phases,[120, 123] which further complicates interpretation of the magnetic properties, nevertheless the results support Mironov's theoretical predictions about anisotropic exchange coupling. Since this time there have been several other 2D and 3D complexes based on this anion, but the most notable result is $V^{II}_2[Mo^{III}(CN)_7]\cdot(pyrimidine)_2\cdot 2H_2O$ reported in 2010 with a Curie temperature of 110 K,[125] supporting theoretical calculations by Ruiz that Mo^{III} ions can be used to form high T_C magnets. Other recent results include several zigzag chains that consist of linkage isomers of Mo^{III} and Mn^{II} ions;[126-128] one of the chains has an energy barrier of 48 cm^{-1}, which results from anisotropic Ising exchange. More recently, chains have been reported by Wang including two $Fe^{II}Mo^{III}$ compounds with different topologies that both show magnetic ordering below 65 K.[129]

The Dunbar group has also worked extensively with the $[Mo^{III}(CN)_7]^{4-}$ moiety, isolating the first discrete complexes with the anion. The first example was reported in 2010 when the docosanuclear complex $[Mn^{II}(dpop)(H_2O)_2]_2[[Mo^{III}(CN)_7]_8[Mn^{II}(dpop)]_{10}[Mn^{II}(dpop)(H_2O)]_4]\cdot xH_2O$ (dpop = 2,13-dimethyl-3,6,9,12,18-pentaazabicyclo-[12.3.1]octadeca-1(18),212,14,16-pentaene), or $[Mo^{III}_8Mn^{II}_{14}]$ was synthesized. [130] The complex, which is a large loop with two cross-links and four terminal Mn^{II}(dpop) appendages, has an S = 31 ground state which is the largest value reported for a cyanide compound. The Mo^{III}—Mn^{II} coupling is predominantly antiferromagnetic, although no coupling constant could be extracted due to the complicated structure. The $[Mo^{III}_8Mn^{II}_{14}]$ molecule exhibits spin glass behavior but no SMM behavior. A similar 2D structure using the same building blocks but in different

ratios exhibits a crystal-to-crystal transformation based on dehydration; the magnetic properties switch from a soft magnet to a hard magnet with dehydration.[131] In 2013 a series of linear trinuclear compounds were reported with Mn(SB) (SB = Schiff base) and the $[Mo^{III}(CN)_7]^{4-}$ anion and all three compounds exhibit antiferromagnetic coupling (Figure 11).[76] Two complexes have the Mn ions bonded through the equatorial cyanides of the heptacyanomolybdate, and they behave as simple paramagnets with no SMM behavior. The third has the Mn ions bonded through axial cyanides to the Mo ion, resulting in Ising anistropic exchange and SMM behavior with an effective barrier of 40.5 cm^{-1} and hysteresis to 3.2 K. Finally, a reversible on-off switching of SMM behavior was observed for a trinuclear $[Mn^{II}(L)(H_2O)]_2[Mo^{III}(CN)_7]\cdot 2H_2O$ (L = N,N'-bis[(1H-imidazol-4-yl)methylene]-2,2-dimethylpropane-1,3-diamine) complex, for which the switching depends on the crystal-to-crystal transformation as a result of dehydration of the water molecules; the solvated compound exhibits SMM behavior and a barrier of 45 cm^{-1}, whereas dehydration leads to simple paramagnetic behavior.[132] Both complexes display antiferromagnetic coupling between metal centers, and the Ising anistropic exchange between the metal ions also contributed to the SMM in the hydrate compound.

The hexacyanomolybdate anion has been isolated in several oxidation states, but the $[Mo^{III}(CN)_6]^{3-}$ anion has been the most studied. The Long group first reported its synthesis and characterization in 2001,[101] which they used to prepare a discrete star-like complex with the formula $[V^{II}(PY5Me_2)]_4[Mo^{III}(CN)_6](PF_6)_5$[133] which contains two terminal cyanides that are *cis* to each other. The magnetic properties reveal antiferromagnetic coupling with a J value of -61 cm^{-1} and a $S = 9/2$ ground state. Several

compounds have also been obtained by loss of a cyanide ligand from the $[Mo^{III}(CN)_7]^{4-}$ anion, resulting in the formation of $[Mo^{III}(CN)_6]$ *in situ*. The first examples were reported by the Dunbar group, namely the two pentanuclear trigonal bipyramidal complexes of formula $[M^{II}(tmphen)_2]_3[Mo^{III}(CN)_6]_2$ (M^{II} = Co, Ni); both complexes exhibit ferromagnetic coupling although no exchange constants were reported as a result of the complexity of the system and neither compound showed SMM behavior.[134] The most interesting result is the trigonal bipramidal complex, $[V^{II}(tmphen)_2]_3[Mo^{III}(CN)_6]_2$ also reported by Dunbar *et al*., which exhibits antiferromagnetic coupling and has the largest recorded antiferromagnetic exchange coupling constant of -114 cm^{-1} for a cyanide molecule.[135]

The octacyanometallates have been much more extensively studied compared to the hepta- and hexacyanometallates owing to their ease of synthesis and the stability of the anions.[136] In particular, the Mo^V and W^V ions are the most prevalent, although Nb^{IV} is also known albeit less studied. In all cases, the anions have a d^1 electronic configuration. Most polynuclear complexes involve extended structures, including 1D chains, 2D grids and layers, and 3D networks; few discrete molecules are known.[100, 137-139] The extended systems can vary drastically based on synthetic conditions, including choice of ligand, solvent, and reactant ratios. Most examples involved use of the Mn^{II} ion, although other 3d and 4f ions have also been studied. Among the molecules, the most common structure is the $M^{II}_9M'^{V}_6$ pentadecanuclear architecture (M^{II} = Mn, Co, and Ni; M′ = Mo and W; Figure 15c);[140-142] the Mn compound does not exhibit SMM behavior but the Co and Ni compounds are SMMs; the Co—M^V coupling is antiferromagnetic while the Ni—M^V

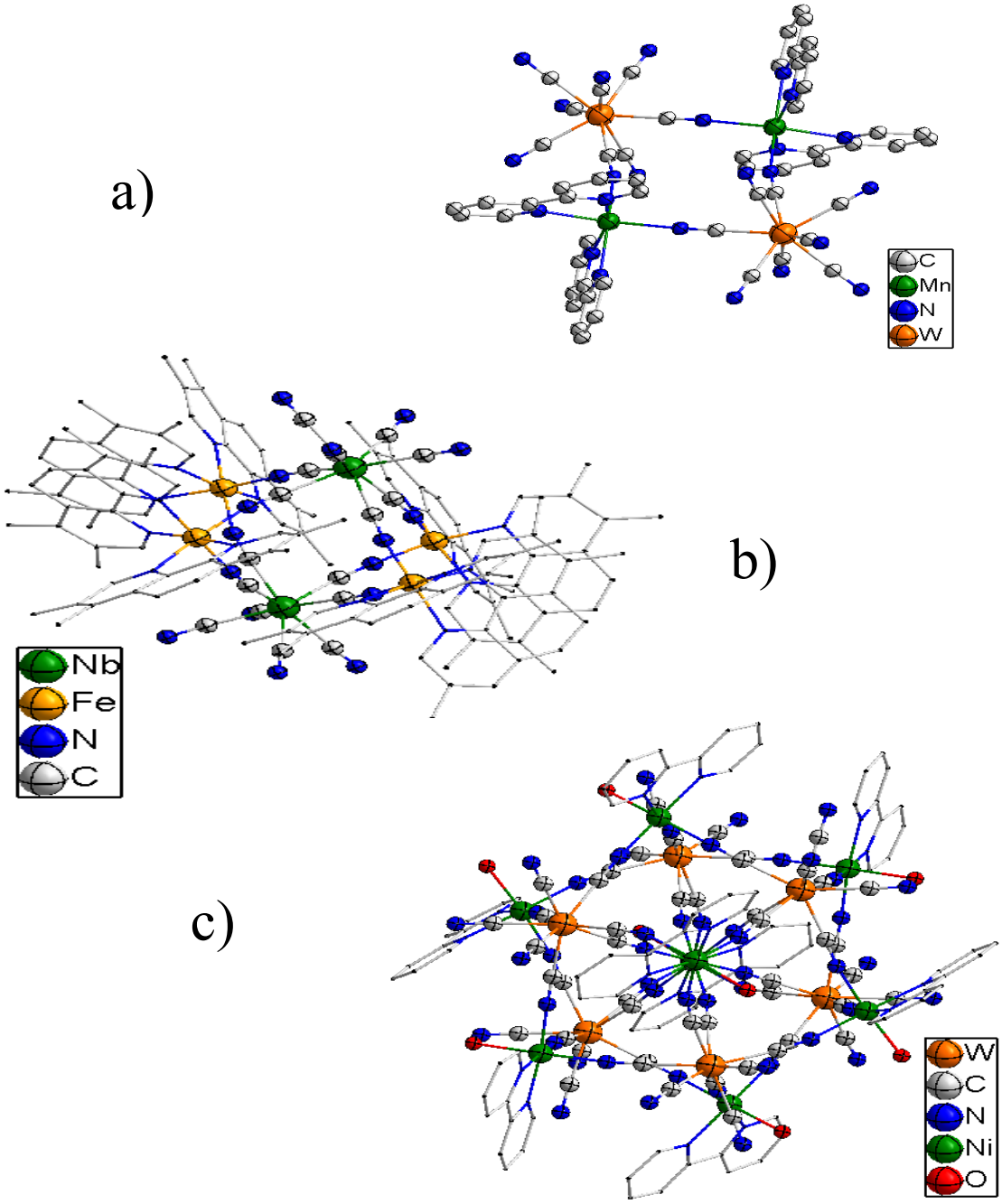

Figure 15: Molecular structures of various geometries utilizing the octacyanometallate anion: a) square $M_2[M'(CN)_8]$ geometry, b) $M_4[M'(CN)_8]_2$ complex, and c) $M_9[M'(CN)_8]_6$ structure.

coupling is ferromagnetic. The other common geometries are tetranuclear squares (or rectangles to be more precise) $M^{II}_2M'_2$ (M^{II} = Mn and M′ = $[W^V(CN)_8]^{3-}$; Figure 15a)[143] and the hexanuclear complexes $M^{II}_4M'_2$ (M^{II} = Mn, Fe, and Co; M′ = Nb^{IV}, Mo^V, and W^V octacyanide) with an octahedral structure (Figure 15b).[144-146] The Mn_4Nb_2 compound has an *S* = 9 ground state as a result of antiferromagnetic coupling and exhibits a magnetocaloric effect, while the $Fe^{II}_4Nb^{IV}_2$ exhibits antiferromagnetic interactions in addition to a spin crossover (SCO) transition and a light-induced excited spin state trapping (LIESST) effect.[145] The $Co^{II}_4Nb^{IV}_2$ has complicated magnetic properties and no analysis of the magnetic data were attempted.[145] Finally, the $[W^V(CN)_6(bpy)]^-$ anion (bpy = 2,2′-bipyridine) has also been used as a metalloligand and adopts a similar geometry to its homoleptic analogue. Bimetallic and trimetallic complexes have been synthesized, including 1D and 2D polymers with both 3d and 4f metals.[147-150]

Summary of work presented in dissertation

In the present work, synthesis and characterization studies were carried out to determine the effect of 4d and 5d anisotropy as a result of orbital degeneracy and spin-orbit coupling on anisotropic exchange coupling between metal centers in polynuclear complexes. In Chapter II, the synthesis and characterization of new heptacyanometallate(IV) anions for Mo and W are reported along with attempts to reduce these compounds to the trivalent state. Chapter III details the synthesis of polynuclear complexes using the heptacyanometallate(IV) anions from Chapter II with various moieties, including 3d and 4f metal ions. Chapter IV describes the synthesis and characterization of compounds prepared from $[M^{II}(PY5Me_2)(CH_3CN)]^{2+}$ and

$(Bu_4N)_3[M^V(CN)_8]$ (M^{II} =Mn, Fe, Ni, Co, and Cu; M^V = Mo, W). Chapter V details the synthesis and characterization of 4d and 5d compounds with the Tp* ligand (Tp* =tris(3,5-dimethyl-1-pyrazolyl)borate), which enforces a trigonal geometry on the metal center. Chapter VI concludes with a summary of the work presented herein and an outlook on the future of molecular magnetism.

CHAPTER II

NEW HEPTACYANOMETALLATE(IV) ANIONS*

Introduction

The field of transition-metal cyanide chemistry, and, indeed, coordination chemistry, dates back to the discovery of Prussian Blue, $Fe_4[Fe(CN)_6]_3 \cdot 14–16H_2O$, by Diesbach and Dippel over three centuries ago. The field has enjoyed a remarkable rebirth in the past two decades owing, in large measure, to the prominent role of cyanide complexes as building blocks for molecular materials including single molecule magnets (SMMs).[151] Of particular interest in the vein of new directions in the field is the synthesis of new paramagnetic 4d and 5d homoleptic cyanometallates.[100] These compounds engage in stronger magnetic interactions with other spin centers compared to 3d analogues as a result of more diffuse valence orbitals and exhibit much higher magnetic anisotropy owing to increased spin-orbit coupling and mixing of the ground state with low-lying excited states. In addition, the heavier elements also tolerate a wider range of oxidation states than their 3d congeners, a situation that allows for more facile tuning of the electronic configuration. Interest in this topic in the Dunbar group was piqued by theoretical

* Reprinted with permission from "The Heptacyanotungstate(IV) Anion: A New 5d Transition-Metal Member of the Rare Heptacyanometallate Family of Anions." By Birk, F. J.; Pinkowicz, D.; Dunbar, K. R. *Angewandte Chemie International Edition*, **2016**,*55*, 11368-11371.

calculations that predict 4d and 5d cyanometallates with orbital degeneracy in the ground state are promising candidates for the design of high blocking temperature SMMs owing to highly anisotropic exchange coupling.[79, 152] In particular, the isoelectronic anions $[Mo^{III}(CN)_7]^{4-}$ and $[Re^{IV}(CN)_7]^{4-}$ were identified as important examples owing to the orbital degeneracy resulting from a d^3 electronic configuration in a pentagonal bipyramidal geometry.[75] The only known 3d heptacyanometallate is $[V^{III}(CN)_7]^{4-}$ which was structurally characterized in 1972.[153]

The known homoleptic cyanotungstate species are $K_4[W^{IV}(CN)_8]$ and $(cat)_3[W^{V}(CN)_8]$ (cat = Na, K, Ag, Cs, and Bu_4N), with the former anion being diamagnetic and the latter one being paramagnetic with S=1/2. [136, 154-155] These anions have been extensively studied for their structural, chemical and magnetic properties. Previous reports of sub-coordinate tungsten cyanide species include $K_4[W^{II}(CN)_6]$ via reduction with H_2 by Yoo and coworkers in 1963, and exposure to air was reported to yield the $K_3[W^{III}(CN)_6]$ salt.[156] These compounds were later found to be $K_2[W(CN)_5H_2O]$ with an unknown impurity as determined by elemental analysis.[157] The $K_5[W(CN)_7H]\cdot 2H_2O$ and $K_5[W(CN)_7]\cdot H_2O$ species reported by Soares and Griffth in 1981 were characterized by NMR, IR, and Raman spectroscopies as well as elemental analysis.[158] The preparation of $K_5[W(CN)_7H]\cdot 2H_2O$ was reported to occur from the reaction of $K_3W_2Cl_9$ with excess aqueous KCN under UV radiation for an unspecified time; attempts to reproduce the synthesis led only to the $K[W^{IV}(CN)_8]$ species, as confirmed by our group as well as Long and coworkers.[159] In all of these earlier publications, the lack of crystallographic evidence leaves doubt as to the exact formulae

and structures of these products, and, in any case, the syntheses have proven to be unreproducible.

As mentioned in the introduction to this dissertation, the $[W^{III}(CN)_7]^{4-}$ moiety is predicted to yield improved SMMs as compared to its molybdenum analogue. Efforts directed at synthesizing this target are described in this chapter. The resulting compounds were characterized by a number of physical methods. Specifically, the synthesis and characterization of the $[M^{IV}(CN)_7]^{3-}$ anion is reported for both molybdenum and tungsten.

Experimental

Unless otherwise stated, all reactions were performed in a drybox or on the Schlenk-line under an inert atmosphere. The solvent CH_3CN (Sigma Aldrich) was pre-dried over 3Å molecular sieves and distilled over 3Å sieves under nitrogen and Et_2O was passed through an activated alumina column (MBraun solvent system). Anhydrous THF (Sigma Aldrich), anhydrous N,N-dimethylformamide (DMF, Alfa Aesar), and anhydrous propylene carbonate (PC, Sigma Aldrich) were used as received. All solvents were stored over molecular sieves in the glovebox. The reagents WCl_6 (Aldrich Chemical Company), Cp_2Co (Beantown Chemical), $(Cp^{Me})_2Co$ (Sigma Aldrich), were purchased and used as received. The starting materials $(Bu_4N)_3[W(CN)_8]$,[160] $(Bu_4N)_3[Mo(CN)_8]$,[160] K(benzophenone),[161] and KC_8[162] were prepared by literature methods.

Synthesis

$[W^{VI}Cl_3O(THF)]_2$-μ-O·2THF (1)

A 100 mL Schlenk flask was charged with 0.5410 g (1.36 mmol) of WCl_6 and ~40 mL of dry CH_2Cl_2 were added to another Schlenk flask; both flasks were set up on the

Schlenk-line under N_2, and the flask with WCl_6 was cooled to -40 ºC in a liquid nitrogen/acetonitrile slush bath. To the chilled flask was added two of 20 mL portions of THF which resulted in color changes to green and then red-brown; dichloromethane was added after five minutes of stirring and the solution was warmed to room temperature which resulted in an emerald green solution and precipitate. The flask was pumped into the glovebox, and X-ray quality crystals were grown in the freezer from slow vapor diffusion of diethyl ether into the filtrate.

$(Bu_4N)_3[W^{IV}(CN)_7]$ (2)

A vial was charged with 2.21 g (2.02 mmol) of $(n\text{-}Bu_4N)_3[W^{V}(CN)_8]$ and 0.38 g (2.03 mmol) of Cp_2Co. Addition of 10 mL of CH_3CN with stirring resulted in the formation of a yellow-green solution with a green precipitate. The reaction was stirred overnight and filtered to give a yellow-green filtrate and a green precipitate. The filtrate was transferred to a large vial and diethyl ether was added to precipitate any remaining cobaltocenium by-product. The solution was then filtered to yield a yellow filtrate which was then set up for slow vapor diffusion with diethyl ether to yield crystals of the product. The crystals were collected by filtration and washed with diethyl ether. Yield: 1.225 g (55%). Elemental analysis: calculated $C_{55}N_{10}H_{108}W_1$: C 60.42, H 9.96, N 12.81; found C 60.21, H 10.03, N 12.72.

$(Cp_2Co)_4[W^{IV}(CN)_8]\cdot 3CH_3CN$ (3)

This compound was obtained as a by-product of the synthesis of **2**. A dark green powder was obtained when **2** was filtered the first time. The second filtration typically yielded a lighter green precipitate. In a reaction with 0.8495 g (0.7589 mmol) of

$(Bu_4N)_3[W^V(CN)_8]$ and 0.1444 g (0.7635 mmol) of Cp_2Co in CH_3CN, 0.0924 g of a green by-product was obtained. An X-ray quality crystal was obtained in the second crop during crystallization of **2**. Mass of product: 0.0924 g, yield: 9.6 %.

$(Bu_4N)_3[Mo^{IV}(CN)_7]$ (4)

A vial was charged with 0.538 g (0.522 mmol) of $(n\text{-}Bu_4N)_3[Mo^V(CN)_8]$ and dissolved in ~10 mL of CH_3CN to give a yellow solution. The addition of 0.103 g (0.5446 mmol) of Cp_2Co resulted in the formation of a dark green precipitate and a dark yellow solution. The reaction was stirred for a week and then filtered to give a dark yellow-brown filtrate and a green precipitate. The filtrate was transferred to a vial and diethyl ether was added to precipitate any remaining Cp_2Co by-product. The solution was filtered once again to yield a brownish white cloudy filtrate with no precipitate. The filtrate was then transferred to large vials for slow vapor diffusion. The resulting crystals of **4** were collected by filtration; yield: 0.3593 g (69%). Elemental analysis: calculated $C_{55}N_{10}H_{108}Mo_1$: C 65.70, H 10.83, N 13.93**;** found C 65.61, H 10.82, N 13.73**.**

$(Cp_2Co)_4[Mo^{IV}(CN)_8]$ (5)

This compound was obtained as a by-product of the synthesis of **4**. A dark green powder was isolated when **4** was filtered the first time and the second filtration typically yielded a lighter green precipitate. For a reaction using 0.5615 g (0.5443 mmol) of $(Bu_4N)_3[Mo^V(CN)_8]$ and 0.1070 g (0.5658 mmol) of Cp_2Co in CH_3CN, 0.1064 g of green by-product was obtained from the first filtration and 0.0269 g in the second filtration. Mass of product: 0.1333 g, yield: 20.1 %.

$(Bu_4N)_3[W^{IV}(CN)_7]$ + KC_8 (6)

A vial was charged with 0.1376 g (0.1258 mmol) of $(Bu_4N)_3[W^{IV}(CN)_7]$ and a magnetic stir bar. Addition of ~10 mL CH_3CN produced a colorless solution upon stirring; addition of 0.0235 g (0.1738 mmol, 1.38 equivalents) of KC_8 produced a black suspension (due to the graphite) and a yellow solution which was stirred overnight. The suspension was then filtered through Celite® to yield a yellow filtrate. A portion of the filtrate was set up for slow vapor diffusion with Et_2O to grow X-ray quality crystals and the rest of the filtrate was stored in a vial. X-ray quality crystals were obtained, and the product was determined to be the starting material **2**.

$(Bu_4N)_3[W^{IV}(CN)_7]$ + Cp_2Co (7)

A vial was charged with 0.203 g (1.07 mmol) of Cp_2Co and 0.554 g (0.495 mmol) of $(Bu_4N)_3[W^{IV}(CN)_8]$. Addition of 15 mL of CH_3CN with stirring yielded a red solution and a turquoise crystalline precipitate. The reaction was filtered to collect a dark green-blue precipitate and a red-brown filtrate. The filtrate was set up for slow vapor diffusion with Et_2O. X-ray quality crystals were obtained, and the product was determined to be the starting material **2**.

$(Bu_4N)_3[W^{IV}(CN)_7]$ + $(Cp^{Me})_2Co$ (8)

A vial was charged with 0.154 g (0.466 mmol) of Cp^*_2Co and a magnetic stir bar. Another vial containing 0.500 g (0.4576 mmol) of $(Bu_4N)_3[W^{IV}(CN)_7]$ was dissolved in CH_3CN to give a colorless solution which was added to the vial containing Cp^*_2Co. The resulting dark yellow filtrate with a violet-green precipitate was stirred for two hours after which time it was filtered through a fine frit. The filtrate was golden in color and the

precipitate was dark violet-black. A slow vapor diffusion was set up with an aliquot of the filtrate and Et_2O which yielded X-ray quality crystal. The product was determined to be the starting material **2**.

$(Bu_4N)_3[W^{IV}(CN)_7]$ + K(benzophenone) + Bu_4NPF_6 (9)

A solution of K(benzophenone) was prepared in a vial which was charged with 0.053 g (1.358 mmol) of potassium metal and 0.101 g (0.5526 mmol) of benzophenone. Addition of ~5 mL THF resulted in the formation of a dark blue solution which was stirred overnight. Another vial was charged with ~10 mL of CH_3CN and stored in a drybox cold well which was chilled liquid N_2. Another vial was charged with 0.513 g (0.4689 mmol) of $(Bu_4N)_3[W^{IV}(CN)_7]$ and 4 mL of chilled CH_3CN was added to yield a colorless solution. Then 0.178 g (0.4604 mmol) of Bu_4NPF_6 was added to the chilled solution of $(Bu_4N)_3[W^{IV}(CN)_7]$. The solution of K(benzophenone) in THF was slowly added via pipette to the solution of $(Bu_4N)_3[W^{IV}(CN)_7]$ resulting in a color change to yellow and then blue-green. The solution was stirred for ~45 minutes and then filtered over Celite®. A yellow filtrate and a red-brown precipitate were obtained. The filtrate was transferred to a vial, and an aliquot was removed for slow vapor diffusion with Et_2O. X-ray quality crystals were obtained, and the product was determined to be the starting material **2**.

$(Bu_4N)_3[W^{IV}(CN)_7]$ + Na/Hg + Bu_4NI (10)

A narrow diameter Schlenk tube was charged with 0.2000 g (0.1829 mmol) of $(Bu_4N)_3[W^{IV}(CN)_7]$ and 0.0615 g (0.1665 mmol) of Bu_4NI. The addition of ~ 15 mL CH_3CN gave a nearly colorless solution with a slight red tinge. The solution was transferred via cannula under an argon pressure to a flask containing the Na/Hg amalgam.

Stirring resulted in a yellow solution and an off-white precipitate. The solution was transferred by cannula needle to a new Schlenk tube and dried *in vacuo*, yielding a yellow solid. The dried yellow solid was then transferred to the drybox, and extracted with THF to give a yellow solution. The solution was filtered and a small amount of yellow precipitate was collected from the yellow filtrate which was treated with Et_2O to produce a yellow precipitate. An aliquot of the filtrate was used for slow vapor diffusion with Et_2O. The remaining precipitate in the Schlenk tube was extracted with CH_3CN and filtered to yield a light-yellow solution. An aliquot was used for slow vapor diffusion with Et_2O. X-ray quality crystals were obtained, and the product was determined to be the starting material **2**.

X-ray Crystallography

A green crystal of **1** was mounted on a Nylon loop using Paratone® oil and placed in a N_2 cold stream at 110 K. The data were collected on a Bruker APEX II diffractometer (MoKα radiation λ = 0.71073 Å) equipped with a CCD detector. The data sets were recorded as three ω-scans and integrated using the Bruker APEXII software package. A colorless single crystal of **2** was mounted on a nylon loop using Paratone® oil and placed in a N_2 cold stream at 110 K. The data were collected on a Bruker APEX II diffractometer (MoKα radiation λ = 0.71073 Å̊) equipped with a CCD detector. The data sets were recorded as four ω-scans and integrated using the Bruker APEXII software package. A green crystal of **3** that forms during the synthesis of **2** was mounted using paraffin oil on a cryo-loop and placed in a N_2 cold stream at 120 K. The data were collected on a Bruker D8 Quest Eco diffractometer (MoKα radiation λ = 0.71073 Å̊) equipped with a Photon50

CMOS detector. The data sets were recorded as four ω-scans and integrated using the Bruker APEX3 software package. A colorless crystal of **4** was mounted using paraffin oil on a cryo-loop and placed in a N_2 cold stream at 110 K. The data were collected on a Bruker D8 Quest Eco diffractometer (MoKα radiation λ = 0.71073 Å) equipped with a Photon50 CMOS detector. For all compounds, the multi-scan absorption correction was performed within the Bruker APEXII software using SADABS (v2014/5) or within the Bruker APEX3 software using SADABS (v2015/10).[163-164] Solution and refinement of the crystal structures were carried out using SHELXT[165] and shelXle (a graphical interface for the SHELX suite of programs), respectively.[166] Structure solution by direct methods resolved positions of all heavy atoms and most of the lighter atoms. The remaining non-hydrogen atoms were located by alternating cycles of least-squares refinements and difference Fourier maps. For **2** and **4**, one of the *n*-butyl groups of a tetrabutylammonium cation was refined as disordered in two positions using PART instruction. Hydrogen atoms were placed at calculated positions. The final refinements were performed with anisotropic thermal parameters for all non-hydrogen atoms. Images of the molecular structures were rendered using DIAMOND software for crystal structure visualization.[167] A summary of pertinent information relating to unit cell parameters, data collection, and refinement is provided in Table 1. The corresponding crystallographic information file was deposited with the Cambridge Structural Database: (**2**) CCDC-1449065, (**3**) CCDC- 1478643.

Physical Methods

IR spectra for **2** were recorded on a Nicolet iN10 FT-IR microscope; for the single crystal a Linkam thermostat was sealed under argon atmosphere to prevent decomposition;

Table 1: Crystallographic data and experimental details for compounds **1**, **2**, **3**, and **4**.

Compound	**1**	**2**	**3**	**4**
Molecular Weight	916.80	1093.36	2386.97	1005.341
Temperature (K)	110	110	120	110
Crystal System	Monoclinic	Monoclinic	Triclinic	Monoclinic
Space Group	Pn	$P2_1/c$	P-1	$P2_1/c$
a (Å)	10.087(8)	22.9799(16)	11.6766(16)	23.0019(13)
b (Å)	11.396(11)	22.999(16)	12.0115(16)	23.0491(14)
c (Å)	12.642(9)	23.007(16)	17.794(2)	22.9723(13)
α (°)	90	90	92.691(3)	90
β (°)	111.31(8)	90.440(9)	91.949(3)	90.133(2)
γ (°)	90	90	114.929(3)	90
V ($Å^3$)	1354(2)	12159(15)	2256.7(5)	12179.3(12)
Z	2	8	1	8
Color	Blue-green	Colorless	Green	Colorless
ρcalc (g/cm^3)	2.249	1.195	1.1756	1.097
μ (mm)	9.114	1.941	4.026	0.256
F(000)	868	4656	1177	4400
Crystal Size (mm)	0.05 x 0.1 x 0.15	0.180 x 0.200 x 0.350	0.07 x 0.15 x 0.20	0.128 x 0.189 x 0.523
Radiation	MoKα (λ = 0.71073)	MoKα (λ = 0.71073)	MoKα (λ = 0.71073)	MoKα (λ = 0.71073)
Index Range	-13≤h≤13 -14≤k≤14 -16≤l≤16	-29≤h≤29 -29≤k≤29 -29≤l≤29	-14≤h≤14 -15≤k≤15 -21≤l≤22	-29≤h≤29 -29≤k≤29 -29≤l≤29
2θ range (°)	3.574 to 55.414	2.504 to 53.964	6.168 to 54.388	3.952 to 27.586
Reflections collected	15178	134366	17374	572068
Unique reflections	6566	26277	9749	25200
Parameters/restraints	281, 2	1234, 51	599, 4	1234, 51
$R_1{}^a$, $wR_2{}^b$ [$I > 2\sigma(I)$]	0.0378, 0.0742	0.0370, 0.0772	0.0619, 0.1201	0.0424, 0.1053
$R_1{}^a$, $wR_2{}^b$ (all data)	0.0519, 0.0807	0.0492, 0.0812	0.0813, 0.1266	0.0518, 0.1133
GooF^c (F^2)	0.954	1.113	1.110	1.000
Largest diff. peak, hole, (e $Å^{-3}$)	1.01, -1.16	2.42, -1.41	2.120, -1.934	1.1, -1.9

$^a R = \Sigma ||F_o| - |F_c|| / \Sigma |F_o|$. $^b wR = \{\Sigma [w(F_o^2 - F_c^2)^2] / \Sigma [w(F_o^2)]^2\}^{1/2}$. ^{c}Goodness-of-fit $= \{\Sigma [w(F_o^2 - F_c^2)^2]/(n-p)\}^{1/2}$, where *n* is the number of reflections and *p* is the total number of parameters refined.

the solution of **2** was measured as a thin film of an anhydrous, oxygen-free dichloromethane solution of **2** which was placed between two polished single crystal KBr windows; all other infrared spectra were recorded on a Nicolet Nexus 470 FT-IR E.S.P spectrophotometer as Nujol® mulls between KBr plates unless otherwise noted. Electronic absorption spectra of **2** in acetonitrile were measured using a Perkin Elmer Lambda 35 double beam spectrophotometer in sealed quartz cuvettes; all other electronic absorption spectra were recorded on a Shimadzu UV-1601PC spectrophotometer. Electrochemical data were collected using a H-CH Instruments analyzer in dry solvents. The working electrode was a BAS Pt disk electrode, the reference electrode was Ag/AgCl, and the counter electrode was a Pt wire. Cyclic voltammetric measurements were performed at room temperature in specified solvents with approximately 0.1 M tetra-*n*-butylammonium hexafluorophosphate ([*n*-Bu_4N][PF_6]) as the supporting electrolyte. The $E_{1/2}$ values were referenced to the Ag/AgCl electrode without correction for the junction potentials [$E_{1/2} = (E_{p,a} + E_{p,c})/2$]. Ferrocene was added at the end of measurements as an additional reference for the $FeCp_2$/[$FeCp_2$]$^+$ couple. Elemental analysis was performed by Atlantic Microlabs, Inc., Norcross, GA. Magnetic measurements were performed on a Quantum Design MPMS-XL SQUID magnetometer equipped with a 7T superconducting magnet in the temperature range 1.8 to 300 K; the diamagnetic contribution of the plastic bag used as a sample holder was subtracted from the raw data, and core diamagnetism of the sample was corrected for using Pascal's constants.[168]

Results and Discussion

Syntheses

The synthetic goal was to isolate the $[W^{III}(CN)_7]^{4-}$ moiety as the 5d congener to the known $[Mo^{III}(CN)_7]^{4-}$ anion. By moving to the 5d analogue, the larger spin-orbit coupling and more diffuse orbitals that engage in enhanced covalent interactions are expected to lead to increased anisotropic exchange coupling, and hence improved SMM behavior. The initial strategy focused on using the WCl_6 starting material and reducing it from the hexavalent to the trivalent oxidation state followed by replacement of the chlorides with cyanide ligands. The first step of this reaction is to reduce WCl_6 with slightly more than three equivalents of the strong reducing agent KC_8. Dissolving the WCl_6 in THF leads to a series of color changes from red-burgundy to yellow to orange and then yellow-green before finally becoming an olive-green color. Upon addition of the KC_8, there is a rapid color change of the original solution to dark red, although it is somewhat difficult to ascertain the solution color due to the black graphite suspended in solution. After stirring for 3 days, the reaction was filtered through Celite® to yield a burgundy-brown filtrate. The filtrate was dried under vacuum, and redissolved in THF with stirring which generates a blue gel-like solid, an indication that a polymer has formed. Altering the reaction conditions by either changing the solvent (dichloromethane, acetonitrile), the amount of cyanide reagent (none, six, excess equivalents), or temperature (23 °C or -40 °C) does not change the formation of the blue precipitate. When the reaction was performed at -40 °C, however, green crystals were obtained that were suitable for X-ray diffraction, suggesting that the WCl_6 is acting as a catalyst for polymerization of THF.

This is consistent with previous literature results which reported that WCl_6 acts as a Lewis acid to oligomerize THF.[169] Solving the structure yielded $[W^{VI}Cl_3O(THF)]_2$-μ-O·2THF (**1**).

Given the results of reactions using WCl_6, a new starting material and synthetic route was devised. To this end, the octacyanotungstate anions, $[W^{IV/V}(CN)_8]^{4/3-}$, were chosen with the reasoning being that it would be easier to remove a cyanide rather than to reduce the W center and then replace six chlorides with six or seven cyanides. The tetravalent potassium salt, $K_4[W^{IV}(CN)_8]$, was chosen initially since it is easily synthesized and is similar to the molybdenum analogue. Attempts at reduction of $K_4[W^{IV}(CN)_8]$ with KC_8 in organic solvents such as THF or CH_3CN, however, resulted in no reaction due the fact that the potassium salt is insoluble in organic solvents and does not react, even in the presence of KC_8. In order to circumvent this issue, the cation was changed to the tetrabutylammonium cation, which, after oxidation, resulted in the $(Bu_4N)_3[W^V(CN)_8]$ starting material. This compound is soluble in acetonitrile but not THF, therefore reactions of $(Bu_4N)_3[W^V(CN)_8]$ with KC_8 were conducted in CH_3CN but yielded no reaction, likely as a result of solvent reduction. Reduction with cobaltocene Cp_2Co, however, led to the formation of a green crystalline precipitate, with concomitant changes in the solution from color from colorless to yellow. The solution was filtered to yield a yellow solution and subjected to slow vapor diffusion with diethyl ether which yielded colorless crystals of $(Bu_4N)_3[W^{IV}(CN)_7]$ (**2**). The green precipitate was found to actually be $(Cp_2Co)_4[W^{IV}(CN)_8]$ (**3**) and not the expected Cp_2CoCN, which explains why yields vary between 30 to 65%.

On the basis of electrochemistry (*vide infra*), it was thought that a reduction to $[W^{III}(CN)_7]^{4-}$ should be possible. The first several reactions focused on using reducing agents Cp_2Co (**7**), $(Cp^{Me})_2Co$ (**8**), and KC_8 (**6**) in acetonitrile which have increasing reducing strength. All three reductions result in a color change of the solution from colorless to yellow; white-colorless crystals were obtained from slow vapor diffusion. X-ray diffraction revealed that the product is the starting material $(Bu_4N)_3[W(CN)_7]$. In the case of Cp_2Co and $(Cp^{Me})_2Co$, it was thought that the reagents were not sufficiently strong to effect the reduction, while in the case of KC_8, the reduction potential of approximately -3 V (vs Ag/AgCl) is too strong and reduces the solvent. The focus then shifted to include tetrabutylammonium salts, initially to ensure there was another cation to induce crystallization and later to try to replicate the electrochemical conditions. Switching to alternative reducing agents[161] such as K(benzophenone) (**9**) or Na/Hg amalgam (**10**) were also unsuccessful in that only starting material was obtained. Switching to different solvents such as DMF were also unsuccessful.

The results obtained from attempting to incorporate the $(Bu_4N)_3[W^{IV}(CN)_7]$ into polynuclear structures indicate that the $[W^{IV}(CN)_7]^{3-}$ anion is unstable and decomposes to the more thermodynamically stable $[W^{IV}(CN)_8]^{4-}$ anion (see Chapter III). Whether it is a result of an unstable electronic configuration or molecular geometry is not certain. The molybdenum analogue was synthesized in order to compare the 4d and 5d analogues with regards to stability. The synthesis of $(Bu_4N)_3[Mo(CN)_7]$ follows the same route via reduction with Cp_2Co in acetonitrile to yield (**4**) and $(Cp_2Co)_4[Mo(CN)_8]$ (**5**), the latter of which was removed via filtration to yield the former as a yellow filtrate. The compound

can be isolated in similar yields by crystallizing from diethyl ether, and its chemistry is similar to the tungsten congener.

Single Crystal X-ray Diffraction Studies

X-ray diffraction data for crystals of **1** revealed that the compound crystallizes as green crystals in the Pn space group. The molecule consists of two tungsten metal ions each in a distorted meridional octahedral geometry with three chloride ligands, and three oxygen ligands (Figure 16). A summary of bond distances and angles is presented in Table 2. The three W-Cl bond distances are 2.3578(43) Å, 2.3678(51) Å, and 2.3824(69) Å, consistent with previously reported W^{VI}—Cl bond distances.[170] The terminal and bridging W—O bond distances are 1.6887(123) Å and 2.3678(51) Å respectively and the W—O distance for the tetrahydrofuran adduct is 2.3015(88) Å which are in accord with the literature for a terminal oxide, a bridging oxide, and a dative bond, respectively.[170-171] The separation between the tungsten atoms is 3.7644(23). The W_1—O_1—W_2 bond angle is 177.992(738)° which is close to a linear geometry. The *cis* bond angles around the tungsten centers are distorted from 90° and vary between 81.607(263)° and 100.594(612)°. The *trans* angles are 164.119(400)°, 164.528(144)°, and 177.521(531)°, which deviate significantly from 180° in an ideal octahedral geometry.

X-ray crystallographic analysis of a single crystal of **2** reveals that the anion in $(n\text{-}Bu_4N)_3[W^{IV}(CN)_7]$ adopts a slightly distorted pentagonal bipyramidal (PBP) geometry, as depicted in Figure 17, similar to both the $[Mo^{III}(CN)_7]^{4-}$ and $[Re^{IV}(CN)_7]^{3-}$ analogues.[102, 172] Relevant bond distances and bond angles are listed in Table 3. The W-C bond lengths vary between 2.148(4) and 2.172(4) Å, longer than the W—C distances of 2.118–2.154 Å

Table 2: Bond distances and angles for $[WCl_3O(THF)]_2$-μ-O·2THF (1). O_1 is the bridging oxygen, O_2 is the terminal oxo, and O_3 corresponds to the THF oxygen bonded to tungsten.

Bond Distance (Å) or Angle (°)	$[WCl_3O(THF)]_2$-μ-O·2THF
W_1—W_2	3.7644(23)
W_1—O_1	2.3678(51)
W_1—O_2	1.6887(123)
W_1—O_3	2.3015(88)
W_1—Cl_1	2.3824(69)
W_1—Cl_2	2.3578(43)
W_1—Cl_3	2.3678(51)
W_1—O_1—W_2	177.992(738)
Cl_1—W_1—O_1	164.119(400)
Cl_1—W_1—O_3	82.303(299)
Cl_1—W_1—O_2	95.286(546)
Cl_1—W_1—Cl_2	88.110(159)
Cl_1—W_1—Cl_3	88.337(171)
O_1—W_1—O_3	81.817(467)
O_1—W_1—O_2	100.594(612)
O_1—W_1—Cl_2	89.858(353)
O_1—W_1—Cl_3	89.479(357)
O_2—W_1—O_3	177.521(531)
O_2—W_1—Cl_2	97.436(451)
O_2—W_1—Cl_3	97.781(476)
O_3—W_1—Cl_2	83.098(253)
O_3—W_1—Cl_3	81.607(263)
Cl_2—W_1—Cl_3	164.628(144)

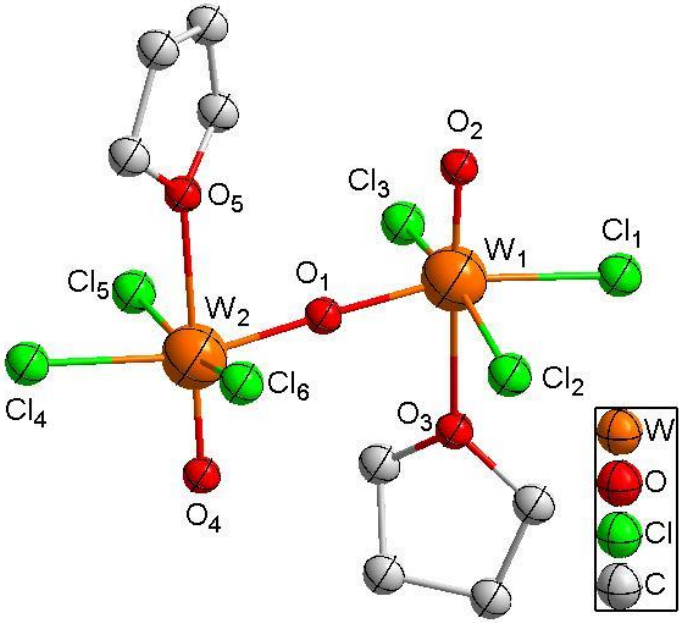

Figure 16: Molecular structure of $[WCl_3O(THF)]$-μ-O·2THF (1); orange = tungsten, green = chloride, red = oxygen, and grey = carbon.

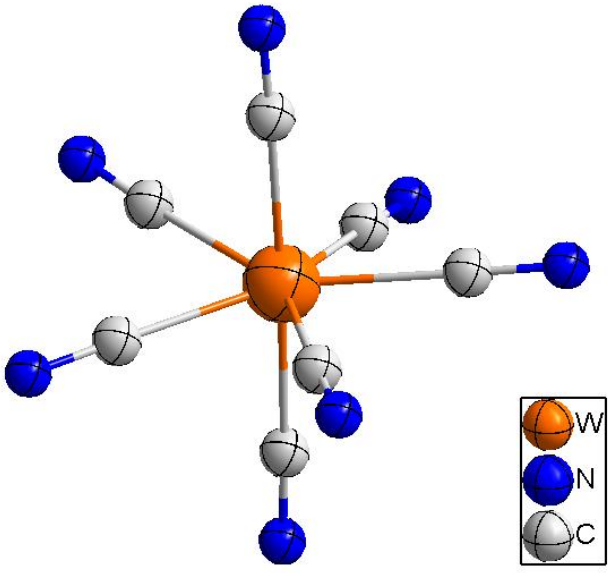

Figure 17: Molecular structure of the pentagonal bipyramidal anion $[W^{IV}(CN)_7]^{3-}$ (**2**)

Table 3: Bond distances and angles for $(Bu_4N)_3[W(CN)_7]$ (**2**)

Select Atoms	Bond Distance (Å)	Select Atoms	Bond Angle (°)
W_1—C_1	2.172(4)	C_2—W_1—C_1	177.07(15)
W_1—C_2	1.162(4)	C_2—W_1—C_4	82.77(16)
W_1—C_3	2.157(4)	C_2—W_1—C_6	89.57(16)
W_1—C_4	2.163(4)	C_2—W_1—C_7	85.41(16)
W_1—C_5	2.148(4)	C_3—W_1—C_1	82.41(15)
W_1—C_6	2.167(4)	C_3—W_1—C_2	97.04(15)
W_1—C_7	2.171(4)	C_3—W_1—C_4	72.08(15)
N_1—C_1	1.143(5)	C_3—W_1—C_6	145.48(15)
N_2—C_2	1.149(5)	C_3—W_1—C_7	74.25(14)
N_3—C_3	1.148(5)	C_4—W_1—C_1	99.76(15)
N_4—C_4	1.154(5)	C_4—W_1—C_6	142.44(16)
N_5—C_5	1.151(5)	C_4—W_1—C_7	142.48(14)
N_6—C_6	1.148(5)	C_5—W_1—C_1	86.05(15)
N_7—C_7	1.148(5)	C_5—W_1—C_2	96.15(15)
		C_5—W_1—C_3	139.96(14)
		C_5—W_1—C_4	72.35(15)
		C_5—W_1—C_6	72.02(15)
		C_5—W_1—C_7	144.54(14)
		C_6—W_1—C_1	89.29(16)
		C_6—W_1—C_7	72.57(15)
		C_7—W_1—C_1	91.68(14)
		N_1—C_1—W_1	177.9(4)
		N_2—C_2—W_1	177.5(4)
		N_3—C_3—W_1	177.2(3)
		N_4—C_4—W_1	177.5(4)
		N_5—C_5—W_1	177.8(4)
		N_6—C_6—W_1	179.4(4)
		N_7—C_7—W_1	178.6(4)

in $Na_3[W^V(CN)_8]$.[173] The bond lengths are also slightly longer than those reported for Mo^{IV}—CN in $K_4[Mo^{IV}(CN)_8]$ whose average is 2.163 Å as expected.[174] The C-N triple bond distances in **1** range from 1.142(5) to 1.155(5) Å which is typical for C—N bonds in cyanometallates. The W—C bonds are also longer than those of the $(n\text{-}Bu_4N)_3[Re^{IV}(CN)_7]$

and $K_4[Re^{III}(CN)_7]\cdot 2H_2O$ analogues; these vary from 2.064–2.123 Å to 2.077–2.099 Å, respectively.[102] The axial C-W-C bond angles are 178.54(13)° and 177.06(15)° and the cyanide ligands in the equatorial plane are distorted from planarity (between +10° and -8°). Similar distortions are noted in $K_4[Mo^{III}(CN)_7]\cdot H_2O$ and $(n\text{-}Bu_4N)_3[Re^{IV}(CN)_7]$.[102, 175]

Colorless blocks of $(n\text{-}Bu_4N)_3[Mo^{IV}(CN)_7]$, **4,** were grown from acetonitrile and diethyl ether by slow vapor diffusion. The compound crystallizes in the $P2_1/c$ space group with two molecules in the asymmetric unit. The structure adopts a distorted pentagonal pyramidal geometry, as shown in Figure 18, which is similar to the Mo^{III}, W^{IV}, and Re^{IV} analogues; bond angles and distances are list4ed in Table 4. The Mo^{IV}—C bond distances

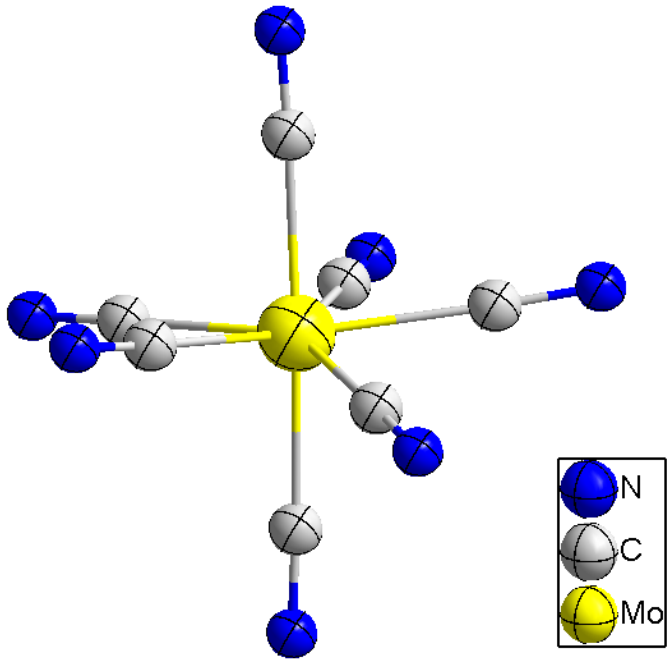

Figure 18: Crystal structure of $[Mo^{IV}(CN)_7]^{3-}$ (**4**) with a pentagonal bipyramidal geometry.

vary between 2.1478(26) Å and 2.1825(26) Å and are similar to those reported for $[Mo^{IV}(CN)_8]^{4-}$.[175] The axial bond distances (2.1765(28) Å and 2.1825(26) Å) are slightly longer than the equatorial bond distances (2.1478(26) Å to 2.1663(28) Å), which was not observed with the $[W^{IV}(CN)_7]^{3-}$ congener. The C—N triple bond distances for $[Mo^{IV}(CN)_7]^{3-}$ for $[Mo^{IV}(CN)_7]^{3-}$ vary between 1.1459(28) Å to 1.1578(39) Å, which is

Table 4: Bond distances and angles for $(Bu_4N)_3[Mo(CN)_7]$ (**4**)

Select Atoms	Bond Distance (Å)	Select Atoms	Bond Angle (°)
Mo_1—C_1	2.1765(28)	C_2—Mo_1—C_1	176.708(101)
Mo_1—C_2	2.1825(26)	C_2—Mo_1—C_4	89.552(103)
Mo_1—C_3	2.1478(26)	C_2—Mo_1—C_6	82.452(96)
Mo_1—C_4	2.1663(28)	C_2—Mo_1—C_7	100.266(98)
Mo_1—C_5	2.1618(29)	C_3—Mo_1—C_1	97.066(99)
Mo_1—C_6	2.1648(26)	C_3—Mo_1—C_2	85.321(95)
Mo_1—C_7	2.1654(28)	C_3—Mo_1—C_4	71.840(103)
N_1—C_1	1.1492(40)	C_3—Mo_1—C_6	139.426(107)
N_2—C_2	1.1551(36)	C_3—Mo_1—C_7	72.636(101)
N_3—C_3	1.1545(36)	C_4—Mo_1—C_1	89.045(105)
N_4—C_4	1.1553(37)	C_4—Mo_1—C_6	146.096(103)
N_5—C_5	1.1578(39)	C_4—Mo_1—C_7	142.122(105)
N_6—C_6	1.1552(35)	C_5—Mo_1—C_1	85.188(107)
N_7—C_7	1.1459(38)	C_5—Mo_1—C_2	91.552(101)
		C_5—Mo_1—C_3	144.426(107)
		C_5—Mo_1—C_4	72.71(11)
		C_5—Mo_1—C_6	74.627(102)
		C_5—Mo_1—C_7	142.374(108)
		C_6—Mo_1—C_1	97.089(100)
		C_6—Mo_1—C_7	71.769(98)
		C_7—Mo_1—C_1	82.645(103)
		N_1—C_1—Mo_1	177.369(251)
		N_2—C_2—Mo_1	177.375(230)
		N_3—C_3—Mo_1	177.642(229)
		N_4—C_4—Mo_1	179.301(245)
		N_5—C_5—Mo_1	178.632(257)
		N_6—C_6—Mo_1	177.013(226)
		N_7—C_7—Mo_1	177.5448(247)

similar to the $[W^{IV}(CN)_7]^{3-}$ anion and typical for transition-metal cyanide bond distances.[173, 176] The C—Mo—C axial angles are 176.708(101)° and 177.982(97)°. Adjacent angles for the equatorial cyanides (i.e. C_4-Mo-C_5) vary between 71.840(103)° and 74.627(102)° (an ideal pentagon would be 72°), and the cyanides are distorted from the equatorial plane at angles of -7.4° and +7.1°; such distortions were observed in the $[W^{IV}(CN)_7]^{3-}$, $[Re^{IV}(CN)_7]^{3-}$, and $[Mo^{III}(CN)_7]^{3-}$ anions as well.

The compound $(Cp_2Co)_4[W(CN)_8]$ was also analyzed by single crystal X-ray diffraction, performed on the green crystals that precipitated from the reaction. The anion adopts a square antiprismatic geometry (Figure 19), with the W—C bond lengths varying between 2.1482(80) and 2.1867(102) Å which is consistent with previously measured $[W^{IV}(CN)_8]^{4-}$ ions. The C-N bond lengths vary between 1.1388(168) and 1.1665(159) Å, in agreement with previous measurements for cyanides bonded to transition metals. The bond angles are also consistent with a square antiprismatic geometry and are in accord with literature values (Table 5).

Infrared Spectroscopy

In the solid state, **1** exhibits two sharp and strong ν(CN) stretches at 2110 and 2079 cm^{-1} (Figure 5a) confirming that the geometry of the $[W^{IV}(CN)_7]^{3-}$ anion is close to an ideal pentagonal bipyramid (IR selection rules for D_{5h} allow for only two vibrations: A_2'' and E_1'). The two main features are accompanied by weak shoulders/peaks at 2121(sh), 2091 and 2068 cm^{-1} which is not unexpected due the slight structural distortion from ideal D_{5h} symmetry. It is also not unusual for solid-state splitting effects to be observed. The IR spectrum recorded in dichloromethane solution is similar to that of the solid with two main

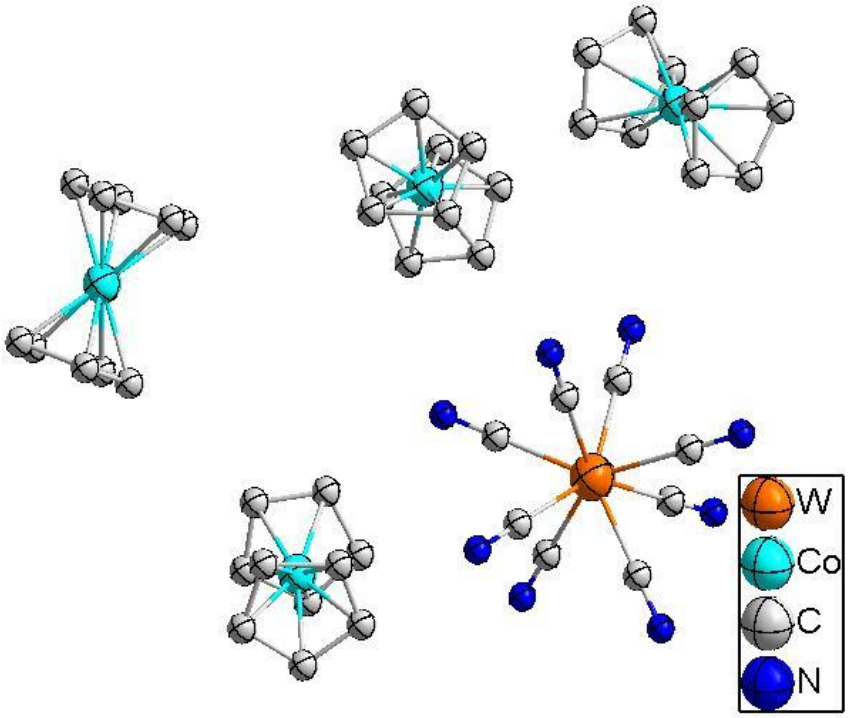

Figure 19: Molecular structure of $(Cp_2Co)_4[W^{IV}(CN)_8]\cdot 3CH_3CN$**.**

Table 5: Bond distances and angles for $(Cp_2Co)_4[W(CN)_8]$ (**3**)

Select Atoms	Bond Distance (Å)	Select Atoms	Bond Angle (°)
W_1—C_1	2.1482(80)	C_1—W_1—C_2	73.841(390)
W_1—C_2	2.1671(123)	C_1—W_1—C_3	76.028(328)
W_1—C_3	2.1783(93)	C_1—W_1—C_4	143.770(411)
W_1—C_4	2.1697(110)	C_1—W_1—C_5	116.183(432)
W_1—C_5	2.1628(106)	C_1—W_1—C_6	139.916(371)
W_1—C_6	2.1867(102)	C_1—W_1—C_7	72.262(411)
W_1—C_7	2.1622(119)	C_1—W_1—C_8	77.884(337)
W_1—C_8	2.1524(84)	C_2—W_1—C_3	76.065(347)
N_1—C_1	1.1575(114)	C_2—W_1—C_4	78.953(409)
N_2—C_2	1.1388(168)	C_2—W_1—C_5	72.672(401)
N_3—C_3	1.1456(131)	C_2—W_1—C_6	142.703(384)
N_4—C_4	1.1389(148)	C_2—W_1—C_7	113.612(410)
N_5—C_5	1.1564(152)	C_2—W_1—C_8	142.801(332)
N_6—C_6	1.1584(146)	C_3—W_1—C_4	74.523(358)
N_7—C_7	1.1665(159)	C_3—W_1—C_5	140.730(377)
N_8—C_8	1.1519(130)	C_3—W_1—C_6	120.031(328)
		C_3—W_1—C_7	141.958(355)
		C_3—W_1—C_8	74.011(306)
		C_4—W_1—C_5	76.659(461)
		C_4—W_1—C_6	74.485(386)
		C_4—W_1—C_7	142.116(445)
		C_4—W_1—C_8	113.099(380)
		C_5—W_1—C_6	76.038(442)
		C_5—W_1—C_7	73.937(430)
		C_5—W_1—C_8	143.061(348)
		C_6—W_1—C_7	75.646(388)
		C_6—W_1—C_8	73.937(430)
		C_7—W_1—C_8	79.215(382)
		N_1—C_1—W_1	179.357(929)
		N_2—C_2—W_1	178.701(936)
		N_3—C_3—W_1	177.780(776)
		N_4—C_4—W_1	177.037(1075)
		N_5—C_5—W_1	178.409(991)
		N_6—C_6—W_1	178.268(889)
		N_7—C_7—W_1	179.784(958)
		N_8—C_8—W_1	178.833(742)

ν(CN) bands at 2112 and 2082 cm^{-1} and slightly shifted weak features. These results indicate that the complex maintains a distorted pentagonal bipyramidal geometry in solution (Figure 20a). The ν(CN) stretches are lower in frequency than the corresponding stretches of $(n\text{-}Bu_4N)_3[W(CN)_8]$ which appear at 2139 cm^{-1} and 2129 cm^{-1}. This shift is consistent with the decrease in oxidation state resulting in stronger π-backbonding and weaker σ-bonding. The ν(CN) frequencies are close to the values reported by Griffith *et al*. for $K_5[W^{II}(CN)_7]$[158] (a compound whose composition remains to be verified) and to the A_2'' and E_1' stretches reported for the pentagonal bipyramidal $K_4[Mo^{III}(CN)_7]$.[172] It is noteworthy that exposing **1** to air results in the appearance of a new band located at 2144 cm^{-1} (Figure 20b), attributed to oxidation.

Similarly, the $(Bu_4N)_3[Mo^{IV}(CN)_7]$ salt also shows two sharp ν(CN) stretching frequencies in the solid state at 2112 cm^{-1} and 2092 cm^{-1} and less intense stretches at 2104 cm^{-1} and 2050 cm^{-1} (Figure 21). This is consistent with a pentagonal bipyramidal geometry with the IR-allowed selection rules for A_2'' and E_1'.[101-102] The weaker stretches are the result of distortions from an ideal D_{5h} symmetry as well as solid-state effects, including cation interactions. In a CH_2Cl_2 solution, the stretching frequencies are nearly the same at 2113 cm^{-1} and 2092 cm^{-1}, with several weaker features at 2070 cm^{-1} and 2055 cm^{-1}, suggesting the $[Mo^{IV}(CN)_7]^{3-}$ remains pentagonal bipyramidal in solution.[172] Compared to $(Bu_4N)_3[Mo^{V}(CN)_8]$, the CN stretches are lower in frequency as a result of weaker σ-bonding and increased π-backbonding owing to a lower oxidation state, although the stretches are not as intense as a result of weaker force constants due to a lower atomic weight of molybdenum as compared to tungsten. Compared to $[Mo^{III}(CN)_7]^{4-}$, the stretches

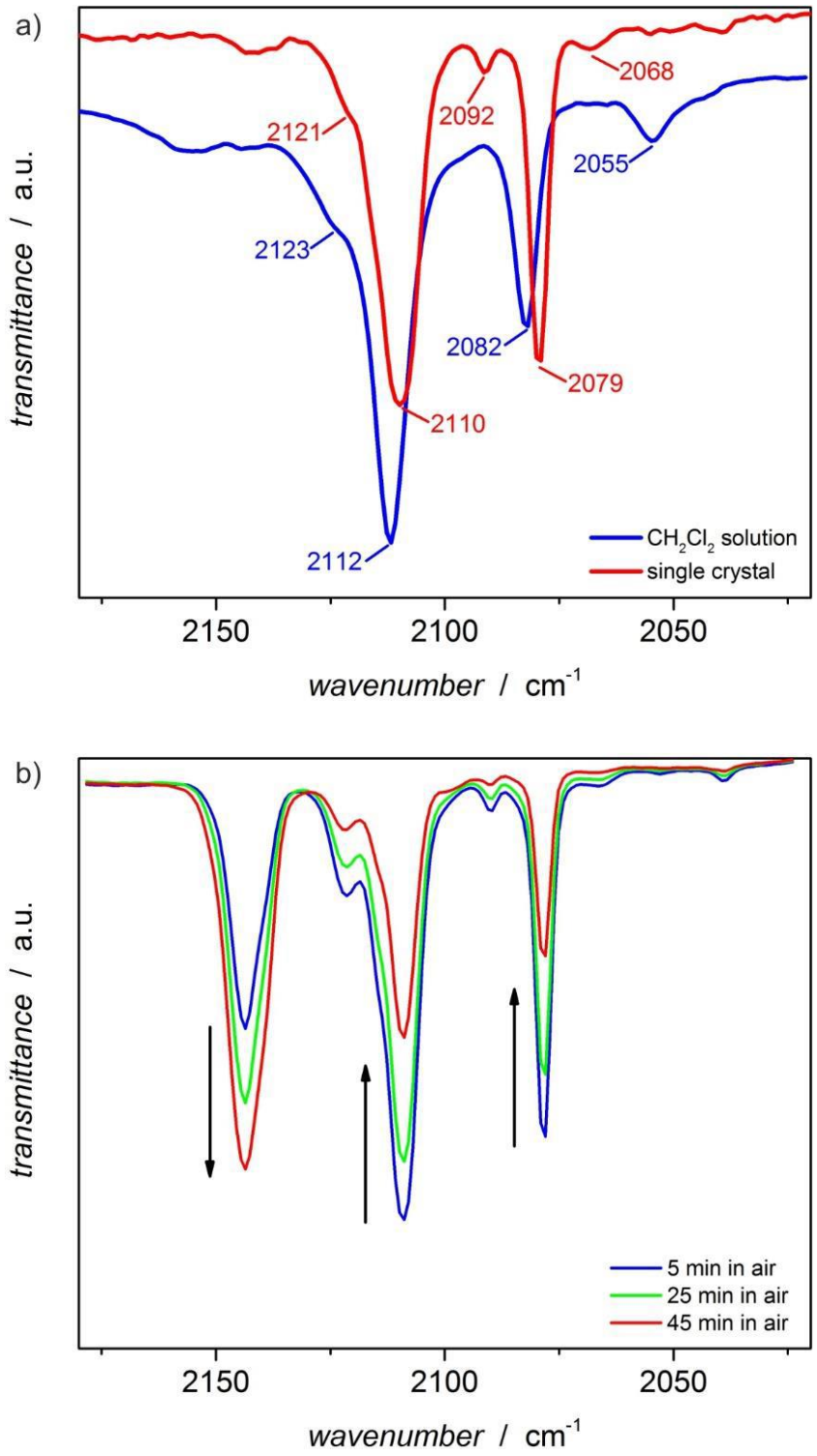

Figure 20: Infrared spectra of (**2**). (a) Compound **2** as both single crystals and in a CH_2Cl_2 solution. (b) Change in CN stretches over time upon exposure to oxygen. Reprinted with permission from reference 176.

are similar. Exposure to oxygen does not lead to rapid decomposition as discerned by the infrared spectrum. The infrared spectrum of $(Cp_2Co)_4[W^{IV}(CN)_8]$ exhibits a strong cyanide stretching vibration at 2089 cm^{-1} with a shoulder at 2104 cm^{-1}, and the $(Cp_2Co)_4[Mo^{IV}(CN)_8]$ shows one broad cyanide stretching frequency at 2091 cm^{-1}. A summary of the cyanide stretches is listed in Table 6.

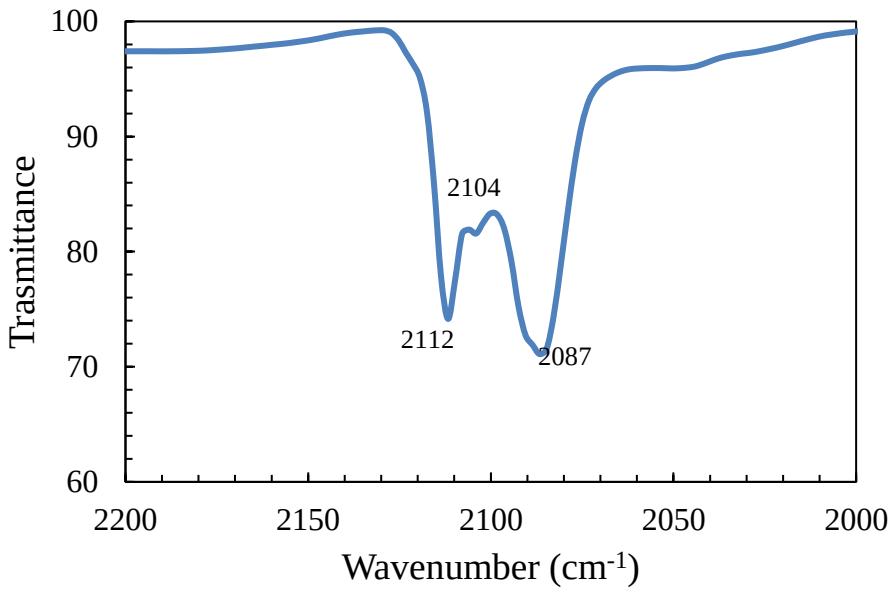

Figure 21: Infrared spectrum of **4** in a Nujol mull.

Table 6: Infrared ν(CN) stretching frequencies for **2**, **3**, **4**, **5**, and starting reagents.

Compound	ν (CN) (cm^{-1})
$(Bu_4N)_3[W^{IV}(CN)_7]$ (**2**)	2110, 2079
$(Bu_4N)_3[W^{V}(CN)_8]$	2129, 2139
$(Bu_4N)_3[Mo^{IV}(CN)_7]$ (**4**)	2112, 2092
$(Bu_4N)_3[Mo^{V}(CN)_8]$	2123, 2139
$(Cp_2Co)_4[W^{IV}(CN)_8]$ (**3**)	2089, 2104
$(Cp_2Co)_4[Mo^{IV}(CN)_8]$ (**5**)	2091

Electronic Spectroscopy

The electronic absorption spectrum of **2** in CH_3CN solution (Figure 22a) exhibits a weak feature at 391 nm ($\varepsilon = 9.9 M^{-1}\cdot cm^{-1}$) which corresponds to the lowest spin-allowed $e_1'' \rightarrow e_2'$ d–d transition and is similar to the corresponding absorptions reported for the heptacyanometallates $(n\text{-}Bu_4N)_3[Re^{IV}(CN)_7]$[102] in CH_3CN and $K_4[Mo^{III}(CN)_7]\cdot 2H_2O$ in water.[172] There are also several features below 350 nm attributed to metal-to-ligand charge transfer (MLCT) and higher d–d transitions. It is noted that exposing the solution of **2** to air leads to an irreversible color change to orange and the appearance of a new absorption at 447 nm with concomitant decrease in intensity of absorption bands below 350 nm (Figure 22b).

The electronic absorption spectrum of **4** in CH_3CN is depicted in Figure 23. The compound exhibits two absorptions in the UV region, namely 278.3 nm ($\varepsilon = 1466\ M^{-1}\cdot cm^{-1}$) and 327.9 nm ($\varepsilon = 1591\ M^{-1}\cdot cm^{-1}$) corresponding to MLCT transitions as in the case of the tungsten analogue. There is a broad peak from ~ 360 to 410 nm, which corresponds to the d-d transitions as ε values are 93 to 45 $M^{-1}\cdot cm^{-1}$ in this range, but no distinct maxima are observed. For the sake of comparison, the $K_4[Mo^{III}(CN)_7]\cdot 2H_2O$ electron absorption

spectrum in deoxygenated water has two strong bands at 216 nm and 289 nm with a prominent shoulder at 402 nm.[172] The 402 shoulder was assigned as the lowest spin-allowed $e_1'' \rightarrow e_2'$ with the higher energy bands being $d \rightarrow \pi^*(CN)$ and d-d transitions. Exposure to oxygen does not result in a noticeable color change, and the electron absorption spectrum appears essentially unchanged after 48 hours except for a decrease in the absorbance for the MLCT peaks.

Electrochemical Studies

The synthesis of the $(Bu_4N)_3[M^{IV}(CN)_7]$ anions of Mo and W was a mixed success: while the desired pentagonal bipyramidal geometry was obtained, the metal centers are in the tetravalent oxidation state, resulting in an isotropic d^2 electronic configuration rather than the desired trivalent oxidation state with an orbitally degenerate ground state. A one-electron reduction would be expected to yield the desired oxidation state, and to determine the potential at which this occurs, electrochemical measurements were performed. In particular, cyclic voltammetry (CV) is a useful tool for determining such a potential and whether it exists.

For compound **2**, cyclic voltammetry is shown in Figure 24. Initially, the product exhibited a reversible reduction at -1.29 V which, naturally, was thought be the reduction to the $[W^{III}(CN)_7]^{4-}$ anion. Numerous attempts to reduce the compound chemically were unsuccessful, as highlighted above. One hypothesis is that the cobaltocenium byproduct is present as an impurity, but the presence of a quasi-reversible feature led to further examination, as detailed below.

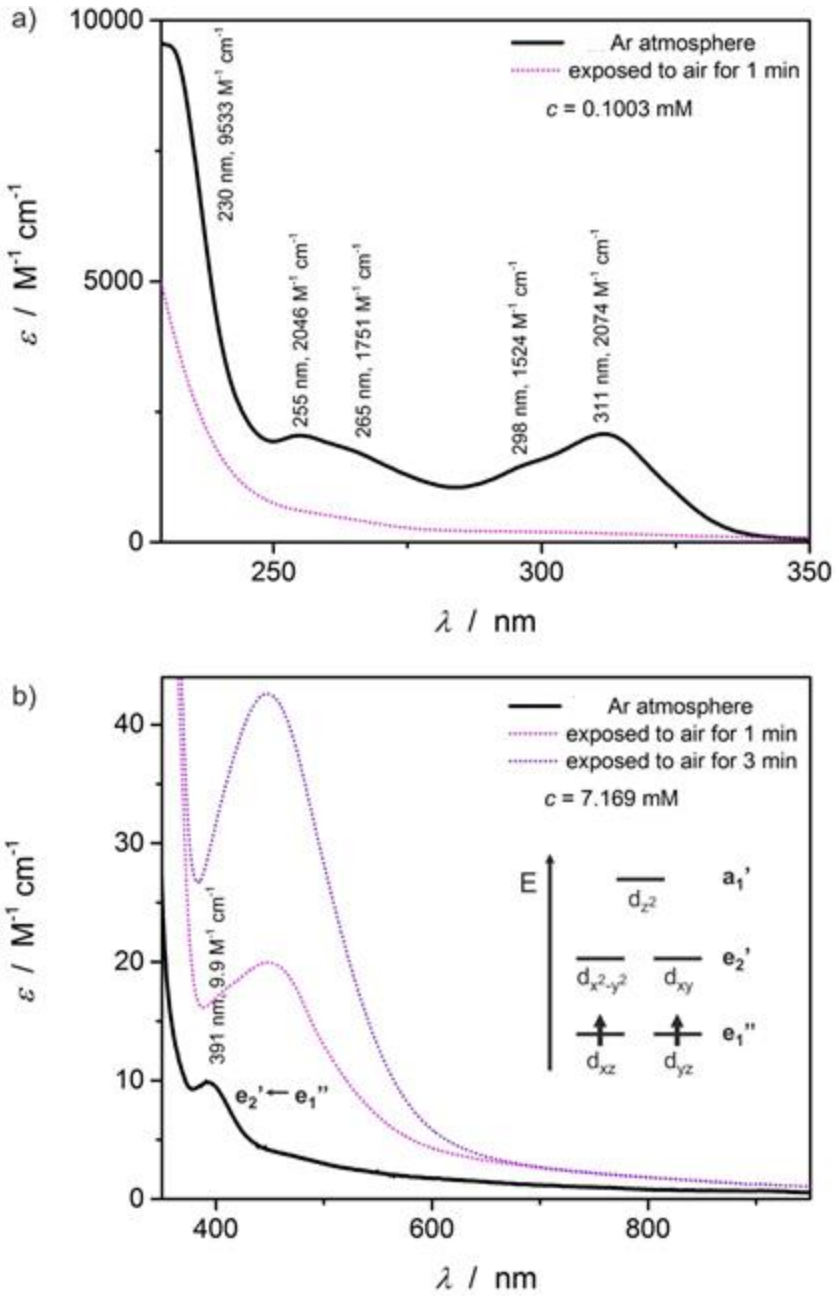

Figure 22: Electronic absorption spectra of **2** in CH_3CN before and after exposure to O_2. Reprinted with permission from reference 176.

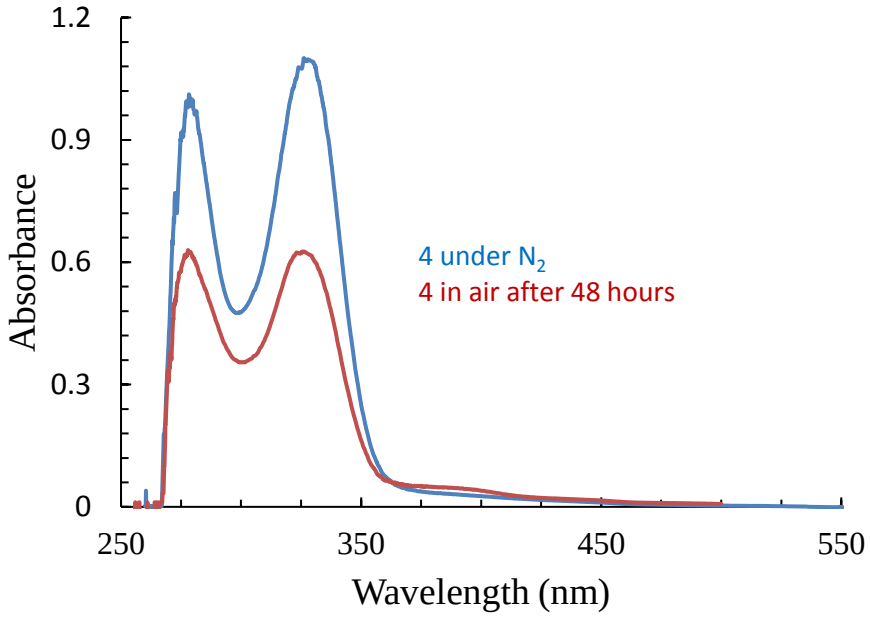

Figure 23: Electron absorbance spectrum of **4**. Spectra were collected in CH_3CN with a 0.6899 mM solution.

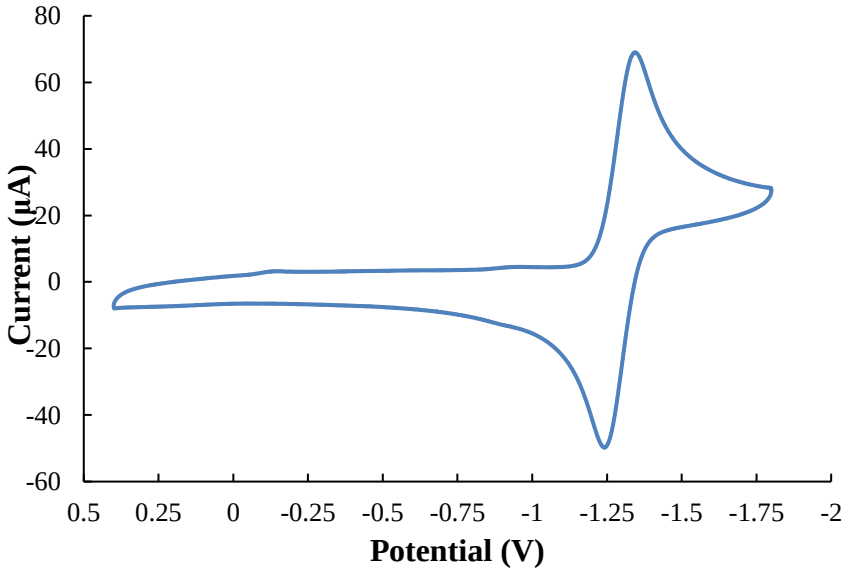

Figure 24: Cyclic voltammogram of **2** in CH_3CN with 0.1 M Bu_4NPF_6 as the supporting electrolyte. Potentials are referenced to Ag/AgCl electrode; the scan rate is 0.2 V/s. Reprinted with permission from, copyright 2008 American Chemical Society.

Given that the $[Mo^{III}(CN)_7]^{4-}$, $[Mo^{II}(CN)_7]^{5-}$, and $[Mo^{III}(CN)_6]^{3-}$ anions are known, the reduction of **4** was of particular interest, especially with respect to the $[Mo^{III}(CN)_7]^{4-}$ or $[Mo^{III}(CN)_6]^{3-}$ species both of which are known to exist.[100] Initial CV measurements revealed a quasi-reversible reduction at -1.13 V, Figure 25, with a peak separation between cathodic ($E_{p,c}$ = -1.18 V) and anodic ($E_{p,a}$ = -1.09 V) potentials of 90 mV, which is significantly more than the 59 mV expected for an ideal reversible reduction. Repeated studies led to similar $E_{1/2}$ values with even greater peak separations, suggesting quasi-reversibility. These results are attributed to the reduction to the $[Mo^{III}(CN)_6]^{3-}$ anion with loss of cyanide.

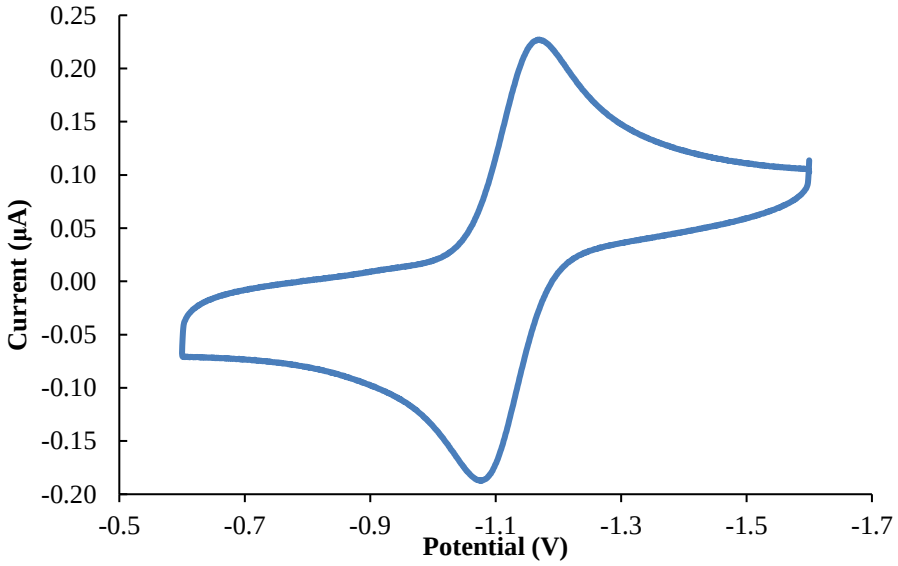

Figure 25: Cyclic voltammogram of **4** in CH_3CN with 0.1 M Bu_4NPF_6 as the supporting electrolyte. Potentials are referenced to the Ag/AgCl electrode; the scan rate is 0.05 V/s.

On the basis of the literature, it is well-known that the $[Fe^{II/III}(CN)_6]^{2/3-}$ redox couple has a 2 V range over which the reduction can occur depending on the choice of solvent.[177] In order to probe whether the same situation holds true for the $[M^{IV}(CN)_7]^{3-}$ species, reductions were measured in different solvents. The results would also would indicate whether the reductions observed earlier were based on the metal center or due to cobaltocene impurities that are undetected as finely divided particulates on the surface of the crystals (as the cobaltocene reduction potential should not change with solvent). The heptacyanometallates are soluble in CH_2Cl_2, CH_3CN, DMF, and propylene carbonate (PC); the reductions were measured in these solvents and the results are reported in Table 7. Additionally, the $[M^{V}(CN)_8]^{3-}$ (M = Mo, W) anions were also measured to provide a control, as the $[M^{V}(CN)_8]^{4/3-}$ redox couple is reported in the literature.[178-180] With the exception of CH_2Cl_2, in which the compounds decompose after the reduction, the solvents led to stable reduction products and it was found that the reduction potentials varied with solvent. Propylene carbonate led to the lowest reduction potential, usually being 0.1 V less reducing than CH_3CN, while DMF led to 0.15 to 0.2 V more negative reduction potentials than CH_3CN. The molybdenum reductions are lower than the tungsten analogues by approximately 0.15 V and 0.25 V for the heptacyanometallates and octacyanometallates, respectively. Curiously, the octacyanometallates only show the reversible $[M(CN)_8]^{3/4-}$ reduction in their CVs, and the lack of an irreversible reduction indictes that the $[M^{IV}(CN)_7]^{3-}$ analogue would not be accessible with cobaltocene. It is also interesting to note that the reductions appeared to be quasi-reversible, as there are large separations between peak potentials.

Table 7: Electrochemical reduction potentials, $E_{1/2}$, as a function of solvent. $E_{1/2}$ are reported for each compound in V with reference to Ag/AgCl, with the ΔE (= $E_{p,c} - E_{p,a}$) given in parenthesis in mV.

Compound	$[Mo^{IV}(CN)_7]^{3-}$	$[Mo^{V}(CN)_8]^{3-}$	$[W^{IV}(CN)_7]^{3-}$	$[W^{V}(CN)_8]^{3-}$
PC	-1.00 (222)	-0.21 (184)	-1.14 (359)	-0.47 (134)
CH_3CN	-1.10 (184)	-0.32 (286)	-1.30 (246)	-0.60 (393)
DMF	-1.30 (113)	-0.51 (118)	-1.47 (134)	-0.77 (116)

To further probe the degree of reversibility of the electrochemistry, CVs were performed for the four compounds at variable scan rates. For a reversible reduction, the peak potential will not change as a function of scan rate, whereas it will shift with scan rate for a quasi-reversible reduction. The reductions at different scan rates were performed in CH_3CN with at least 0.15 M of Bu_4NPF_6 as the supporting electrolyte. The scan rates were varied from 0.02 V/s to 0.5 V/s. For compound **4**, there is an obvious shift of the anodic peak potential with scan rate, shifting to more oxidizing potentials as the scan rate increases (Figure 26); at increased scan rates it is difficult to discern a cathodic peak potential, but it is clear that the peak separation increases which indicates quasi-reversibility. In contrast, $(Bu_4N)_3[Mo^{V}(CN)_8]$ shows a significantly smaller shift in peak potentials with scan rates (Figure 27), which confirms the reversible reduction between the $[Mo^{V}(CN)_8]^{3-}$ and $[Mo^{IV}(CN)_8]^{4-}$.

Compound **2** also has an obvious shift of the anodic peak potential with scan rate and shifts to more oxidizing potentials as the scan rate increases similar to **4**. In addition, increasing the scan rate results in large peak separations between cathodic and anodic peak potentials, an indication of quasi-reversibility (Figure 28). In contrast, the

$(Bu_4N)_3[W(CN)_8]$ exhibits much smaller shifts in peak potentials with scan rates (Figure 29), although there is a larger shift at higher scan speeds, which confirms the reversible reduction between the $[W^{V}(CN)_8]^{3-}$ and $[W^{IV}(CN)_8]^{4-}$.

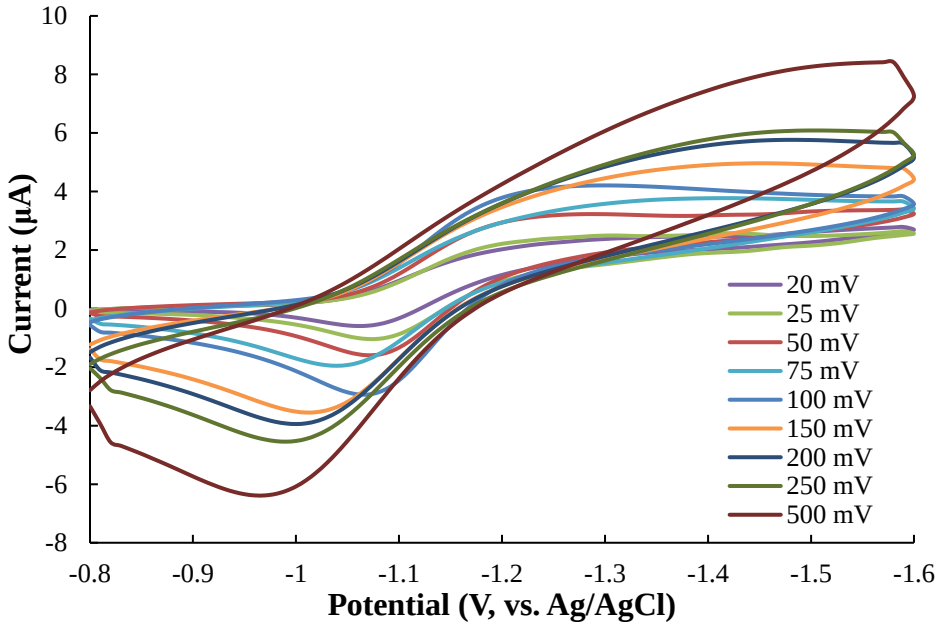

Figure 26: Cyclic voltammogram of $(Bu_4N)_3[Mo^{IV}(CN)_7]$ in CH_3CN at various scan rates with 0.192 M Bu_4NPF_6 as the supporting electrolyte. Potentials are referenced to Ag/AgCl.

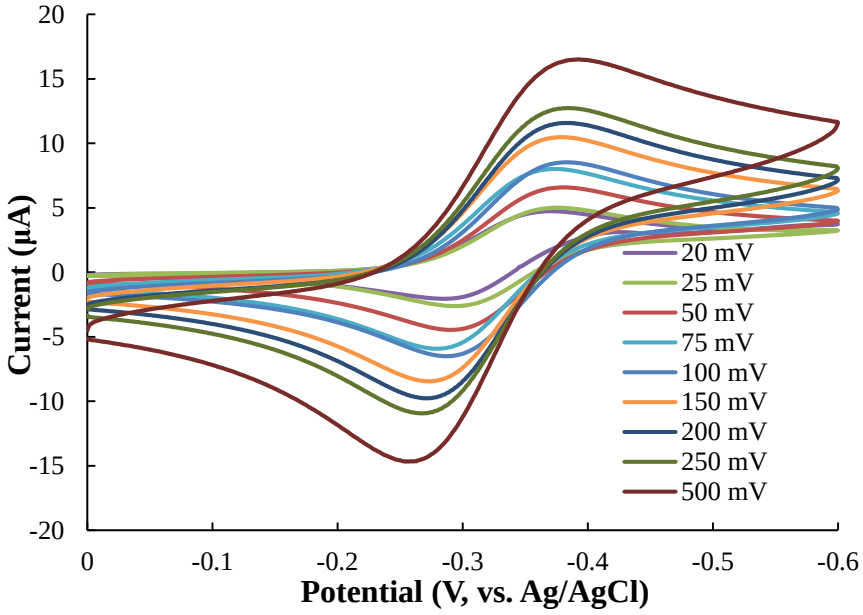

Figure 27: Cyclic voltammogram of $(Bu_4N)_3[Mo^V(CN)_8]$ in CH_3CN at various scan rates with 0.186 M Bu_4NPF_6 as the supporting electrolyte. Potentials are referenced to Ag/AgCl.

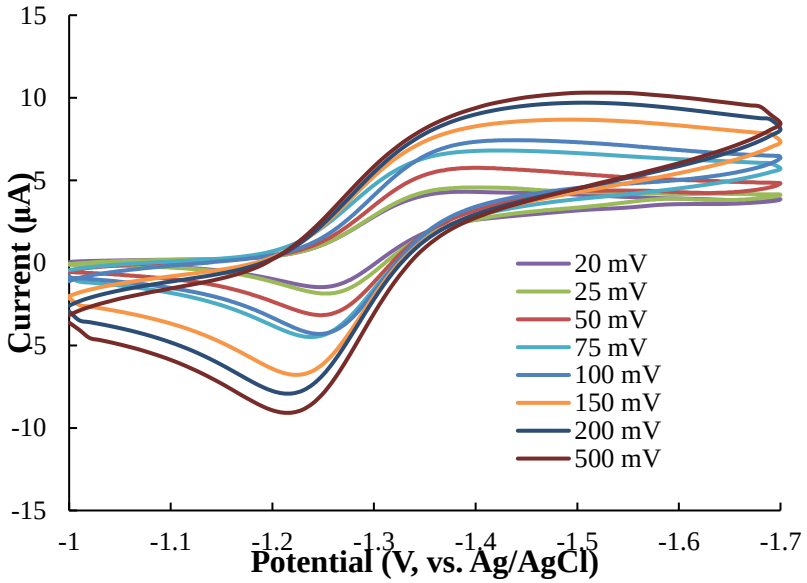

Figure 28: Cyclic voltammogram of $(Bu_4N)_3[W^{IV}(CN)_7]$ in CH_3CN at various scan rates with 0.183 M Bu_4NPF_6 as the supporting electrolyte. Potentials are referenced to Ag/AgCl.

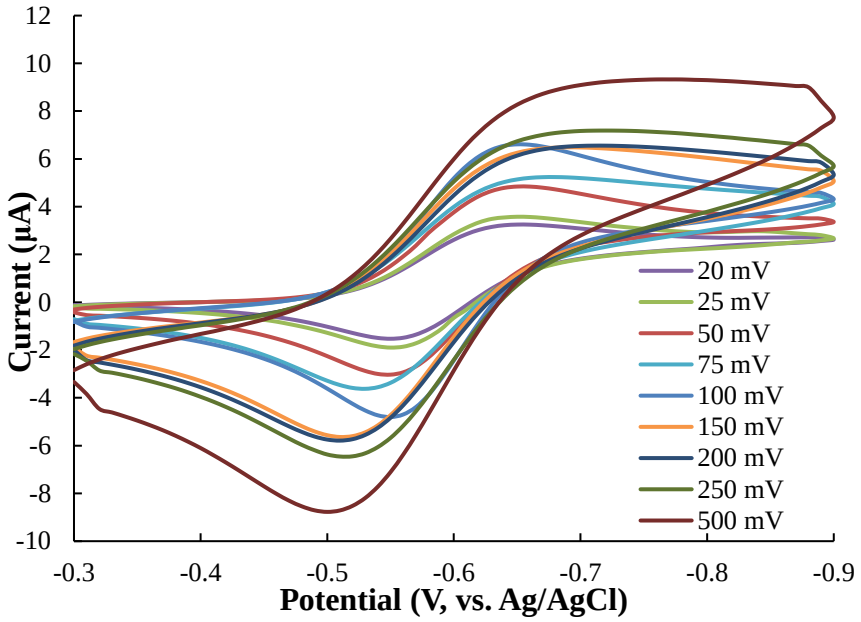

Figure 29: Cyclic voltammogram of $(Bu_4N)_3[W^V(CN)_8]$ in CH_3CN at various scan rates with 0.210 M Bu_4NPF_6 as the supporting electrolyte. Potentials are referenced to Ag/AgCl.

Magnetic Measurements

The magnetic properties of **2** were measured in the solid state using a MPMS-XL SQUID magnetometer. The χT value at room temperature is 0.77 emu·K·mol^{-1} (Figure 30), which is less than the spin-only value of 1.00 emu·K·mol^{-1} expected for an S=1 system assuming the d-orbital splitting presented in Figure 22b and a g-factor of 2.0. The χT value steadily decreases to zero as the temperature is lowered (Figure 30) which is ascribed to a significant zero field splitting (zfs) with large positive *D* value. The best fit using the Hamiltonian in Equation 27:

$$\widehat{H} = DS_z^2 + E\left(S_x^2 - S_y^2\right) + \mu_B\mu_0 H_z gS \qquad \text{Equation 27}$$

(where D and E are the axial and rhombic crystal field parameters, $S = 1$ is the spin of the system, g is the g-factor and H_z is the applied magnetic field) leads to the following parameters: g = 1.9(1), D = 330(10) cm^{-1}, E = 110(5) cm^{-1}. The magnetization at 1.8 K (Figure 30, inset) has a maximum value of 0.04 μ_B at 7 T without saturation, indicating that the ground state is non-magnetic. The best fit parameters from the magnetization dependence: g = 2.0(1), D = 430(10) cm^{-1}, and E = 41(5) cm^{-1} are consistent with those obtained from the χT versus T fitting. Simultaneous fitting of both χT vs.T and M vs. H did not lead to satisfactory results (Figure 31). The reduced magnetization (M versus HT^{-1}) plot is shown in Figure 32. The best fit parameters are similar to those obtained from the M vs. H dependence: g = 2.0(1), D = 430(10) cm^{-1}, and E = 38(5) cm^{-1}. The obtained D value is very large, but not entirely unreasonable for a pentagonal bipyramidal 5d metal ion complex.[181] It is unlikely that the magnetic properties of **2** arise from spin-orbit coupling since the orbital angular momentum for a d^2 pentagonal bipyramidal complex should be quenched. Nevertheless, we concede that the large inherent spin-orbit coupling of 5d elements may still play a role owing to the slight distortion from the ideal pentagonal bipyramidal geometry. Our attempts to include the orbital contribution in the fits led to severe overparametrization and were unsuccessful, leading to poor results and/or non-physical, negative g values. All fittings were performed using the PHI program.[182]

Mironov has also performed Ligand-Field (LF) calculations on the $[W^{IV}(CN)_7]^{3-}$ anion utilizing the Hamiltonian in equation 28[183]:

$$\widehat{H} = \sum_{i>j} \frac{e^2}{|\boldsymbol{r_i} - \boldsymbol{r_j}|} + \zeta_{5d} \sum_i \boldsymbol{l_i s_i} + V_{LF} + \mu_B (k\boldsymbol{L} + 2\boldsymbol{S})\boldsymbol{H} \qquad \text{Equation 28}$$

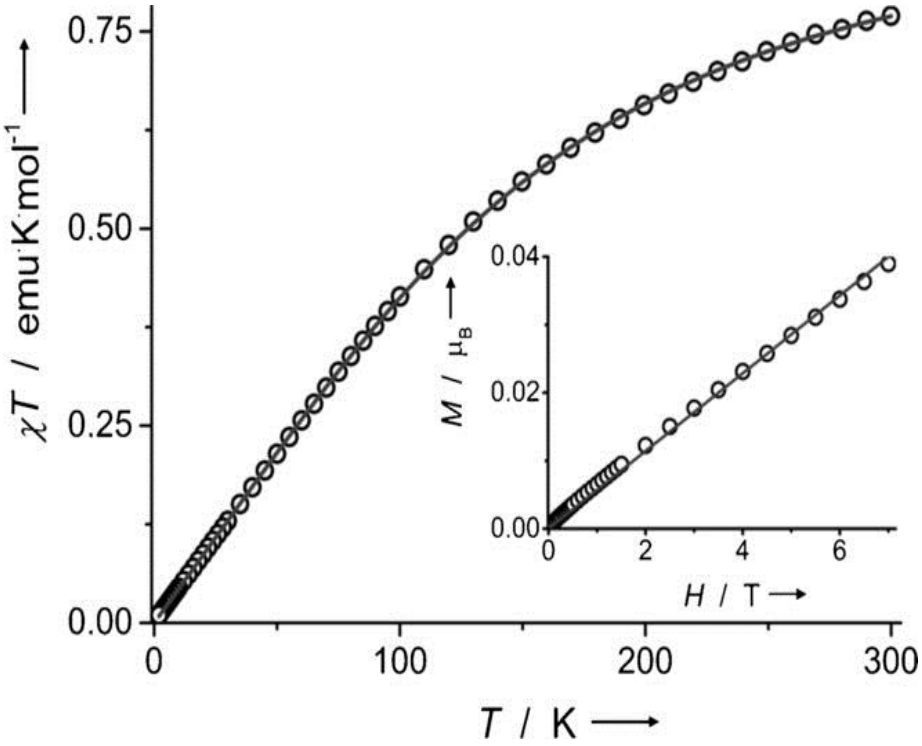

Figure 30: Variable DC susceptibility (H = 0.1 T) and magnetization (inset; T = 1.8 K) plots for **2**. Solid lines are the best fits to the experimental data. Reprinted with permission from reference 176.

where the first, second, third, and fourth terms account for the Coulomb repulsion energy, spin-orbit coupling, LF Hamiltonian, and Zeeman interactions, respectively. The calculated Racah parameters for the Coulomb term are B = 400 cm^{-1} and C = 1800 cm^{-1}, ζ is the spin-orbit coupling constant for tungsten, $\boldsymbol{l}$ and $\boldsymbol{s}$ are the angular momentum and spin operators, V_{LF} is calculated using angular overlap parameters, μ_B is Bohr magnetons, k is the orbital reduction factor and H is the magnetic field. The calculations for $\chi_M T$ resulted in a D value of 280 cm^{-1} and an E value of 0.14 cm^{-1}. While the large positive D

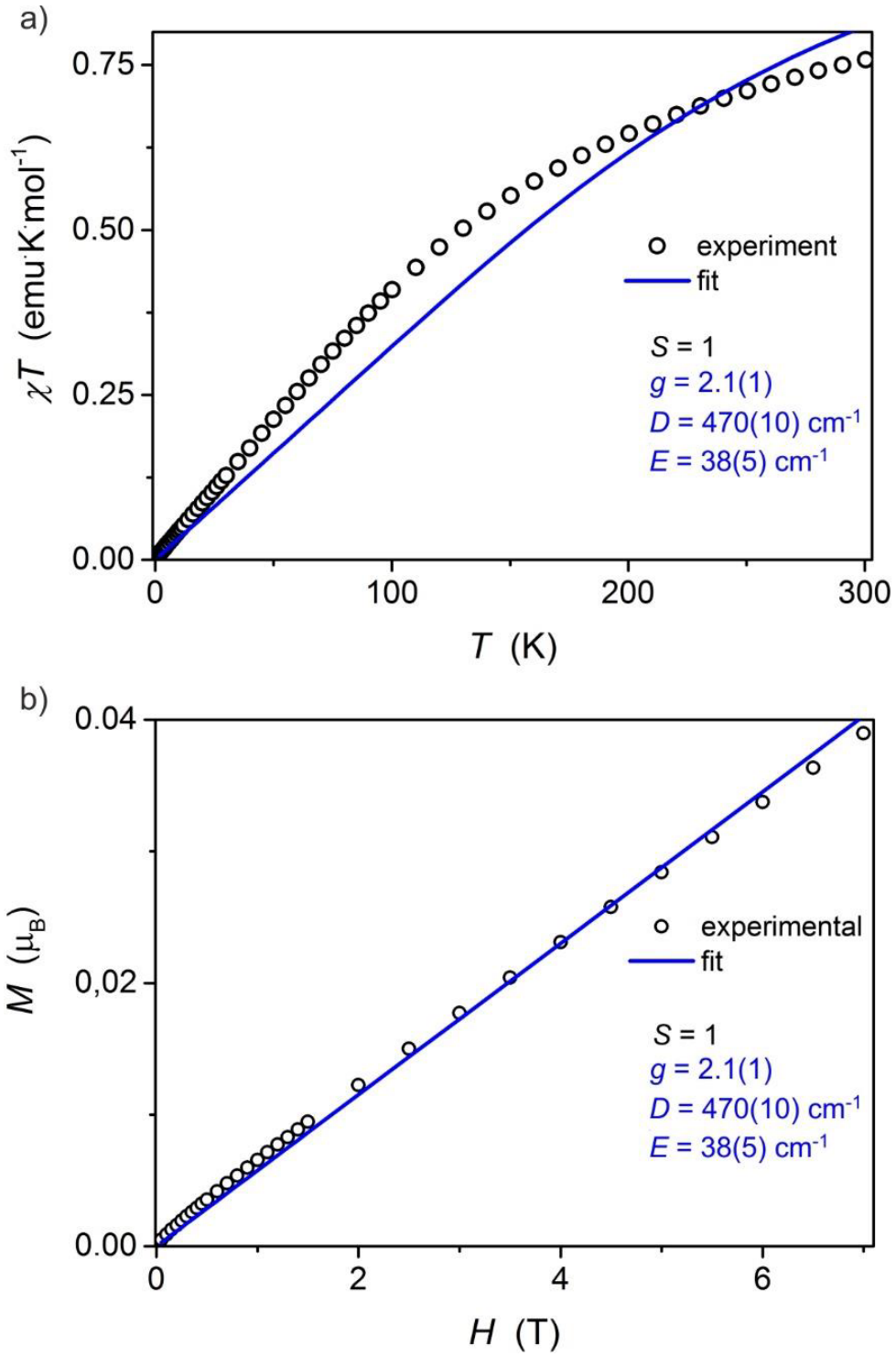

Figure 31: $\chi_M T$ versus T and 1.8 K magnetization plots for 2. (a) $\chi_M T$ vs T (main, H = 0.1 T) and (b) M vs H at 1.8 K for 2. Solid lines are best fit to both sets simultaneously. Reprinted with permission from reference 176.

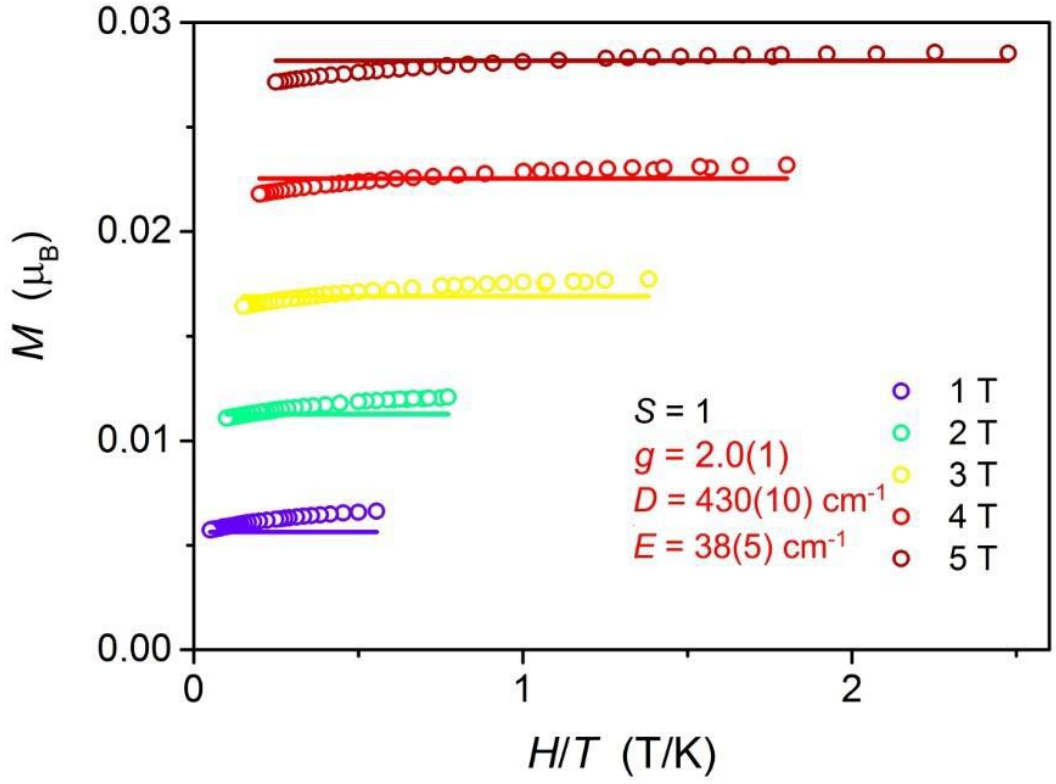

Figure 32: Reduced magnetization (M vs H/T) for **2** measured at 1, 2, 3, 4, and 5 T (violet to red points) between 1.8 and 20 K. Solid lines are the best fit using the following parameters. Reprinted with permission from reference 176.

value agrees with our magnetic fitting, there is a significant difference in the *E* values obtained.

Magnetic studies were also performed on compound **4** in the solid state. The $\chi_M T$ value at 300 K was found to be 1.13 emu·K·mol^{-1} (Figure 18), which is higher than the expected 1.00 emu·K·mol^{-1} for an $S = 1$ system with $g = 2.0$. As the temperature decreases, there is a gradual decrease in $\chi_M T$ until 30 K and then a sharp decrease towards zero, the result of zero field splitting (ZFS). This is in contrast to **2**, for which there is a constant gradual decrease from 0.77 emu·K·mol^{-1}. Fitting the data for **4** to equation 27 yields g =

1.96, D = 30 cm^{-1}, and E = 15 cm^{-1}. The 2 K magnetization data (Figure 19) exhibit a maximum value of 0.47 μ_B at 7 T without saturation, and the fitted magnetization parameters yielded g = 1.01, D = 10 cm^{-1}, and E = 5 cm^{-1}; this is significantly different from other fits of the susceptibility of both magnetization and susceptibility. These results confirm that the ground state is m_s = 0. It is worth noting that D is an order of magnitude smaller for **4** as compared to **2**. Simultaneous fitting of $\chi_M T$ and magnetization yields acceptable results with g = 1.96, D = 32.6 cm^{-1}, and E = 0.1 cm^{-1} (Figure 20). Fitting of the reduced magnetization, Figure 21, leads to parameters g = 1.74, D = 115 cm^{-1}, and E = 100 cm^{-1} when g can vary, while fixing g at 1.9 leads to D = 716 cm^{-1} and E = 700 cm^{-1}. The former case is more likely than the latter and, although g is not expected to be lower than 1.9, the value of 1.74 is not entirely unreasonable. Additionally, the separated isofield lines indicates the presence of magnetic anisotropy. Overall, the calculated values for **4** suggest that the D value is significantly less than **2**, lending support to the idea that moving to 5d metal ions will lead to larger ZFS.

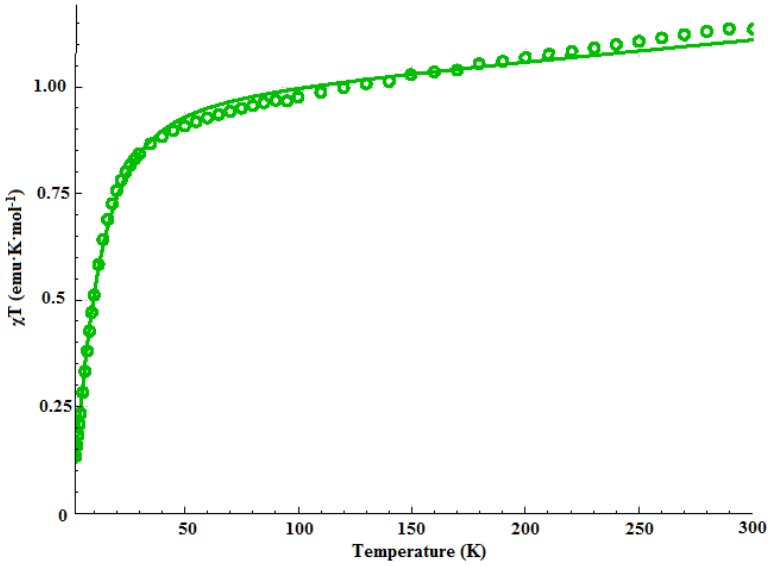

Figure 33: Variable-temperature dc susceptibility plot for **4** from 300 to 2 K. Solid line represents best fit with g = 1.96, D = 30 cm^{-1}, and E = 15 cm^{-1}.

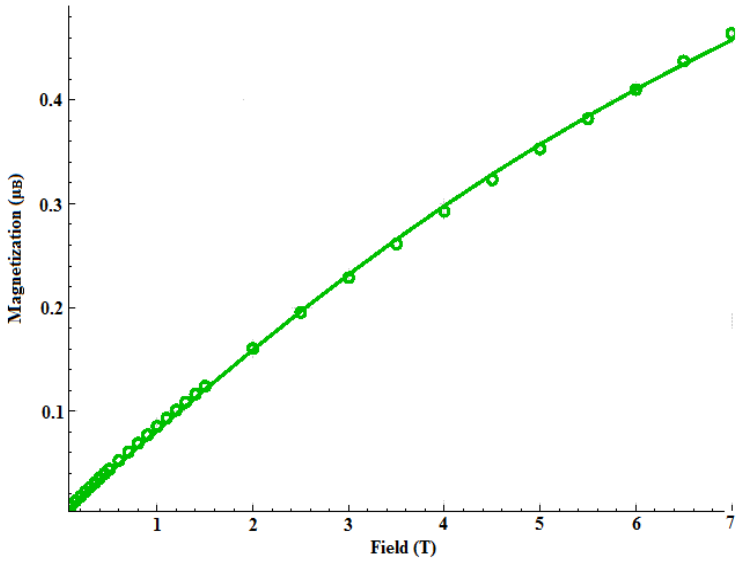

Figure 34: Magnetization versus H plot at 2 K for **4**. Green line represents best fit with parameters g = 1.01, D = 10 cm^{-1}, and E = 5 cm^{-1}.

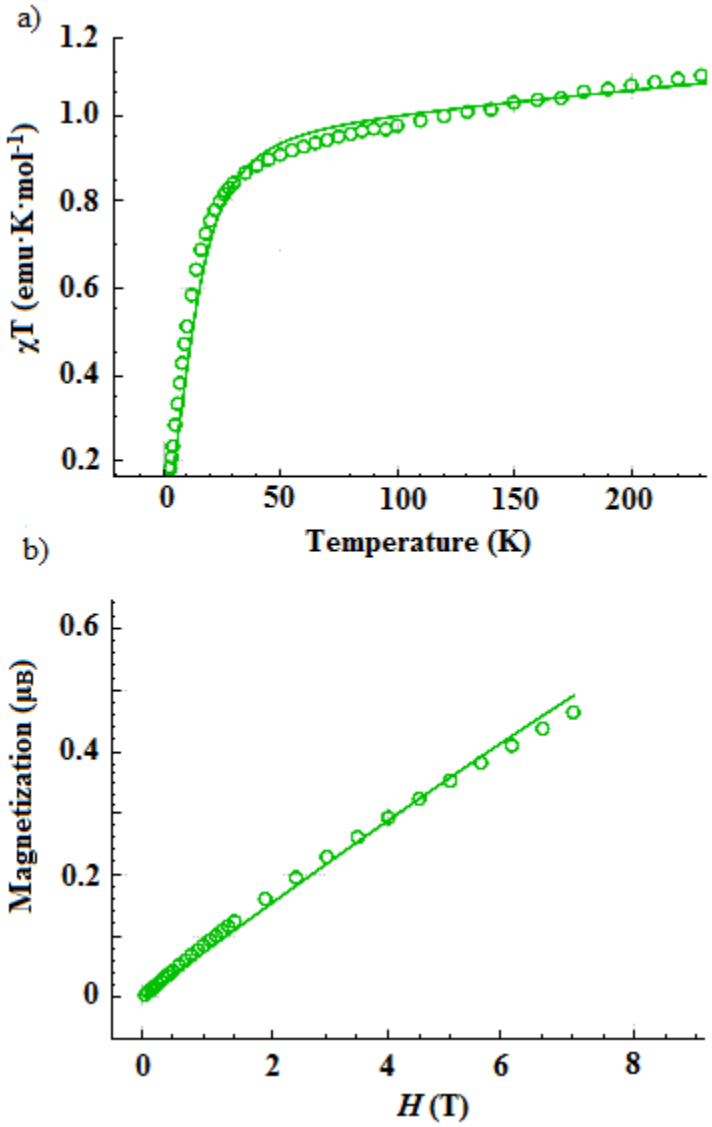

Figure 35: Simultaneous fitting of both χT susceptibility and 2 K magnetization of **4**. (a) χT susceptibility and (b) magnetization at 2 K.

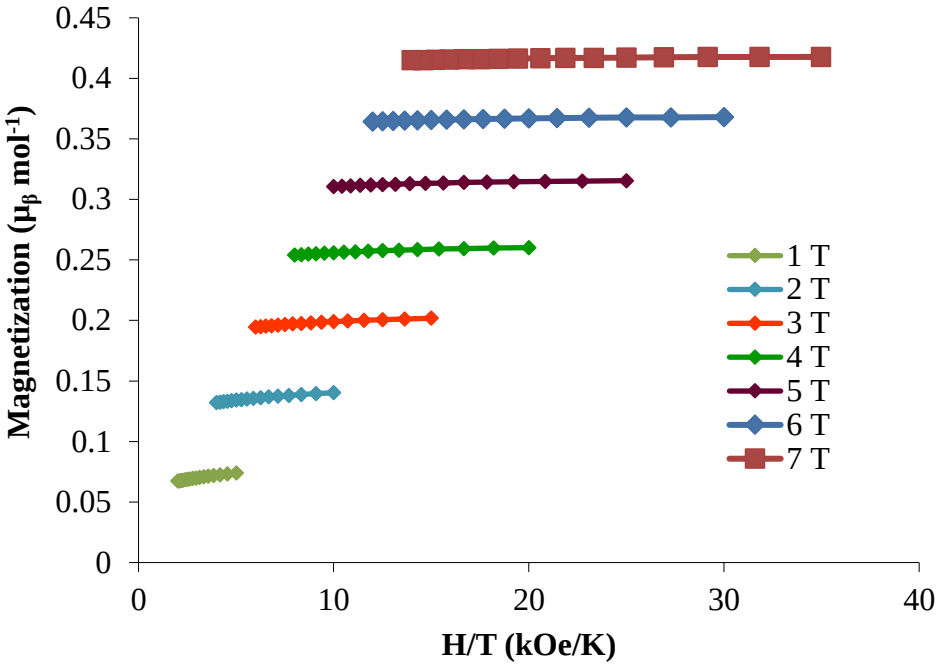

Figure 36: Reduced magnetization of **4**. Colors represent different isofield lines with best fit parameters g = 1.01, D = 10 cm^{-1}, and E = 5 cm^{-1}.

Conclusions

The synthesis of new heptacyanometallate(IV) compounds for molybdenum and tungsten were achieved by reduction of $[M^{V}(CN)_8]^{3-}$ with cobaltocene in acetonitrile. The compounds were characterized by X-ray crystallography, IR and electronic absorption spectroscopies, cyclic voltammetry, and SQUID magnetometry. The X-ray data revealed that $[M^{IV}(CN)_7]^{3-}$ (M = Mo, W) adopt a pentagonal bipyramidal geometry and the magnetic studies indicate the ground state is S = 1 with a non-magnetic m_s = 0 ground state due to positive zero-field splitting. This conclusion is supported by the large D values

for Mo (30 cm^{-1}) and W (330 cm^{-1}). It is also worth noting that moving from the 4d to 5d metal center results in an order of magnitude increase in D. The cyclic voltammograms show a quasi-reversible reduction for both heptacyanometallates which is expected to indicate a reduction to the $[M^{III}(CN)_6]^{3-}$ compound with loss of a cyanide but all attempts to reduce the compounds to the desired trivalent oxidation state were unsuccessful. While the original target $[W^{III}(CN)_7]^{4-}$ was not obtained, importantly, the $[M^{IV}(CN)_7]^{3-}$ compounds are the first examples of S = 1 heptacyanometallates and polynuclear complexes incorporating these anions remain interesting targets.

CHAPTER III

POLYNUCLEAR COMPLEXES BASED ON HEPTACYANOMOLYBDATE(IV) AND HEPTACYANOTUNGSTATE(IV) ANIONS

Introduction

As previously outlined in the introduction chapter, anisotropic exchange is obtained via coupling through the axial cyanides of heptacyanometallates with large spin-orbit coupling parameters and orbital degeneracy, both of which are operative for the Mo^{III} and Re^{IV} ions. Both ions have been incorporated into a number of different polynucear architectures, but it is important to note that it is common to observe decomposition to octacyanometallate ions, or in the case of Mo, the loss of a cyanide ligand with formation of the hexacyanomolybdate anion. Another issue is that coupling to paramagnetic metal ions in equatorial cyanides for both $[Mo^{III}(CN)_7]^{4-}$ and $[Re^{IV}(CN)_7]^{3-}$ reduces the effect of the desired anisotropic exchange coupling.[77, 138] These issues notwithstanding, the heptacyanometallate moiety remains a viable route for taking advantage of anisotropic exchange in the development of SMMs with improved properties.

The synthesis and characterization of the $(Bu_4N)_3[M^{IV}(CN)_7]$ salts described in the previous chapter offers an opportunity to study the exchange coupling for S = 1 spin systems, which has not been investigated. Such information will provide valuable information regarding the importance of orbital degeneracy for engendering anisotropic coupling. In particular, the trinuclear complexes obtained with $MnCl_2(L_{N5})$ and

$K_4[Mo(CN)_7]^{76-}$ and the $[M_4(PY5Me_2)_4Re(CN)_7]^{5+}$ molecules [104] are excellent templates for probing exchange interactions, in order to compare to the previous examples.

Experimental

All reactions were performed in a drybox or on a Schlenk-line under an inert atmosphere unless otherwise stated. The solvents CH_3CN (Sigma Aldrich) and CH_3OH (MeOH, KOPTEC) were pre-dried over 3Å molecular sieves; CH_3CN was then distilled over 3Å sieves under nitrogen, while MeOH was distilled over Mg powder activated with I_2. Diethyl ether (Et_2O, EMD Millipore) was passed through an activated alumina column (MBraun solvent system). Anhydrous THF (Sigma Aldrich) and anhydrous N,N-dimethylformamide (DMF, Alfa Aesar) were used as received. All solvents were stored over molecular sieves in a drybox. The reagents $(Bu_4N)_3[Mo(CN)_7]$, $(Bu_4N)_3[W(CN)_7]$,[176] $PY5Me_2$ ligand,[184] $[Mn(L_{N5})(H_2O)]$,[76] $[Mn(PY5Me_2)(CH_3CN)](PF_6)_2$,[103] $[Ni(PY5Me_2)(CH_3CN)](PF_6)_2$,[104] $[Co(PY5Me_2)(CH_3CN)](PF_6)_2$,[104] and $[Cu(PY5Me_2)(CH_3CN)](PF_6)_2$[104] were prepared according to literature methods, while 3,4,7,8-tetramethylphenanthroline (Alfa Aesar) was used as received.

Synthesis

$[Fe^{II}(PY5Me_2)(CH_3CN)](CF_3SO_3)_2$ (11)

A vial was charged with 0.0623 g (0.1759 mmol) of $Fe(CF_3SO_3)_2$ and 0.0781 g (0.176 mmol) of the $PY5Me_2$ ligand. Addition of 8 mL of CH_3CN resulted in a yellow-red slurry that was stirred for 24 hours during which time the solution turned red. The solution was transferred to larger vials for slow vapor diffusion with diethyl ether, and X-ray quality crystals were obtained within 24 hours. The product was collected on a frit as

dark red crystals, washed with diethyl ether, and dried under vacuum. Mass of product: 0.1117 g, yield: 75.72 %.

$[Zn^{II}(PYPY5Me_2)(CH_3CN)](PF_6)_2$ (12)

A vial was charged with 0.1049 g (0.2364 mmol) of $PY5Me_2$ ligand and 0.0954 g (0.2366 mmol) of $[Zn(CH_3CN)_4](BF_4)_2$; addition of 7 mL of CH_3CN with stirring resulted in a yellow solution. After stirring for 48 hours, the solution is colorless/faint yellow. The solution was transferred to two larger vials for slow vapor diffusion with diethyl ether. X-ray quality crystals were obtained within 3 days, and the crystals were collected on a medium frit, washed with diethyl ether, and dried under vacuum. The compound was then transferred to a vial. Mass of product: 0.1249 g, yield: 72.91 %.

$\{[Mn^{II}(L_{N5})]_2[Mo^{IV}(CN)_8]\}_\infty$ (13)

A vial was charged with 0.025 g (0.0248 mmol) of $(Bu_4N)_3[Mo(CN)_7]$ and dissolved in 1.30 mL of CH_3CN to give a colorless solution. Separately, a vial was charged with 0.018 g (0.0449 mmol) of $MnCl_2$ dissolved in 1.78 mL of CH_3OH to give a yellow solution. The solution of $(Bu_4N)_3[Mo(CN)_7]$ was added with stirring to the solution of $Mn(L_{N5})$, which resulted in the formation of a red-brown precipitate. A 1 mL aliquot was removed for slow vapor diffusion with diethyl ether which produced yellow needles suitable for X-ray diffraction.

$\{[Mn^{II}(L_{N5})]_2[W^{IV}(CN)_8]\}_\infty$ (14)

A small vial was charged with 0.069 g (0.0631 mmol) of $(Bu_4N)_3[W(CN)_7]$ and dissolved in 3 mL of CH_3CN; a separate vial was charged with 0.055 g (0.137 mmol) of $MnCl_2(L_{N5})$ and a solution of 1.67 mL volume of CH_3CN and 1.69 mL of deoxygenated

H_2O were added to give a yellow solution. Approximately 6 mL of CH_3CN were added as a buffer layer, and then the solution of $(Bu_4N)_3[W(CN)_7]$ was carefully added as a layer to give a cloudy interface. The solution was stored in the dark and red needles suitable for X-ray diffraction formed after two days.

$\{[Sm^{III}(tmphen)_2(DMF)_2][W^V(CN)_8]\}_\infty$ (15)

A vial was charged with 0.017 g (0.0466 mmol) of $SmCl_3 \cdot 6H_2O$ and 0.024 g (0.1016 mmol) of tmphen ligand; addition of 2.0 mL H_2O, 2.53 mL of MeOH, and 3.18 mL of DMF with stirring gave a colorless/light orange solution. Separately, 0.051 g (0.0466 mmol) of $(Bu_4N)_3[W(CN)_7]$ was dissolved in 2.30 mL of H_2O, 1.27 mL of DMF, and 3.03 mL of MeOH to give a colorless solution. The solution of $(Bu_4N)_3[W(CN)_7]$ was added to the solution of $SmCl_3(tmphen)_2$ resulting in a dark yellow and then orange solution with no precipitate. Crystals were grown via slow vapor diffusion of the reaction solution with diethyl ether. Mass of product: 0.022 g, yield: 57.1%.

$\{[Dy^{III}(tmphen)_2(DMF)_2][W^V(CN)_8]\}_\infty$ (16)

A vial was charged with 0.016 g (0.0431 mmol) of $DyCl_3 \cdot 6H_2O$ and 0.018 g (0.0762 mmol) of tmphen ligand; addition of 3.2 mL of H_2O, 3.03 mL of MeOH, and 3.28 mL of DMF with stirring gave a colorless solution. Separately, 0.037 g (0.0338 mmol) of $(Bu_4N)_3[W(CN)_7]$ was dissolved in 2.75 mL DMF and 2.28 mL MeOH to give a colorless solution. The solution of $(Bu_4N)_3[W(CN)_7]$ was added to the solution of $DyCl_3(tmphen)_2$, resulting in a dark yellow and then an orange solution with no precipitate. Crystals were grown via slow vapor diffusion diethyl ether into the reaction solution.

$[Mn^{II}(PY5Me_2)]_4[W^{IV}(CN)_8](PF_6)_4$ (17)

A vial was charged with 0.0115 g (0.0105 mmol) of $(Bu_4N)_3[W(CN)_7]$ which was dissolved in 0.80 mL of CH_3CN to give a colorless solution. Separately, a thin vial was charged with 0.0362 g (0.0436 mmol) of $[Mn(PY5Me_2)(CH_3CN)](PF_6)_2$ and dissolved in 0.97 mL of CH_3CN to give a colorless solution with manual stirring. The solution of $(Bu_4N)_3[W(CN)_7]$ was then slowly added via pipette to the solution of $Mn(PY5Me_2)^{2+}$, resulting in a light yellow and then orange solution. The vial was placed in a jar with THF for slow vapor diffusion. After 6 weeks, a yellow precipitate was collected on a frit, washed with THF to remove the Bu_4NPF_6 by-product, and washed with diethyl ether and dried under vacuum. Mass of product: 0.0197 g, yield: 53.7 % (based on $C_{143}H_{126}N_{37}Mn_4WP_4F_{24}$).

$[Fe^{II}(PY5Me_2)]_4[W^{IV}(CN)_8](PF_6)_4$ (18)

A vial was charged with 0.0155 g (0.0141 mmol) of $(Bu_4N)_3[W(CN)_7]$ and dissolved in 0.73 mL of CH_3CN to give a colorless solution. Separately, a second vial was charged with 0.0472 g (0.0562 mmol) of $[Fe(PY5Me_2)(CH_3CN)](CF_3SO_3)_2$ and dissolved in 1.86 mL of CH_3CN to give a dark red solution. The solution of $(Bu_4N)_3[W(CN)_7]$ was then slowly added via pipette to the solution of $Fe(PY5Me_2)^{2+}$, resulting in a lighter red solution and a precipitate that redissolved upon stirring. The vial was placed in a jar with diethyl ether for slow vapor diffusion. After 3 weeks, dark red crystals along with an orange precipitate was collected on a frit, washed with THF to remove the Bu_4NPF_6 by-product, then washed with diethyl ether and dried under vacuum. Mass of product: 0.0121 g, yield: 25.6% (based on $C_{143}H_{126}N_{37}Fe_4WP_4F_{24}$).

$[Co^{II}(PY5Me_2)]_4[Mo^{IV}(CN)_8](PF_6)_4$ (19)

A vial was charged with 0.0101 g (0.0101 mmol) of $(Bu_4N)_3[Mo(CN)_7]$ and dissolved in 2.43 mL of CH_3CN to give a colorless solution. Separately, a vial was charged with 0.0275 g (0.0328 mmol) of $[Co(PY5Me_2)(CH_3CN)](PF_6)_2$ and dissolved in 3.37 mL of CH_3CN to give a gold-brown solution with manual stirring. The solution of $(Bu_4N)_3[Mo(CN)_7]$ was then slowly added via pipette to the solution of $Co(PY5Me_2)^{2+}$ resulting in a layer with a white, cloudy precipitate. The vial was placed in a jar with diethyl ether for slow vapor diffusion. After 4 months, red crystals and a red-grey precipitate were observed, which was collected on a frit, washed with THF to remove Bu_4NPF_6 byproduct, and redissolved in CH_3CN to give a dark red solution for crystallization. Attempts to recrystallize led to yellow and white powder precipitates, which were washed with THF and diethyl ether, and then dried under vacuum. Mass of product: 0.0253 g, yield: 74.9 %.

$[Co^{II}(PY5Me_2)]_4[W^{IV}(CN)_8](PF_6)_4$ (20)

A vial was charged with 0.0473 g (0.0432 mmol) of $(Bu_4N)_3[W(CN)_7]$ and dissolved in 1.25 mL of CH_3CN to give a colorless solution. Separately, a vial was charged with 0.1421 g (0.1704 mmol) of $[Co(PY5Me_2)(CH_3CN)](PF_6)_2$ and dissolved in 4.10 mL of CH_3CN to give an orange solution with manual stirring. The solution of $(Bu_4N)_3[W(CN)_7]$ was then added via pipette to the solution of $Co(PY5Me_2)^{2+}$, resulting in a layer with a dark red solution with some precipitate. The vial was placed in a jar with diethyl ether for slow vapor diffusion. After four months, green crystals were collected on a frit, washed with THF to remove the Bu_4NPF_6 by-product, and dried under vacuum.

Mass of product: 0.0670 g, yield: 53.6 %. Elemental analysis: Theoretical C: 50.16, H: 3.58, N: 13.37; actual C: 47.21, H: 3.40, N: 12.16.

$[Ni^{II}(PY5Me_2)]_4[Mo^{IV}(CN)_8](PF_6)_4$ (21)

A vial was charged with 0.0215 g (0.0213 mmol) of $(Bu_4N)_3[Mo(CN)_7]$ and dissolved in 2.61 mL of CH_3CN to give a colorless/pale yellow solution. Separately, a vial was charged with 0.0702 g (0.0842 mmol) of $[Ni(PY5Me_2)(CH_3CN)](PF_6)_2$ and dissolved in 3.47 mL of CH_3CN to give a light pink solution with manual stirring. The solution of $(Bu_4N)_3[Mo(CN)_7]$ was then slowly added via pipette to the solution of $Ni(PY5Me_2)^{2+}$, resulting in a layer with white, cloudy precipitate. The vial was placed in a jar with diethyl ether for slow vapor diffusion. After 3 weeks, orange crystals had formed which were collected on a frit, washed with THF to remove the Bu_4NPF_6 byproduct, washed with diethyl ether and dried under vacuum. Mass of product: 0.0294 g, yield: 47.7 %.

$[Ni^{II}(PY5Me_2)]_4[W^{IV}(CN)_8](PF_6)_4$ (22)

A vial was charged with 0.0683 g (0.0624 mmol) of $(Bu_4N)_3[W(CN)_7]$ and dissolved in 2.51 mL of CH_3CN to give a colorless solution. Separately, a vial was charged with 0.2087 g (0.2504 mmol) of $[Ni(PY5Me_2)(CH_3CN)](PF_6)_2$ and dissolved in 3.97 mL of CH_3CN to give a light pink solution with manual stirring. The solution of $(Bu_4N)_3[W(CN)_7]$ was then slowly added via pipette to the solution of $Ni(PY5Me_2)^{2+}$, resulting in an orange-red solution with precipitate that redissolved upon stirring. The vial was placed in a jar with diethyl ether for slow vapor diffusion. After 2 weeks, orange crystals had formed which was collected on a frit, washed with THF to remove Bu_4NPF_6

by-product, then washed with diethyl ether and dried under vacuum. Mass of product: 0.1685 g, yield: 86.3%.

$[Cu^{II}(PY5Me_2)]_4[W^{IV}(CN)_8](PF_6)_4$ (23)

A vial was charged with 0.0384 g (0.0351 mmol) of $(Bu_4N)_3[W(CN)_7]$ and dissolved in 1.43 mL of CH_3CN to give a colorless solution. Separately, another vial was charged with 0.1169 g (0.1394 mmol) of $[Cu(PY5Me_2)(CH_3CN)](PF_6)_2$ and dissolved in 3.44 mL of CH_3CN to give a blue solution with manual stirring. The solution of $(Bu_4N)_3[W(CN)_7]$ was then added via pipette to the solution of $Cu(PY5Me_2)^{2+}$ with stirring, resulting in a darker blue solution. The vial was placed in a jar with diethyl ether for slow vapor diffusion. After 4 months, the resulting blue product was collected on a frit, washed with THF to remove the Bu_4NPF_6 by-product, washed with diethyl ether, and dried under vacuum. Mass of product: 0.1075 g, yield: 90.6 (% (based on $C_{143}H_{126}N_{37}Cu_4WP_4F_{24}$).

X-ray Crystallography

Crystals of compounds **11**, **12**, **13**, **15**, and **21** were mounted on a Nylon loop using Paratone® oil and placed in a N_2 cold stream at 110 K. The data were collected on a Bruker D8 Quest Eco diffractometer (MoKα radiation λ = 0.71073 Ǻ) equipped with a Photon50 CMOS detector. The data sets were recorded as four ω-scans and integrated using the Bruker APEX3 software package. Compound **14** was mounted on a Nylon loop in Paratone® oil, placed in a N_2 cold stream at 110 K, and the data were collected on a Bruker APEX II diffractometer (MoKα radiation λ = 0.71073 Å) equipped with a CCD detector. For all the data sets, the multi-scan absorption correction was performed within the Bruker

APEXII software using SADABS (v2014/5) or within the Bruker APEX3 software using SADABS (v2015/10).[163-164] Solution and refinement of the crystal structures were carried out using SHELXT and shelXle (a graphical interface for the SHELX suite of programs), respectively or Olex programs.[165-166, 185] Single crystal diffraction data for compounds **16** and **19** were collected at 110 K at the ChemMatCars beamline 15-ID-B at the Advanced Photon Source (APS), Argonne National Lab. The data collection strategy consisted of obtaining three ω-scans with one full-sphere and two half-spheres for a total of 1440 frames with a 0.5º width. Integration was performed with the Bruker-APEXII software package, and the absorption correction (SADABS) was based on fitting a function to the empirical transmission surface as sampled by multiple equivalent measurements. Compound **20** was collected at the Advanced Light Source at Lawrence Berkeley National Lab. The data collection strategy consisted of obtaining five ω-scans, integration was performed with the Bruker-APEXII software package, and the absorption correction (SADABS) was based on fitting a function to the empirical transmission surface as sampled by multiple equivalent measurements. Structure solution by direct methods resolved positions of all heavy atoms and most of the lighter atoms. The remaining non-hydrogen atoms were located by alternating cycles of least-squares refinements and difference Fourier maps. The final refinements were performed with anisotropic thermal parameters for all non-hydrogen atoms. Images of the molecular structures were rendered using DIAMOND software for crystal structure visualization.[167] A summary of pertinent information relating to unit cell parameters, data collection, and refinement is provided in Table 8.

Physical Methods

IR spectra were recorded on a Nicolet Nexus 470 FT-IR E.S.P spectrophotometer Nujol® mulls of the samples between two KBr paltes unless otherwise noted. Elemental analysis was performed by Atlantic Microlabs, Inc., Norcross, GA. Magnetic measurements were performed on a Quantum Design MPMS-XL SQUID magnetometer equipped with a 7T superconducting magnet over the temperature range 1.8 to 300 K; the diamagnetic contribution of the plastic bag used as a sample holder was subtracted from the raw data, and core diamagnetism of the sample was corrected for using Pascal's constants.[168]

Results and Discussion

Syntheses

Initial syntheses focused on the use of the $MnCl_2(L_{N5})$ compound, which had previously been used in reactions with $K_4[Mo(CN)_7]$ to obtain a linear trinuclear compound with the highest U_{eff} barrier for a cyanide compound. Reaction of the $MnCl_2(L_{N5})$ with $(Bu_4N)_3[W(CN)_7]$ in a 2:1 ratio in H_2O/CH_3CN resulted in the formation of red crystals of **14**, which was determined to be a 2D polymeric chain of alternating Mn and W ions bridged by cyanide ligands. The heptacyanotungstate(IV) anion also acquires another cyanide ligand, resulting in the diamagnetic octacyanotungstate(IV) species.

In an attempt to prevent the decomposition to the octacyanometallate(IV) anion and the formation of 2D networks, the capping ligand $PY5Me_2$ ligand was used. The Long group successfully employed this ligand in reactions with $(Bu_4N)_3[Re(CN)_7]$, which is isomorphous with the molybdenum and tungsten starting materials. The syntheses of the

Table 8: Crystallographic data and experimental details for compounds **11 – 16** and **19 – 21**.

Compound	**11**	**12**	**13**	**14**	**15**
MW (g/mol)	920.69	723.58	1142.92	1226.80	826.9
Temperature	110	110	110	110	110
Crystal System	Monoclinic	Triclinic	Hexagonal	Hexagonal	Monoclinic
Space Group	$P2_1/n$	P1b	$P3_221$	$P3_121$	P2/c
a (Å)	12.4725(6)	12.8118(7)	19.0407(6)	19.030(3)	19.155(5)
b (Å)	15.7642(7)	15.6259(8)	19.0407(6)	19.030(3)	21.150(5)
c (Å)	19.9465(8)	15.9553(9)	12.4554(5)	12.413(2)	14.821(4)
α (°)	90	93.394(2)	90	90	90
β (°)	90.910(2)	91.011(2)	90	90	111.673(8)
γ (°)	90	106.121(2)	120	120	90
V ($Å^3$)	3921.4(3)	3061.3(3)	3910.7(3)	3893.1(12)	5580(2)
Z	4	4	3	3	6
Color	Red	Colorless	Yellow	Red	Orange
ρcalc (g/cm^3)	1.559	1.570	1.456	1.570	1.477
μ (mm)	0.578	0.885	0.782	2.758	3.223
F(000)	1888.0	1472.0	1782.0	1866.0	2446.0
Crystal Size (mm)	0.100 x 0.219 x 0.252	0.106 x 0.199 x 0.333	0.076 x 0.088 x 0.429	0.050 x 0.060 x 0.200	0.069 x 0.08 x 0.220
Radiation	MoKα (λ = 0.71073)	MoKα (λ = 0.71073)	MoKα (λ = 0.71073)	MoKα (λ = 0.71073)	MoKα (λ = 0.71073)
Index Range	-16≤h≤16 -20≤k≤20 -25≤l≤25	-16≤h≤16 -20≤k≤20 -20≤l≤20	-24≤h≤24 --24≤k≤24 -16≤l≤16	-22≤h≤22 -22≤k≤22 -14≤l≤14	-22≤h≤22 -25≤k≤25 -17≤l≤17
2θ range (°)	4.616 – 55.178	4.112 – 55.188	4.098 – 55.066	2.472 - 50.218	4.480 – 50.178
Reflections collected	62642	149205	46540	38014	82469
Unique reflections	9057	14175	6023	4612	9911
Parameters/restraints	546, 0	871, 0	331, 0	331, 0	609, 0
R_1, wR_2 [$I > 2\sigma(I)$]	0.0492, 0.1019	0.0471, 0.1355	0.0546, 0.1297	0.0344, 0.0866	0.0709, 0.2039
R_1, wR_2 (all data)	0.0730, 0.1129	0.0757, 0.1565	0.0634, 0.1358	0.0376, 0.0953	0.0895, 0.2229
GooF (F^2)	1.015	1.059	1.080	1.136	1.043
Largest diff. peak, hole, ($e Å^{-3}$)	-0.63, 0.61	-0.79, 0.92	-0.96, 1.04	-0.78, 1.37	-2.54, 4.02

[a]$R = \Sigma ||F_o| - |F_c|| / \Sigma |F_o|$. [b]$wR = <\Sigma [w(F_o^2 - F_c^2)^2] / \Sigma [w(F_o^2)]^2\}^{1/2}$. [c]Goodness-of-fit $= <\Sigma [w(F_o^2 - F_c^2)^2]/(n-p)\}^{1/2}$, where *n* is the number of reflections and *p* is the total number of parameters refined.

Table 8 Continued

Formula	**16**	**19**	**20**	**21**
Molecular Weight	651.71	3342.45	3011.83	2935.04
Temperature (K)	110	110	110	110
Crystal System	Monoclinic	Triclinic	Triclinic	Triclinic
Space Group	P2/c	P1b	P1b	P1b
a (Å)	19.1500(6)	17.1052(19)	17.1894(9)	17.497(4)
b (Å)	20.9911(7)	22.172(3)	20.1086(11)	20.812(5)
c (Å)	14.7681(5)	22.593(2)	21.9737(12)	22.100(6)
α (°)	90	97.437(2)	86.177(3)	83.379(6)
β (°)	112.258(1)	104.911(2)	83.283(3)	82.055(6)
γ (°)	90	109.247(2)	73.203(3)	73.372(6)
V (Å^3)	5494.1(3)	7598.5(14)	7217.0(7)	7613(3)
Z	8	2	2	2
Color	Orange	Pink	Red	Orange
ρcalc (g/cm^3)	1.576	1.461	1.386	1.280
μ (mm)	3.505	0.644	1.374	0.689
F(000)	2588.0	3420.0	3032.0	2986.0
Crystal Size (mm)	0.08 x 0.23 x 0.36	0.184 x 0.184 x 0.196	0.050 x0.080 x0.100	0.103 x 0.189 x 0.292
Radiation	APS Synchrotron	APS Synchrotron	ALS Synchrotron	MoKα (λ = 0.71073)
Index Range	-24≤h≤24 -27≤k≤27 -19≤l≤19	-22≤h≤22 -28≤k≤28 -29≤l≤29	-15≤h≤16 -19≤k≤19 -21≤l≤20	-17≤h≤17 -20≤k≤20 -22≤l≤22
2θ range (°)	3.008 – 55.070	4.820 – 54.970	4.058 – 40.668	4.098 – 42.052
Reflections collected	222690	184068	23240	98561
Unique reflections	12610	33332	12354	16176
Parameters/restraints	678, 0	1923, 0	1652, 0	1597, 3
[a]R_1, [b]wR_2 [$I > 2\sigma(I)$]	0.0534, 0.1604	0.1791, 0.5024	0.1563, 0.4028	0.2322, 0.5611
R_1, wR_2 (all data)	0.0666, 0.1740	0.1885, 0.5078	0.2024, 0.4355	0.2891, 0.5989
[c]GooF (F^2)	1.033	2.220	1.649	2.577
Largest diff. peak, hole, (e Å^{-3})	-2.49, 3.26	-1.322, 4.963	-1.215, 3.329	-1.272, 3.418

[a]$R = \Sigma ||F_o| - |F_c|| / \Sigma |F_o|$. [b]$wR = \{\Sigma [w(F_o^2 - F_c^2)^2] / \Sigma [w(F_o^2)]^2\}^{1/2}$. [c]Goodness-of-fit = $\{\Sigma [w(F_o^2 - F_c^2)^2]/(n-p)\}^{1/2}$, where *n* is the number of reflections and *p* is the total number of parameters refined.

starting materials $[M^{II}(PY5Me_2)(CH_3CN)](PF_6)_2$ (M^{II} = Mn, Ni, Co, Cu) were carried out following literature methods,[104] and procedures were developed for the Fe and Zn analogues. In the case of Fe, the previous report was of the $[Fe(PY5Me_2)]^{2+}$ compound,[186] but the reaction involved the use of hydrated perchlorate salts;[187] attempts to replicate the normal synthetic route were unsuccessful. As an alternative, the reaction of $Fe^{II}(CF_3SO_3)_2$ was reacted with the $PY5Me_2$ ligand in CH_3CN to give in dark red solution, which, when crystallized from diethyl ether, gave red crystals of **11**. Similarly, reacting $[Zn^{II}(CH_3CN)_4](BF_4)_2$ with the $PY5Me_2$ ligand results in white crystals of compound **12**. These results indicate that the starting material for $[M^{II}(PY5Me_2)(CH_3CN)]X_2$ can be synthesized for a variety of 3d metals and different anions X^- by using fully solvated starting materials with acetonitrile as the solvating ligand.

The reaction of $[M^{II}(PY5Me_2)(CH_3CN)]X_2$ with $(Bu_4N)_3[W^{IV}(CN)_7]$ was performed by first dissolving the $(Bu_4N)_3[W^{IV}(CN)_7]$ in CH_3CN and then adding four equivalents of $[M^{II}(PY5Me_2)(CH_3CN)]^{2+}$ in CH_3CN. The use of four equivalents of $[M^{II}(PY5Me_2)(CH_3CN)]^{2+}$ results in better yields of the product and attempts to vary the stoichiometry by using a 2:1 ratio of $[M^{II}(PY5Me_2)(CH_3CN)]$ to $(Bu_4N)_3[W^{IV}(CN)_7]$ in order to obtain a product with only axial coordination merely resulted in the formation of the pentanuclear complex in a lower yield. The cations in the resulting salts $[M^{II}(PY5Me_2)]_4[W^{IV}(CN)_8]X_4$, (M = Mn, **17**; Fe, **18**, Co, **20**; Ni, **22**; and Cu, **23**), are star-like complexes. Moreover, there is still decomposition to $[W^{IV}(CN)_8]^{4-}$, resulting in a diamagnetic central ion. Attempts to prevent this outcome by varying the solvents (CH_2Cl_2 or DMF for the reaction, or THF for the crystallizing solvent) produced the same result,

as did performing the reaction at -30 °C. It is important to point out that the Long group reported that reactions of $(Bu_4N)_3[Re^{IV}(CN)_7]$ were initially performed at -42 °C to avoid spontaneous reduction of $(Bu_4N)_3[Re^{III}(CN)_7]$,[104] but it was found that, with the exception of Cu, the reactions could all be carried out at ambient temperatures. The $[Cu^{II}(PY5Me_2)]_4[Re^{IV}(CN)_7]$ compound was only stable at low temperature according to the Long group. In contrast, the $[W^{IV}(CN)_7]^{3-}$ reactions performed at -30 °C still decomposed; colder temperatures could forestall the decomposition but this remains untested. Of the reactions **17**, **18**, **20**, **22**, and **23**, only the Co (**20**) and Ni (**22**) products produced crystals that were discernable from the starting materials. In the case of Mn (**17**), Fe (**18**), and Cu (**23**), the products were either powders or crystals formed were similar in color to the starting material, making characterization difficult. This was confirmed by a red crystal of **18**; the preliminary diffraction data showed the crystal to have the structure $[Fe^{II}(PY5Me_2)]_4[W^{IV}(CN)_8]^{4+}$, but when crystals from the same reaction were sent to Argonne National Laboratory for synchrotron diffraction, the crystals turned out to be starting material **11**.

The reactions of $Ln^{III}(tmphen)_2Cl_3$ (Ln^{III} = Sm, Dy; tmphen = 3,4,7,8-tetramethylphenanthroline) with $(Bu_4N)_3[W^{IV}(CN)_7]$ in a 1:1 ratio were performed in CH_3CN/MeOH/DMF to determine whether charge-balancing the tris-anionic charge of $(Bu_4N)_3[W^{IV}(CN)_7]$ with a trivalent lanthanide ion would prevent the decomposition to $[W^{IV}(CN)_8]^{4-}$. Previous work with $Ln(tmphen)_2Cl_3$ and $K_4[Mo^{III}(CN)_7]$ resulted in cyanide loss to form a series of 1D chains that contain the $[Mo^{III}(CN)_6]^{3-}$ anion. The reactions with $[W^{IV}(CN)_7]^{3-}$ resulted in a 1D chain for both Sm (**15**) and Dy (**16**), with alternating

lanthanide and tungsten metal ions bridged by the cyanide ligand. The products contain the $[W^{V}(CN)_8]^{3-}$ ion, however, on the basis of the absence of a cation for charge balancing.

To determine whether the decomposition of $[W^{IV}(CN)_7]^{3-}$ is due to inherent thermodynamic instability or a result of the reaction conditions, the $[Mo^{IV}(CN)_7]^{3-}$ analogue was synthesized and reactions were carried out under similar conditions. Reaction of $Mn^{II}Cl_2(L_{N5})$ with $(Bu_4N)_3[Mo^{IV}(CN)_7]$ in a 2:1 ratio in a mixture of CH_3CN/MeOH produces yellow needles for **13**. The product was found to be a 2D network of alternating Mn and Mo ions, namely $[Mn^{II}(L_{N5})]_2[Mo^{IV}(CN)_8]\}_{\infty}$. The main point is that the heptacyanomolybdate anion decomposes to octacyanomolybdate(IV). Likewise, reactions of $[M^{II}(PY5Me_2)(CH_3CN)]X_2$ with $(Bu_4N)_3[Mo^{IV}(CN)_7]$ also yields star-like complexes with the $[Mo^{IV}(CN)_8]^{4-}$ ion in the center. These findings indicate that the $(Bu_4N)_3[M^{IV}(CN)_7]$ salts, while able to be isolated and crystallized, are unstable in the presence of cationic metal reagents precursors which trigger loss of a cyanide to form $[M^{IV}(CN)_8]^{4-}$. It remains to be determined whether the heptacyano derivatives will maintain their integrity at very low temperatures. Similar to the tungsten reactions, the molybdenum reactions were performed with the 3d metals Mn, Fe, Co, Ni, and Cu, but only the Co (**19**) and Ni (**21**) reactions produced crystals that could be characterized via crystallography.

Single Crystal X-ray Diffraction

Compound **11** crystallizes as red blocks in the monoclinic space group $P2_1/n$; the asymmetric unit contains $[Fe^{II}(PY5Me_2)(CH_3CN)](CF_3SO_3)_2 \cdot CH_3CN$ (Figure 37). The Fe metal center adopts a slightly distorted octahedral geometry, coordinating to the $PY5Me_2$

ligand in five sites with CH_3CN occupying the sixth position. The Fe—N_1(axial) bond distance is 1.970(2) Å, the Fe—$N_{equatorial}$ bond distances vary from 1.997(2) to 2.021(2) Å and the Fe—$NCCH_3$ bond distance is 1.941(2) Å. Similar results were reported for $[Fe^{II}(PY5Me_2)(CH_3CN)](ClO_4)_2 \cdot H_2O$.[186-187] The bond angles between the equatorial nand axial nitrogen donors vary between 88.07(8) to 90.41(8) °, the *cis* equatorial N—Fe—N bond angles range from 82.47(8) to 97.97(8) °, the *trans* equatorial N—Fe—N bond angles are 178.42(9) ° and 177.44(9) ° and the axial N_1—Fe—$NCCH_3$ bond angle is 177.26 °. The new triflate salt exhibits significantly less distortion from the ideal octahedral geometry as compared to the perchlorate salt. The angles indicate slight deviations from the octahedral geometry and the Fe metal ion lies 0.02 Å above the equatorial plane. Select bond distances and bond angles are reported in Table 11.

Compound **12** crystallizes as white-colorless blocks in the triclinic space group P-1 and the asymmetric unit contains two molecules of $[Zn^{II}(PY5Me_2)(CH_3CN)](BF_4)_2$ (Figure 38). The Zn metal center adopts a slightly distorted octahedral geometry. The Zn—N_1(axial) bond distance is 2.104(3) Å, the Zn—$N_{equitorial}$ bond distances vary between 2.119(3) to 2.191(4) Å, and the Zn—$NCCH_3$ bond distance is 2.174(4) Å. These results mostly agree with a previously reported $[Zn^{II}(2PYN2Q)(CH_3CN)](ClO_4)_2 \cdot CH_3CN$, although the Zn—$NCCH_3$ bond distance in that structure is 2.07 Å, which is significantly shorter.[188] Additionally, the bond angles between the equatorial and axial nitrogen donors vary between 86.11(14) to 88.60(14) °, the *cis* equatorial N—Zn—N bond angles range from 82.62(14) to 95.66(13) °, and the *trans* equatorial N—Zn—N bond angles are 171.48(13) ° and 176.26(14) °; the axial N_1—Zn—$NCCH_3$ bond angle is 176.19(14) °.

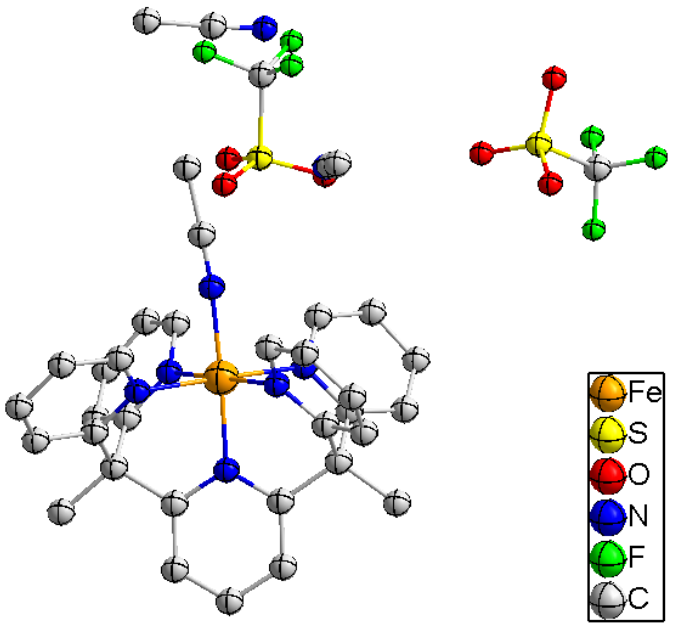

Figure 37: Molecular structure of compound **11**. Hydrogen atoms are omitted for the sake of clarity.

Table 9: Select bond distances and bond angles for compound **11**.

Select Bond	Bond Distance (Å)	Select Bond	Bond Angle (°)
Fe—N_1	1.970(2)	N_1—Fe—N_2	90.41(8)
Fe—N_2	2.009(2)	N_1—Fe—N_3	90.05(8)
Fe—N_3	2.007(2)	N_1—Fe—N_4	88.07(8)
Fe—N_4	2.021(2)	N_1—Fe—N_5	89.07(8)
Fe—N_5	1.997(2)	N_2—Fe—N_4	178.42(9)
Fe—N_6	1.941(2)	N_3—Fe—N_2	82.47(8)
N_6—C_{30}	1.142(3)	N_3—Fe—N_4	97.97(8)
		N_6—Fe—N_1	177.26(9)
		N_6—Fe—N_2	92.20(9)
		N_6—Fe—N_3	91.11(9)
		N_6—Fe—N_4	89.31(9)
		N_6—Fe—N_5	89.87(9)
		N_5—Fe—N_2	95.14(8)
		N_5—Fe—N_3	177.44(9)
		N_5—Fe—N_4	84.40(8)
		C_{30}—N_6—Fe	178.0(3)

This compound exhibits significantly more distortion from an ideal octahedral geometry as compared to both the zinc perchlorate salt and the iron triflate analogue.[188] Additionally, the Zn metal ion lies 0.11 Å above the equatorial plane formed by the equatorial N atoms. Select bond distances and bond angles are reported in Table 10.

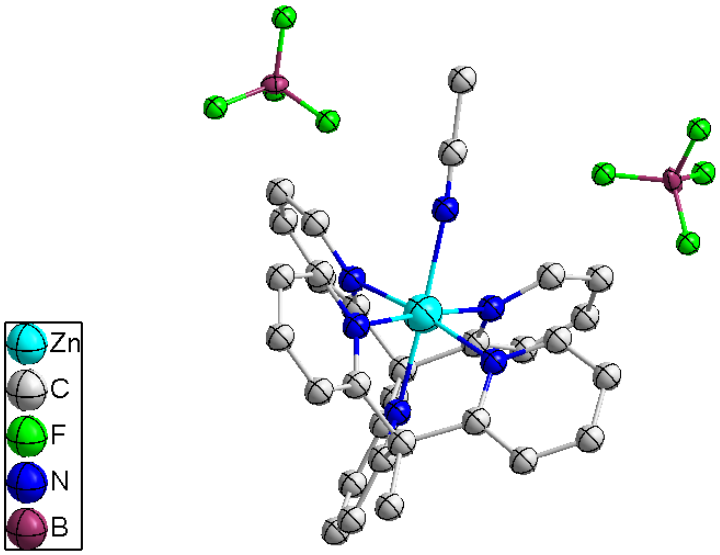

Figure 38: Molecular structure of compound **12**. Hydrogen atoms and solvent molecules are omitted for the sake of clarity.

Table 10: Select bond distances and bond angles for compound **12**.

Select Bond	Bond Distance (Å)	Select Bond	Bond Angle (°)
Zn—N_1	2.104(3)	N_1—Zn—N_3	88.60(14)
Zn—N_3	2.138(4)	N_1—Zn—N_4	86.13(13)
Zn—N_4	2.169(4)	N_1—Zn—N_5	87.97(13)
Zn—N_5	2.119(3)	N_1—Zn—N_6	176.19(14)
Zn—N_6	2.174(4)	N_1—Zn—N_2	86.11(14)
Zn—N_2	2.191(4)	N_3—Zn—N_4	95.66(13)
N_6—C_{30}	1.133(6)	N_3—Zn—N_6	90.05(14)
		N_3—Zn—N_2	80.61(14)
		N_4—Zn—N_6	97.55(14)
		N_4—Zn—N_2	171.48(13)
		N_5—Zn—N_3	176.26(14)
		N_5—Zn—N_4	82.62(14)
		N_5—Zn—N_6	93.47(14)
		N_5—Zn—N_2	100.64(14)
		N_6—Zn—N_2	90.15(14)
		C_{30}—N_6—Zn	170.0(4)

In the case of compound **13**, the yellow needles crystallize in the hexagonal space group $P3_221$, and the asymmetric unit contains the $[Mn^{II}(L_{N5})Mo^{IV}(CN)_4]$ fragment with the remainder of the compound being generated by symmetry (Figure 39). The Mo—CN bond distances vary from 2.151(8) to 2.183(7) Å and the C—N bond distances range between 1.137(10) to 1.157(9) Å, consistent with the previously reported $[Mo^{IV}(CN)_7]^{3-}$ starting material. The Mn—N bond distances are 2.247(6) and 2.261(6) Å, consistent with previously reported bond distances for manganese-molybdenum compounds.[121, 138] The $[Mo^{IV}(CN)_8]^{4-}$ anion adopts a square antiprismatic geometry, as evidenced by the bond angles. The Mo—CN bond angles vary between 176.7(6) to 179.7(9) °, and the C—N—Mn and axial N—Mn—N bond angles are 154.5(6) ° and 166.6(3) °, respectively. Select

bond distances and bond angles are reported in Table 11. In the *ab* plane, the 2D architecture forms a hexagonal network with $[Mo^{IV}(CN)_8]^{4-}$ anions at the vertices with the smaller triangles between the vertices being composed of the $Mn^{II}(L_{N5})$ cations. The void space inside the hexagon being is filled with solvent molecules (Figure 40).

Compound **14** forms red needles that crystallize in the hexagonal space group $P3_121$. The asymmetric unit contains the $[Mn^{II}(L_{N5})W^{IV}(CN)_4]$ fragment similar to its molybdenum analogue (Figure 41). The W—CN bond distances range from 2.160(9) to 2.183(8) Å and the C—N bond distances are between 1.137(10) and 1.152(12) Å, consistent with the previously reported $[W^{IV}(CN)_7]^{3-}$ starting material. The Mn—N bond distances are 2.256(7) and 2.239(7) Å, which are similar to reported bond distances for manganese(II)-tungsten(IV) compounds.[189] The $[W^{IV}(CN)_8]^{4-}$ ion adopts a square antiprismatic geometry, as evidenced by the bond angles; additionally, the W—CN bond angles vary between 176.4(7) to 178.9(10) ° with the C—N—Mn and axial N—Mn—N bond angles being 160.1(7) ° and 166.8(3) °, respectively. Select bond distances and bond angles are reported in Table 12. As in the case of the Mo analogue, the 2D structure forms a hexagonal network in the *ab* plane with $[W^{IV}(CN)_8]^{4-}$ anions at the vertices and the smaller triangles between vertices being composed of the $Mn^{II}(L_{N5})$ cations. Solvent molecules occupy the space inside the hexagonal rings (Figure 42).

Orange crystals of **15** crystallize in the space group P2/c with $[Sm^{III}(tmphen)(DMF)][W^{V}(CN)_8]$ as the asymmetric unit. The compound forms a 1D helical chain of alternating Sm and W metal ions (Figure 43). The W—C bond distances vary from 2.137(15) to 2.177(16) Å and the C—N bond distances range from 1.134(16)

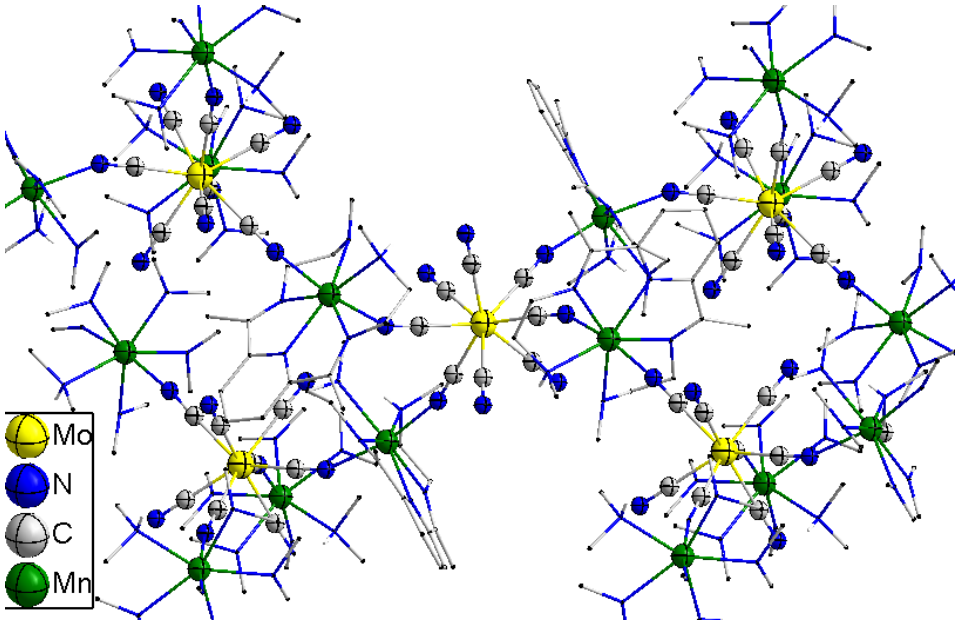

Figure 39: Molecular structure of **13**. Hydrogen atoms and solvent molecules are omitted for the sake of clarity. The L_{N5} ligand atoms are displayed as a wire model.

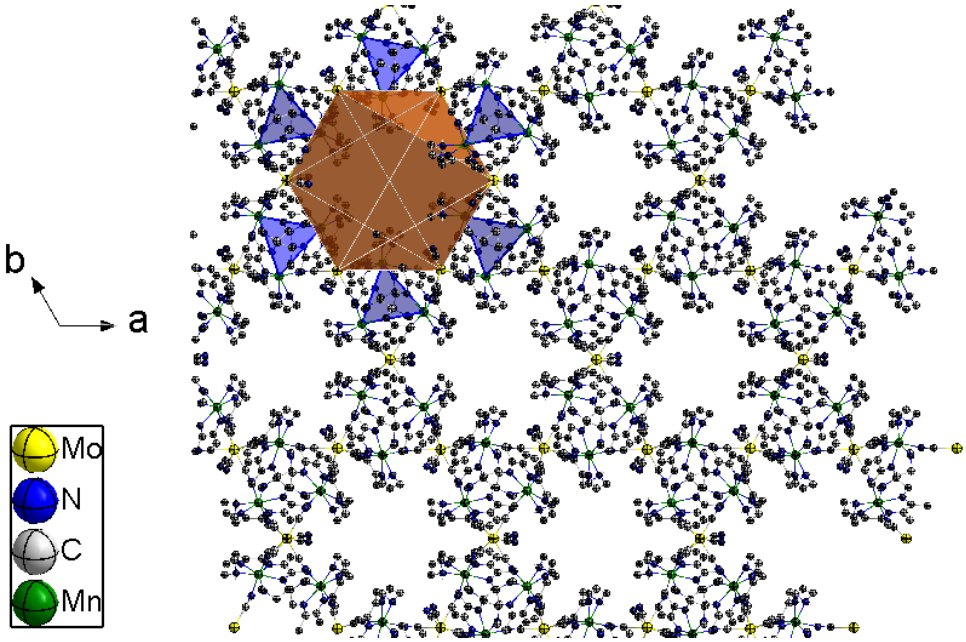

Figure 40: Compound **13** parallel to the *c* axis viewing the *ab* plane. Blue triangles are formed by Mn ions and the orange hexagon shows the void formed by the Mo ions.

Table 11: Select bond distances and bond angles for compound **13**.

Select Bond	Bond Distance (Å)	Select Bond	Bond Angle (°)
Mo—C_1	2.179(7)	C_1—Mo_1—C_1'	115.6(4)
Mo—C_2	2.153(7)	C_1—Mo_1—C_3	145.0(3)
Mo—C_3	2.183(7)	C_1'—Mo_1—C_3'	145.0(3)
Mo—C_4	2.151(8)	C_1'—Mo_1—C_3	78.9(3)
Mn_1—N_1	2.247(6)	C_1—Mo_1—C_3'	78.9(3)
Mn_2—N_2	2.261(6)	C_3'—Mo_1—C_3	108.0(4)
Mn_1—N_5	2.299(7)	C_2—Mo_1—C_1'	138.5(3)
Mn_1—N_6	2.366(7)	C_2'—Mo_1—C_1	138.5(3)
Mn_1—N_7	2.328(7)	C_2—Mo_1—C_1	78.3(2)
Mn_1—N_8	2.346(7)	C_2'—Mo_1—C_1'	78.2(2)
Mn_1—N_9	2.410(10)	C_2—Mo_1—C_3	71.5(2)
C_1—N_1	1.141(9)	C_2'—Mo_1—C_3	73.6(2)
C_2—N_2	1.157(9)	C_2'—Mo_1—C_3'	71.5(2)
C_3—N_3	1.137(10)	C_2—Mo_1—C_3'	73.6(2)
C_4—N_4	1.155(11)	C_2—Mo_1—C_2'	118.5(3)
		C_4'—Mo_1—C_1	73.9(3)
		C_4—Mo_1—C_1'	73.9(3)
		C_4'—Mo_1—C_1'	69.7(3)
		C_4—Mo_1—C_1	69.7(3)
		C_4—Mo_1—C_3'	83.0(3)
		C_4'—Mo_1—C_3	83.0(3)
		C_4'—Mo_1—C_3'	144.0(3)
		C_4—Mo_1—C_3	144.0(3)
		C_4—Mo_1—C_2'	78.2(3)
		C_4—Mo_1—C_2	143.4(3)
		C_4'—Mo_1—C_2'	143.4(3)
		C_4'—Mo_1—C_4	108.4(5)
		C_1—N_1—Mn	160.4(7)
		N_1—C_1—Mo	179.5(8)
		N_2—C_2—Mo	176.7(6)
		N_3—C_3—Mo	178.4(7)
		N_4—C_4—Mo	179.7(9)
		C_2—N_2—Mn′	154.5(6)
		N_1—Mn_1—N_2'	166.6(3)

Table 12: Select bond distances and bond angles for compound **14**.

Select Bond	Bond Distance (Å)	Select Bond	Bond Angle (°)
W—C_1	2.164(8)	C_1—W_1—C_1'	117.7(4)
W—C_2	2.181(8)	C_1'—W_1—C_3'	71.8(3)
W—C_3	2.183(8)	C_1'—W_1—C_3	73.3(3)
W—C_4	2.160(9)	C_1—W_1—C_3'	73.3(3)
Mn_1—N_1	2.256(7)	C_1—W_1—C_3	71.8(3)
Mn_2—N_2	2.239(7)	C_1—W_1—C_2'	139.3(3)
Mn_1—N_5	2.296(8)	C_1'—W_1—C_2'	78.1(3)
Mn_1—N_6	2.331(8)	C_1—W_1—C_2	78.1(3)
Mn_1—N_7	2.352(8)	C_1'—W_1—C_2	139.3(3)
Mn_1—N_8	2.412(10)	C_3—W_1—C_3'	109.3(4)
Mn_1—N_9	2.353(8)	C_2'—W_1—C_3	78.6(3)
C_1—N_1	1.152(11)	C_2'—W_1—C_3'	144.6(3)
C_2—N_2	1.137(10)	C_2—W_1—C_3'	78.6(3)
C_3—N_3	1.140(11)	C_2—W_1—C_3	144.6(3)
C_4—N_4	1.152(12)	C_2'—W_1—C_2	115.6(4)
		C_4'—W_1—C_1'	143.2(3)
		C_4—W_1—C_1'	78.1(3)
		C_4—W_1—C_1	143.6(3)
		C_4'—W_1—C_1	78.1(3)
		C_4'—W_1—C_3'	143.6(3)
		C_4—W_1—C_3'	81.9(3)
		C_4'—W_1—C_3	81.9(3)
		C_4—W_1—C_3	143.6(3)
		C_4—W_1—C_2'	73.9(4)
		C_4—W_1—C_2	70.5(3)
		C_4'—W_1—C_2'	70.5(3)
		C_4'—W_1—C_2	73.9(4)
		C_4'—W_1—C_4	110.0(6)
		C_1—N_1—Mn	154.4(6)
		N_1—C_1—W	176.4(7)
		N_2—C_2—W	178.0(7)
		N_3—C_3—W	177.8(7)
		N_4—C_4—W	178.9(10)
		C_2—N_2—Mn′	160.1(7)
		N_2'—Mn_1—N_1	166.8(3)

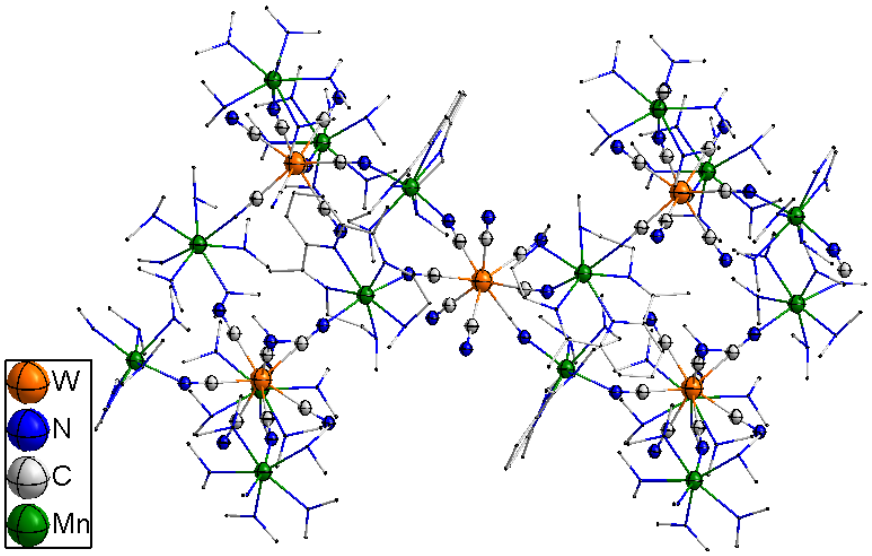

Figure 41: Compound **14** molecular structure. Hydrogen atoms and solvent molecules omitted for clarity. The L_{N5} ligand atoms are displayed as a wire model.

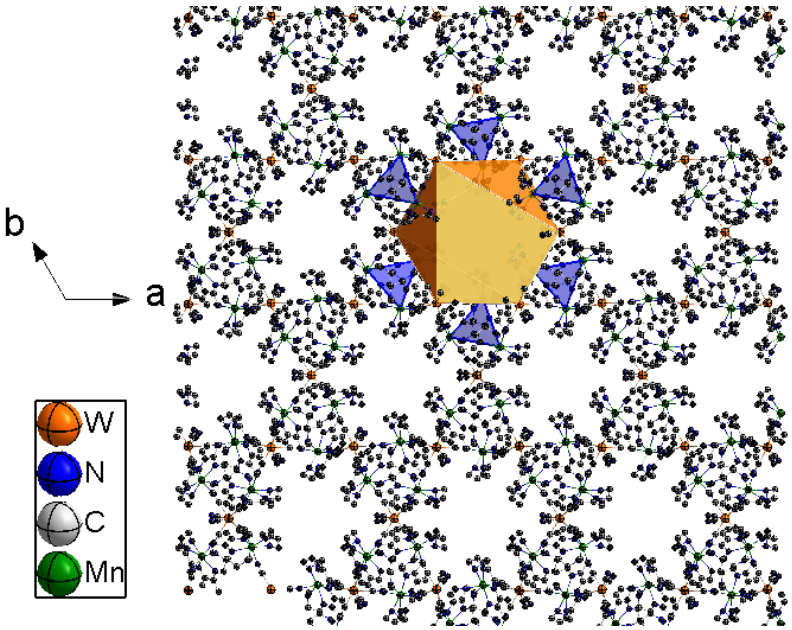

Figure 42: Structure of **14** parallel to the *c* axis viewing the *ab* plane. Blue triangles are formed by Mn ions and the orange hexagon shows the void formed by the W ions.

to 1.163(19)Å, which is consistent with previously reported W^{V}—C—N bond distances. The Sm^{III}—NC distance is 2.480(10) Å, which is slightly shorter than the 2.53–2.57 Å reported for $[Sm^{III}(tmphen)_2(DMF)_2][W^{V}(CN)_8]$ reported by Qian *et al*.[190] The $[W^{V}(CN)_8]^{3-}$ anion adopts a square antiprismatic geometry with the W—CN bonds to the Sm ions forming a V-shape at opposite faces of the square antiprismatic geometry. Tthe CN—Sm—NC bond angle is 145.8(5) °. Select bond distances and bond angles are reported in Table 13. The extended structure is very similar to that reported by Qian *et al*, with the 1D helixes running along the 2_1 screw axis. The packing arrangement results in the presence of cavities of 8 Å x 8 Å that allow for solvent molecules to occupy the channels (Figure 44). The tmphen ligands participate in π-stacking interactions between chains at a distance of 3.85 Å, which is slightly larger than the 3.65 Å value reported by Qian;[190] the interchain distance is 9.3 Å. The lack of a tetrabutylammonium cation indicates that the tungsten ion has been oxidized from +4 to +5.

Compound **16** is isomorphous with **15**. The space group is P2/c with $[Dy^{III}(tmphen)(DMF)][W^{V}(CN)_8]$ as the asymmetric unit; the compound also forms a 1D helical chain of alternating Dy and W metal ions (Figure 45). The W—C bond distances vary from 2.125(10) to 2.179(9) Å and the C—N bond distances range between 1.137(12) to 1.182(13) Å, consistent with W^{V}—C—N bond distances previously reported. The Dy—NC bond distances are 2.423(5) and 2.417(6) Å, which is shorter than the 2.52 to 2.54 Å distance reported for a Dy-W^{V} chain by Przychodzen et al.[191] The $[W^{V}(CN)_8]^{3-}$ anion, which is pentavalent as deduced by charge balance considerations, adopts a square

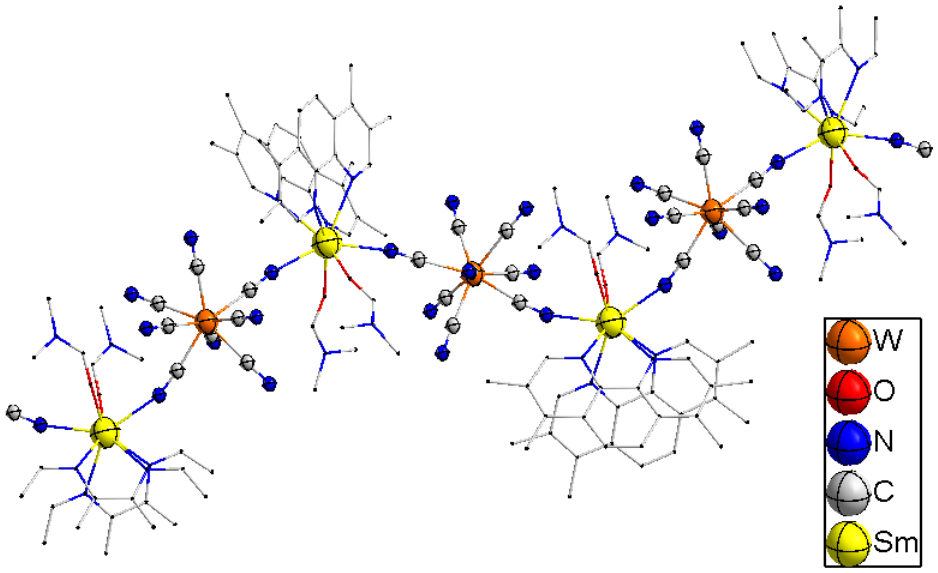

Figure 43: Molecular structure of compound **15**. Hydrogen atoms and solvent molecules omitted for clarity; tmphen and DMF ligands on the Sm ion are presented as wire models.

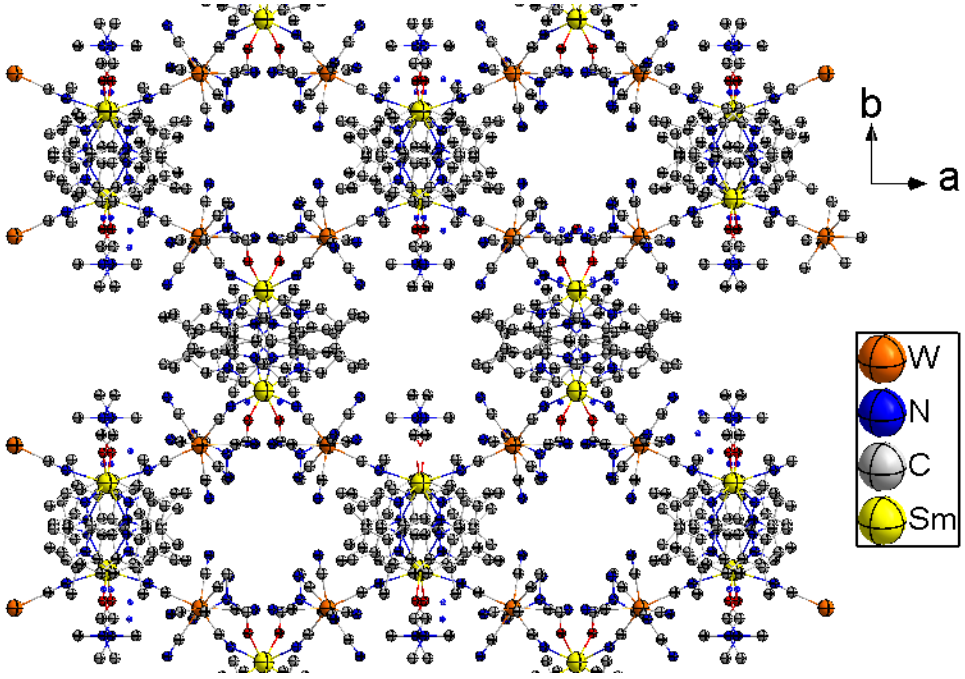

Figure 44: View of **15** parallel to the *c* axis and perpendicular to the *ab* plane.

Table 13: Select bond distances and bond angles for compound **15**.

Select Bond	Bond Distance (Å)	Select Bond	Bond Angle (°)
W—C_1	2.154(13)	C_1—W_1—C_6	72.9(5)
W—C_2	2.134(13)	C_1—W_1—C_8	144.0(5)
W—C_3	2.137(15)	C_1—W_1—C_4	80.4(5)
W—C_4	2.168(14)	C_1—W_1—C_5	72.7(5)
W—C_5	2.173(16)	C_7—W_1—C_1	107.1(5)
W—C_6	2.177(16)	C_7—W_1—C_6	72.4(7)
W—C_7	2.140(18)	C_7—W_1—C_8	78.5(5)
W—C_8	2.166(14)	C_7—W_1—C_4	142.7(6)
Sm—N_1	2.480(10)	C_7—W_1—C_5	73.7(6)
Sm—N_1'	2.480(10)	C_8—W_1—C_6	75.4(6)
Sm—N_9	2.576(10)	C_8—W_1—C_4	117.2(5)
Sm—N_{10}	2.581(10)	C_8—W_1—C_5	140.2(5)
Sm—O_1	2.352(8)	C_2—W_1—C_1	145.3(5)
C_1—N_1	1.134(16)	C_2—W_1—C_6	139.0(6)
C_2—N_2	1.149(17)	C_2—W_1—C_7	79.2(6)
C_3—N_3	1.163(19)	C_2—W_1—C_8	70.4(5)
C_4—N_4	1.154(19)	C_2—W_1—C_3	113.8(5)
C_5—N_5	1.15(2)	C_2—W_1—C_4	75.6(5)
C_6—N_6	1.15(2)	C_2—W_1—C_5	76.8(5)
C_7—N_7	1.14(2)	C_3—W_1—C_1	81.3(5)
C_8—N_8	1.149(18)	C_3—W_1—C_6	77.8(6)
		C_3—W_1—C_7	144.5(6)
		C_3—W_1—C_8	75.8(5)
		C_3—W_1—C_4	72.0(5)
		C_3—W_1—C_5	139.9(6)
		C_4—W_1—C_6	142.2(6)
		C_4—W_1—C_5	74.0(6)
		C_5—W_1—C_6	120.7(7)
		C_1—N_1—Sm	169.6(10)
		N_1—C_1—W	177.3(11)
		N_2—C_2—W	174.0(12)
		N_3—C_3—W	178.3(13)
		N_4—C_4—W	179.2(14)
		N_5—C_5—W	179.3(15)
		N_6—C_6—W	176.8(19)
		N_7—C_7—W	174.6(16)
		N_8—C_8—W	176.4(13)
		N_1'—Sm—N_1	145.8(5)

antiprismatic geometry based on the bond angles. The W—CN unit coordinates to the Dy ions at opposite vertices of the alternating squares of the octacyanotungstate center, with a CN—Dy—NC bond angle of 144.9(3) ° which is similar to the Sm analogue. Select bond distances and bond angles are reported in Table 14 As in the case of the Sm analogue, the 1D chain is helical along the 2_1 screw axis, with an interchain distance of ~13.9 Å. In the ab plane there is a void between chains of approximately 8 Å x 9 Å, which houses solvent molecules (Figure 46). The tmphen ligand forms π-stacks between chains at 3.91 Å, slightly longer than the 3.85 Å separation observed for the Sm compound.

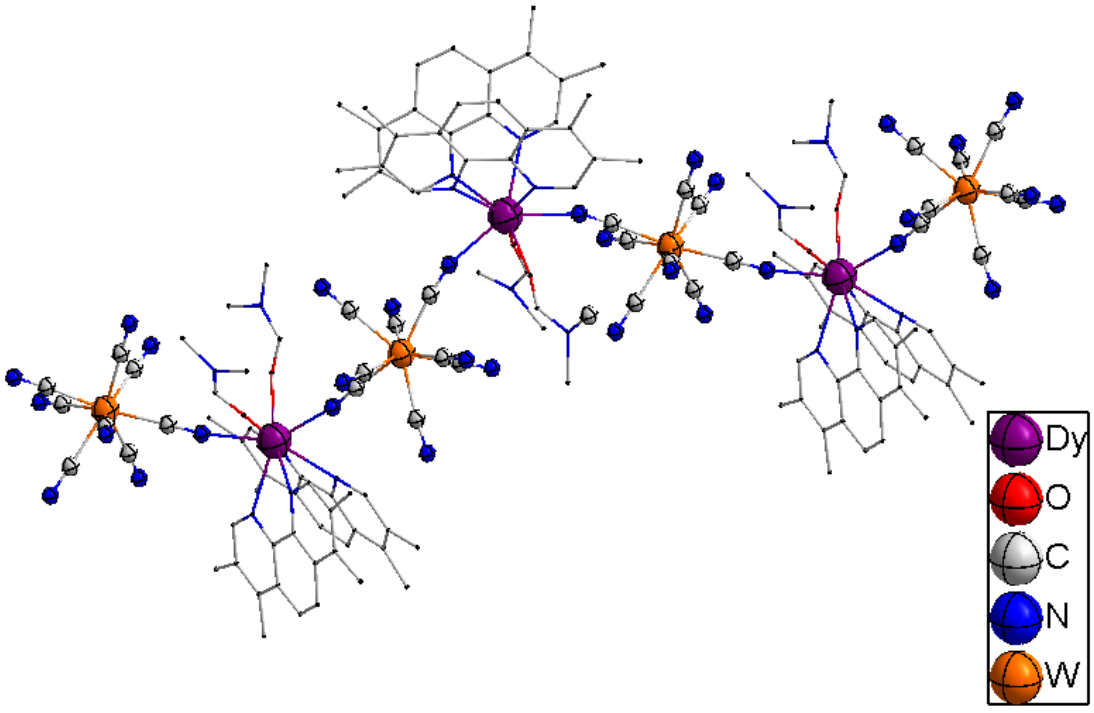

Figure 45: Compound **16** molecular structure. Hydrogen atoms and solvent molecules are omitted for the sake of clarity. The tmphen and DMF ligands on the Dy ion are presented as wire models.

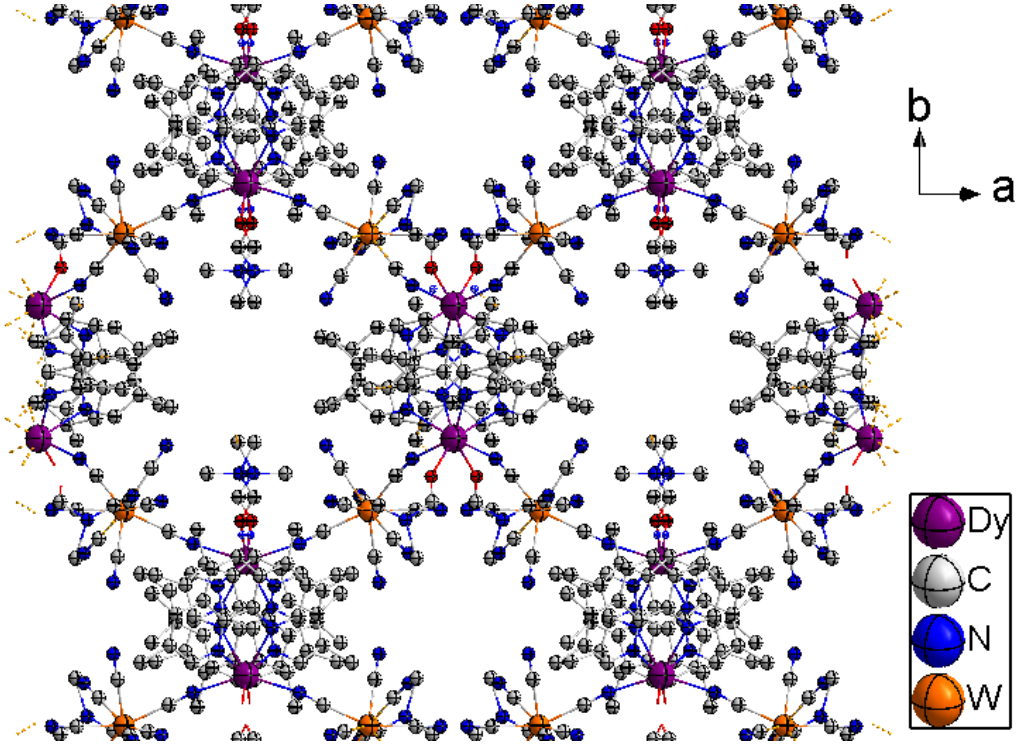

Figure 46: View of **16** parallel to the *c* axis and perpendicular to the *ab* plane.

Table 14: Select bond distances and bond angles for compound **16**.

Select Bond	Bond Distance (Å)	Select Bond	Bond Angle (°)
W—C_1	2.135(7)	C_1—W_1—C_6	143.1(3)
W—C_2	2.135(7)	C_1—W_1—C_8	82.4(3)
W—C_3	2.179(9)	C_1—W_1—C_4	73.5(3)
W—C_4	2.142(10)	C_1—W_1—C_5	107.0(3)
W—C_5	2.141(10)	C_7—W_1—C_1	71.7(3)
W—C_6	2.164(8)	C_7—W_1—C_6	75.7(3)
W—C_7	2.171(9)	C_7—W_1—C_8	78.3(4)
W—C_8	2.125(10)	C_7—W_1—C_4	120.6(4)
Dy_1—N_1	2.423(5)	C_7—W_1—C_5	72.1(4)
Dy_2—N_2	2.417(6)	C_8—W_1—C_6	74.4(3)
Dy—N_9	2.521(5)	C_8—W_1—C_4	140.7(3)
Dy—N_{10}	2.525(5)	C_8—W_1—C_5	143.7(4)
Dy—O_1	2.294(5)	C_2—W_1—C_1	146.6(3)
C_1—N_1	1.162(9)	C_2—W_1—C_6	70.0(3)
C_2—N_2	1.158((10)	C_2—W_1—C_7	138.9(3)
C_3—N_3	1.153(12)	C_2—W_1—C_8	112.3(3)
C_4—N_4	1.182(13)	C_2—W_1—C_3	75.6(3)
C_5—N_5	1.142(13)	C_2—W_1—C_4	77.1(3)
C_6—N_6	1.137(12)	C_2—W_1—C_5	79.2(3)
C_7—N_7	1.157(12)	C_3—W_1—C_1	81.3(3)
C_8—N_8	1.179(13)	C_3—W_1—C_6	117.0(3)
		C_3—W_1—C_7	142.3(4)
		C_3—W_1—C_8	72.3(3)
		C_3—W_1—C_4	73.8(4)
		C_3—W_1—C_5	142.8(4)
		C_4—W_1—C_6	140.3(3)
		C_4—W_1—C_5	74.2(4)
		C_5—W_1—C_6	78.2(4)
		C_1—N_1—Dy	170.1(6)
		N_1—C_1—W	177.5(6)
		N_2—C_2—W	173.9(7)
		N_3—C_3—W	178.9(8)
		N_4—C_4—W	179.1(9)
		N_5—C_5—W	175.5(10)
		N_6—C_6—W	177.8(10)
		N_7—C_7—W	174.1(11)
		N_8—C_8—W	178.3(8)
		N_1'—Dy—N_1	144.9(3)

Compound **19** crystallizes as pink crystals in the space group P-1, with the asymmetric consisting of $[(Co^{II}PY5Me_2)_4Mo^{IV}(CN)_8](PF_6)_4 \cdot 4THF \cdot 4CH_3CN$. The compound forms a star-like cluster similar to the Re analogue[104] and the $[Mo^{IV}(CN)_8]^{4-}$ anion is in a distorted square antiprismatic geometry based on the bond angles (Figure 47). The bond distances range from 2.122(9) to 2.196(10) Å for Mo—CN and 1.136(13) to 1.172(12) Å for C—N. The Co—NC distances are from 2.025(8) to 2.046(8) Å, although the fourth Co—NC bond is 1.928(8) Å. These data are consistent with previously reported Mo^{IV}—Co^{II} compounds;[192] and, unlike the Re compound, there does not appear to be charge transfer resulting in a Co^{III} ion as deduced from the bond distances. The C—N—Co bond angles range between 162.5(8) to 178.4(3) °, while the Mo—C—N bond angles vary from 176.6(8) to 178.9(9) °, resulting in deviations from linear bonds between the Mo and Co metal ions. Select bond distances and bond angles are reported in Table 15.

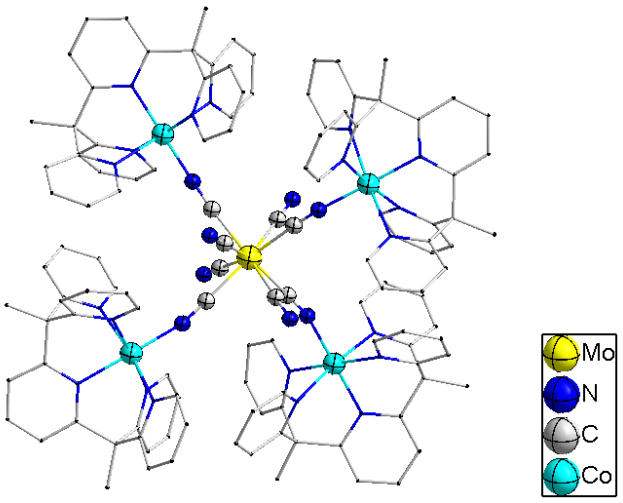

Figure 47: Molecular structure of **19**. Hydrogen atoms and solvent molecules are omitted for the sake of clarity. The $PY5Me_2$ ligand is shown as a wire model.

Table 15: Select bond distances and bond angles for compound **19**.

Select Bond	Bond Distance (Å)	Select Bond	Bond Angle (°)
Mo—C_1	2.135(8)	C_1—Mo_1—C_6	76.2(4)
Mo—C_2	2.127(10)	C_1—Mo_1—C_8	145.3(3)
Mo—C_3	2.122(9)	C_1—Mo_1—C_4	94.1(4)
Mo—C_4	2.141(10)	C_1—Mo_1—C_5	75.8(3)
Mo—C_5	2.175(10)	C_7—Mo_1—C_1	71.3(3)
Mo—C_6	2.196(10)	C_7—Mo_1—C_6	128.9(4)
Mo—C_7	2.175(10)	C_7—Mo_1—C_8	74.1(3)
Mo—C_8	2.184(9)	C_7—Mo_1—C_4	75.9
Co_1—N_1	2.025(8)	C_7—Mo_1—C_5	131.0(4)
Co_2—N_2	2.027(8)	C_8—Mo_1—C_6	129.5(4)
Co_3—N_3	1.928(8)	C_8—Mo_1—C_4	75.8(4)
Co_4—N_4	2.046(8)	C_8—Mo_1—C_5	128.8(4)
Co—N_{ax}	1.989 - 2.119	C_2—Mo_1—C_1	95.7(3)
Co—N_{eq}	2.112 - 2.229	C_2—Mo_1—C_6	71.1(3)
C_1—N_1	1.165(12)	C_2—Mo_1—C_7	74.0(4)
C_2—N_2	1.152(13)	C_2—Mo_1—C_8	76.2(4)
C_3—N_3	1.172(12)	C_2—Mo_1—C_3	94.7(3)
C_4—N_4	1.148(13)	C_2—Mo_1—C_4	143.4(4)
C_5—N_5	1.163(14)	C_2—Mo_1—C_5	145.3(4)
C_6—N_6	1.136(13)	C_3—Mo_1—C_1	143.8(3)
C_7—N_7	1.157(13)	C_3—Mo_1—C_6	74.6(4)
C_8—N_8	1.149(13)	C_3—Mo_1—C_7	144.8(3)
		C_3—Mo_1—C_8	70.8(3)
		C_3—Mo_1—C_4	98.0(4)
		C_3—Mo_1—C_5	76.1(4)
		C_4—Mo_1—C_6	145.5(4)
		C_4—Mo_1—C_5	71.3(4)
		C_5—Mo_1—C_6	74.2(4)
		C_1—N_1—Co_1	162.5(8)
		C_2—N_2—Co_2	166.5(8)
		C_3—N_3—Co_3	178.4(3)
		C_4—N_4—Co_4	165.4(8)
		N_{ax}—Co—N_{Mo}	178.3 - 179.3
		N_1—C_1—Mo	177.1(8)
		N_2—C_2—Mo	176.6(8)
		N_3—C_3—Mo	176.8(9)
		N_4—C_4—Mo	177.4(9)
		N_5—C_5—Mo	178.6(10)
		N_6—C_6—Mo	178.8(9)
		N_7—C_7—Mo	178.9(9)
		N_8—C_8—Mo	177.2(9)

Compound **20** crystallizes in the space group P-1, and the asymmetric unit contains $[(Co^{II}PY5Me_2)_4W^{IV}(CN)_8](PF_6)_4$. The compound forms the same star-like cluster as described above for $[(Co^{II}PY5Me_2)_4Mo^{IV}(CN)_8]$ (Figure 48) with the $[W^{IV}(CN)_8]^{4-}$ anion being in a more distorted square antiprismatic geometry. The W—CN bond distances range from 1.99(3) to 2.28(4) Å, the C—N bond distances from 1.06(4) to 1.33(6) Å, which are significantly more spread out than previously observed, which is likely a limit of the crystal quality during data collection ALS. The Co—NC bond distances are between 1.92(3) to 2.01(2) Å, which is consistent with previously measured W^{IV}—Co^{II} compounds.[193] The C—N—Co bond angles are between 171(3) to 179(2) °, while the W—C—N bond angles vary from 171(2) to 178(2) °, resulting in slight deviations from linearity between the W and Co metal ions. Select bond distances and bond angles are reported in Table 16.

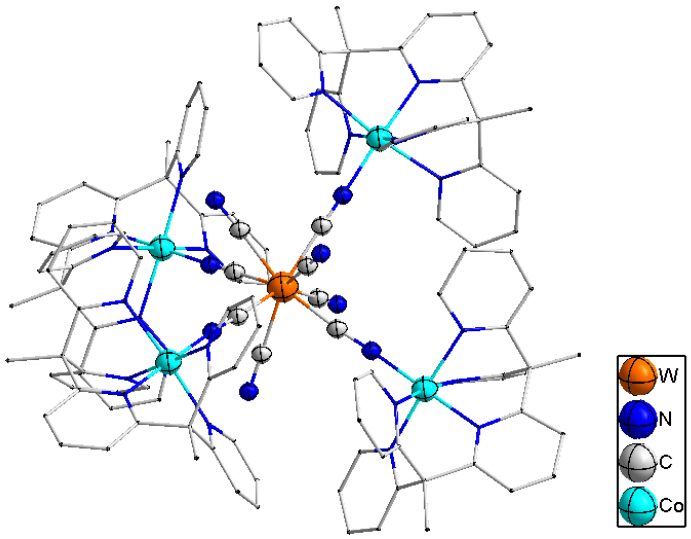

Figure 48: Molecular structure of **20**. Hydrogen atoms and solvent molecules are omitted for the sake of clarity clarity. The $PY5Me_2$ ligand is shown as a wire model.

Table 16: Select bond distances and bond angles for compound **20**.

Select Bond	Bond Distance (Å)	Select Bond	Bond Angle (°)
W—C_1	2.15(3)	C_1—W_1—C_6	74.7(9)
W—C_2	2.16(3)	C_1—W_1—C_8	148.2(10)
W—C_3	2.02(3)	C_1—W_1—C_4	96.2(10)
W—C_4	1.99(3)	C_1—W_1—C_5	72.3(10)
W—C_5	2.19(3)	C_7—W_1—C_1	75.4(10)
W—C_6	2.25(4)	C_7—W_1—C_6	74.8(10)
W—C_7	2.28(4)	C_7—W_1—C_8	129.3(10)
W—C_8	2.14(3)	C_7—W_1—C_4	73.9(12)
Co_1—N_1	2.01(2)	C_7—W_1—C_5	130.7(11)
Co_2—N_2	1.92(3)	C_8—W_1—C_6	126.6(9)
Co_3—N_3	1.98(3)	C_8—W_1—C_4	76.1(11)
Co_4—N_4	1.98(4)	C_8—W_1—C_5	75.9(10)
Co—N_{ax}	1.918 - 2.03	C_2—W_1—C_1	93.9(10)
Co—N_{eq}	2.05 – 2.16	C_2—W_1—C_6	68.2(9)
C_1—N_1	1.08(3)	C_2—W_1—C_7	143.0(10)
C_2—N_2	1.13(3)	C_2—W_1—C_8	76.7(10)
C_3—N_3	1.22(3)	C_2—W_1—C_3	97.6(13)
C_4—N_4	1.28(4)	C_2—W_1—C_4	143.0(12)
C_5—N_5	1.33(6)	C_2—W_1—C_5	75.9(11)
C_6—N_6	1.13(4)	C_3—W_1—C_1	141.8(11)
C_7—N_7	1.06(4)	C_3—W_1—C_6	76.2(11)
C_8—N_8	1.19(3)	C_3—W_1—C_7	73.5(13)
		C_3—W_1—C_8	70.0(11)
		C_3—W_1—C_4	96.1(12)
		C_3—W_1—C_5	145.8(11)
		C_4—W_1—C_6	148.7(12)
		C_4—W_1—C_5	73.6(12)
		C_5—W_1—C_6	128.6(11)
		C_1—N_1—Co_1	179(2)
		C_2—N_2—Co_2	171(3)
		C_3—N_3—Co_3	171(3)
		C_4—N_4—Co_4	172(2)
		N_{ax}—Co—N_W	174.2 – 178.1
		N_1—C_1—W	178(2)
		N_2—C_2—W	176(3)
		N_3—C_3—W	176(3)
		N_4—C_4—W	171(2)
		N_5—C_5—W	177(3)
		N_6—C_6—W	175(3)
		N_7—C_7—W	175(3)
		N_8—C_8—W	177(2)

Compound **21** crystallizes as orange crystals in space group P1b, and the asymmetric unit contains $[(Ni^{II}PY5Me_2)_4Mo^{IV}(CN)_8](PF_6)_4$. The compound also forms a star-like cluster with the $[Mo^{IV}(CN)_8]^{4-}$ anion in a geometry between distorted square antiprismatic and dodecahedral. (Figure 49). The Mo—CN bond distances range from 2.08(3) to 2.17(3) Å, the C—N bond distances from 1.09(3) to 1.22(3) Å, and the Ni—NC bond distances between 1.96(2) to 2.05(3) Å, consistent with previously measured Mo^{IV}—Ni^{II} compounds.[194-195] The C—N—Ni bond angles range between 163(2) to 175.0(18) °, while the Mo—C—N bond angles vary from 169(2) to 180(3) °, resulting in deviations between linearity of the Mo and Ni metal ions. Select bond distances and bond angles are reported in Table 17.

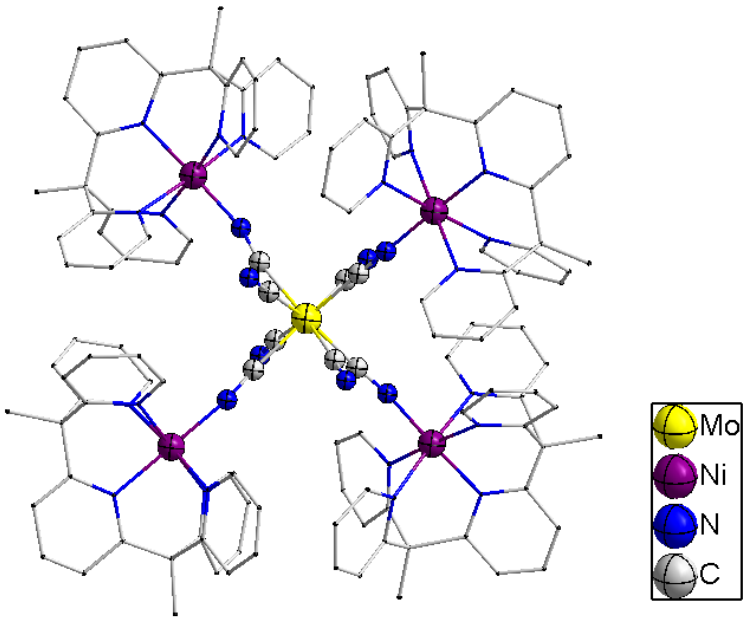

Figure 49: Molecular structure of **21**. Hydrogen atoms and solvent molecules were omitted for the sake of clarity. The $PY5Me_2$ ligand is shown as a wire model.

Table 17: Select bond distances and bond angles for compound **21**.

Select Bond	Bond Distance (Å)	Select Bond	Bond Angle (°)
Mo—C_1	2.14(3)	C_1—Mo_1—C_6	73.6(10)
Mo—C_2	2.08(3)	C_1—Mo_1—C_8	146.6(10)
Mo—C_3	2.11(4)	C_1—Mo_1—C_4	96.2(9)
Mo—C_4	2.16(3)	C_1—Mo_1—C_5	70.8(9)
Mo—C_5	2.16(3)	C_7—Mo_1—C_1	75.1(9)
Mo—C_6	2.15(3)	C_7—Mo_1—C_6	74.4(9)
Mo—C_7	2.17(3)	C_7—Mo_1—C_8	128.1(9)
Mo—C_8	2.15(3)	C_7—Mo_1—C_4	71.7(8)
Ni_1—N_1	2.02(2)	C_7—Mo_1—C_5	129.7(9)
Ni_2—N_2	2.05(3)	C_8—Mo_1—C_6	131.2(9)
Ni_3—N_3	1.979(19)	C_8—Mo_1—C_4	73.9(8)
Ni_4—N_4	1.96(2)	C_8—Mo_1—C_5	75.8(10)
Ni—N_{ax}	2.06 – 2.104	C_2—Mo_1—C_1	96.6(9)
Ni—N_{eq}	2.07 – 2.142	C_2—Mo_1—C_6	68.9(10)
C_1—N_1	1.14(3)	C_2—Mo_1—C_7	143.2(10)
C_2—N_2	1.18(3)	C_2—Mo_1—C_8	77.6(10)
C_3—N_3	1.20(3)	C_2—Mo_1—C_3	94.6(9)
C_4—N_4	1.16(3)	C_2—Mo_1—C_4	145.0(9)
C_5—N_5	1.13(3)	C_2—Mo_1—C_5	77.3(10)
C_6—N_6	1.18(3)	C_3—Mo_1—C_1	142.3(10)
C_7—N_7	1.22(3)	C_3—Mo_1—C_6	77.2(10)
C_8—N_8	1.09(3)	C_3—Mo_1—C_7	74.5(8)
		C_3—Mo_1—C_8	71.1(10)
		C_3—Mo_1—C_4	76.4(9)
		C_3—Mo_1—C_5	146.9(10)
		C_4—Mo_1—C_6	146.0(9)
		C_4—Mo_1—C_5	76.4(9)
		C_5—Mo_1—C_6	126.8(9)
		C_1—N_1—Ni_1	165(2)
		C_2—N_2—Ni_2	163(2)
		C_3—N_3—Ni_3	172(2)
		C_4—N_4—Ni_4	175.0(18)
		N_{ax}—Ni—N_{Mo}	175.0 - 178.3
		N_1—C_1—Mo	169(2)
		N_2—C_2—Mo	170(2)
		N_3—C_3—Mo	176(2)
		N_4—C_4—Mo	175.3(18)
		N_5—C_5—Mo	180(3)
		N_6—C_6—Mo	175(2)
		N_7—C_7—Mo	179(2)
		N_8—C_8—Mo	175(3)

Finally, attempts to crystallize **22** resulted in orange crystals, but attempts to obtain diffraction data were unsuccessful although diffraction of an orange crystal did yield a unit cell similar to the Mo analogue.

Infrared Spectroscopy

Infrared spectra were collected for compounds **11** and **12**. For $[Fe^{II}(PY5Me_2)(CH_3CN)](CF_3SO_3)_2$, the compound exhibits stretches at 2273 cm^{-1}, 1586 and 1811 cm^{-1}, and 1028 cm^{-1}, corresponding to acetonitrile, pyridyl, and $CF_3SO_3^-$ stretching frequencies, respectively. The Zn analogue has stretching frequencies of 2276 cm^{-1} (CH_3CN), 1597 and 1580 cm^{-1} (pyridyl), and a broad stretching vibration at 1050 cm-1 (BF_4^-).

For the $PY5Me_2$ star-like complexes, the infrared spectra of the compounds typically contain either two peaks or one broad peak for cyanide stretching vibrations, as summarized in Table 18. For the molybdenum complexes, both Co and Ni products were measured, and each exhibit two stretching vibrations. The lower stretching vibration for both is at 2118 cm^{-1} and corresponds to the terminal cyanide on the $[Mo^{IV}(CN)_8]^{4-}$ center, while the higher stretching frequency modes at 2130 cm^{-1} for Co and 2149 cm^{-1} for Ni are assigned to the bridging cyanides connected to the $[M(PY5Me_2)]^{2+}$ units. For tungsten, the lower frequency cyanide stretching vibration is between 2105 to 2122 cm^{-1}, which corresponds to the terminal ν(CN) stretching frequency. The higher frequency cyanide vibration is between 2130 to 2200 cm^{-1} and corresponds to the bridging cyanide to the 3d metal center except for the Fe and Co complexes. In the case of the Fe and Co compounds,

only one broad peak is observed in the range 2000 to 2250 cm^{-1}, which may indicate the two cyanide vibrations are close enough to overlap with each other.

Table 18: Summary of ν(CN) stretching frequencies for $[(MPY5Me_2)_4M'(CN)_8]^{4+}$ (M = Mn, Fe, Co, Ni, Cu; M′ = Mo, W) complexes.

Element	Mn	Fe	Co	Ni	Cu
Mo	NA	NA	2118, 2130	2118, 2149	NA
W	2105, 2142	2120	2119	2125, 2134	2122, 2200
Re^{IV}	2031, 2098	NA	2056, 2102	2089, 2120	2256, 2287

Electrochemical Studies

The cyclic voltammogram of **11** in CH_3CN exhibits a reversible oxidation at +1.18 V (Figure 50), which corresponds to the $Fe^{II/III}$ oxidation couple, consistent with what was previously reported.[187, 196] Attempts to determine the $Fe^{II/I}$ reduction couple were unsuccessful, including changing the solvent to THF in order to reach more reducing voltages.

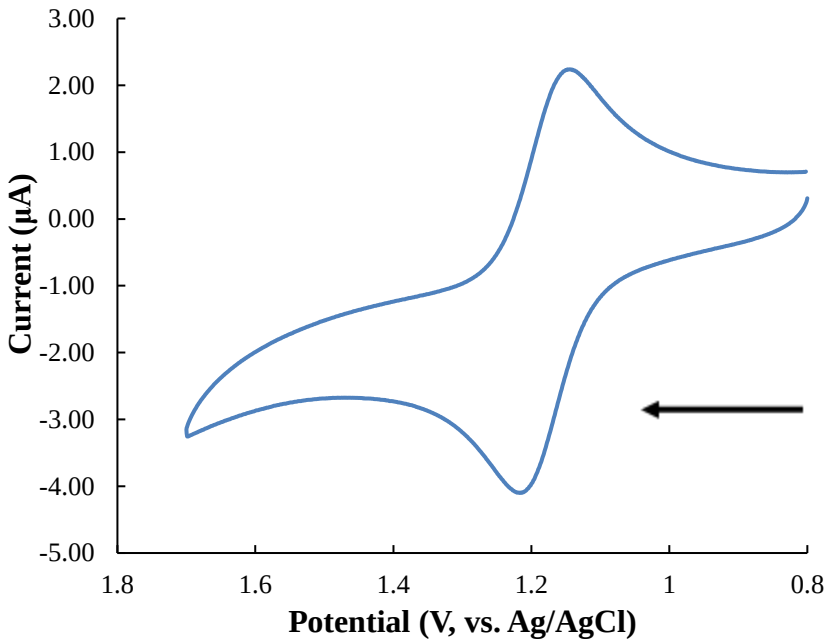

Figure 50: Cyclic voltammogram of **11** in CH_3CN with 0.1 M Bu_4NPF_6 as the supporting electrolyte.

Magnetic Measurements

Compound **11** is diamagnetic when according to the variable-temperature DC susceptibility, indicating that the Fe^{II} center has a low spin ground state t_{2g}^6, corresponding to S = 0. This is consistent with the $PY5Me_2$ ligand being a strong-field ligand that enforces the low-spin electronic configuration, and it agrees with similar complexes previously reported.[196]

Compound **19** behaves as four Co S = 3/2 spin centers, given that the $[Mo^{IV}(CN)_8]^{4-}$ anion is diamagnetic. The $\chi_M T$ value at 300 K is 10.75 emu·K·mol^{-1}, which is higher than the expected value of 7.52 emu·K·mol^{-1} for four independent S = 3/2 spin

centers; as temperature decreases $\chi_M T$ decreases to 5.96 emu·K·mol^{-1} at 2 K. The gradual decrease in $\chi_M T$ vs T (Figure 51) is a result of spin-orbit coupling from the Co^{II} ion, which was observed for the $[Co^{II}(PY5Me_2)(CH_3CN)](PF_6)_2$ starting material as well.[104] The 2 K magnetization data (Figure 52) exhibits near saturation at 7 T with a value of 8.27 μ_B, which would correspond to eight unpaired electrons; this is lower than the expected value of 12 μ_B, which may be due to both ZFS and spin-orbit coupling effects. The reduced magnetization data (Figure 53) contain overlapping isofield lines, suggesting the compound is magnetically isotropic.

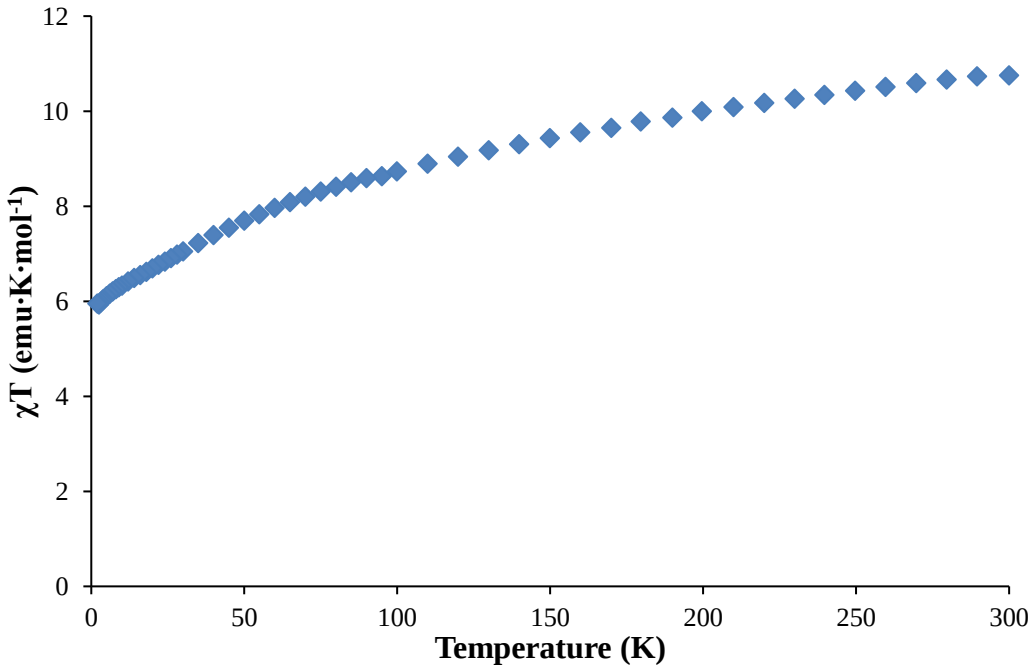

Figure 51: Variable-temperature DC susceptibility plot of **19**.

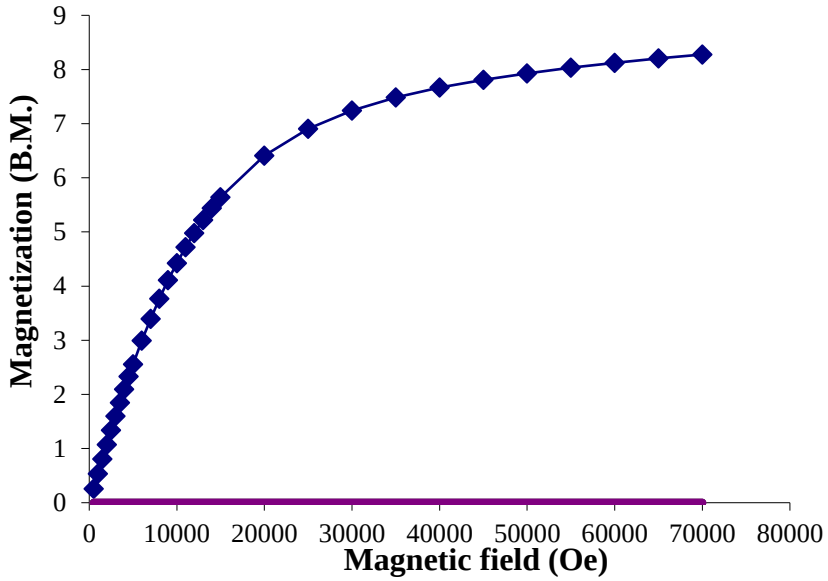

Figure 52: Magnetization data at 2 K for compound **19**. Solid lines are a guide for the eye.

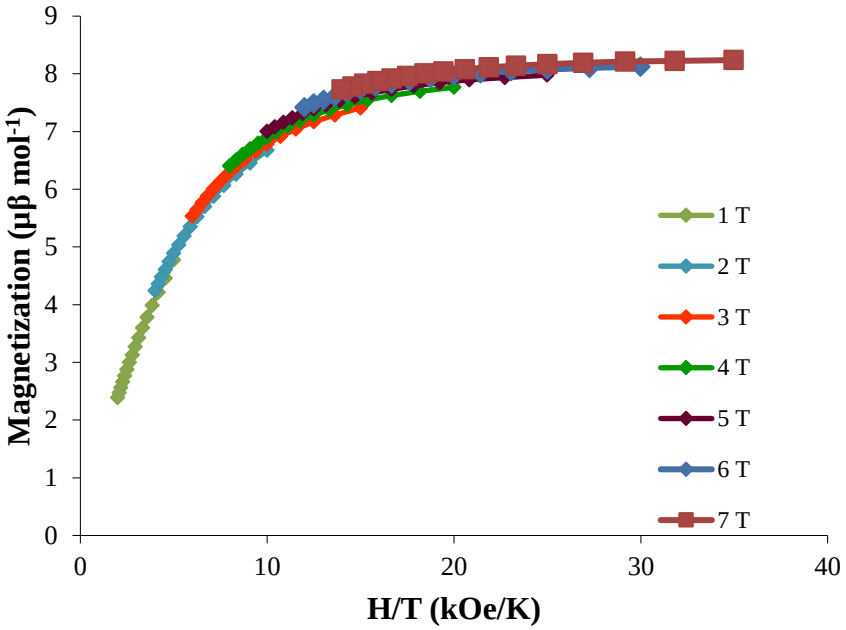

Figure 53: Reduced magnetization data for compound **19**. Solid lines are a guide for the eye.

Compound **20** behaves similarly to its molybdenum analogue; the compound has four Co^{II} S= 3/2 spin centers connected by a diamagnetic $[W^{IV}(CN)]^{4-}$ center, resulting in spin-independent centers. The variable-temperature DC susceptibility data exhibit a $\chi_M T$ value at 300 K of 9.35 emu·K·mol^{-1}, which is higher than the expected value of 7.52 emu·K·mol^{-1} for four S = 3/2 independent spin centers. As the temperature is lowered, $\chi_M T$ decreases to 5.55 emu·K·mol^{-1} at 2 K (Figure 54); both values are slightly lower than the molybdenum analogue, and the decrease is due to spin-orbit coupling and ZFS. The 2 K magnetization data (Figure 55) shows near saturation at 7 T with a value of 7.35 μ_B, which corresponds to approximately seven unpaired electrons and is less than the expected value of 12; this likely results from ZFS and spin-orbit coupling. The reduced magnetization data (Figure 56) consist of overlapping isofield lines, indicating that the compound is magnetically isotropic as well.

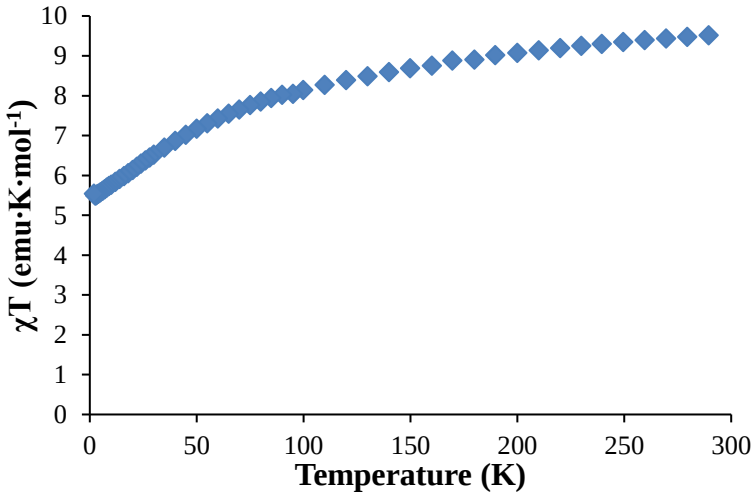

Figure 54: Variable temperature DC susceptibility plot for **20**.

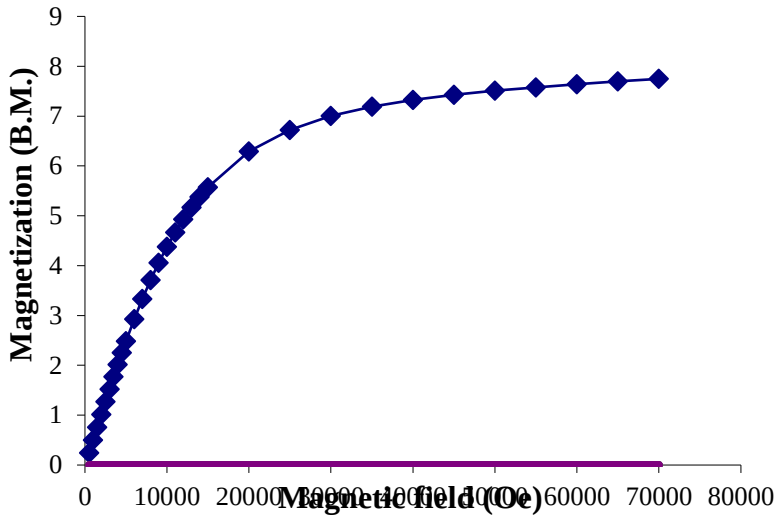

Figure 55: Magnetization data at 2 K for compound **20**. Solid lines are a guide for the eye.

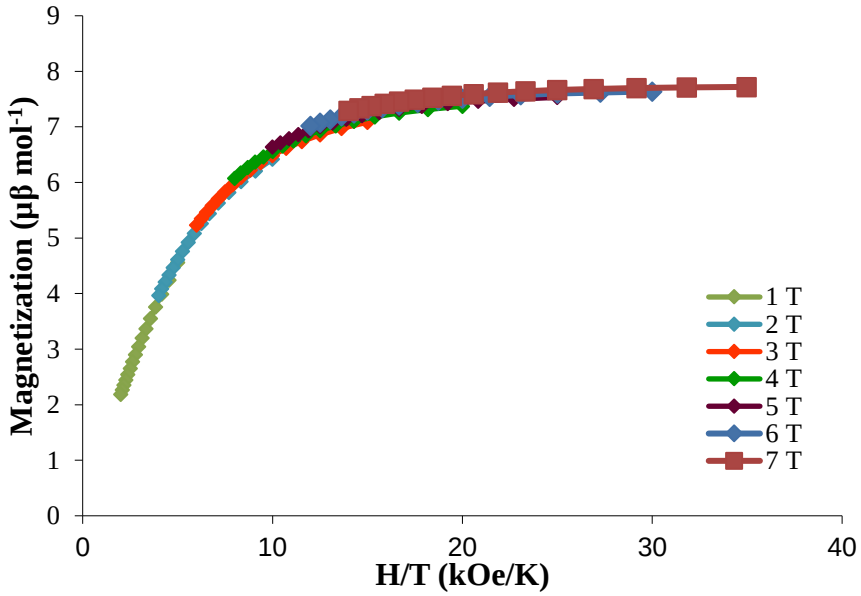

Figure 56: Reduced magnetization data for **20** from 2 to 5 K and 1 to 7 T. Solid lines are a guide for the eye.

Compound **21** contains four Ni^{II} cationic molecules coordinated to the diamagnetic $[Mo^{IV}(CN)_8]^{4-}$ anion resulting in four S =1 independent spin centers. The $\chi_M T$ value at 300 K is 4.87 emu·K·mol^{-1} which gradually decreases to 3.92 emu·K·mol^{-1} at 2 K (Figure 57); this value is consistent with four equivalents of the starting material $[Ni^{II}(PY5Me_2)(CH_3CN)](PF_6)_2$ which has a reported $\chi_M T$ value of 1.2 emu·K·mol^{-1} at 300 K.[104] The slight decrease in $\chi_M T$ as the temperature is lowered may be due to ZFS. The 2 K magnetization data (Figure 58) begin to reach saturation at 7 T with a value of 7.81 μ_B, which is slightly below the expected value for eight unpaired electrons from four Ni^{II} spin centers. The reduced magnetization data (Figure 59) exhibit overlapping isofield lines, indicating the compound is magnetically isotropic as expected.

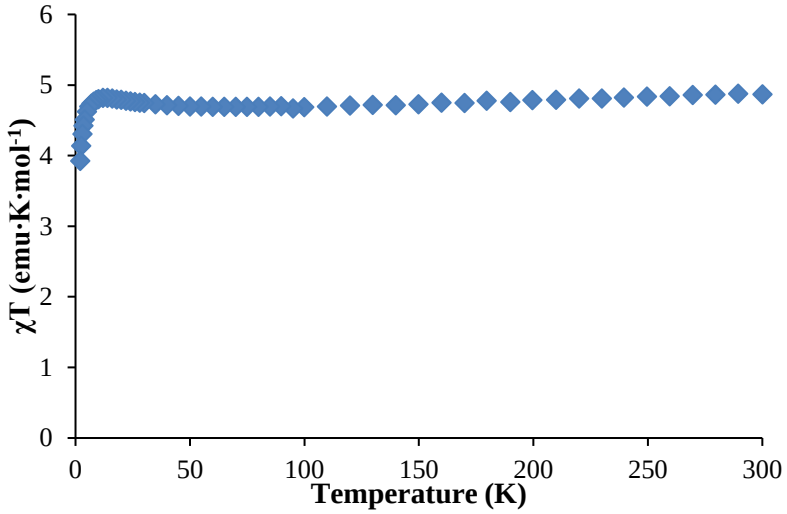

Figure 57: Variable-temperature DC susceptibility plot for **21**.

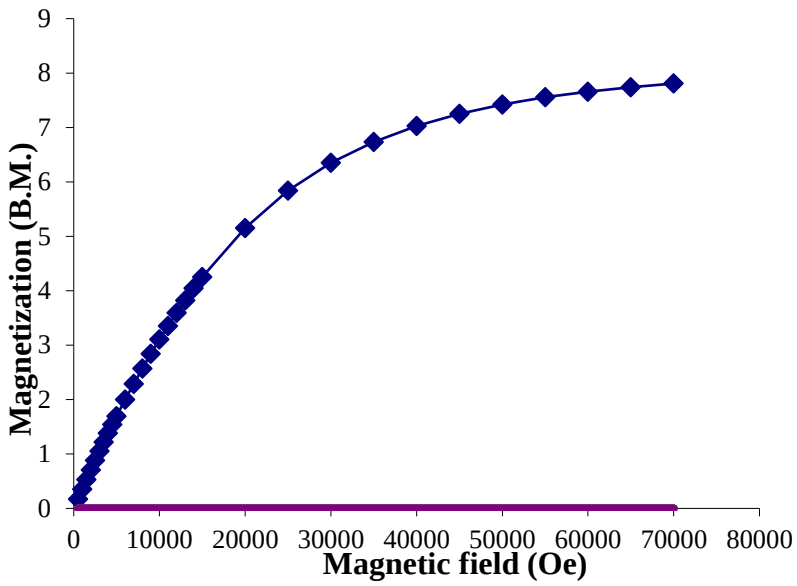

Figure 58: Magnetization data at 2 K for **21**. Solid lines are a guide for the eye.

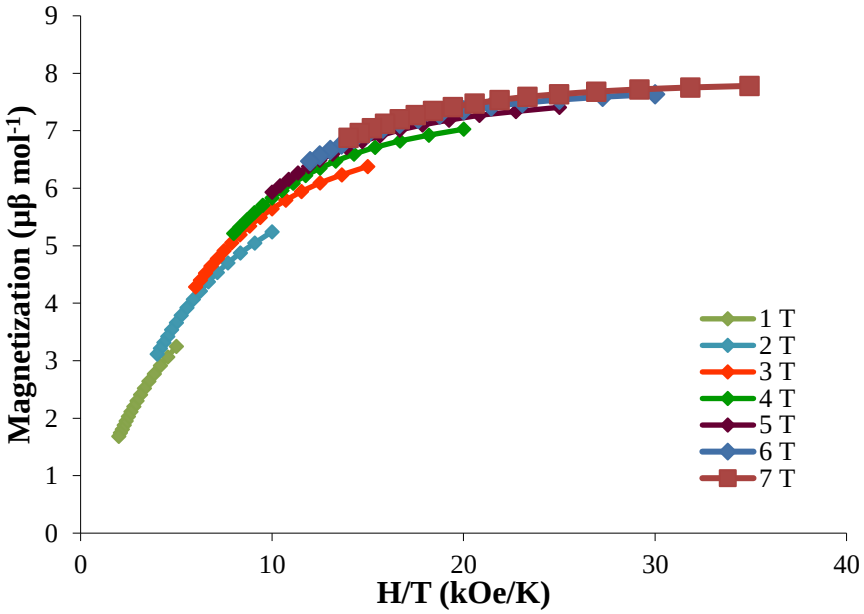

Figure 59: Reduced magnetization data for **21** from 2 to 5 K and 1 to 7 T. Solid lines are a guide for the eye.

Compound **22** behaves in a similar manner to its molybdenum analogue; four divalent nickel groups are bound to the diamagnetic $[W^{IV}(CN)_8]^{4-}$ center which yields a molecule with four S =1 independent spin centers. The $\chi_M T$ value at 300 K is 4.57 emu·K·mol^{-1} which gradually decreases to 3.21 emu·K·mol^{-1} at 2 K (Figure 60). These data are consistent with four equivalents of the starting material $[Ni^{II}(PY5Me_2)(CH_3CN)](PF_6)_2$, and the decrease is likely due to ZFS. The 2 K magnetization plot (Figure 61) at 7 T exhibits a value of 7.31 μ_B, which is slightly below the expected value of 8 μ_B for eight unpaired electrons from the four Ni^{II} spin centers, but saturation does not occurred and ZFS may affect the values. The reduced magnetization plot (Figure 62) shows overlapping isofield lines, suggesting the compound is magnetically isotropic.

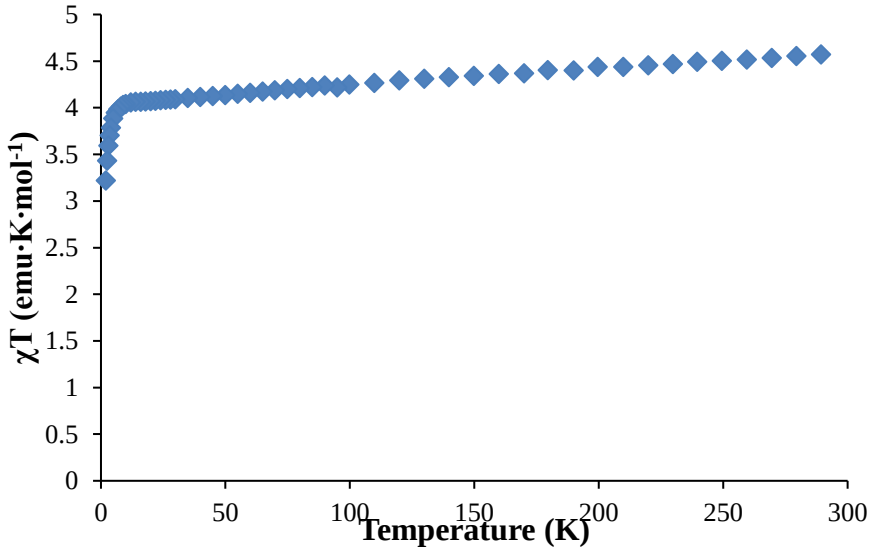

Figure 60: Variable-temperature DC susceptibility plot of **22**.

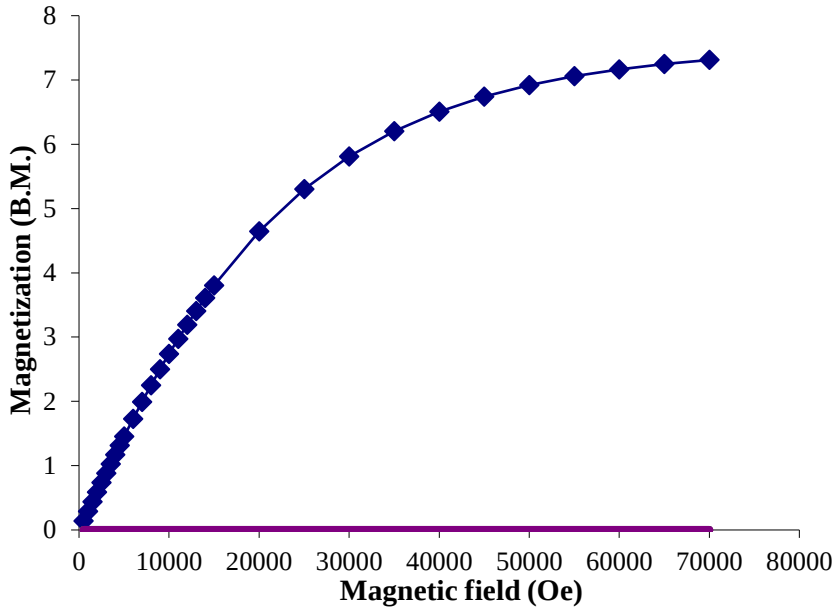

Figure 61: Magnetization data for **22** at 2 K. Solid lines are a guide for the eye.

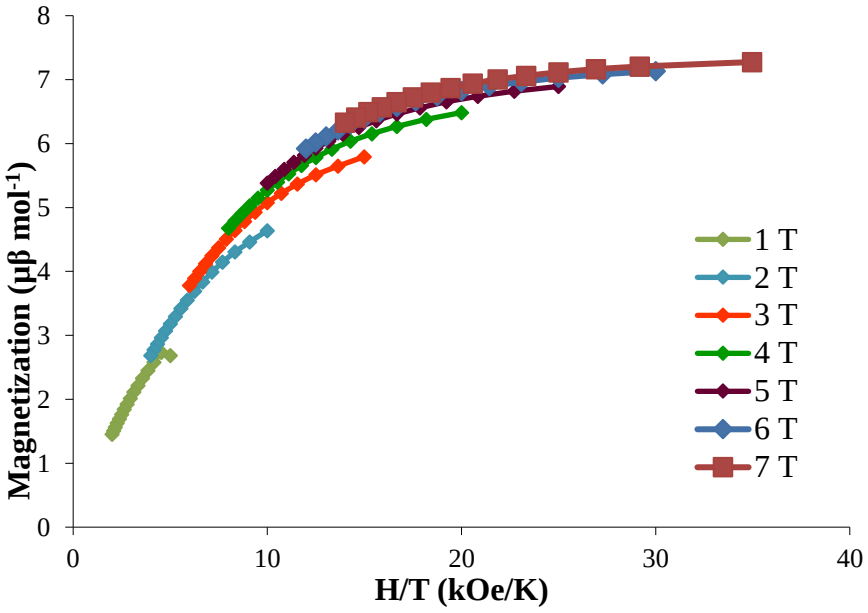

Figure 62: Reduced magnetization data for **22** from 2 to 5 K and 1 to 7 T. Solid lines are a guide for the eye.

Conclusions

The $[M^{II}(PY5Me_2)(CH_3CN)]X_2$ (M = Fe, X = $CF_3SO_3^-$; M = Zn, X = BF_4^-) compounds for Fe and Zn were prepared by an alternative route and characterized by X-ray crystallography and IR spectroscopy. Reactions of the $[M^{IV}(CN)_7]^{3-}$ anions with these cationic metal compounds were studied with the aim being to probe nature of anisotropic exchange interactions and 3d-5d coupling. Reactions of $[M(PY5Me_2)]^{2+}$ resulted, however, in 2D networks and yield star-like complexes similar to its rhenium analogue. Although all of the compounds are new, they contain the diamagnetic $[M^{IV}(CN)_8]^{4-}$ at the center of the polynuclear complexes as a result of decomposition. Regardless of ligand choice (L_{N5}, tmphen, or $PY5Me_2$), metal centers coupled to (Mn, Fe, Co, Ni, Cu, Sm, or Dy), solvents (CH_3CN, DMF, MeOH, or CH_2Cl_2), temperatures (room temperature or -30 °C), or other reaction conditions, the conversion of the $[M^{IV}(CN)_7]^{3-}$ anion to $[M^{IV}(CN)_8]^{4-}$ was always the outcome. The loss of cyanide from the heptacyano analogues results in the more highly stable octacyanometallates. Isolation of 5d-3d with both transition metals having non-zero spin states will likely require the use of heteroleptic cyanide precursors. with desired geometries and electronic configurations (i.e. pentagonal bipyramidal with a d^1 or d^3 electronic configuration) that engage in uniaxial exchange coupling. Additionally, such complexes can be designed to prevent equatorial coupling, and decomposition to the octacyanometallate(IV) anion. Heteroleptic complexes are further discussed in Chapter V.

CHAPTER IV

STAR-LIKE COMPLEXES BASED ON OCTACYANOMETALLATE(V) ANIONS

Introduction

As discussed in the introduction chapter, the octacyanometallates of the 4d and 5d transition metals have been much more thoroughly studied as compared to the hepta- and hexacyanometallates owing to the ease of syntheses and stabilities of the anions. In particular, the Mo^{V} and W^{V} ions are the most prevalent, given that their S =1/2 spin states allow for exchange coupling, whereas the Mo^{IV} and W^{IV} derivatives are diamagnetic. Most compounds that contain these anions tend to form extended structures with discrete examples being rare. Among the molecules reported, the $M^{II}_{9}M'^{V}_{6}$ pentadecanuclear compounds (M^{II} = Mn, Co, and Ni; M' = Mo^{V} and W^{V})[140-142] the tetranuclear squares $Mn^{II}_{2}M'_{2}$ (M' = $[W^{V}(CN)_{8}]^{3-}$),[143] and the hexanuclear complexes $M^{II}_{4}M'_{2}$ (M^{II} = Mn, Fe, and Co; M' = Nb^{IV}, Mo^{V}, and W^{V}) are known.[144-146] Only a few complexes involve a single $[M^{IV/V}(CN)_{8}]^{4/3-}$ anion, namely $[(Cu^{II}TPA)_{6}Mo^{IV}(CN)_{8}](ClO_{4})_{8}$ (TPA = tris(2-pyridylmethyl)amine),[197] $[Cu^{II}(bpy)]_{2}[W^{V}(CN)_{8}]\}Cu^{II}(bpy)_{2}][\ [W^{V}(CN)_{8}]\}\cdot 4H_{2}O$ (bpy = 2,2′-bipyridine),[198] and $[(Cu^{II}L)W(CN)_{8}]\cdot 4H_{2}O$ and $[(Cu^{II}L)_{2}W(CN)_{8}]\cdot 4H_{2}O$ (L = 3,7-bis(2-aminoethyl)-1,3,5,7-tetraazabicyclo[3.3.2]decane), which are dinuclear and trinuclear, respectively.[199]

As described in Chapter III, reactions of the $[M^{IV}(CN)_{7}]^{3-}$ anions of Mo and W with 3d containing $[M^{II}(PY5Me_{2})]^{2+}$ cations resulted in star-like complexes but the reactions resulted in the formation of the diamagnetic $[M^{IV}(CN)_{8}]^{4-}$ at the center of the

molecule. In order to better understand the magnetic properties of these compounds, the reactions were repeated using the $[M^{V}(CN)_8]^{3-}$ anions instead of the tetravalent analogies, with the goal being to achieve similar star-like clusters that would be magnetically interesting and exhibit exchange coupling.

Experimental

All reactions were performed in a drybox or on a Schlenk-line under an inert atmosphere unless otherwise stated. The solvent CH_3CN (Sigma Aldrich) was pre-dried over 3Å molecular sieves and then distilled over 3Å sieves under nitrogen, Et_2O was passed through an activated alumina column (MBraun solvent system) and anhydrous THF (Sigma Aldrich) was used as received. All solvents were stored over molecular sieves in the drybox. The starting materials $(Bu_4N)_3[Mo^{V}(CN)_8]$,[160] $(Bu_4N)_3[W^{V}(CN)_8]$,[160] $[Mn^{II}(PY5Me_2)(CH_3CN)](PF_6)_2$,[103] $[Ni^{II}(PY5Me_2)(CH_3CN)](PF_6)_2$, $[Co^{II}(PY5Me_2)(CH_3CN)](PF_6)_2$, and $[Cu^{II}(PY5Me_2)(CH_3CN)](PF_6)_2$ were prepared according to literature methods.[104]

Synthesis

$[Mn^{II}(PY5Me_2)]_4[Mo^{V}(CN)_8](PF_6)_5$ (24)

A vial was charged with 0.0140 g (0.0135 mmol) of $(Bu_4N)_3[Mo^{V}(CN)_8]$ and treated with 1.57 mL CH_3CN to give a yellow solution. Separately, a small vial was charged with 0.0463 g (0.0558 mmol) of $[Mn^{II}(PY5Me_2)(CH_3CN)](PF_6)_2$ and dissolved in 2.75 mL of CH_3CN with manual stirring to give a light yellow-colorless solution. The solution of $(Bu_4N)_3[Mo^{V}(CN)_8]$ was then slowly added via pipette to the solution of $[Mn^{II}(PY5Me_2)(CH_3CN)]^{2+}$, resulting in color changes to teal and then blue-green with

the formation of a microcrystalline precipitate. The vial was placed in a jar with diethyl ether for slow vapor diffusion. After 4 weeks, yellow crystals and a white precipitate were collected on a frit, washed with THF to remove the Bu_4NPF_6 by-product and dried. The solid was redissolved in 5 mL CH_3CN to give a light-yellow solution for crystallization by slow vapor diffusion with diethyl ether. Attempts to recrystallize the product led to a yellow precipitate which was collected by filtration, washed with THF and diethyl ether, and then dried under vacuum. Mass of product: 0.0078 g.

$[Mn^{II}(PY5Me_2)]_4[W^V(CN)_8](PF_6)_5$ (25)

A vial was charged with 0.0424 g (0.0378 mmol) of $(Bu_4N)_3[W^V(CN)_8]$ and dissolved in 1.1 mL CH_3CN to give a colorless solution. Separately, a small vial was charged with 0.1249 g (0.1505 mmol) of $[Mn^{II}(PY5Me_2)(CH_3CN)](PF_6)_2$ and dissolved in 2.0 mL of CH_3CN with manual stirring to give a light yellow solution. The solution of $(Bu_4N)_3[W^V(CN)_8]$ was then slowly pipetted into the solution of $[Mn^{II}(PY5Me_2)(CH_3CN)]^{2+}$, resulting in color changes to blue, then dark blue, teal green, and finally lavender, along with a cloudy precipitate. The vial was placed in a jar with diethyl ether for slow vapor diffusion. After 3 weeks, lavender and a light yellow precipitate was collected on a medium frit, washed with THF to remove the Bu_4NPF_6 by-product, then washed with diethyl ether and dried under vacuum. Mass of product: 0.0980 g.

$[Fe^{II}(PY5Me_2)]_4[Mo^V(CN)_8](CF_3SO_3)_5$ (26)

A vial was charged with 0.0101 g (0.097 mmol) of $(Bu_4N)_3[Mo^V(CN)_8]$ and dissolved in 0.93 mL CH_3CN to give a light yellow solution. Separately, a small vial was

charged with 0.0338 g (0.0403 mmol) of $[Fe^{II}(PY5Me_2)(CH_3CN)](CF_3SO_3)_2$ and dissolved in 1.86 mL of CH_3CN to give a dark red solution. The solution of $(Bu_4N)_3[Mo^V(CN)_8]$ was then slowly pipetted into the solution of $[Fe^{II}(PY5Me_2)(CH_3CN)]^{2+}$, resulting in the formation of a lighter red solution with some precipitate that redissolved with stirring. The vial was placed in a jar with diethyl ether for slow vapor diffusion. After 3 weeks, the red product was collected on a medium frit, washed with THF to remove the Bu_4NPF_6 by-product, washed with diethyl ether and dried under vacuum. Mass of product: 0.1121 g.

$[Fe^{II}(PY5Me_2)]_4[W^V(CN)_8](CF_3SO_3)_5$ (27)

A vial was charged with 0.0463 g (0.0413 mmol) of $(Bu_4N)_3[W^V(CN)_8]$ and dissolved in 0.88 mL CH_3CN to give a colorless solution. Separately, a small vial was charged with 0.1393 g (0.1661 mmol) of $[Fe^{II}(PY5Me_2)(CH_3CN)](CF_3SO_3)_2$ and dissolved in 2.34 mL of CH_3CN to give a dark red solution with orange precipitate which is not completely soluble in CH_3CN. The solution of $(Bu_4N)_3[W^V(CN)_8]$ was then slowly pipetted into the solution of $[Fe^{II}(PY5Me_2)(CH_3CN)]^{2+}$, resulting in the formation of a cloudy dark red solution. The vial was placed in a jar with diethyl ether for slow vapor diffusion. After 3 weeks, dark red crystals and an orange precipitate were collected on a medium frit, washed with THF to remove the Bu_4NPF_6 by-product, then washed with diethyl ether and dried under vacuum. Mass of product: 0.1213 g.

$[Co^{II}(PY5Me_2)]_4[Mo^V(CN)_8](PF_6)_5$ (28)

A vial was charged with 0.0281 g (0.0272 mmol) of $(Bu_4N)_3[Mo^V(CN)_8]$ and dissolved in 1.30 mL of CH_3CN to give a yellow solution. Separately, a small vial was

charged with 0.0909 g (0.1090 mmol) of $[Co^{II}(PY5Me_2)(CH_3CN)](PF_6)_2$ and dissolved in 2.60 mL of CH_3CN to give an orange solution. The solution of $(Bu_4N)_3[Mo^V(CN)_8]$ was then added via pipette with manual stirring to the solution of $[Co^{II}(PY5Me_2)(CH_3CN)]^{2+}$, resulting in a dark orange solution that turns maroon and becomes cloudy with precipitate. The vial was placed in a jar with diethyl ether for slow vapor diffusion. After 4 months, dark green crystals and a pale blue powder were collected on a medium frit, washed with THF to remove the Bu_4NPF_6 by-product, then washed with diethyl ether and dried under vacuum. Mass of product (crystals and powder): 0.0772 g, yield: 88.8 %.

$[Co^{II}(PY5Me_2)]_4[W^V(CN)_8](PF_6)_5$ (29)

A vial was charged with 0.0456 g (0.0407 mmol) of $(Bu_4N)_3[W^V(CN)_8]$ and dissolved in 0.94 mL of CH_3CN to give a colorless solution. Separately, a small vial was charged with 0.1353 g (0.1622 mmol) of $[Co^{II}(PY5Me_2)(CH_3CN)](PF_6)_2$ and dissolved in 2.53 mL of CH_3CN with manual stirring to give an orange solution. The solution of $(Bu_4N)_3[Mo^V(CN)_8]$ was then added via pipette to the solution of $[Co^{II}(PY5Me_2)(CH_3CN)]^{2+}$ with stirring, resulting in a dark orange solution that turns to a maroon color and becomes cloudy with a teal precipitate. The vial was placed in a jar with diethyl ether for slow vapor diffusion. After 3 weeks, a green product was collected on a frit, washed with THF to remove the Bu_4NPF_6 by-product, and washed with diethyl ether and dried under vacuum. Mass of product: 0.1232 g, yield: 97.0 %.

$[Ni^{II}(PY5Me_2)]_4[Mo^V(CN)_8](PF_6)_5$ (30)

A vial was charged with 0.0510 g (0.0494 mmol) of $(Bu_4N)_3[Mo^V(CN)_8]$ and dissolved in 2.02 mL of CH_3CN to give a yellow solution. Separately, a thin vial was

charged with 0.1644 g (0.1972 mmol) of $[Ni^{II}(PY5Me_2)(CH_3CN)](PF_6)_2$ and dissolved in 3.02 mL of CH_3CN with manual stirring to give a light pink solution. The solution of $(Bu_4N)_3[Mo^V(CN)_8]$ was then slowly added via pipette to the solution of $[Ni^{II}(PY5Me_2)(CH_3CN)]^{2+}$, resulting in a brown-yellow to olive solution along with light orange precipitate that dissolves upon stirring. The vial was placed in a jar with diethyl ether for slow vapor diffusion. After 3 weeks, some orange crystals and orange precipitate formed; the orange product was collected on a frit, washed with THF to remove the Bu_4NPF_6 by-product, then washed with diethyl ether and dried under vacuum. Mass of product: 0.0692 g, yield: 41.6 % (based off $Mo_1Ni_4P_5F_{30}N_{37}C_{143}H_{126}$). Elemental analysis: Theoretical C: 50.22, H: 3.72, N: 15.16; actual C: 48.26, H: 3.96, N: 14.42.

$[Ni^{II}(PY5Me_2)]_4[W^V(CN)_8](PF_6)_5$ (31)

A vial was charged with 0.0474 g (0.0423 mmol) of $(Bu_4N)_3[W^V(CN)_8]$ and dissolved in 2.18 mL of CH_3CN to give a colorless solution. Separately, a thin vial was charged with 0.1409 g (0.169 mmol) of $[Ni^{II}(PY5Me_2)(CH_3CN)](PF_6)_2$ and dissolved in 3.23 mL of CH_3CN with manual stirring to give a light pink solution. The solution of $(Bu_4N)_3[W^V(CN)_8]$ was then slowly added via pipette to the solution of $[Ni^{II}(PY5Me_2)(CH_3CN)]^{2+}$, resulting in a red-brown solution, with precipitate that dissolves upon stirring. The vial was placed in a jar with diethyl ether for slow vapor diffusion. After 3 weeks, orange precipitate had formed; the orange product was collected on a frit, washed with THF to remove the Bu_4NPF_6 by-product, then washed with diethyl ether and dried under vacuum. Mass of product: 0.0598 g, yield: 40.9 %. Elemental analysis: Theoretical C: 48.97, H: 3.62, N: 14.78; actual C: 50.49, H: 3.72, N: 16.38.

$[Cu^{II}(PY5Me_2)]_4[Mo^V(CN)_8](PF_6)_5$ (32)

A vial was charged with 0.0279 g (0.027 mmol) of $(Bu_4N)_3[Mo^V(CN)_8]$ and dissolved in 1.30 mL of CH_3CN to give a yellow solution. Separately, a thin vial was charged with 0.0928 g (0.1107 mmol) of $[Cu^{II}(PY5Me_2)(CH_3CN)](PF_6)_2$ and dissolved in 2.21 mL of CH_3CN to give a dark blue solution with manual stirring. The solution of $(Bu_4N)_3[Mo^V(CN)_8]$ was then slowly added via pipette to the solution of $[Cu^{II}(PY5Me_2)(CH_3CN)]^{2+}$, resulting in a darker blue solution that turns teal-green with a cloudy precipitate. The vial was placed in a jar with diethyl ether for slow vapor diffusion. After 4 months, the pale blue solid was collected on a frit, washed with THF to remove the Bu_4NPF_6 by-product, washed with diethyl ether, and dried under vacuum. Mass of product: 0.0554 g.

$[Cu^{II}(PY5Me_2)]_4[W^V(CN)_8](PF_6)_5$ (33)

A vial was charged with 0.0561 g (0.0501 mmol) of $(Bu_4N)_3[W^V(CN)_8]$ and dissolved in 1.10 mL of CH_3CN to give a colorless solution. Separately, a thin vial was charged with 0.1689 g (0.2015 mmol) of $[Cu^{II}(PY5Me_2)(CH_3CN)](PF_6)_2$ and dissolved in 2.15 mL of CH_3CN with manual stirring to give a dark blue solution. The solution of $(Bu_4N)_3[W^V(CN)_8]$ was then slowly added via pipette to the solution of $[Cu^{II}(PY5Me_2)(CH_3CN)]^{2+}$, resulting in a violet solution with a dark blue precipitate. The vial was set in a jar with diethyl ether for slow vapor diffusion. After 3 weeks, the blue precipitate was collected on a frit, washed with THF to remove the Bu_4NPF_6 by-product, then washed with diethyl ether and dried under vacuum. Mass of product: 0.1103.

X-ray Crystallography

Single crystal diffraction data for **28** and **29** were collected at 110 K on the ChemMatCars beamline 15-ID-B at the Advanced Photon Source (APS), Argonne National Lab. The data collection strategy consisted of obtaining three ω-scans with one full-sphere and two half-spheres for a total 1440 frames with a 0.5º width. Integration was performed with the Bruker-APEXII software package, and the absorption correction (SADABS) was based on fitting a function to the empirical transmission surface as sampled by multiple equivalent measurements. An orange crystal of **31** was mounted on a Nylon loop using Paratone® oil and placed in a N_2 cold stream at 110 K. The data were collected on a Bruker D8 Quest Eco diffractometer (MoKα radiation λ = 0.71073 Ǻ) equipped with a Photon50 CMOS detector. For all compounds, the multi-scan absorption correction was performed within the Bruker APEXII software using SADABS (v2014/5) or within the Bruker APEX3 software using SADABS (v2015/10).[163-164] Solution and refinement of the structures were carried out using SHELXT and shelXle or Olex2 (a graphical interface for the SHELX suite of programs), respectively.[165-166, 185] Structure solution by direct methods resolved positions of all heavy atoms and most of the lighter atoms. The remaining non-hydrogen atoms were located by alternating cycles of least-squares refinements and difference Fourier maps. Except for **1**, which was refined isotropically, the final refinements were performed with anisotropic thermal parameters for all non-hydrogen atoms. Images of the molecular structures were rendered using DIAMOND software for crystal structure visualization.[167] A summary of pertinent information relating to unit cell parameters, data collection, and refinement is provided in

Table 19: Crystallographic data and experimental details for compounds **28**, **29**, and **31**.

Formula	**28**	**29**	**31**
Molecular Weight	3195.43	3115.69	3455.22
Temperature (K)	110	110	110
Crystal System	Monoclinic	Monoclinic	Tetragonal
Space Group	P2/c	$P2_1/m$	I4/m
a (Å)	34.352(12)	16.938(4)	33.287(2)
b (Å)	12.686(4)	23.443(5)	33.287(2)
c (Å)	38.352(12)	39.223(9)	29.0002(16)
α (°)	90	90	90
β (°)	99.663(5)	92.614(4)	90
γ (°)	90	90	90
V ($Å^3$)	16477(9)	15558(6)	32132(3)
Z	4	4	16
Color	Green	Green	Orange
ρcalc (g/cm^3)	1.288	1.330	1.429
μ (mm)	0.610	1.292	1.316
F(000)	6462.0	6236.0	13984.0
Crystal Size (mm)	0.05 x 0.08 x0.150	0.05 x 0.08 x 0.12	0.080 x 0.115 x 0.260
Radiation	APS Synchrotron	APS Synchrotron	MoKα (λ = 0.71073)
Index Range	-31≤h≤31 -11≤k≤11 -34≤l≤34	-16≤h≤17 -23≤k≤23 -39≤l≤39	-39≤h≤30 -39≤k≤39 -34≤l≤34
2θ range (°)	3.866 – 37.696	4.026 – 41.83	4.388 – 50.178
Reflections collected	149485	202216	58607
Unique reflections	12415	16991	14565
Parameters/restraints	805, 0	1501, 0	1013, 6
R_1, wR_2 [$I > 2\sigma(I)$]	0.2103, 0.4854	0.2217, 0.5532	0.0814, 0.2106
R_1, wR_2 (all data)	0.2792, 0.5361	0.2505, 0.5729	0.1223, 0.2571
GooF (F^2)	1.980	2.446	0.995
Largest diff. peak, hole, (e $Å^{-3}$)	-1.57, 3.97	-2.16, 5.12	-2.32, 4.93

[a]$R = \Sigma \, ||F_o| - |F_c|| / \Sigma |F_o|$. [b]$wR = \{\Sigma \, [w(F_o^2 - F_c^2)^2] / \Sigma \, [w(F_o^2)]^2\}^{1/2}$. [c]Goodness-of-fit = $\{\Sigma \, [w(F_o^2 - F_c^2)^2]/(n-p)\}^{1/2}$, where *n* is the number of reflections and *p* is the total number of parameters refined.

Table 19.

Physical Methods

IR spectra were recorded on a Nicolet Nexus 470 FT-IR E.S.P spectrophotometer between KBr plates with the powdered samples being suspended in Nujol® mulls. Elemental analyses were performed by Atlantic Microlabs, Inc., Norcross, GA. Magnetic measurements were performed on a Quantum Design MPMS-XL SQUID magnetometer equipped with a 7 T superconducting magnet over the temperature range of 1.8 to 300 K. The diamagnetic contribution of the plastic bag used as a sample holder was subtracted from the raw data, and the core diamagnetism of the sample was corrected for using Pascal's constants.[168] Magnetic data were fit using the PHI program.[182]

Results and Discussion

Synthesis

The reactions were performed by dissolving $(Bu_4N)_3[M^V(CN)_8]$ in CH_3CN and then slowly adding the solution to four equivalents of the $[M^{II}(PY5Me_2)(CH_3CN)]^{2+}$ cation in CH_3CN with manual swirling of the vial. The solutions were then placed in a jar with a screw cap that contains diethyl ether to induce crystallization. The isolated products were washed with THF to remove the Bu_4NPF_6 by-product. In the cases of Mn (**24** and **25**), Fe (**26** and **27**), and Cu (**32** and **33**), the reactions produced powder products; attempts to recrystallize the powder to obtain suitable crystals for X-ray diffraction were unsuccessful, despite the alteration of crystallization conditions such as solvent, temperature, or concentration. Typically, any crystals that formed turned out to be unreacted starting materials. In the case of Fe and Cu, the powder product was also similar

in color to the starting materials, which rendered separation of the product from the reactant difficult given their similar solubilities. In the cases of Co (**28** and **29**) and Ni (**31**) crystals were obtained. For Co and Ni, there was a change in the color of the product from that of the starting material, which allowed for manual separation of the product crystals from unreacted starting material crystals. All products were characterized by infrared spectroscopy (*vide infra*) which indicated, in all cases, that the reactions yield polynuclear complexes as deduced from the presence of bridging cyanide stretches. The only difference between the molybdenum and tungsten reactions occurs with Ni; orange crystals were obtained for W and an orange-tan powder was obtained for Mo.

Single Crystal X-ray Diffraction Studies

Compound **28** crystallizes as green blocks in the space group P2/c with one molecule in the asymmetric unit. The molecule is a star-like cluster as previously observed for reactions of the $[W^{IV}(CN)_7]^{3-}$ and $[Re^{IV}(CN)_7]^{3-}$ anions (Figure 60). It was necessary to refine the structure isotropically due to the weak nature of the data. The $[Mo^{V}(CN)_8]^{3-}$ anion adopts a distorted geometry between square antiprismatic and dodecahedral based on the bond angles. The Mo—CN bond distances range from 2.11(2) to 2.22(3) Å, the C—N bond distances vary from 1.13(4) to 1.21(4) Å, and the Co—NC bond distances are between 1.88(3) and 2.06(3) Å. These distances are similar to the Mo^{V} bond ranges previously observed and to those reported for other compounds.[141] The Mo—C—N angles vary between 173(3)° to 178(3)°, while the Co—N—C angles are between 170(2)° and 178(2)°, indicating distortion from linearity. Important bond distances and bond angles are listed in Table 20.

Table 20: Select bond distances and bond angles for **28**.

Select Bond	Bond Distance (Å)	Select Bond	Bond Angle (°)
Mo—C_1	2.13(3)	C_1—Mo_1—C_6	74.3(12)
Mo—C_2	2.13(3)	C_1—Mo_1—C_8	68.8(12)
Mo—C_3	2.11(2)	C_1—Mo_1—C_4	143.9(13)
Mo—C_4	2.17(4)	C_1—Mo_1—C_5	76.3(12)
Mo—C_5	2.17(3)	C_2—Mo_1—C_1	91.9(11)
Mo—C_6	2.22(3)	C_2—Mo_1—C_6	146.1(11)
Mo—C_7	2.18(4)	C_2—Mo_1—C_8	78.1(10)
Mo—C_8	2.14(3)	C_2—Mo_1—C_4	101.4(11)
Co_1—N_1	1.88(3)	C_2—Mo_1—C_5	73.3(11)
Co_2—N_2	2.06(3)	C_4—Mo_1—C_5	75.7(12)
Co_3—N_3	1.94(2)	C_5—Mo_1—C_6	73.3(12)
Co_4—N_4	2.01(3)	C_5—Mo_1—C_8	133.6(12)
Co—N_{ax}	1.91(3)– 2.10(3)	C_4—Mo_1—C_6	76.1(12)
Co—N_{eq}	1.94(2) – 2.19(3)	C_4—Mo_1—C_8	146.6(12)
C_1—N_1	1.16(3)	C_6—Mo_1—C_8	122.4(11)
C_2—N_2	1.15(3)	C_7—Mo_1—C_1	142.9(13)
C_3—N_3	1.15(3)	C_3—Mo_1—C_1	99.0(10)
C_4—N_4	1.14(4)	C_7—Mo_1—C_5	130.5(12)
C_5—N_5	1.21(4)	C_3—Mo_1—C_2	144.7(10)
C_6—N_6	1.13(4)	C_3—Mo_1—C_4	89.3(11)
C_7—N_7	1.17(4)	C_7—Mo_1—C_4	73.3(13)
C_8—N_8	1.19(3)	C_3—Mo_1—C_6	69.1(11)
		C_3—Mo_1—C_8	74.8(10)
		C_7—Mo_1—C_8	74.3(12)
		C_7—Mo_1—C_6	132.4(12)
		C_7—Mo_1—C_3	74.9(11)
		C_7—Mo_1—C_2	76.2(11)
		C_5—Mo_1—C_3	141.9(11)
		C_1—N_1—Co_1	173(2)
		C_2—N_2—Co_2	170(2)
		C_3—N_3—Co_3	178(2)
		C_3—N_4—Co_4	171(3)
		N_{ax}—Co—N_{Mo}	178.5(11) - 178.9(11)
		N_1—C_1—Mo	173(3)
		N_2—C_2—Mo	178(2)
		N_3—C_3—Mo	177(2)
		N_4—C_4—Mo	174(4)
		N_5—C_5—Mo	177(3)
		N_6—C_6—Mo	176(3)
		N_7—C_7—Mo	178(3)
		N_8—C_8—Mo	178(3)

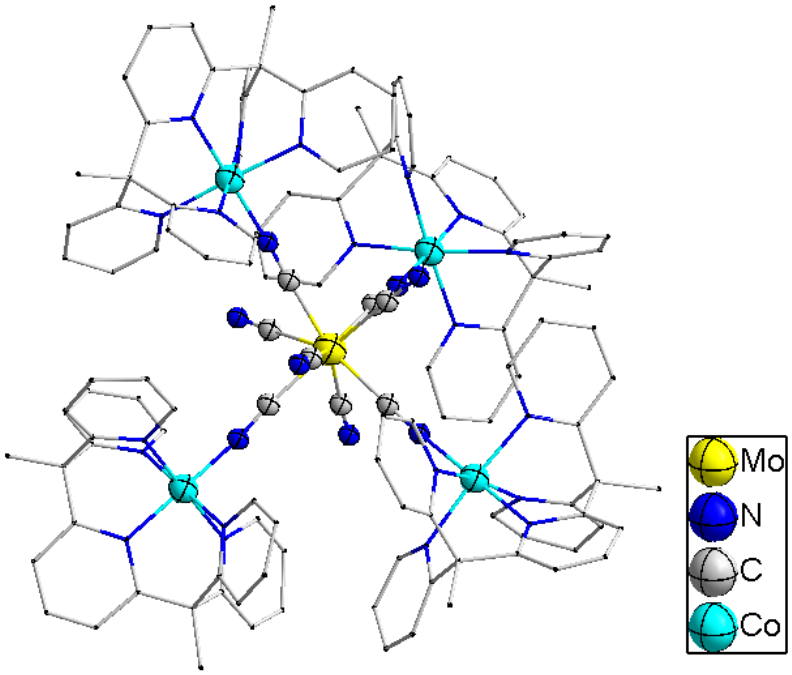

Figure 63: Molecular structure of **28**. Hydrogen atoms are omitted for the sake of clarity.

Compound **29** crystallizes as green blocks and crystallizes in the space group $P2_1/n$. The molecule adopts a star-like geometry as in the case of compounds (Figure 64); the $[W^V(CN)_8]^{3-}$ metal ion is in a distorted square prismatic geometry in contrast to the square antiprismatic geometry observed in the molybdenum analogue. The W—C bond distances vary between 2.02(3) to 2.30(5) Å, which is a considerably wider range than expected as a consequence of the limited data obtained. The 2.02(3) Å bond distance agrees with previously measured W^V—CN bond distances for a terminal cyanide; the C—N bond distances vary from 1.02(5) to 1.34(5) Å, with most of them falling in the more

realistic range of 1.12(6) to 1.18(4) Å. The Co—NC bond distances are 1.96(3) Å, 2.02(3) Å, and 2.09(4) Å, consistent with Co^{II}.[141] The W—C—N bond angles vary from 175(2)° to 180(5)° and the Co—N—C bond distances range from 163(4)° to 177(3)°. A summary of important bond distances and angles are compiled in Table 21.

Finally, compound **31** crystallizes as orange crystals in the tetragonal space group I4/m; the asymmetric unit contains $[(Ni^{II}PY5Me_2)_2W^V(CN)_6](PF_6)_3$, with the remaining atoms being generated by symmetry (Figure 65). As before, the molecule is a star-like cluster. The $[W^V(CN)_8]^{3-}$ is in a distorted square antiprismatic geometry. The W—CN bond distances range from2.108(1) to 2.195(9) Å, the C—N bond distances from 1.129(11) to 1.218(15) Å; the Ni—NC bond distances are between 2.003(10) to 2.058(10)

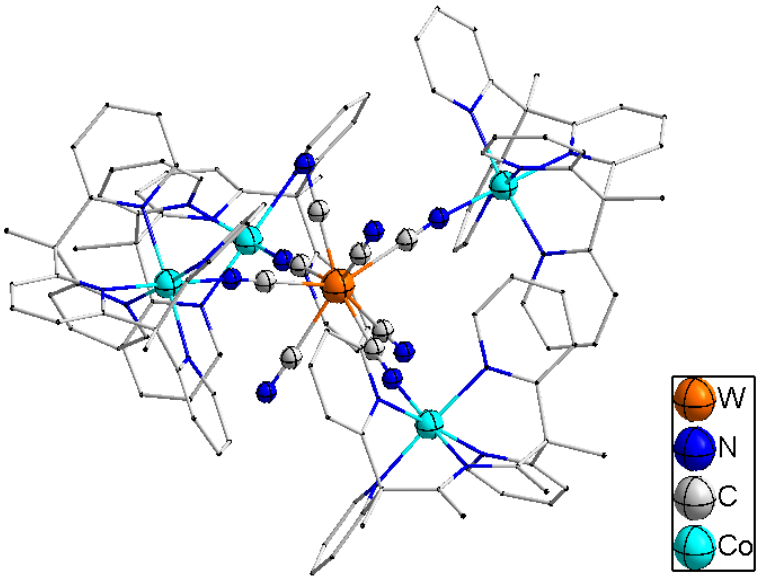

Figure 64: Molecular structure of **29**. Hydrogen atoms are omitted for the sake of clarity.

Table 21: Select bond distances and bond angles for **29**.

Select Bond	Bond Distance (Å)	Select Bond	Bond Angle (°)
W—C_1	2.19(7)	C_1—W_1—C_6	143.5(17)
W—C_2	2.30(5)	C_1—W_1—C_4'	77.2(13)
W—C_3	2.06(3)	C_1—W_1—C_4	77.2(13)
W—C_3'	2.06(3)	C_1—W_1—C_5	65.4(18)
W—C_4	2.19(4)	C_2—W_1—C_1	144.3(15)
W—C_5	2.26(3)	C_2—W_1—C_6	71.8(14)
W—C_6	2.02(3)	C_2—W_1—C_4'	75.3(10)
W—C_4'	2.19(4)	C_2—W_1—C_4	75.3(10)
Co_1—N_1	1.96(3)	C_2—W_1—C_5	149.9(16)
Co_2—N_2	2.09(4)	C_4—W_1—C_5	126.3(11)
Co_3—N_3	2.02(3)	C_5—W_1—C_6	78.1(17)
Co_4—N_4	2.02(3)	C_5—W_1—C_4'	126.3(11)
Co—N_{ax}	2.044(14) – 2.16(3)	C_4—W_1—C_6	128.8(11)
Co—N_{eq}	2.07(2) - 2.141(16)	C_4—W_1—C_4'	76.5(15)
C_1—N_1	1.12(6)	C_6—W_1—C_4'	128.8(11)
C_2—N_2	1.02(5)	C_3'—W_1—C_1	92.1(10)
C_3—N_3	1.18(4)	C_3—W_1—C_1	92.1(10)
C_3'—N_3'	1.18(4)	C_3'—W_1—C_5	73.9(10)
C_4—N_4	1.17(4)	C_3—W_1—C_2	99.0(10)
C_5—N_5	1.34(5)	C_3—W_1—C_4	70.4(11)
C_6—N_6	1.34(5)	C_3'—W_1—C_4	146.8(12)
C_4'—N_4'	1.17(4)	C_3—W_1—C_6	77.3(9)
		C_3—W_1—C_4'	146.8(12)
		C_3'—W_1—C_4'	70.4(11)
		C_3'—W_1—C_6	77.3(9)
		C_3'—W_1—C_3	142.2(18)
		C_3'—W_1—C_2	99.0(10)
		C_5—W_1—C_3	73.9(10)
		C_1—N_1—Co_1	177(5)
		C_2—N_2—Co_2	163(4)
		C_3—N_3—Co_3	177(3)
		C_3—N_4—Co_4	177(3)
		N_{ax}—Co—N_W	177.2(12) - 180(2)
		N_1—C_1—W	180(5)
		N_2—C_2—W	175(2)
		N_3—C_3—W	176(3)
		N_4—C_4—W	176(3)
		N_5—C_5—W	168(5)
		N_6—C_6—W	178(3)
		N_3'—C_3'—W	176(3)
		N_4'—C_4'—W	176(3)

Å, which are consistent with previously measured W^{V}—Ni^{II} compounds.[140, 142] The C—N—Ni bond angles range between 167.3(9)° to 168.8(9)°, while the W—C—N bond angles vary from 173.8(11)° to 179.3(9)°. Select bond distances and bond angles are reported in Table 22.

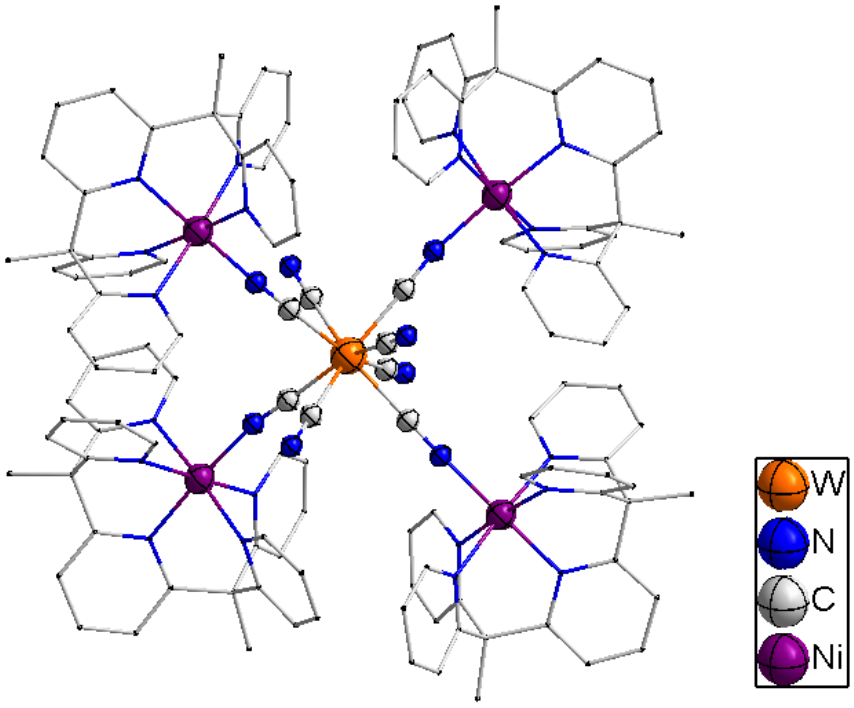

Figure 65: Molecular structure of **31**. Hydrogen atoms and solvent molecules are omitted for the sake of clarity.

Table 22: Select bond distances and bond angles for **31**.

Select Bond	Bond Distance (Å)	Select Bond	Bond Angle (°)
W—C_1	2.144(11)	C_1—W_1—C_6	75.4(3)
W—C_2	2.108(13)	C_1—W_1—C_6'	75.4(3)
W—C_3	2.113(9)	C_1—W_1—C_4	143.8(4)
W—C_3'	2.113(9)	C_1—W_1—C_5	70.0(5)
W—C_4	2.150(13)	C_2—W_1—C_1	144.7(4)
W—C_5	2.136(12)	C_2—W_1—C_6	76.4(3)
W—C_6	2.195(9)	C_2—W_1—C_6'	76.4(3)
W—C_6'	2.195(9)	C_2—W_1—C_4	71.5(4)
Ni_1—N_1	2.058(10)	C_2—W_1—C_5	145.3(5)
Ni_2—N_2	2.003(10)	C_4—W_1—C_5	73.8(5)
Ni_3—N_3	2.038(7)	C_5—W_1—C_6	129.1(3)
Ni_3'—N_3'	2.038(7)	C_5—W_1—C_6'	129.1(3)
Ni—N_{ax}	2.052 - 2.062	C_4—W_1—C_6	130.7(3)
Ni—N_{eq}	2.088 - 2.102	C_4—W_1—C_6'	130.7(3)
C_1—N_1	1.176(15)	C_6—W_1—C_6'	73.3(4)
C_2—N_2	1.218(15)	C_3'—W_1—C_1	97.5(2)
C_3—N_3	1.189(11)	C_3—W_1—C_1	97.5(2)
C_3'—N_3'	1.189(11)	C_3'—W_1—C_5	76.5(2)
C_4—N_4	1.169(16)	C_3—W_1—C_1	76.5(2)
C_5—N_5	1.187(16)	C_3—W_1—C_4	73.7(2)
C_6—N_6	1.129(11)	C_3'—W_1—C_4	73.7(2)
C_6'—N_6'	1.129(11)	C_3—W_1—C_6	145.4(3)
		C_3—W_1—C_6'	72.2(3)
		C_3'—W_1—C_6'	145.4(3)
		C_3'—W_1—C_6	72.3(3)
		C_3'—W_1—C_3	142.2(5)
		C_5—W_1—C_1	70.0(5)
		C_5—W_1—C_4	73.8(5)
		C_1—N_1—Ni_1	167.3(9)
		C_2—N_2—Ni_2	168.8(9)
		C_3—N_3—Ni_3	167.5(7)
		C_3'—N_4'—Ni_3'	167.5(7)
		N_{ax}—Ni—N_W	175.7 - 178.8
		N_1—C_1—W	179.3(9)
		N_2—C_2—W	179.0(9)
		N_3—C_3—W	177.9(8)
		N_3'—C_3'—W	177.9(8)
		N_4—C_4—W	178.4(11)
		N_5—C_5—W	173.8(11)
		N_6—C_6—W	179.3(8)
		N_6'—C_6'—W	179.3(8)

Infrared Spectroscopy

IR spectra were measured for all products (**24** – **33**). In the case of the molybdenum samples, both Mn and Fe exhibit one broad stretch at 2108 cm^{-1} and 2078 cm^{-1}, respectively, while the Co, Ni, and Cu compounds exhibit two ν(CN) stretching vibrations at higher frequencies. The lower frequency vibrations correspond to terminal cyanides and the higher frequency modes indicate bridging cyanides between Mo and the metal center. The increase of the bridging stretching frequencies from 2138 cm^{-1} to 2210 cm^{-1} is attributed to the increasing electronegativity and *d*-electron count of the 3d metal center; the σ-donation by the nitrogen lone pair leads to the higher stretching frequency.[97] This also matches the trend observed for the products based on $[Re^{IV}(CN)_7]^{3-}$.[97, 103-104]

Similarly, the tungsten complexes also display two stretches with the exception of the Fe sample which exhibits one broad ν(CN) stretch at 2117 cm^{-1}. The lower frequency bands correspond to terminal cyanides while the higher frequency peak is due to bridging cyanides.[97] In a similar manner, the increase in stretching frequency of the bridging ν(CN) (Mn = 2142 cm^{-1}, Co = 2148 cm^{-1}, Ni = 2185 cm^{-1}, and Cu = 2172 cm^{-1}) corresponds to increasing electronegativity and d-electron count of the 3d metal ion which increases σ-donation, and matches the trend observed for the rhenium analogues.[103-104]

Table 23: Infrared spectra of star-like complexes formed from $[M^{V}CN)_8]^{3-}$ for Mo and W. The $[Re^{IV}(CN)_7]^{3-}$ analogues are included as for reference.

Element	Mn	Fe	Co	Ni	Cu
Mo^{V}	2108	2078	2122, 2138	2143, 2182	2122, 2210
W^{V}	2135, 2142	2117	2118, 2148	2145, 2185	2121, 2172
$Re^{IVa,b}$	2098, 2031	NA	2102, 2056	2120, 2089	2287, 2256

Magnetic Measurements

Variable-temperature DC susceptibility data for **28** were measured from 300 to 2 K under an applied field of 1,000 Oe (Figure 66). At 300 K, the $\chi_M T$ value is 7.74 emu·K·mol^{-1}, which is close to the expected value of 7.85 emu·K·mol^{-1} for four independent S = 3/2 spin centers and an isolated S = 1/2 spin center. The value is higher than 7.03 emu·K·mol^{-1} reported in $[(Co^{II}PY5Me_2)_3(Co^{III}PY5Me_2)Re^{IV}(CN)_7]$,[104] but significantly below the values of 17.9 emu·K·mol^{-1} or 24.4 emu·K·mol^{-1} expected for antiferromagnetic or ferromagnetic coupling, respectively, between the Mo^V and Co^{II} spin centers. There is a gradual decrease in $\chi_M T$ as the temperature is lowered to 3.53 emu·K·mol^{-1} at 2 K which is due to the spin-orbit coupling of the Co^{II} ions, although weak antiferromagnetic coupling may also be operative. Attempts to fit the coupling between Mo^V and Co^{II} with the PHI program were unsuccessful. The 2 K magnetization value is 5.13 μ_B (Figure 67), and the reduced magnetization has overlapping isofield lines, suggesting no magnetic anisotropy (Figure 68). AC measurements revealed no slow relaxation behavior.

Compound **29** with tungsten behaves similarly to its molybdenum analogue. The $\chi_M T$ value is 7.74 emu·K·mol^{-1} at 300 K which is similar to that of Mo and consistent with isolated spin centers for four S = 3/2 Co^{II} ions and an S = 1/2 W^V spin center (Figure 69).[104] As the temperature is lowered there is a gradual decrease in $\chi_M T$ to 3.53 emu·K·mol^{-1} at 2 K which is attributed to spin-orbit coupling of the cobalt ions; weak antiferromagnetic coupling may also be operative. Attempts to fit the coupling between the W^V and Co^{II} ions with the PHI program were unsuccessful. The 2 K magnetization

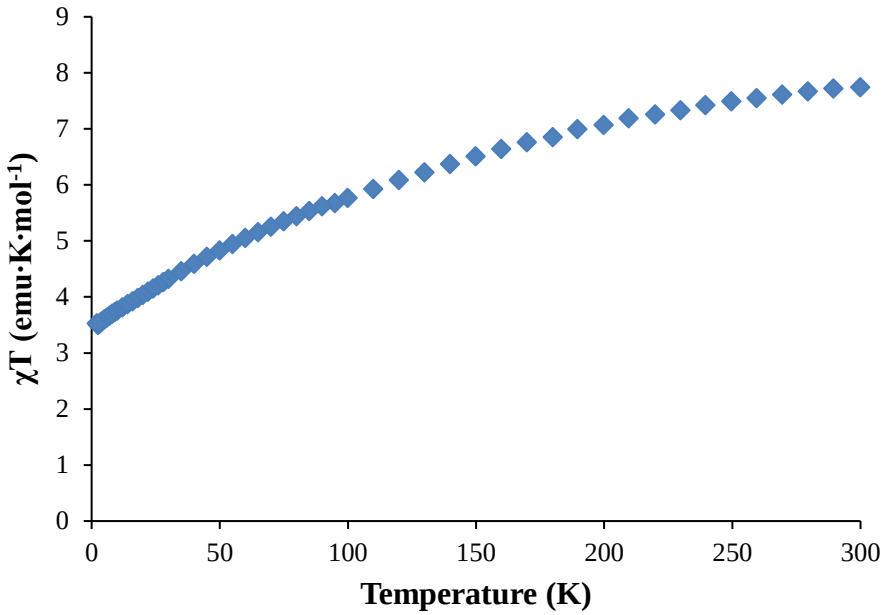

Figure 66: Variable-temperature DC susceptibility data plot for **28**.

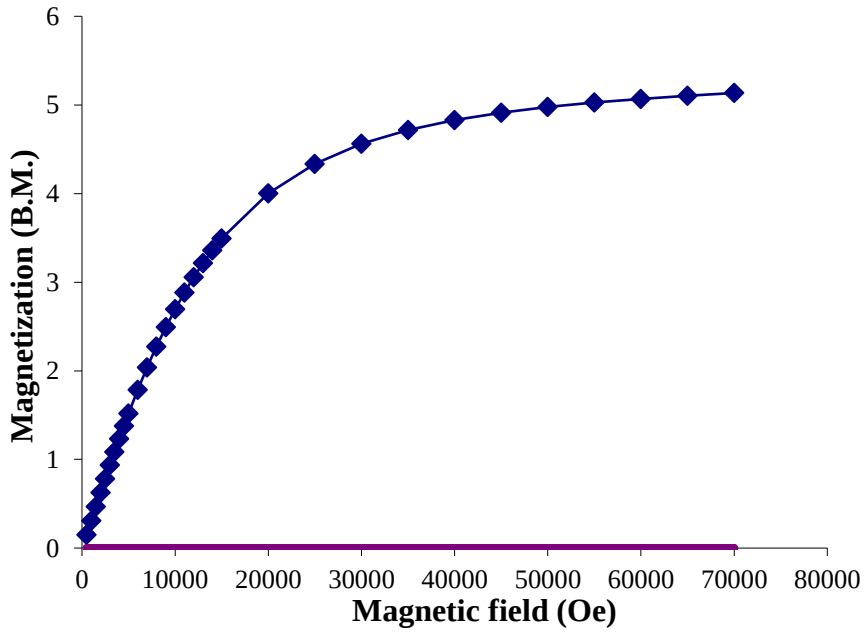

Figure 67: Magnetization data at 2 K for **28.** Solid lines are a guide for the eye.

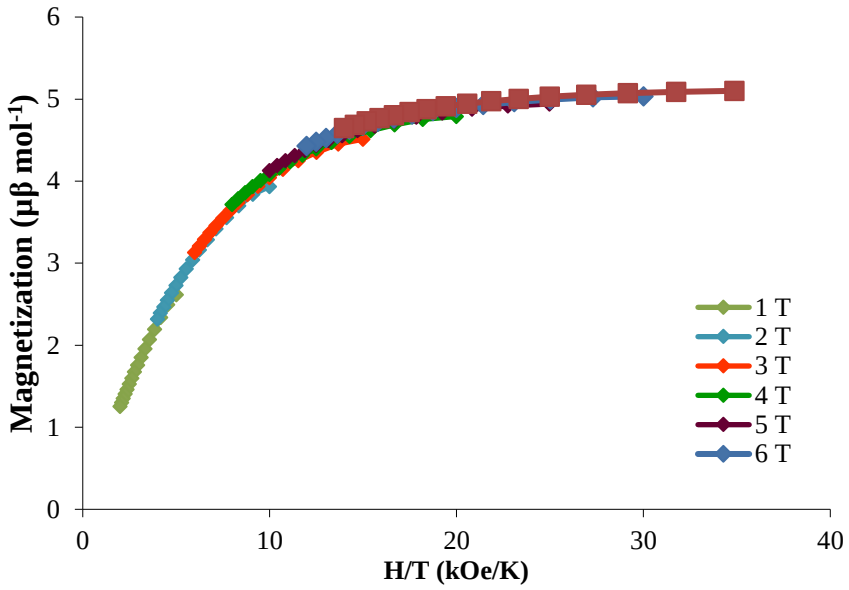

Figure 68: Reduced magnetization data for **28**. Solid lines are a guide for the eye.

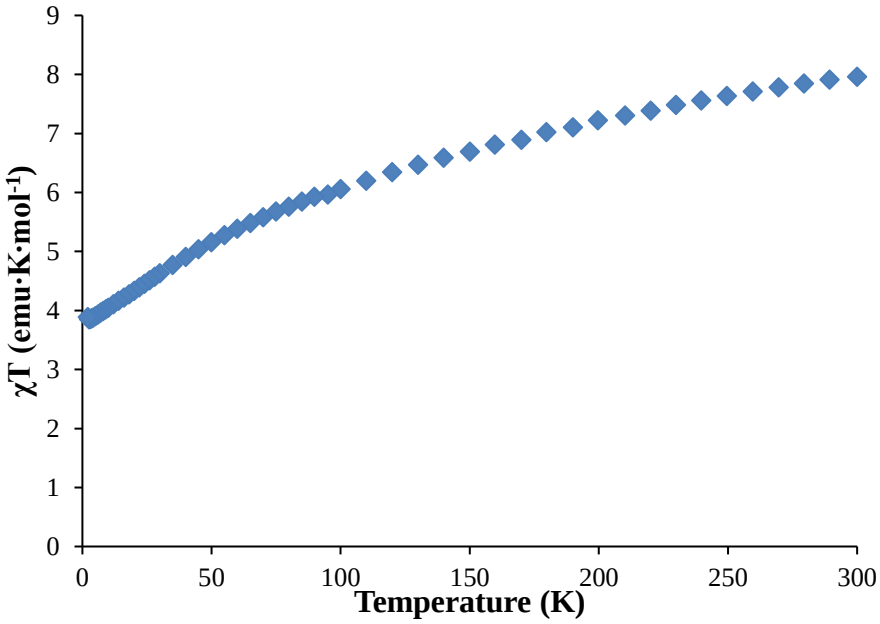

Figure 69: Variable-temperature DC susceptibility data plot for **29**.

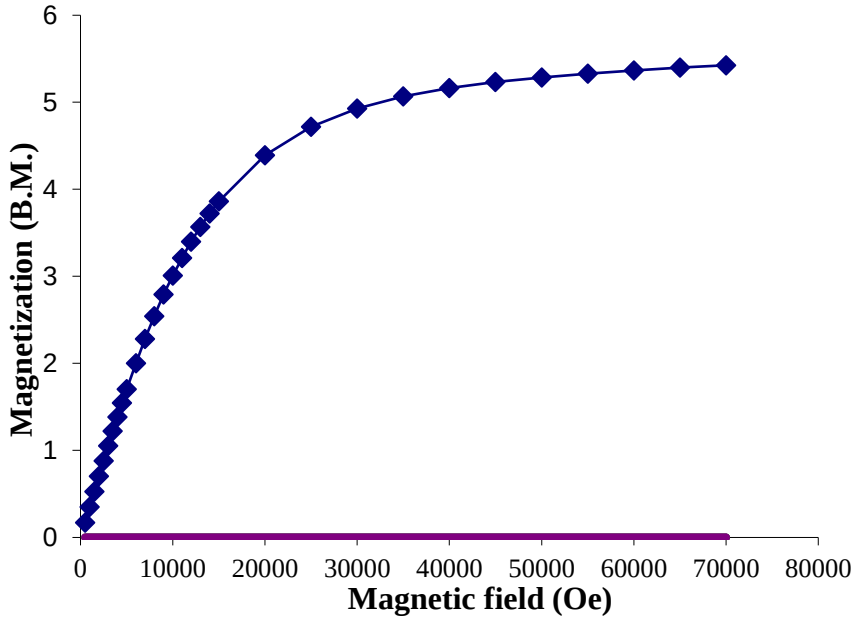

Figure 70: Magnetization data at 2 K for **29**. Solid lines are a guide for the eye.

exhibits a value of 5.42 μ_B (Figure 70), and the reduced magnetization plot has overlapping isofield lines, indicating no magnetic anisotropy (Figure 71); the AC measurements revealed no slow relaxation behavior as expected.

For compound **30**, $\chi_M T$ at 300 K is 5.44 emu·K·mol^{-1}, and, as the temperature is lowered, the value increases to a maximum of 7.47 emu·K·mol^{-1} at 7 K before decreasing to 6.01 emu·K·mol^{-1} at 2 K (Figure 72). The values are below the expected 12.38 emu·K·mol^{-1} for an S = 9/2 ground state with ferromagnetic coupling. The increase is indicative of ferromagnetic coupling between the Ni^{II} (S = 1) spin centers and Mo^{V} (S = 1/2) ions, which is consistent with the previously measured Ni^{II} and Re^{IV} analogue.[104]

Fitting the susceptibility with equation 21 led to a J value of approximately +4 cm^{-1}, indicating ferromagnetic coupling as expected, and the low magnitude is similar to the rhenium analogue. The 2 K magnetization data saturate at 9.48 μ_B, which is slightly higher than the expected value of nine unpaired electrons for an S = 9/2 ground state based on ferromagnetic coupling (Figure 73). The reduced magnetization data exhibit overlapping isofield lines, an indication of a lack of magnetic anisotropy (Figure 74), and, indeed, the AC measurements did not reveal slow relaxation behavior.

For compound **31**, the variable-temperature DC susceptibility data exhibit a $\chi_M T$ at 300 K of 8.57 emu·K·mol^{-1} which increases at lower temperatures, reaching a maximum of 9.78 emu·K·mol^{-1} at 7 K before decreasing to 7.66 emu·K·mol^{-1} at 2 K (Figure 75). The increase in $\chi_M T$ suggests ferromagnetic coupling between the Ni ions and tungsten ions, which is consistent with the previously measured Ni^{II} and Re^{IV} complex and the molybdenum analogue,[104] but does not reach the expected value of 12.38 emu·K·mol^{-1} for an S = 9/2 ground state. Attempts to model the coupling between the W^{V} and Ni^{II} ions using equation 21gave a J coupling of about +14 cm^{-1}; although the fitting is poor the J value is significantly larger compared to its molybdenum analogue, supporting the hypothesis that the 5d metals achieve better exchange coupling compared to the 4d ions due to greater orbital overlap. The 2 K magnetization exhibits a value of 10.88 μ_B, which is higher than the expected value of nine unpaired electrons for an S = 9/2 ground state (Figure 76). The reduced magnetization shows overlapping isofield lines, suggesting no magnetic anisotropy (Figure 77); the AC measurements did not reveal any sign of slow relaxation behavior.

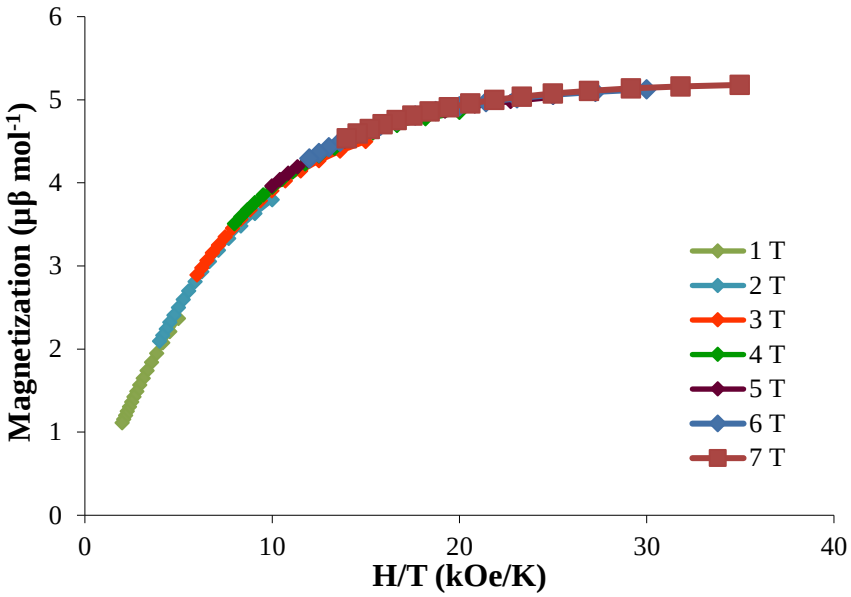

Figure 71: Reduced magnetization data for **29**. Solid lines are a guide for the eye.

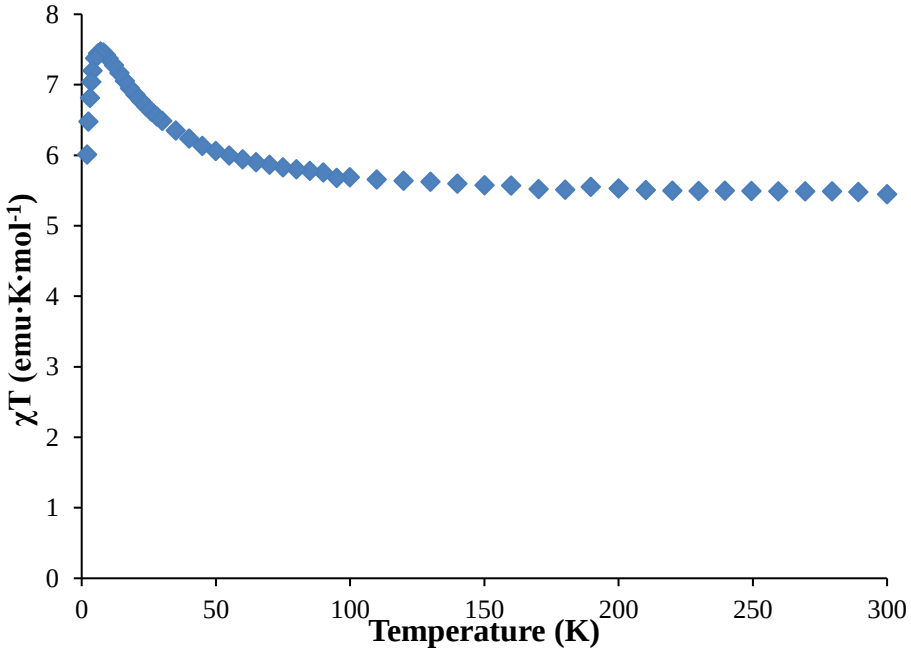

Figure 72: Variable-temperature DC susceptibility data for **30**.

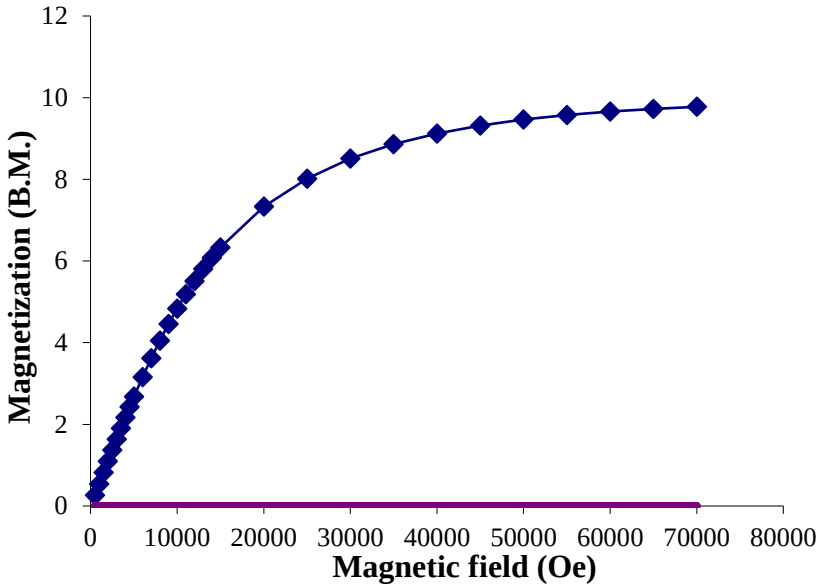

Figure 73: Magnetization data at 2 K for compound **30**. Solid lines are a guide for the eye.

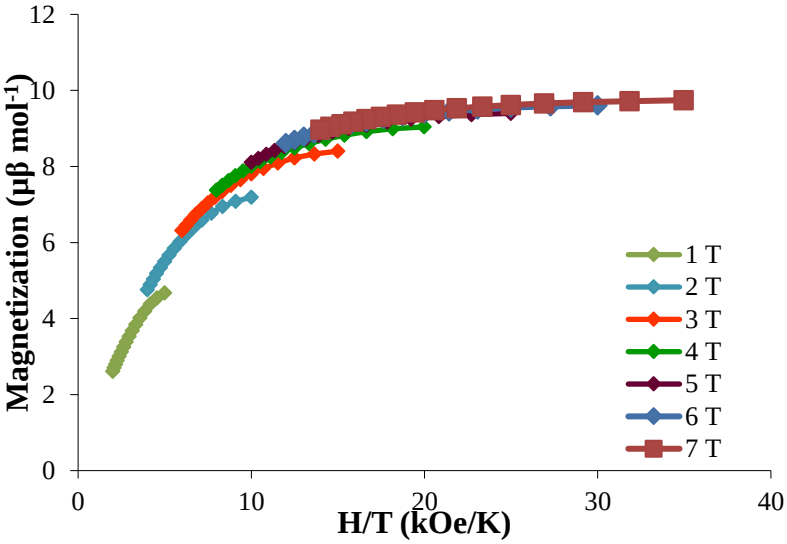

Figure 74: Reduced magnetization data for compound **30**. Solid lines are a guide for the eye.

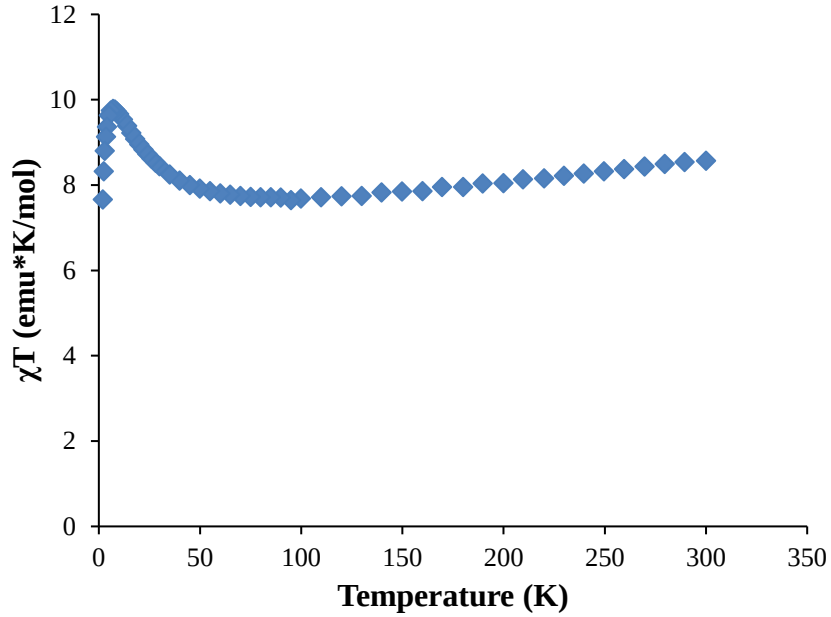

Figure 75: Variable-temperature dc or DC susceptibility data plot for **31**.

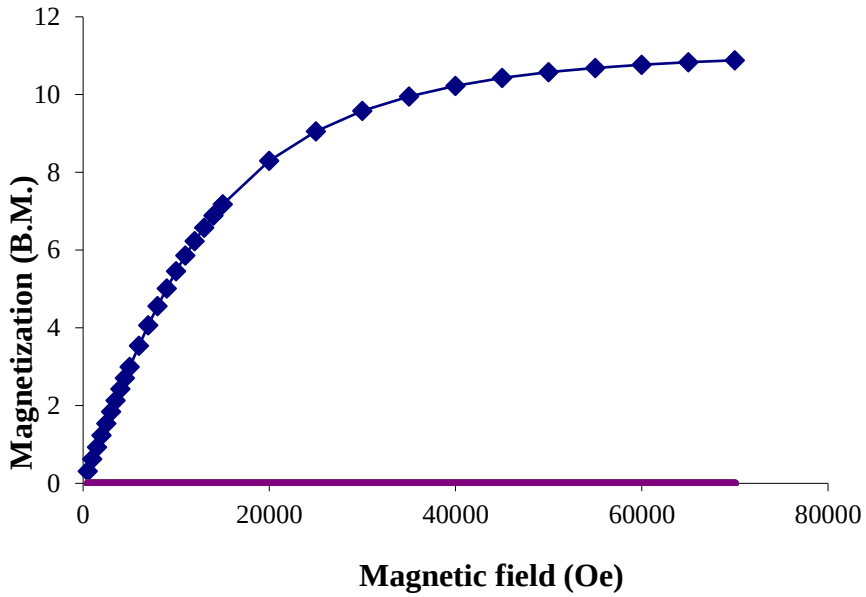

Figure 76: Magnetization data at 2 K for compound **31**. Solid lines are a guide for the eye.

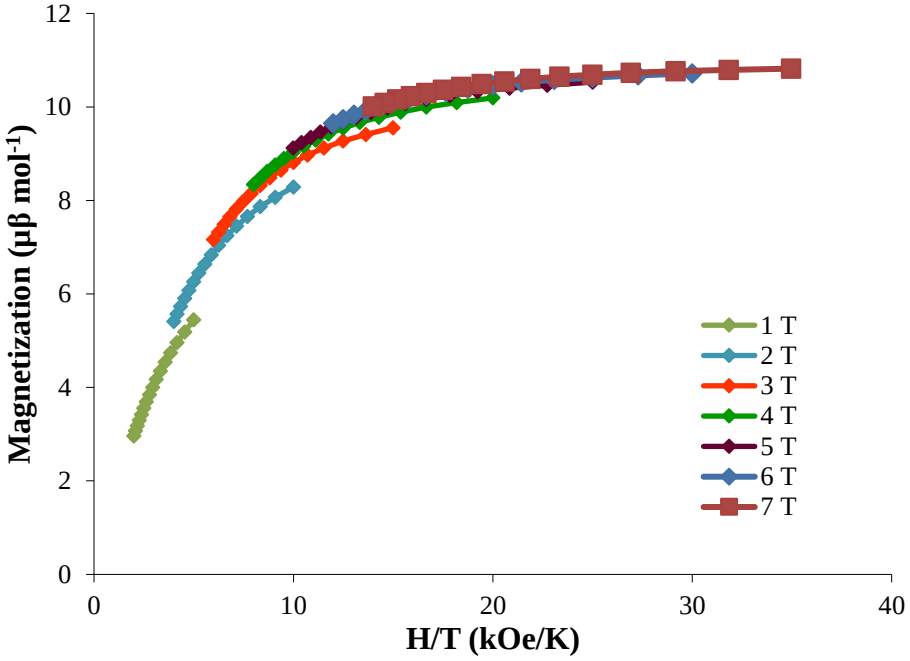

Figure 77: Reduced magnetization data for compound **31**. Solid lines are a guide for the eye.

Conclusions

The reactions of the $[M^{V}(CN)_8]^{3-}$ (Mo, W metal) anions with $[M^{II}(PY5Me_2)(CH_3CN)]^{2+}$ cations (M^{II} = Mn, Fe, Co, Ni, and Cu) yielded powder products in the cases of Mn, Fe, and Cu and crystals in the cases of Co and Ni, similar to the previous reactions with the heptacyanometallate(IV) anions. Single crystal X-ray data for Co and Ni revealed that the structures are the expected star-like complexes previously obtained with the $[M^{IV}(CN)_7]^{3-}$ anions, with four of the $[M^{II}(PY5Me_2)]^{2+}$ cations bound

through cyanide ligands to the octacyanometallate(V) anion. Infrared spectra of the products (powder and crystal) exhibit ν(CN) stretching vibrations consistent with polynuclear species that contain bridging cyanides between two metal centers. Magnetic measurements were performed on the Co and Ni complexes for both molybdenum and tungsten, and the variable-temperature DC susceptibilities indicate there is coupling between the 3d metal ion and the octacyanometallate(V) anion, in contrast to the complexes formed with the heptacyanomolydate(IV) or heptacyanotungstate(IV) anions, which consist of spin-independent centers with no magnetic coupling. For Co, the exchange coupling was difficult to model, but, qualitatively, the $\chi_M T$ susceptibility data exhibit a decrease as temperature is lowered, which results from spin-orbit coupling of the Co^{II} ions and possibly antiferromagnetic coupling between Co^{II} and Mo^{V}/W^{V}. In the case of Ni, there is ferromagnetic coupling between both Ni^{II} and Mo^{V}/W^{V}, with the J exchange constants calculated to be +4 cm^{-1} and +14 cm^{-1} for molybdenum and tungsten, respectively. The coupling constant for tungsten supports Mironov's hypothesis that 5d cyanometallates can achieve larger exchange coupling constants as a result of improved orbital overlap. None of the compounds, however, exhibited any slow relaxation behavior under an AC field. The compounds presented in this chapter are among the few known discrete complexes based on the octacyanomolybdate(V) or octacyanotungstate(V), which often form extended structures, and are also distinguished by the fact that they contain only one octacyanometallate anion.

CHAPTER V

TRIS(3,5-DIMETHYLPYRAZOYL)BORATE COMPOUNDS BASED ON NIOBIUM, MOLYBDENUM, AND TUNGSTEN METAL CENTERS

Introduction

Since Trofinmenko synthesized the first tris(1-pyrazoyl)borate complexes in 1966,[200] scorpionate compounds have been used in a wide variety applications, including for catalysis, C—H bond activation, metal extraction, and as a capping moiety to enforce discrete structures.[201] The ease of steric and electronic tuning of tris(1-pyrazoyl)borate ligands, and Tp* (Tp* = tris(3,5-dimethylpyrazoyl)borate), in particular, as an alternative to the Cp* ligand (Cp* = 1,2,3,4,5-pentamethylcyclopentadiene) has facilitated the isolation of numerous derivatives with different oxidation states and geometries for nearly all of the transition metals.[202] More recently, these ligands have been used as capping groups for designing small polynuclear complexes.

Recent work has focused on the Tp* ligand to enforce desired geometries in order to increase the anisotropy of magnetic systems.[203] Notably cyanometallates have been used in conjunction with Tp ligands because bridging cyanides offer predictable exchange interactions between metal spin centers and lend themselves to a variety of geometries, which enables a building block approach to be employed. A number of heteroleptic cyanide compounds have been prepared with the Tp* ligand, including the 3d transition metal complexes $Tp^*M(CN)_3$ (M = Ti^{III}, $V^{II/III}$, Cr^{III}, Mn^{III}, Fe^{III}, and Co^{III}) and $Tp^*M(CN)_2$ (M = Cr^{II}, Ni^{II}, Co^{II}),[203-204]. These species have been used as precursors for

assembling polynuclear structures with a variety of synthons; the list includes squares, cubes, pentagonal bipyramids, and chains.[204-211] An excellent review of the literature up to 2013 is provided by Ferko and Holmes.[203] One of the highlights of this work is that structures incorporating the $Tp^*Fe(CN)_3$ moiety exhibit slow relaxation above 1.8 K.[208-209, 211]

Previous work in the Dunbar group with the Tp* ligand focused on early 3d metal centers, namely Ti and V. The synthesis and characterization of $[Et_4N][Tp^*Ti^{III}(CN)_3]$ was reported and it was found that the compound exhibits significant van Vleck temperature independent magnetism (TIP).[212] A previous group member conducted magnetic studies on $[A][Tp^*V^{II}X_3]$ (A = alkylammonium cation, X = halide) to explore the effect of small distortions on the trigonal geometry as well as the heavy-halide effect. More recently, our focus turned to 4d and 5d cyanometallates in order to explore anisotropic coupling and it was postulated that $Tp^*M(CN)_3$ ($M = Nb^{IV}$, Mo^{III}, W^{III}) would be excellent candidates for study.[100]

While there has been ample research on the subject of 3d Tp* compounds, the 4d and 5d metals remain much less studied. Millar and Lincoln reported Tp^*MCl_3, (M = Mo, W) although no synthetic details were provided and attempts to reproduce their work were unsuccessful;[213] Young *et al.*, established a synthetic procedure for Tp^*WCl_3 without characterizing the compound.[214] Additionally, Tp^*NbCl_3 was reported by Mashima which was said to be identified from a crystal structure, but no deposited structure was

reported.[215] Our previous work with $[(triphos)Re^{II}(CN)_3]^-$, an anion with the same geometry as the $Tp^*M^{III}(CN)_3$ molecules, led to interesting results and several SMMs.[216-218] In this vein, the synthesis and characterization of corresponding Tp* compounds for niobium, molybdenum, and tungsten was explored in this dissertation research.

Experimental

All reactions were performed in the drybox or on the Schlenk-line under an inert atmosphere unless otherwise stated. The solvent CH_3CN (Sigma Aldrich) was pre-dried over 3Å molecular sieves and then distilled over 3Å sieves under nitrogen; Et_2O was passed through an activated alumina column (MBraun solvent system); CH_3OH was pre-dried with 3Å molecular sieves and then distilled over Mg activated by I_2 under nitrogen and anhydrous THF (Sigma Aldrich) was used as received. All solvents were stored over molecular sieves in the drybox. The $SOCl_2$ (Sigma Aldrich) was used as received. Crown ethers 18-crown-6 (Sigma Aldrich) and (2.2.2.)-cryptand (Sigma Aldrich) were dried under vacuum overnight and used as received. The starting materials $MoCl_3(THF)_3$,[219] $NbCl_4(DME)$,[220] Tp^*WCl_3,[214] and KTp*[221] were prepared according to the literature procedures.

Synthesis

$[K(18\text{-crown-}6)]_2[Mo^{III}Cl_5(pz)]$ (34)

A 100 mL Schlenk flask was charged with 0.506 g (1.208 mmol) of $MoCl_3(THF)_3$, 0.407 (1.210 mmol) of KTp*, and 0.676 g (2.558 mmol) of 18-crown-6 ether. Addition of 40 mL of CH_3CN with stirring resulted in a dark orange solution, which was stirred for two days and then reduced to dryness under vacuum. The solid was redissolved in a minimal volume of CH_3CN to give an orange-brown solution which was transferred to thin vials and stored in a jar with Et_2O for slow vapor diffusion; X-ray quality red crystals were obtained within one week. The dark red crystals were collected by filtration on a frit and washed with Et_2O. Colorless crystals were also observed, which were determined to be $[HB(pz)]_2$-μ-$(pz)_2$. Mass of product: 0.1567 g, yield: 12.3 %.

[K(18-crown-6)][Tp*$Mo^{III}Cl_3$] (35)

A vial was charged with 0.526 g (1.563 mmol) of KTp*, 0.6550 g (1.565 mmol) of $MoCl_3(THF)_3$, and 0.454 g (1.719 mmol) of 18-crown-6 ether. Addition of 10 mL of THF led to the formation of a red-brown suspension that was stirred for one week and then filtered to give a light red precipitate (mass: 0.856 g) and a dark red filtrate. An aliquot was removed and placed in a thin vial for slow vapor diffusion with Et_2O; X-ray quality crystals produced in five days. The remainder of the solution was set up for crystallization in a similar manner. Mass of product 0.1550 g, yield: 12.4%.

[K(2.2.2)cryptand][Tp*$Mo^{III}Cl_3$] (36)

A vial was charged with 0.249 g (0.739 mmol) of KTp*, 0.303 g (0.7226 mmol) of $MoCl_3(THF)_3$, and 0.271 g (0.721 mmol) of (2.2.2)cryptand; addition of 10 mL of

CH_3CN produced a red solution that was stirred for one week and then filtered through a fine frit to give a dark red filtrate. The filtrate was transferred to large vials which were placed in a jar with Et_2O for slow vapor diffusion to give X-ray quality crystals. Mass of product 0.552 g, yield: 78.1%. Elemental analysis: Theoretical C: 41.27, H: 5.85, N: 11.62; actual C: 37.24, H: 5.07, N: 13.13.

Tp*$W^{IV}Cl_3$ (37)

A 50 mL Erlenmeyer flask was charged with 2.02 g (2.9 mmol) of $(Et_4N)[Tp^*W(CO)_3]$ and dissolved in about 10 mL of CH_2Cl_2. Approximately 0.5 mL of $SOCl_2$ was then added to the yellow solution to give a dark green-brown solution which was heated to 50 °C for five hours before being filtered through a fine frit. The resulting dark green filtrate was treated with 25 mL of methanol to yield a green precipitate. Green crystals suitable for X-ray diffraction were grown by recrystallizing the powder from CH_2Cl_2 and Et_2O using slow vapor diffusion.

[Tp*$Nb^{IV}Cl_2(OCH_3)$] (38)

A 50 mL Schlenk flask was charged with 0.509 g (1.344 mmol) of $NbCl_4(THF)_2$ and 0.453 g (1.35 mmol) of KTp*; addition of 40 mL of CH_3CN and 2 mL of CH_3OH with stirring resulted in a dark green solution which was stirred for an additional 48 hours and then dried under vacuum, pumped into the drybox, and dissolved in a minimal volume of CH_3CN. The reaction solution was filtered through Celite® to give a yellow-brown filtrate and a white precipitate. The filtrate was transferred to thin vials which were stored

in a jar with Et_2O for slow vapor diffusion. X-ray quality crystals were obtained after 2 weeks. The product was collected via filtration on a medium frit and washed with Et_2O. Mass of product 0.1550 g, yield: 23.4 %.

X-ray Crystallography

Compounds **34** (red crystal), **35** (yellow crystal), and **37** (green crystal) were mounted on a Nylon loop using Paratone® oil and placed in a N_2 cold stream at 110 K. The data were collected on a Bruker APEX II diffractometer (MoKα radiation λ = 0.71073 Å) equipped with a CCD detector. The data sets were recorded as three *ω*-scans and integrated using the Bruker APEXII software package. A yellow crystal of **36** and was mounted using Paratone® oil on a cryo-loop and placed in a N_2 cold stream at 120 K. The data were collected on a Bruker D8 Quest Eco diffractometer (MoKα radiation λ = 0.71073 Ǻ) equipped with a Photon50 CMOS detector. The data sets were recorded as four *ω*-scans and integrated using the Bruker APEX3 software package. The data were collected on a Bruker APEX II diffractometer (MoKα radiation λ = 0.71073 Ǻ) equipped with a CCD detector. The data sets were recorded as four *ω*-scans and integrated using the Bruker APEXII software package. A colorless crystal of **38** was mounted using Paratone® oil on a cryo-loop and placed in a N_2 cold stream at 110 K. The data were collected on a Bruker D8 Quest Eco diffractometer (MoKα radiation λ = 0.71073 Ǻ) equipped with a Photon50 CMOS detector. For all data collections, the multi-scan absorption correction was performed within the Bruker APEXII software using SADABS (v2014/5) or within

the Bruker APEX3 software using SADABS (v2015/10).[163-164] Solution and refinement of the crystal structures were carried out using SHELXT and OLEX2 or shelXle (a graphical interface for the SHELX suite of programs), respectively.[165-166, 185] Structure solution by direct methods resolved positions of all heavy atoms and most of the lighter atoms. The remaining non-hydrogen atoms were located by alternating cycles of least-squares refinements and difference Fourier maps. Hydrogen atoms were placed at calculated positions. The final refinements were performed with anisotropic thermal parameters for all non-hydrogen atoms. A summary of pertinent information relating to unit cell parameters, data collection, and refinement is provided in Table 24.

Physical Methods

IR spectra were recorded on a Nicolet Nexus 470 FT-IR E.S.P spectrophotometer between KBr plates on powder samples suspended in a ®Nujol mull unless otherwise noted. Electrochemical data were collected using a H-CH Instruments analyzer in dry solvents. The working electrode was a BAS Pt disk electrode, the reference electrode was Ag/AgCl, and the counter electrode was a Pt wire. Cyclic voltammetric measurements were performed at ambient temperatures in specified dry solvents with approximately 0.1 M tetra-*n*-butylammonium hexafluorophosphate ([*n*-Bu_4N][PF_6]) as the supporting electrolyte. The $E_{1/2}$ values were referenced to the Ag/AgCl electrode without correction for junction potentials [$E_{1/2} = (E_{p,a} + E_{p,c})/2$]. Ferrocene was added at the end of the experiment as an additional reference for the $FeCp_2$/[$FeCp_2$]$^+$ couple. Elemental analysis

Table 24: Crystallographic data and experimental details for compounds **34** – **38**.

Compound	**34**	**35**	**36**
Molecular Weight	528.12	802.90	956.12
Temperature (K)	110	110	110
Crystal System	Triclinic	Trigonal	Trigonal
Space Group	P-1	R3m	R3
a (Å)	12.6549(9)	14.067(3)	12.0573(3)
b (Å)	12.7716(9)	14.067(3)	12.0573(3)
c (Å)	15.4243(10)	18.472(3)	26.1955(8)
α (°)	96.382(3)	90	90
β (°)	92.096(3)	90	90
γ (°)	96.424(3)	120	120
V (Å^3)	2458.9(3)	3165.4(13)	3298.1(2)
Z	2	3	3
Color	Red	Yellow	Yellow
ρcalc (g/cm^3)	1.428	1.264	1.444
μ (mm)	0.763	0.639	0.628
F(000)	1094.0	1245.0	1497.0
Crystal Size (mm)	0.511 x 0.631 x 0.884	0.520 x 0.522 x 0.558	0.052 x 0.102 x 0.137
Radiation	MoKα (λ = 0.71073)	MoKα (λ = 0.71073)	MoKα (λ = 0.71073)
Index Range	-16≤h≤16 -16≤k≤14 -13≤l≤20	-18≤h≤18 -18≤k≤18 -24≤l≤24	-15≤h≤15 -15≤k≤15 -33≤l≤33
θ range (°)	3.944 – 55.464	5.792 – 55.128	4.2 – 55.056
Reflections collected	12639	11943	38131
Unique reflections	10195	1819	3404
Parameters/restraints	518, 0	90, 1	174, 1
R_1, wR_2 [$I > 2\sigma(I)$]	0.0546, 0.1235	0.0319, 0.0990	0.0205, 0.0525
R_1, wR_2 (all data)	0.0863, 0.1415	0.0319, 0.0990	0.0219, 0.0536
GooF (F^2)	1.038	0.959	0.990
Largest diff. peak, hole, (e Å^{-3})	1.3, -1.0	1.4, -0.3	0.4, -0.3

[a]$R = \Sigma \, ||F_o| - |F_c|| / \Sigma |F_o|$. [b]$wR = \{\Sigma \, [w(F_o^2 - F_c^2)^2] / \Sigma \, [w(F_o^2)]^2\}^{1/2}$. [c]Goodness-of-fit = $\{\Sigma \, [w(F_o^2 - F_c^2)^2]/(n-p)\}^{1/2}$, where *n* is the number of reflections and *p* is the total number of parameters refined.

Table 24 Continued

Compound	**37**	**38**
Molecular Weight	588.39	492.04
Temperature (K)	110	110
Crystal System	Monoclinic	Orthorhombic
Space Group	$P2_1/m$	Pbca
a (Å)	8.046(12)	15.4102(18)
b (Å)	13.96(2)	16.2618(19)
c (Å)	9.047(14)	16.777(2)
α (°)	90	90
β (°)	99.946(16)	90
γ (°)	90	90
V ($Å^3$)	1001(3)	4204.3(9)
Z	2	8
Color	Green	Colorless
ρcalc (g/cm^3)	1.949	1.555
μ (mm)	6.183	0.845
F(000)	568.0	2008.0
Crystal Size (mm)	0.052 x 0.102 x 0.137	0.134 x 0.222 x 0.303
Radiation	MoKα (λ = 0.71073)	MoKα (λ = 0.71073)
Index Range	$-9 \leq h \leq 9$	$-20 \leq h \leq 20$
	$-16 \leq k \leq 16$	$-21 \leq k \leq 21$
	$-10 \leq l \leq 10$	$-21 \leq l \leq 21$
θ range (°)	4.572 – 50.38	4.376 – 55.33
Reflections collected	8569	62442
Unique reflections	1868	4890
Parameters/restraints	140, 0	251, 0
R_1, wR_2 [$I > 2\sigma(I)$]	0.0405, 0.0936	0.0419, 0.0978
R_1, wR_2 (all data)	0.0489, 0.0971	0.0547, 0.1047
GooF (F^2)	1.085	1.087
Largest diff. peak, hole, (e $Å^{-3}$)	1.2, -1.9	1.4, -0.7

[a]$R = \Sigma \, ||F_o| - |F_c|| / \Sigma |F_o|$. [b]$wR = \{\Sigma \, [w(F_o^2 - F_c^2)^2] / \Sigma \, [w(F_o^2)]^2\}^{1/2}$. [c]Goodness-of-fit = $\{\Sigma \, [w(F_o^2 - F_c^2)^2]/(n-p)\}^{1/2}$, where *n* is the number of reflections and *p* is the total number of parameters refined.

was performed by Atlantic Microlabs, Inc., Norcross, GA. Magnetic measurements were performed on a Quantum Design MPMS-XL SQUID magnetometer equipped with a 7 T superconducting magnet over the temperature range 1.8 to 300 K; the diamagnetic contribution of the plastic bag used as a sample holder was subtracted from the raw data and core diamagnetism of the sample was corrected for using Pascal's constants.[168]

Results and Discussion

Syntheses

The compounds $[Tp^*Mo^{III}Cl_3]^-$ and $Tp^*W^{IV}Cl_3$ were previously reported but experimental details were lacking.[213] Attempts to replicate the reported conditions were unsuccessful, therefore an alternative route was developed. The reaction of $MoCl_3(THF)_3$ with KTp* was performed as in the literature report, but an encapsulating crown ether was added with the goal of more easily obtaining crystalline product. The use of 18-crown-6 ligand resulted in a red powder, which after recrystallization, led to a mixture of red and yellow crystals; the red crystals were found to be compound $[K(18\text{-crown-}6)]_2[Mo^{III}Cl_5(pz)]$ (**34**) and the yellow crystals are $[K(18\text{-crown-}6)][Tp^*Mo^{III}Cl_3]$ (**35**). Additionally, colorless crystals were obtained from the recrystallization **34**, which were determined to be $[HB(pz)]_2\text{-}\mu\text{-}(pz)_2$, which explains the formation of the pyrazoyl ligand in **34**. This by-product results from cleavage of the Tp* ligand, a previously observed reaction.[212] Switching to (2.2.2)-cryptand as the encapsulating crown ether results in better yields and less decomposition with the formation of $[K(2.2.2)crptand][Tp^*Mo^{III}Cl_3]$ (**35**),

which form as large yellow crystals. In general, the use of crown ethers leads to better crystalline product that can be easily separated, improving the synthesis of the starting material.

The compound $Tp^*W^{IV}Cl_3$ (**35**) was prepared according to the literature report,[214] although the synthesis also was slightly modified: a larger volume of $SOCl_2$ was used and the reaction was heated for a longer period of time. The product was isolated as a green color powder and green crystals that were suitable for X-ray diffraction were obtained upon recrystallization from CH_2Cl_2 and Et_2O. Compound **36**, $[Tp^*Nb^{IV}Cl_2(OCH_3)]$, was isolated by accident, as the reaction of $NbCl_4(THF)_2$ and KTp^* in CH_3CN was contaminated with CH_3OH which led to partial substitution of the chloride ligand for methoxide. Colorless crystals were obtained in the workup by slow vapor diffusion with Et_2O.

Given that the ultimate goal was to obtain cyanometallate complexes with the Tp* ligand, additional reactions were performed with both compounds **35** and **36** as starting materials. The parameters used in the reactions of $[Tp^*MoCl_3]^-$ with cyanide were varied by using different cyanide reagents (Bu_4N, Et_4N, Na, and K), solvents (THF, CH_3CN, and DMF), and temperatures (room temperature and 60 °C). In all cases a red solution was obtained but no crystals could be obtained. Additionally, the reaction of $[Tp^*MoCl_3]^-$ with $TlPF_6$ and Bu_4NCN (with the goal being to use the Tl^+ ion to abstract the chloride ligand) yielded a tan powder which could not be definitively identified due to lack of crystals.

Single Crystal X-ray Diffraction Studies

Compound **34** crystallizes as red blocks, and the structure consists of the salt $[K(18\text{-crown-}6)]_2[Mo^{III}Cl_5(pz)]$ in the P-1 space group. The $[Mo^{III}Cl_5(pz)]^-$ anion adopts a slightly distorted octahedral geometry, with five chlorides and one pyrazoyl ligand (Figure 78). This outcome results from cleavage of the Tp* ligand, which has been previously observed and confirmed in this case by the isolation of colorless crystals consisting of $[HB(pz)]_2\text{-}\mu\text{-}(pz)_2$ obtained as a by-product. The Mo—Cl bond distances vary between 2.4442(12) to 2.4563(10) Å, the N_{pz}—Mo bond distance is 2.1936(40) Å, which are consistent with typical Mo^{III}—Cl and Mo^{III}—N_{pz} bonds lengths.[213] The K—Mo bond distances are 4.00 and 4.02 Å, which is slightly longer than the Mo—K bond in [K(18-crown-6)][$MoCl_3$Tp*], which is 3.910(22) Å. The *cis* bond angles around the Mo center vary from 84.743(85)° to 93.491(13)°, while the *trans* bond angles are 177.283(35)°, 179.249(40)°, and 175.030(104)° which indicates distortion from an ideal octahedral geometry. Relevant bond distances and angles are listed in Table 25.

The compound [K(18-crown-6)][Tp*$Mo^{III}Cl_3$] crystallizes as large yellow blocks in the R3m space group, with C_3 symmetry as a result of the [K(18-crown-6)] cation bonding below the chlorides (Figure 79). The compound has Mo—Cl bond distances of 2.427(12) Å, which agrees with the previously reported Mo—Cl bond distance of 2.43 Å.[213] The pyrazoyl N—Mo bond distances are 2.178(3) Å, slightly shorter compared the previously reported 2.19 Å value. The *cis* bond angles around the molybdenum center vary

Table 25: Select bond distances and bond angles for compound **34**.

Bond Distance (Å) or Angle (°)	$[K(18\text{-crown-6})]_2[Mo^{III}Cl_5(pz)]$
Mo—Cl_{1ax}	2.4494(12)
Mo—Cl_{2eq}	2.4532(12)
Mo—Cl_{3eq}	2.4458(10)
Mo—Cl_{4eq}	2.4563(10)
Mo—Cl_{5eq}	2.4442(12)
Mo—N_{pz}	2.1936(40)
Mo—K_1	3.9963(12)
Mo—K_2	4.0241(12)
Cl_{1ax}—Mo—N_{pz}	175.030(104)
Cl_{1ax}—Mo—Cl_2	91.072(37)
Cl_{1ax}—Mo—Cl_3	91.379(36)
Cl_{1ax}—Mo—Cl_4	91.301(35)
Cl_{1ax}—Mo—Cl_5	89.450(37)
N_{pz}—Mo—Cl_{2eq}	85.951(103)
N_{pz}—Mo—Cl_{3eq}	92.557(85)
N_{pz}—Mo—Cl_{4eq}	84.743(85)
N_{pz}—Mo—Cl_{5eq}	93.490(103)
Cl_{2eq}—Mo—Cl_{3eq}	89.207(35)
Cl_{2eq}—Mo—Cl_{4eq}	90.294(35)
Cl_{2eq}—Mo—Cl_{5eq}	179.249(40)
Cl_{3eq}—Mo—Cl_{4eq}	177.283(35)
Cl_{3eq}—Mo—Cl_{5eq}	91.321(35)
Cl_{4eq}—Mo—Cl_{5eq}	89.155(35)

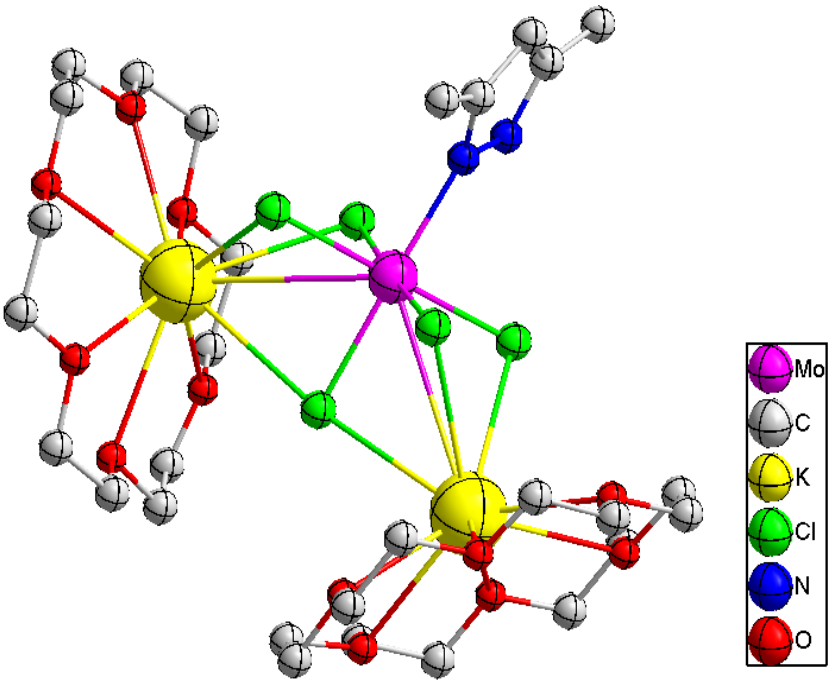

Figure 78: Molecular structure of **34**. Hydrogen atoms are omitted for the sake of clarity.

between 86.032(13)° to 92.227(33)°, and the *trans* bond angles are between 175.647(11)° to 175.682(11)°, indications that the Tp* ligand distorts the molecule slightly from octahedral geometry. Relevant bond distances and angles are reported in Table 26.

The [K(2.2.2)crptand][Tp*$Mo^{III}Cl_3$] salt also crystallizes as yellow blocks but in the space group R3. The Mo—Cl bond distances are 2.4309(9) Å, only slightly longer than the [K(18-crown-6)] congener and close to that of the reported Et_4N^+ salt.[213] The

pyrazoyl N—Mo bond distances are 2.1937(26) Å, which also agrees with the previously reported Et_4N^+ compound and the 18-crown-6 analogue. The *cis* bond angles about the molybdenum center vary from 84.735(83)° to 93.080(64)°, and the *trans* bond angles are between 175.473(60)° and 175.510(65)°, which are slightly larger distortions as compared to the 18-crown-6 analogue. Relevant bond distances and angles are compiled in Table 27, and the molecular structure is shown in Figure 80.

In contrast, the $Tp^*W^{IV}Cl_3$ compound crystallizes as green blocks in space group $P2_1/m$, and the asymmetric unit contains one molecule (Figure 81). The W—Cl bond distances are 2.2877(22) and 2.3127(26) Å, which are shorter than those of the $[Tp^*Mo^{III}Cl_3]^-$ congener, a difference that can be ascribed to the higher oxidation state. The pyrazoyl W—N bond distances are 2.1778(24) and 2.1775(20) Å, in agreement with the previous compounds. The *cis* bond angles are in the range 85.309(42)° - 95.213(31)°, and the *trans* angles are between 173.161(43)° and 173.740(58)°, which constitute slightly larger distortions as compared to the $[Tp^*Mo^{III}Cl_3]^-$ analogue. Relevant bond distances and angles are reported in Table 28.

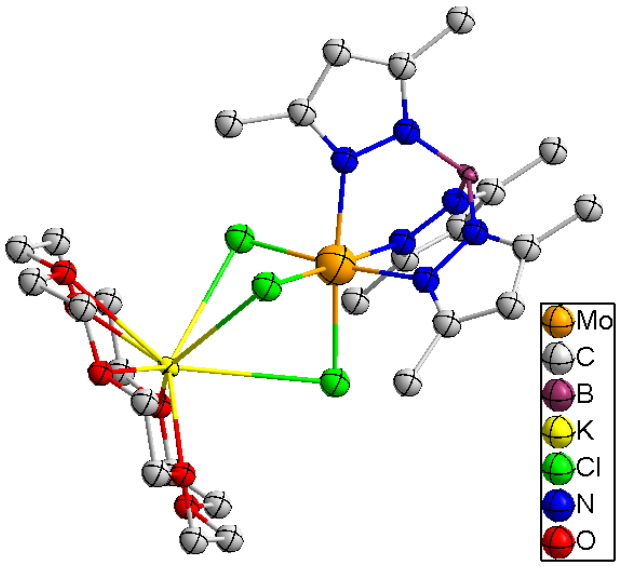

Figure 79: Molecular structure of **35**. Hydrogen atoms are omitted for the sake of clarity.

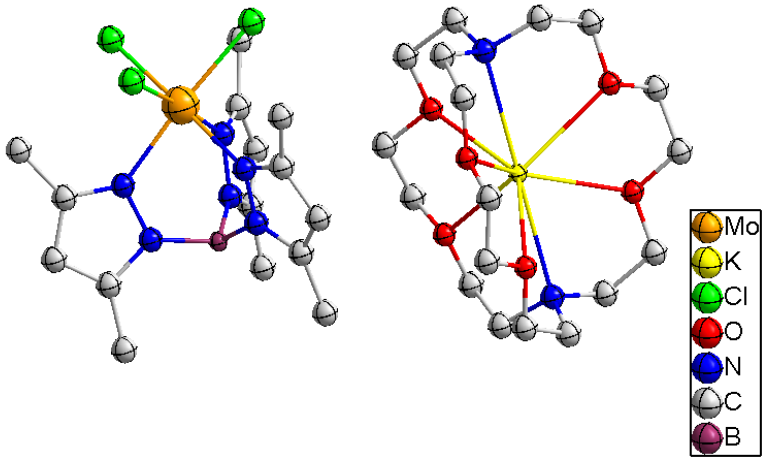

Figure 80: Molecular structure of **36**. Hydrogen atoms are omitted for the sake of clarity.

Table 26: Select bond distances and bond angles for compound **35**.

Bond Distance (Å) or Angle (°)	[K(18-crown-6)][Tp*$Mo^{III}Cl_3$]
Mo—Cl	2.427(12)
Mo—N	2.178(3)
Mo—K	3.910(22)
N_1—Mo—Cl_1	90.778(108)
N_1—Mo—Cl_2	90.778(75)
N_1—Mo—Cl_3	175.682(108)
N_2—Mo—Cl_1	90.751(109)
N_2—Mo—Cl_2	175.682(75)
N_2—Mo—Cl_3	90.805(109)
N_3—Mo—Cl_1	175.647(109)
N_3—Mo—Cl_2	90.828(75)
N_3—Mo—Cl_3	90.801(108)
N_1—Mo—N_2	86.032(131)
N_1—Mo—N_3	86.055(142)
N_2—Mo—N_3	86.055(131)
Cl_1—Mo—Cl_2	92.203(33)
Cl_1—Mo—Cl_3	92.203(35)
Cl_2—Mo—Cl_3	92.227(33)

Table 27: Select bond distances and bond angles for compound **36**.

Bond Distance (Å) or Angle (°)	[K(2.2.2-cryptand)][Tp*Mo^{III}Cl$_3$]
Mo—Cl	2.4309(9)
Mo—N	2.1937(26)
N_1—Mo—Cl_1	93.038(57)
N_1—Mo—Cl_2	175.510(65)
N_1—Mo—Cl_3	91.119(60)
N_2—Mo—Cl_1	91.126(57)
N_2—Mo—Cl_2	93.080(64)
N_2—Mo—Cl_3	175.473(60)
N_3—Mo—Cl_1	175.480(57)
N_3—Mo—Cl_2	91.159(65)
N_3—Mo—Cl_3	93.069(60)
N_1—Mo—N_2	84.735(83)
N_1—Mo—N_3	84.742(83)
N_2—Mo—N_3	84.757(80)
Cl_1—Mo—Cl_2	90.924(23)
Cl_1—Mo—Cl_3	90.931(23)
Cl_2—Mo—Cl_3	90.908(22)

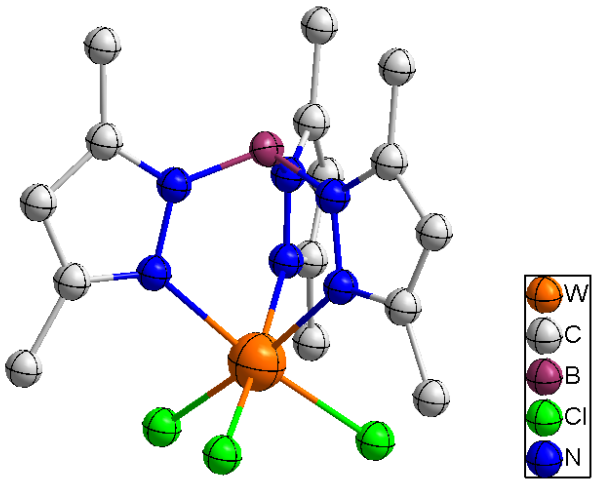

Figure 81: Molecular structure of **37**. Hydrogen atoms omitted for the sake of clarity.

Table 28: Select bond distances and bond angles for compound **37**.

Bond Distance (Å) or Angle (°)	Tp*$W^{IV}Cl_3$
W—Cl_1	2.3127(26)
W—Cl_2	2.2877(22)
W—N_1	2.1778(24)
W—N_2	2.1775(20)
N_1—W—Cl_1	90.104(42)
N_1—W—Cl_2	90.054(41)
N_1—W—Cl_3	173.161(43)
N_2—W—Cl_1	90.104(42)
N_2—W—Cl_2	173.161(43)
N_2—W—Cl_3	90.054(41)
N_3—W—Cl_1	90.35(4)
N_3—W—Cl_2	90.35(4)
N_3—W—Cl_3	173.740(58)
N_1—W—N_2	84.284(34)
N_1—W—N_3	85.309(42)
N_2—W—N_3	85.309(42)
Cl_1—W—Cl_2	95.213(31)
Cl_1—W—Cl_3	93.867(41)
Cl_2—W—Cl_3	93.867(41)

Finally, [Tp*$Nb^{IV}Cl_2(OCH_3)$] crystallizes in the space group Pbca as colorless blocks. The Nb—Cl bond distances are 2.4170(3) and 2.40(3) Å and the Nb—OCH_3 bond distance is 1.8461(2) Å which are similar to previously reported compounds.[215] The *cis* bond angles around the Nb center are between 85.965(4) to 99.821(4)° and the trans bond angles are 162.017(5)°, 168.711(4)°, and 173.753(4)°. The geometry is slightly more distorted as compared to the molybdenum analogue (Figure 82). Select bond distances and angles are reported in Table 29.

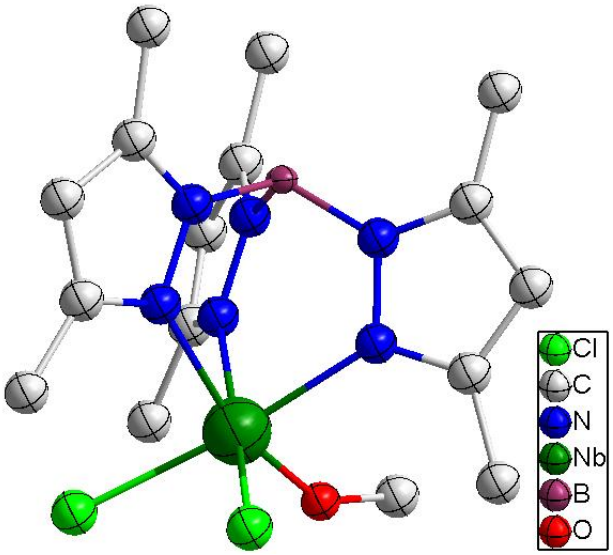

Figure 82: Molecular structure of **38**. Hydrogen atoms are omitted for the sake of clarity.

Electrochemical Studies

Cyclic voltammetry measurements were performed on compound **35** to determine accessible oxidation states. The first measurement was performed in CH_3CN in which the compound undergoes a reversible oxidation at $E_{1/2}$ = +0.48 V (Figure 83) which is similar to the reported $Mo^{III/IV}$ oxidation couple of +0.49 V (vs Saturated Calomel Electrode, SCE); the $Mo^{IV/V}$ oxidation couple reported by Millar to occur at +1.55 V vs. SCE was

also observed.[213] No $Mo^{III/II}$ reduction was observed, however. Performing the experiment in THF to determine if the reduction was accessible resulted in the previously mentioned $Mo^{III/IV}$ oxidation couple at +0.47 V vs Ag/AgCl, but no reduction couple was observed up to -2.4 V (Figure 84).

Table 29: Select bond distances and bond angles for compound **38**.

Bond Distance (Å) or Angle (°)	[Tp*$Nb^{IV}Cl_2(OCH_3)$]
Nb—Cl_1	2.4170(3)
Nb—Cl_2	2.4052(3)
Nb—O	1.8461(2)
Nb—N_1	2.2394(3)
Nb—N_2	2.2078(3)
Nb—N_3	2.2143(3)
N_1—Nb—Cl_1	92.031(3)
N_1—Nb—Cl_2	89.108(3)
N_1—Nb—O	162.017(5)
N_2—Nb—Cl_1	173.753(4)
N_2—Nb—Cl_2	90.168(3)
N_2—Nb—O	86.159(4)
N_3—Nb—Cl_1	92.935(3)
N_3—Nb—Cl_2	168.711(4)
N_3—Nb—O	85.965(4)
N_1—Nb—N_2	81.732(3)
N_1—Nb—N_3	79.925(3)
N_2—Nb—N_3	85.643(3)
Cl_1—Nb—Cl_2	90.101(3)
Cl_1—Nb—O	99.821(4)
Cl_2—Nb—O	104.235(4)

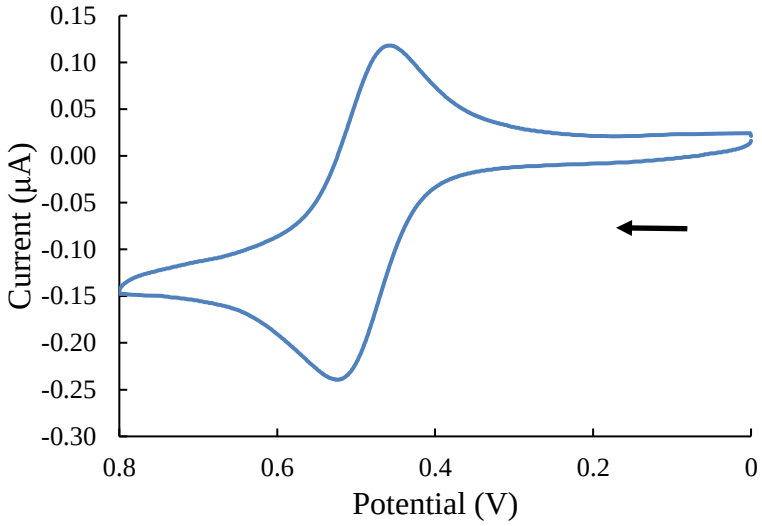

Figure 83: Cyclic voltammogram of compound **35** in CH_3CN with 0.1 M Bu_4NPF_6 as the supporting electrolyte. Scan rate was 0.10 V/s starting in the positive direction; the $E_{1/2}$ was reported to be +0.491 V vs Ag/AgCl.

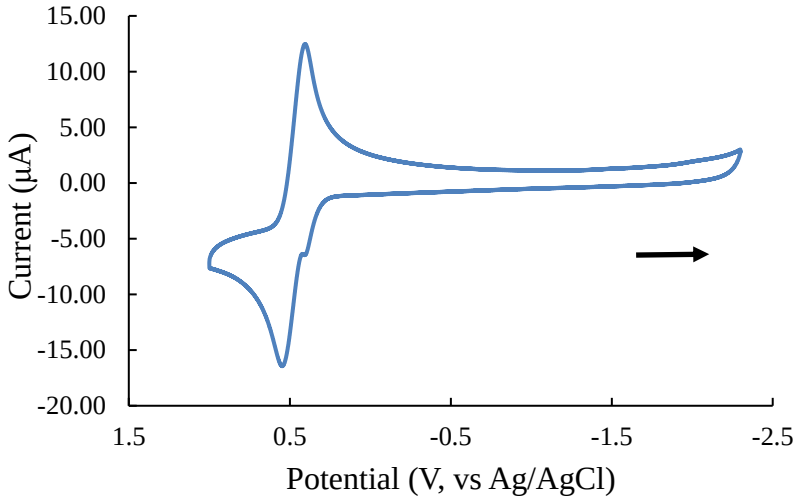

Figure 84: Cyclic voltammogram of compound **35** in THF with 0.1 M Bu_4NPF_6 as the supporting electrolyte. Scan rate was 0.10 V/s starting in the negative direction; the $E_{1/2}$ was reported to be +0.47 V vs Ag/AgCl.

Magnetic Measurements

$[K(18\text{-crown-}6)]_2[Mo^{III}Cl_5(pz)]$ behaves as an S = 3/2 paramagnet. The variable-temperature DC susceptibility data revealed a $\chi_M T$ value of 1.91 emu·K·mol^{-1} at 300 K which is in accord with the expected value of 1.88 emu·K·mol^{-1} (Figure 85). As the temperature decreases, $\chi_M T$ remains constant until 10 K, after which temperature there is a decrease to 1.60 emu·K·mol^{-1} at 2 K, likely the result of ZFS. The magnetization data at 2 K exhibit saturation at 7 T with a value of 2.89 Bohr magnetons which is slightly below the expected value of three unpaired electrons for the S = 3/2 ground state that corresponds to t_{2g}^3 (Figure 86). The reduced magnetization reveals overlapping isofield lines, indicating that no magnetic anisotropy is present (Figure 87).

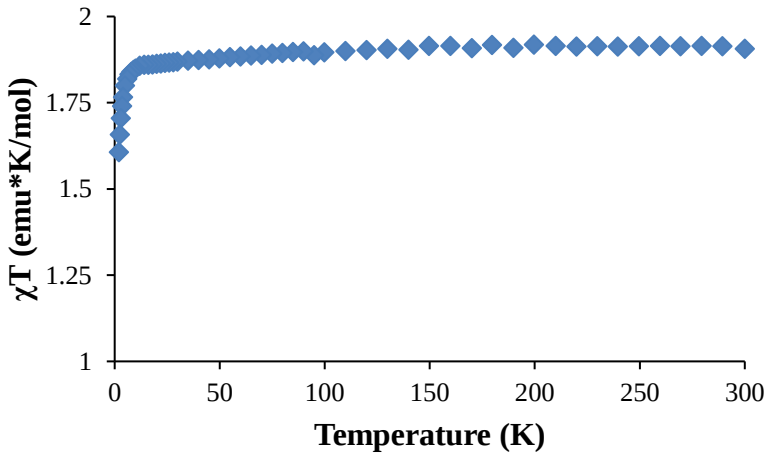

Figure 85: Variable-temperature DC susceptibility plot for $[K(18\text{-crown-}6)]_2[Mo^{III}Cl_5(pz)]$.

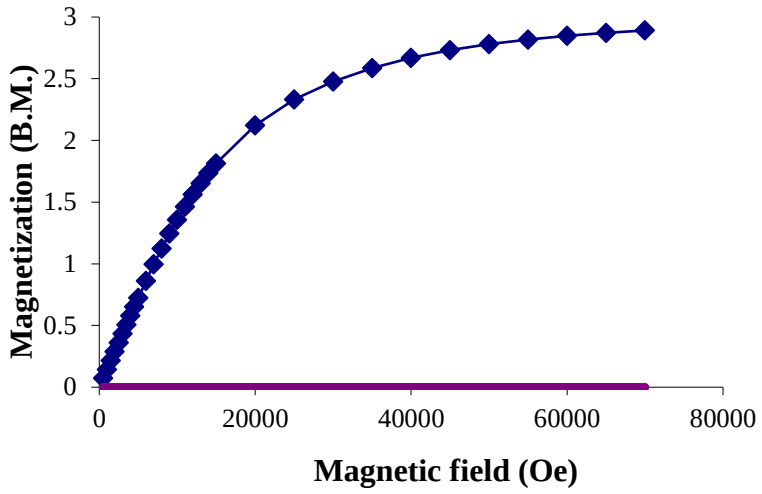

Figure 86: Magnetization data at 2 K for $[K(18\text{-crown-6})]_2[Mo^{III}Cl_5(pz)]$.

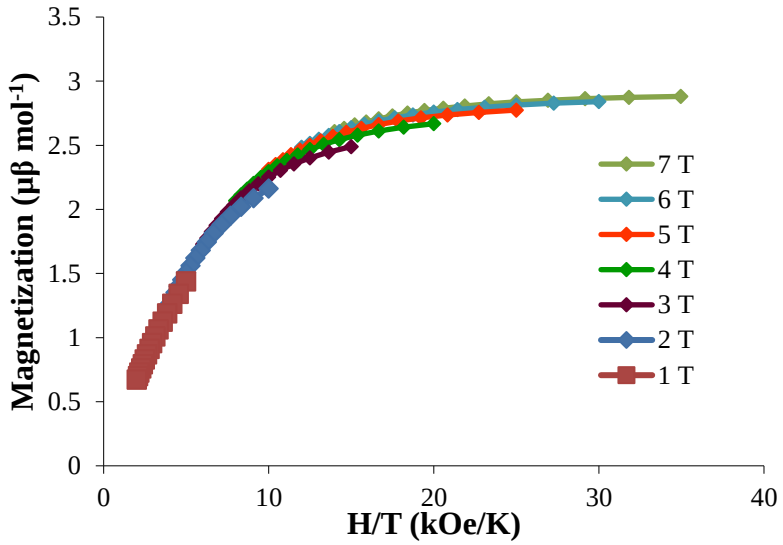

Figure 87: Reduced magnetization data for $[K(18\text{-crown-6})]_2[Mo^{III}Cl_5(pz)]$.

The [K(18-crown-6)][Tp*$Mo^{III}Cl_3$] salt exhibits a $\chi_M T$ value of 2.07 emu·K·mol^{-1} at 300 K, which is slightly higher than the expected value of 1.88 emu·K·mol^{-1} for an S = 3/2 paramagnet. The $\chi_M T$ value remains constant as the temperature decreases until 20 K; the 2 K value is 1.77 emu·K·mol^{-1} (Figure 88). The 2 K magnetization data saturate at 7 T with a value of 3.12 μ_B which is slightly higher than the expected value of 3.0 for three unpaired electrons for an S = 3/2 ground state (Figure 89). The reduced magnetization data (Figure 90) exhibit nearly overlapping isofield lines, indicating the molecule is magnetically isotropic, consistent with an octahedral geometry as opposed to a trigonally-distorted molecule with an S = 1/2 ground state.

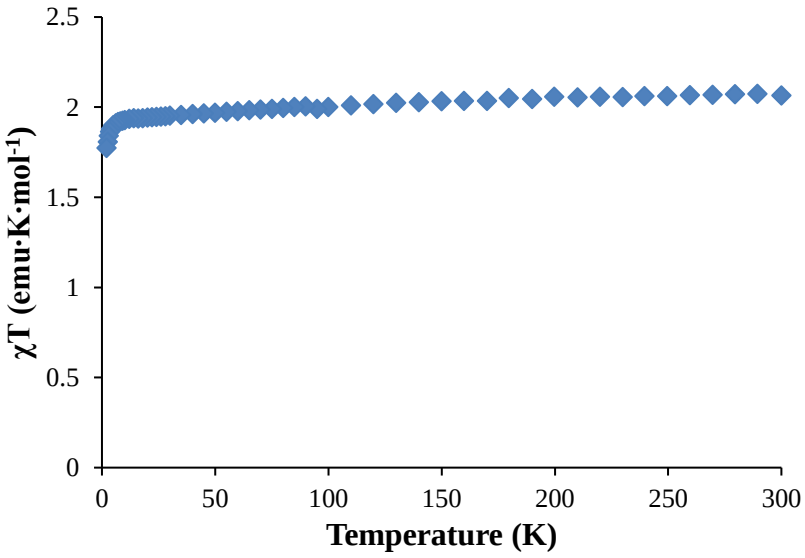

Figure 88: Variable-temperature DC susceptibility plot for [K(18-crown-6)][Tp*$Mo^{III}Cl_3$].

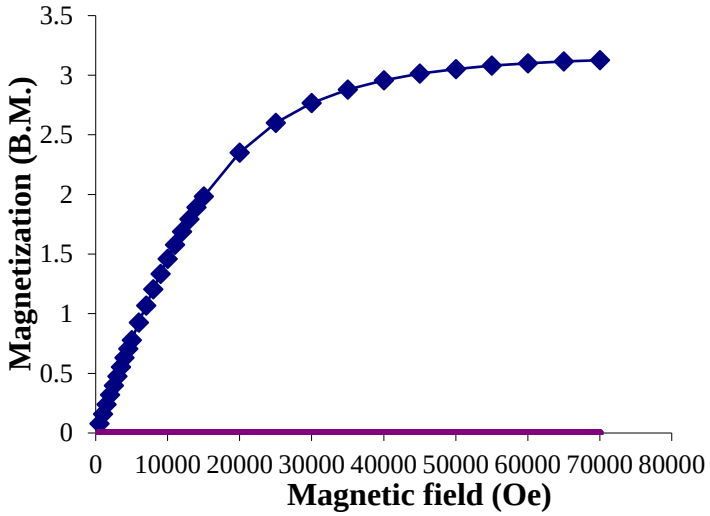

Figure 89: Magnetization data at 2 K for [K(18-crown-6)][Tp*Mo^{III}Cl$_3$]. Solid lines are a guide for the eye.

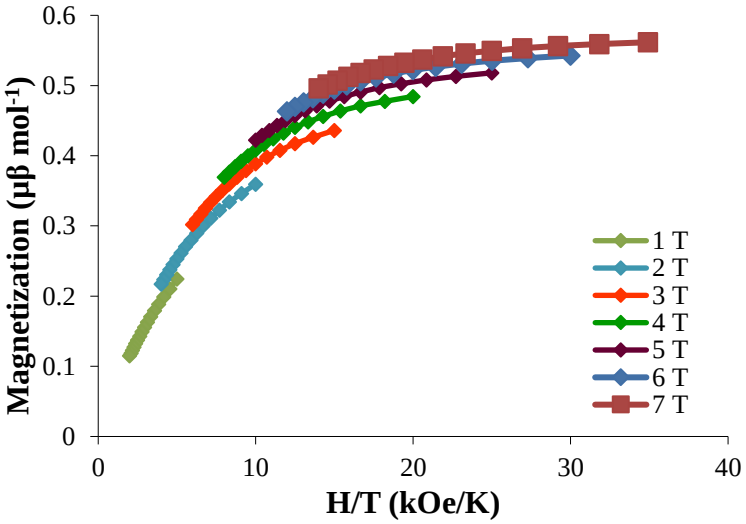

Figure 90: Reduced magnetization data for [K(18-crown-6)][Tp*Mo^{III}Cl$_3$]. Solid lines are a guide for the eye.

[K(2.2.2)cryptand][Tp*$Mo^{III}Cl_3$] behaves similarly to compound **35** as a paramagnet with an S = 3/2 spin state. The $\chi_M T$ value at 300 K is 2.20 emu·K·mol^{-1} which is slightly higher than the 18-crown-6 analogue (**35**) and the theoretical value of 1.88 emu·K·mol^{-1}. Unlike compound **35**, the $\chi_M T$ value decreases steadily as the temperature decreases until ~ 20 K, at which temperature there is a rapid decrease to 1.46 emu·K·mol^{-1} at 2 K (Figure 91). The 2 K magnetization data show saturation or near saturation at 7 T with a value of 2.91 μ_B, slightly lower than the expected value for three unpaired electrons which corresponds to an S = 3/2 ground state (Figure 92). The reduced magnetization data (Figure 93) show nearly overlapping isofield lines, indicating no magnetic anisotropy.

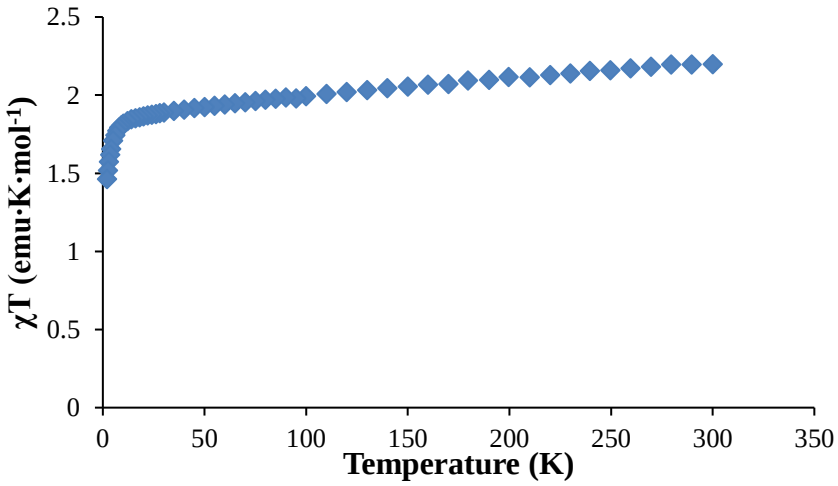

Figure 91: Variable-temperature DC susceptibility data plot for [K(2.2.2)cryptand][Tp*$Mo^{III}Cl_3$].

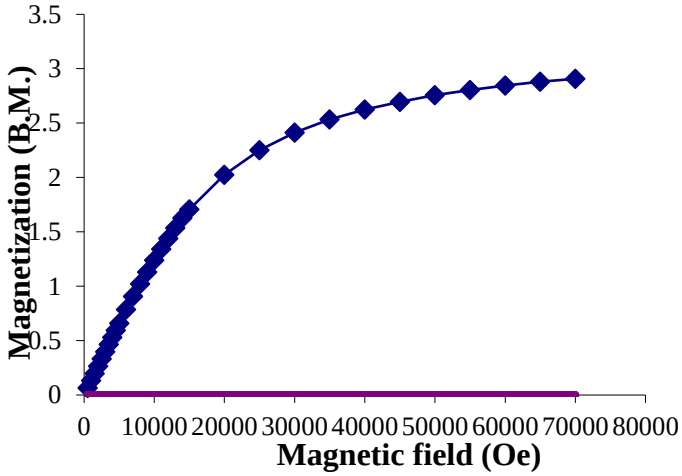

Figure 92: Magnetization data at 2 K for compound [K(2.2.2)cryptand][Tp*Mo^{III}Cl$_3$]. Solid lines are a guide for the eye.

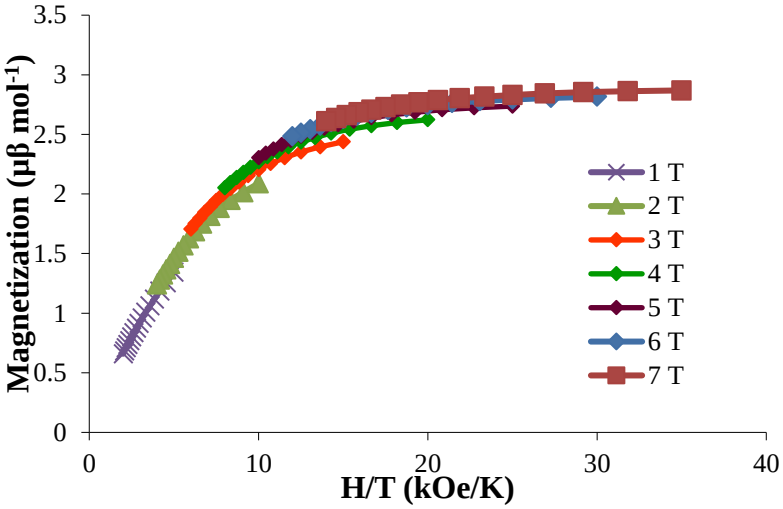

Figure 93: Reduced magnetization data for [K(2.2.2)cryptand][Tp*Mo^{III}Cl$_3$]. Solid lines are a guide for the eye.

$Tp^*Nb^{IV}Cl_2(OCH_3)$ is an S = 1/2 paramagnet with significant Temperature Independent Paramagnetism (TIP). The compound exhibits a $\chi_M T$ value of 0.47 emu·K·mol^{-1} at 300 K, significantly higher than the expected value of 0.32 emu·K·mol^{-1} for an S = 1/2 ground state as a result of TIP. The $\chi_M T$ value exhibits a constant decrease as the temperature decreases to 2 K, with a value of 0.32 emu·K·mol^{-1} at 2 K (Figure 94). Fitting the susceptibility with the PHI program yields g = 1.89 and a TIP of 4 x 10^{-3} emu·mol^{-1}, which is similar to the TIP reported for titanium(III) Tp* compounds.[212] The 2 K magnetization saturates at 7 T, with a value of 0.89 μ_B; this is slightly lower than the expected value of 1.0 for an unpaired electron (Figure 95). The reduced magnetization data show overlapping isofield lines, indicating the molecule is magnetically isotropic (Figure 96).

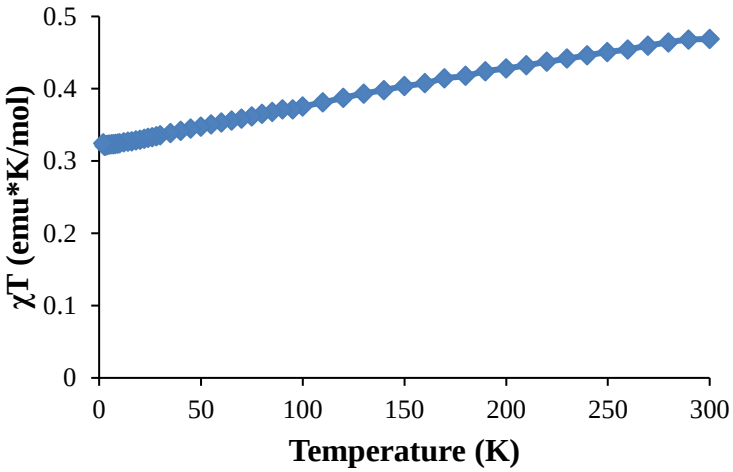

Figure 94: Variable-temperature DC susceptibility plot for $Tp^*Nb^{IV}Cl_2(OCH_3)$.

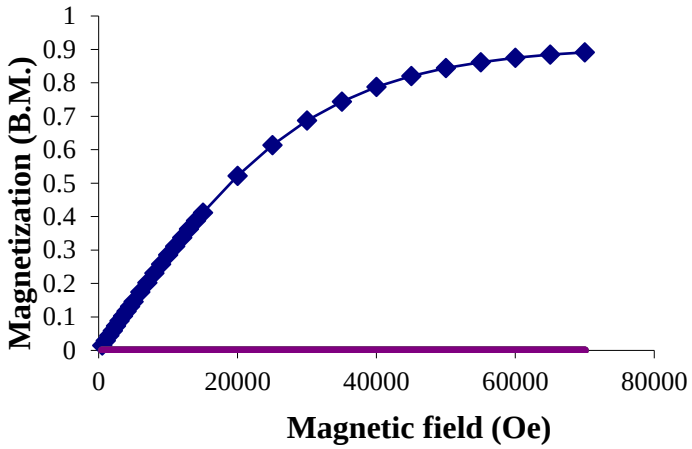

Figure 95: Magnetization data at 2 K for Tp*Nb^{IV}Cl$_2$(OCH$_3$). Solid lines are a guide for the eye.

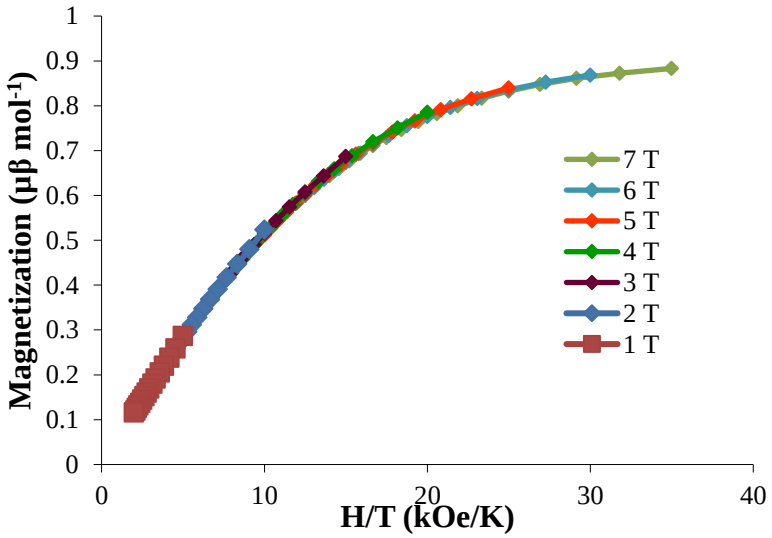

Figure 96: Reduced magnetization data for Tp*Nb^{IV}Cl$_2$(OCH$_3$). Solid lines are a guide for the eye.

Conclusions

The synthesis and characterization of 4d and 5d complexes with the Tp* ligand was undertaken. The $[Tp^*Mo^{III}Cl_3]^-$ anion with potassium encapsulated by different crown ethers was characterized by X-ray crystallography, cyclic voltammetry, and magnetometry, which agree with the Et_4N^+ salt isolated by Millar. In the case of $Tp^*W^{IV}Cl_3$, the crystal structure, which was lacking in the literature, was determined. The $Tp^*Nb^{IV}Cl_2(OCH_3)$ compound was also characterized by X-ray crystallography and magnetometry. The compounds adopt distorted octahedral geometries, a fact that is underscored by the results of the magnetic measurements which indicate a general lack of anisotropy. Attempts to synthesize the cyanide analogues have been unsuccessful to date, despite varying the solvent, temperature, and source of cyanide reagent. Further combinations of conditions are underway in the hopes of isolating the $[Tp^*M(CN)_3]$ moiety which is viable target as a building block for anisotropic exchange.

CHAPTER VI

CONCLUSIONS AND FUTURE OUTLOOK

The search for SMMs with improved properties has advanced considerably over the past several years owing, in large measure, to the success of strategies aimed at increasing magnetic anisotropy. Mononuclear molecules with rigid geometries and polynuclear complexes that engage in direct coupling with radical bridging ligands or in anisotropic superexchange coupling are the most promising targets for this research. While "single-ion" or mononuclear species and radical containing transition metal and lanthanide molecules have received much attention, anisotropic exchange remains an underexplored, albeit challenging, route towards developing SMMs with higher barriers and for understanding molecular magnetism in general. The work in this dissertation focused on synthesizing and characterizing 4d and 5d cyanometallate precursors that could be useful for anisotropic exchange. The difficulty in handling 4d and 5d cyanometallate compounds led to some unpredictable results but also some interesting precursors that were tested for anisotropic exchange in polynuclear systems.

In chapter II, the synthesis and characterization of an unknown class of paramagnetic cyanometallates, namely the heptacyanomolybdate(IV) and heptacyanotungstate(IV) anions were described. The compounds adopt the desired pentagonal bipyramidal geometry and both are S = 1 spin systems, the first examples in

the vast literature of homoleptic cyanide chemistry. Electrochemical studies indicate that the compounds are capable of being reduced to the trivalent state, and, given that the heptacyanomolybdate(III) is known to exist from an independent route, it was hypothesized that the tungsten derivative might also be accessible. The quasi-reversible nature of the reductions and the fact that reactions of the $[Mo^{III}(CN)_7]^{4-}$ anion have been known to lead to $[M^{III}(CN)_6]^{3-}$ containing products underscores the fragile nature of this chemistry and, indeed, the $[W^{III}(CN)_7]^{4-}$ derivative is apparently not stable. The chemistry of the oxidized $[W^{IV}(CN)_7]^{3-}$ species is also fraught with issues as described in chapter III.

Chapter III was aimed at exploring reactions of the $[Mo^{IV}(CN)_7]^{3-}$ and $[W^{IV}(CN)_7]^{3-}$ anions with a variety of 3d and 4f precursors in order to probe magnetic exchange interactions of the S = 1 $[M^{IV}(CN)_7]^{3-}$ moiety in polynuclear compounds. Reactions with the $Mn^{II}(L_{N5})$ resulted in the 2D networks $\{[Mn^{II}(L_{N5})]_2[M^{IV}(CN)_8]\}_\infty$ for molybdenum and tungsten, while reactions with $[M^{II}(PY5Me_2)]^{2+}$ (M = Mn, Fe, Co, Ni, and Cu) resulted in star-like complexes based on $[(M^{II}PY5Me_2)_4M^{IV}(CN)_8]X_4$ (M^{II}= Mn, Fe, Co, Ni, and Cu; M^{IV} = Mo, W; X = PF_6^- or $CF_3SO_3^-$). Finally, reactions with $[Ln^{III}(tmphen)_2(DMF)_2]$ (Ln = Sm, Dy) and $[W^{IV}(CN)_7]^{3-}$ resulted in 1-D chains of $\{Ln^{III}(tmphen)_2(DMF)_2W^{IV}(CN)_8\}$. Despite varying the reagents and conditions, however, the polynuclear compounds, inevitably contained the diamagnetic octacyanometallate $[M^{IV}(CN)_8]^{4-}$ anion, resulting in no exchange interactions with other metal spin centers.

In chapter IV, the syntheses and characterization of star-like complexes based on $[M^{II}(PY5Me_2)(CH_3CN)]^{2+}$ (M^{II} = Mn, Fe, Co, Ni, and Cu) in reactions with the S = 1/2 $[M^{V}(CN)_8]^{3-}$ (M^{V} = Mo, W) paramagnetic anions are reported. X-ray structures were obtained for $[(Co^{II}PY5Me_2)_4M(CN)_8]^{5+}$ (M = Mo, W) and $[(Ni^{II}PY5Me_2)_4W(CN)_8]^{5+}$, whereas the other reactions produced only powders. The magnetic properties of the Co and Ni complexes indicate magnetic coupling between the $[M^{V}(CN)_8]^{3-}$ and 3d metal centers, in contrast to the $[M^{IV}(CN)_8]^{4-}$ metals centers reported in Chapter III. The $[(Co^{II}PY5Me_2)_4M(CN)_8]^{5+}$ (M = Mo, W) engage in antiferromagnetic coupling, while the $[(Ni^{II}PY5Me_2)_4M(CN)_8]^{5+}$ (M = Mo, W) result in ferromagnetic coupling. None of the compounds exhibit an out-of-phase peak in the AC susceptibility data, however. The star-like complexes are also a rare example of a discrete complex incorporating $[M^{V}(CN)_8]^{3-}$, as most complexes that contain this anion tend to form polymeric chains or networks.

Finally, chapter V described the synthesis and magnetic properties of tris(3,5-dimethylpyrazoyl)borate complexes of niobium, molybdenum, and tungsten. In the case of molybdenum, improved synthetic routes were detailed for trivalent $[Tp^*Mo^{III}Cl_3]^{-}$, and the properties matched previously described results. The X-ray structure of $Tp^*W^{IV}Cl_3$ was also analyzed. The compound $Tp^*Nb^{IV}Cl_2(OCH_3)$ was isolated and structurally characterized as well and was found exhibit significant temperature-independent paramagnetism. All of the compounds studied, however, behave as simple paramagnets. Further work directed at synthesizing the cyanide analogues of the compounds and

incorporating them into polynuclear structures is expected to yield interesting magnetic complexes and potentially SMMs.

The work presented in this dissertation focused on the study of homoleptic cyanometallate compounds, particularly the $[M^{IV}(CN)_7]^{3-}$ moiety. A recurring problem was the decomposition of the moiety to the $[M^{IV}(CN)_8]^{4-}$ species, an issue that has been reported for other homoleptic cyanometallate anions, thereby preventing the study of anisotropic axial superexchange interactions. A future endeavor is to use heteroleptic cyanometallate compounds with macrocyclic or other equatorial capping ligands to circumvent decomposition and cyanide lability. For example, the $DAPBH_2$ ($DAPBH_2$ = 2,6-diacetylpyridinebis(benzoylhydrazone), Figure 97) ligand is a five-fold macrocyclic ligand that coordinates in the equatorial plane, allowing for only axial coordination. Such a molecule would allow for only axial exchange coupling with the desired geometry, preventing both decomposition and coordination of groups in the *xy* plane. Another ligand system that is an interesting possibility is a bulky tris(2-amidoethyl)amine ligand (Figure 97) which allows for the adoption of a trigonal geometry with one axial cyanide ligand for coupling to other spin centers. Of course, the geometry in this case is very different and theory predictions would be required to guide this research. Such heteroleptic complexes offer the opportunity to explore exchange coupling for 4d and 5d metal ions.

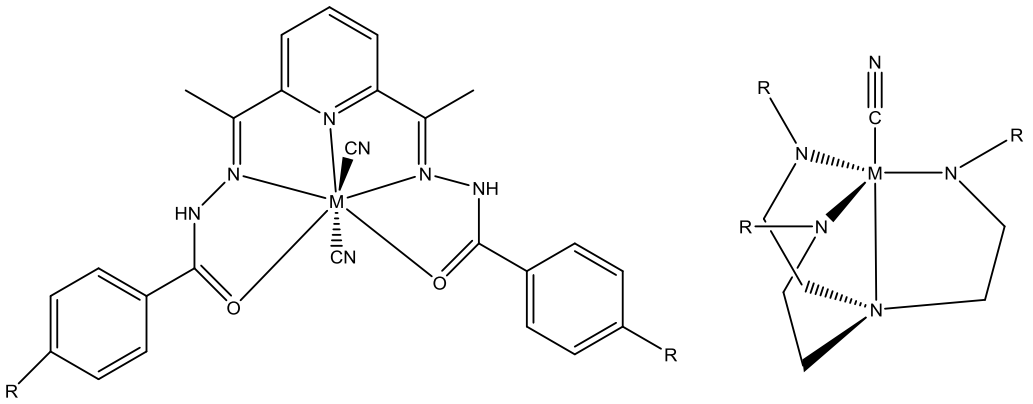

Figure 97: Structure of the $DAPBH_2$ (left) and tris(2-amidoethyl)amine (right) ligands. The R group indicates sites available for different substituents.

The pursuit of SMMs that retain slow paramagnetic relaxation at high temperatures remains the focus of chemists and physicists alike, but there are hurdles that must be overcome before they can be used in devices for high density storage, spintronics, or quantum computing. One compelling research area is to master the deposition of SMMs on surfaces, which is an important step towards developing SMM containing devices.[8, 222-223] Another area is using SMMs as molecular junctions, where the magnetic state of the molecule can be read out via an external stimulus.[14, 224-226] The field of molecular magnetism is still in a nascent stage, and there remain many opportunities and challenges in this exciting and fascinating area.

REFERENCES

1. Landee, C. P.; Turnbull, M. M., Review: A gentle introduction to magnetism: units, fields, theory, and experiment. *Journal of Coordination Chemistry* **2014,** *67* (3), 375-439.

2. Mattis, D. C., History of Magnetism. In *The Theory of Magnetism I: Statics and Dynamics*, Springer Berlin Heidelberg: Berlin, Heidelberg, 1981; pp 1-38.

3. Jiles, D., Introduction to Magnetism and Magnetic Materials. **1998**.

4. Boles, L. C.; Lohmann, K. J., True navigation and magnetic maps in spiny lobsters. *Nature* **2003,** *421*, 60.

5. Mora, C. V.; Davison, M.; Martin Wild, J.; Walker, M. M., Magnetoreception and its trigeminal mediation in the homing pigeon. *Nature* **2004,** *432*, 508.

6. Blakemore, R., Magnetotactic bacteria. *Science* **1975,** *190* (4212), 377-379.

7. Vleck, J. H. V., The Theory of Electric and Magnetic Susceptibilities. **1932**.

8. Bogani, L.; Wernsdorfer, W., Molecular spintronics using single-molecule magnets. *Nat Mater* **2008,** *7* (3), 179-186.

9. Sanvito, S., Molecular spintronics. *Chemical Society Reviews* **2011,** *40* (6), 3336-3355.

10. Aromi, G.; Aguila, D.; Gamez, P.; Luis, F.; Roubeau, O., Design of magnetic coordination complexes for quantum computing. *Chemical Society Reviews* **2012,** *41* (2), 537-546.

11. Moreno-Pineda, E.; Godfrin, C.; Balestro, F.; Wernsdorfer, W.; Ruben, M., Molecular spin qudits for quantum algorithms. *Chemical Society Reviews* **2018,** *47* (2), 501-513.

12. Pearson, T. J.; Laorenza, D. W.; Krzyaniak, M. D.; Wasielewski, M. R.; Freedman, D. E., Octacyanometallate qubit candidates. *Dalton Transactions* **2018,** *47* (34), 11744-11748.

13. Winpenny, R. E. P., Quantum Information Processing Using Molecular Nanomagnets As Qubits. *Angewandte Chemie International Edition* **2008,** *47* (42), 7992-7994.

14. Vincent, R.; Klyatskaya, S.; Ruben, M.; Wernsdorfer, W.; Balestro, F., Electronic read-out of a single nuclear spin using a molecular spin transistor. *Nature* **2012,** *488*, 357.

15. Raman, K. V.; Kamerbeek, A. M.; Mukherjee, A.; Atodiresei, N.; Sen, T. K.; Lazić, P.; Caciuc, V.; Michel, R.; Stalke, D.; Mandal, S. K.; Blügel, S.; Münzenberg, M.; Moodera, J. S., Interface-engineered templates for molecular spin memory devices. *Nature* **2013,** *493*, 509.

16. Corradini, V.; Ghirri, A.; Candini, A.; Biagi, R.; del Pennino, U.; Dotti, G.; Otero, E.; Choueikani, F.; Blagg, R. J.; McInnes, E. J. L.; Affronte, M., Magnetic Cooling at a Single Molecule Level: a Spectroscopic Investigation of Isolated Molecules on a Surface. *Advanced Materials* **2013,** *25* (20), 2816-2820.

17. Pichon, A., Gadolinium keeps its cool. *Nature Chemistry* **2009**.

18. Wang, W.-M.; Duan, W.-W.; Yue, L.-C.; Wang, Y.-L.; Ji, W.-Y.; Zhang, C.-F.; Fang, M.; Wu, Z.-L., Magnetic refrigeration and single-molecule magnet behaviour of two lanthanide dinuclear complexes (Ln=GdIII, TbIII) based on 8-hydroxyquinolin derivatives. *Inorganica Chimica Acta* **2017,** *466*, 145-150.

19. Peng, J.-B.; Zhang, Q.-C.; Kong, X.-J.; Zheng, Y.-Z.; Ren, Y.-P.; Long, L.-S.; Huang, R.-B.; Zheng, L.-S.; Zheng, Z., High-Nuclearity 3d–4f Clusters as Enhanced Magnetic Coolers and Molecular Magnets. *Journal of the American Chemical Society* **2012,** *134* (7), 3314-3317.

20. Bleaney, B.; Bowers, K. D., Anomalous paramagnetism of copper acetate. *Proceedings of the Royal Society of London. Series A. Mathematical and Physical Sciences* **1952,** *214* (1119), 451-465.

21. Buschow, K. H. J.; Boer, F. R. d., Physics of Magnetism and Magnetic Materials. **2003**.

22. Gatteschi, D.; Sessoli, R.; Villain, J., *Molecular Nanomagnets*. 2006; Vol. 376.

23. Carlin, R. L., Magnetochemistry. **1986**.

24. Christou, G.; Gatteschi, D.; Hendrickson, D. N.; Sessoli, R., Single-Molecule Magnets. *MRS Bulletin* **2000,** *25* (11), 66-71.

25. Caneschi, A.; Gatteschi, D.; Sessoli, R.; Barra, A. L.; Brunel, L. C.; Guillot, M., Alternating current susceptibility, high field magnetization, and millimeter band EPR evidence for a ground S = 10 state in [Mn12O12(Ch3COO)16(H2O)4].2CH3COOH.4H2O. *Journal of the American Chemical Society* **1991,** *113* (15), 5873-5874.

26. Sessoli, R.; Tsai, H. L.; Schake, A. R.; Wang, S.; Vincent, J. B.; Folting, K.; Gatteschi, D.; Christou, G.; Hendrickson, D. N., High-spin molecules: [Mn12O12(O2CR)16(H2O)4]. *Journal of the American Chemical Society* **1993,** *115* (5), 1804-1816.

27. Lis, T., Preparation, structure, and magnetic properties of a dodecanuclear mixed-valence manganese carboxylate. *Acta Crystallographica Section B* **1980,** *36* (9), 2042-2046.

28. Sun, Z.; Ruiz, D.; Rumberger, E.; Incarvito, C. D.; Folting, K.; Rheingold, A. L.; Christou, G.; Hendrickson, D. N., Isomeric Forms of [Mn12O12(O2CR)16(H2O)4] Single-Molecule Magnets. *Inorganic Chemistry* **1998,** *37* (19), 4758-4759.

29. Thuijs, A. E.; King, P.; Abboud, K. A.; Christou, G., New Structural Types of Mn16 Single-Molecule Magnets: W-Shaped Topology from Reductive Aggregation. *Inorganic Chemistry* **2015,** *54* (18), 9127-9137.

30. Sañudo, E. C.; Wernsdorfer, W.; Abboud, K. A.; Christou, G., Synthesis, Structure, and Magnetic Properties of a Mn21 Single-Molecule Magnet. *Inorganic Chemistry* **2004,** *43* (14), 4137-4144.

31. Brechin, E. K.; Sañudo, E. C.; Wernsdorfer, W.; Boskovic, C.; Yoo, J.; Hendrickson, D. N.; Yamaguchi, A.; Ishimoto, H.; Concolino, T. E.; Rheingold, A. L.; Christou, G., Single-Molecule Magnets: Structure and Properties of [Mn18O14(O2CMe)18(hep)4(hepH)2(H2O)2](ClO4)2 with Spin S = 13. *Inorganic Chemistry* **2005,** *44* (3), 502-511.

32. Brockman, J. T.; Stamatatos, T. C.; Wernsdorfer, W.; Abboud, K. A.; Christou, G., Synthesis and Characterization of a Mn22 Single-Molecule Magnet and a [Mn22]n Single-Chain Magnet. *Inorganic Chemistry* **2007,** *46* (22), 9160-9171.

33. Bagai, R.; Christou, G., A Fourth Isolated Oxidation Level of the [Mn12O12(O2CR)16(H2O)4] Family of Single-Molecule Magnets. *Inorganic Chemistry* **2007,** *46* (25), 10810-10818.

34. Yang, C.-I.; Zhang, Z.-Z.; Lin, S.-B., A review of manganese-based molecular magnets and supramolecular architectures from phenolic oximes. *Coordination Chemistry Reviews* **2015,** *289-290*, 289-314.

35. Ako, A. M.; Hewitt, I. J.; Mereacre, V.; Clérac, R.; Wernsdorfer, W.; Anson, C. E.; Powell, A. K., A Ferromagnetically Coupled Mn19 Aggregate with a Record S=83/2 Ground Spin State. *Angewandte Chemie International Edition* **2006,** *45* (30), 4926-4929.

36. Waldmann, O., A Criterion for the Anisotropy Barrier in Single-Molecule Magnets. *Inorganic Chemistry* **2007,** *46* (24), 10035-10037.

37. Neese, F.; Pantazis, D. A., What is not required to make a single molecule magnet. *Faraday Discussions* **2011,** *148* (0), 229-238.

38. Ishikawa, N.; Sugita, M.; Ishikawa, T.; Koshihara, S.-y.; Kaizu, Y., Lanthanide Double-Decker Complexes Functioning as Magnets at the Single-Molecular Level. *Journal of the American Chemical Society* **2003,** *125* (29), 8694-8695.

39. Dey, A.; Kalita, P.; Chandrasekhar, V., Lanthanide(III)-Based Single-Ion Magnets. *ACS Omega* **2018,** *3* (8), 9462-9475.

40. Woodruff, D. N.; Winpenny, R. E. P.; Layfield, R. A., Lanthanide Single-Molecule Magnets. *Chemical Reviews* **2013,** *113* (7), 5110-5148.

41. Habib, F.; Murugesu, M., Lessons learned from dinuclear lanthanide nano-magnets. *Chemical Society Reviews* **2013,** *42* (8), 3278-3288.

42. Liddle, S. T.; van Slageren, J., Improving f-element single molecule magnets. *Chemical Society Reviews* **2015,** *44* (19), 6655-6669.

43. Chilton, N. F., Design Criteria for High-Temperature Single-Molecule Magnets. *Inorganic Chemistry* **2015,** *54* (5), 2097-2099.

44. Bar, A. K.; Kalita, P.; Singh, M. K.; Rajaraman, G.; Chandrasekhar, V., Low-coordinate mononuclear lanthanide complexes as molecular nanomagnets. *Coordination Chemistry Reviews* **2018,** *367*, 163-216.

45. Sessoli, R.; Powell, A. K., Strategies towards single molecule magnets based on lanthanide ions. *Coordination Chemistry Reviews* **2009,** *253* (19), 2328-2341.

46. Chen, Y.-C.; Liu, J.-L.; Ungur, L.; Liu, J.; Li, Q.-W.; Wang, L.-F.; Ni, Z.-P.; Chibotaru, L. F.; Chen, X.-M.; Tong, M.-L., Symmetry-Supported Magnetic Blocking at 20 K in Pentagonal Bipyramidal Dy(III) Single-Ion Magnets. *Journal of the American Chemical Society* **2016,** *138* (8), 2829-2837.

47. Liu, J.; Chen, Y.-C.; Liu, J.-L.; Vieru, V.; Ungur, L.; Jia, J.-H.; Chibotaru, L. F.; Lan, Y.; Wernsdorfer, W.; Gao, S.; Chen, X.-M.; Tong, M.-L., A Stable Pentagonal Bipyramidal Dy(III) Single-Ion Magnet with a Record Magnetization Reversal Barrier over 1000 K. *Journal of the American Chemical Society* **2016,** *138* (16), 5441-5450.

48. Ding, Y.-S.; Chilton, N. F.; Winpenny, R. E. P.; Zheng, Y.-Z., On Approaching the Limit of Molecular Magnetic Anisotropy: A Near-Perfect Pentagonal Bipyramidal Dysprosium(III) Single-Molecule Magnet. *Angewandte Chemie International Edition* **2016,** *55* (52), 16071-16074.

49. Goodwin, C. A. P.; Ortu, F.; Reta, D.; Chilton, N. F.; Mills, D. P., Molecular magnetic hysteresis at 60 kelvin in dysprosocenium. *Nature* **2017,** *548*, 439.

50. Guo, F.-S.; Day, B. M.; Chen, Y.-C.; Tong, M.-L.; Mansikkamäki, A.; Layfield, R. A., A Dysprosium Metallocene Single-Molecule Magnet Functioning at the Axial Limit. *Angewandte Chemie International Edition* **2017,** *56* (38), 11445-11449.

51. Ding, Y.-S.; Yu, K.-X.; Reta, D.; Ortu, F.; Winpenny, R. E. P.; Zheng, Y.-Z.; Chilton, N. F., Field- and temperature-dependent quantum tunnelling of the magnetisation in a large barrier single-molecule magnet. *Nature Communications* **2018,** *9* (1), 3134.

52. Zhang, P.; Guo, Y.-N.; Tang, J., Recent advances in dysprosium-based single molecule magnets: Structural overview and synthetic strategies. *Coordination Chemistry Reviews* **2013,** *257* (11), 1728-1763.

53. Rinehart, J. D.; Long, J. R., Exploiting single-ion anisotropy in the design of f-element single-molecule magnets. *Chemical Science* **2011,** *2* (11), 2078-2085.

54. Aravena, D.; Ruiz, E., Shedding Light on the Single-Molecule Magnet Behavior of Mononuclear DyIII Complexes. *Inorganic Chemistry* **2013,** *52* (23), 13770-13778.

55. Chilton, N. F.; Goodwin, C. A. P.; Mills, D. P.; Winpenny, R. E. P., The first near-linear bis(amide) f-block complex: a blueprint for a high temperature single molecule magnet. *Chemical Communications* **2015,** *51* (1), 101-103.

56. Ungur, L.; Chibotaru, L. F., Magnetic anisotropy in the excited states of low symmetry lanthanide complexes. *Physical Chemistry Chemical Physics* **2011,** *13* (45), 20086-20090.

57. Rinehart, J. D.; Fang, M.; Evans, W. J.; Long, J. R., A N23– Radical-Bridged Terbium Complex Exhibiting Magnetic Hysteresis at 14 K. *Journal of the American Chemical Society* **2011,** *133* (36), 14236-14239.

58. Freedman, D. E.; Harman, W. H.; Harris, T. D.; Long, G. J.; Chang, C. J.; Long, J. R., Slow Magnetic Relaxation in a High-Spin Iron(II) Complex. *Journal of the American Chemical Society* **2010,** *132* (4), 1224-1225.

59. Craig, G. A.; Murrie, M., 3d single-ion magnets. *Chemical Society Reviews* **2015,** *44* (8), 2135-2147.

60. Zadrozny, J. M.; Xiao, D. J.; Atanasov, M.; Long, G. J.; Grandjean, F.; Neese, F.; Long, J. R., Magnetic blocking in a linear iron(I) complex. *Nature Chemistry* **2013,** *5*, 577.

61. Zadrozny, J. M.; Atanasov, M.; Bryan, A. M.; Lin, C.-Y.; Rekken, B. D.; Power, P. P.; Neese, F.; Long, J. R., Slow magnetization dynamics in a series of two-coordinate iron(ii) complexes. *Chemical Science* **2013,** *4* (1), 125-138.

62. Zadrozny, J. M.; Xiao, D. J.; Long, J. R.; Atanasov, M.; Neese, F.; Grandjean, F.; Long, G. J., Mössbauer Spectroscopy as a Probe of Magnetization Dynamics in the Linear Iron(I) and Iron(II) Complexes [Fe(C(SiMe3)3)2]1–/0. *Inorganic Chemistry* **2013,** *52* (22), 13123-13131.

63. Harman, W. H.; Harris, T. D.; Freedman, D. E.; Fong, H.; Chang, A.; Rinehart, J. D.; Ozarowski, A.; Sougrati, M. T.; Grandjean, F.; Long, G. J.; Long, J. R.; Chang, C. J., Slow Magnetic Relaxation in a Family of Trigonal Pyramidal Iron(II) Pyrrolide Complexes. *Journal of the American Chemical Society* **2010,** *132* (51), 18115-18126.

64. Bar, A. K.; Pichon, C.; Gogoi, N.; Duhayon, C.; Ramasesha, S.; Sutter, J.-P., Single-ion magnet behaviour of heptacoordinated Fe(ii) complexes: on the importance of supramolecular organization. *Chemical Communications* **2015,** *51* (17), 3616-3619.

65. Poulten, R. C.; Page, M. J.; Algarra, A. G.; Le Roy, J. J.; López, I.; Carter, E.; Llobet, A.; Macgregor, S. A.; Mahon, M. F.; Murphy, D. M.; Murugesu, M.; Whittlesey, M. K., Synthesis, Electronic Structure, and Magnetism of [Ni(6-Mes)2]+: A Two-Coordinate Nickel(I) Complex Stabilized by Bulky N-Heterocyclic Carbenes. *Journal of the American Chemical Society* **2013,** *135* (37), 13640-13643.

66. Bryan, A. M.; Merrill, W. A.; Reiff, W. M.; Fettinger, J. C.; Power, P. P., Synthesis, Structural, and Magnetic Characterization of Linear and Bent Geometry Cobalt(II) and Nickel(II) Amido Complexes: Evidence of Very Large Spin–Orbit Coupling Effects in Rigorously Linear Coordinated Co2+. *Inorganic Chemistry* **2012,** *51* (6), 3366-3373.

67. Novikov, V. V.; Pavlov, A. A.; Nelyubina, Y. V.; Boulon, M.-E.; Varzatskii, O. A.; Voloshin, Y. Z.; Winpenny, R. E. P., A Trigonal Prismatic Mononuclear Cobalt(II) Complex Showing Single-Molecule Magnet Behavior. *Journal of the American Chemical Society* **2015,** *137* (31), 9792-9795.

68. Mondal, A. K.; Mondal, A.; Dey, B.; Konar, S., Influence of the Coordination Environment on Easy-Plane Magnetic Anisotropy of Pentagonal Bipyramidal Cobalt(II) Complexes. *Inorganic Chemistry* **2018,** *57* (16), 9999-10008.

69. Zhang, J.; Li, J.; Yang, L.; Yuan, C.; Zhang, Y.-Q.; Song, Y., Magnetic Anisotropy from Trigonal Prismatic to Trigonal Antiprismatic Co(II) Complexes: Experimental Observation and Theoretical Prediction. *Inorganic Chemistry* **2018,** *57* (7), 3903-3912.

70. Gomez-Coca, S.; Cremades, E.; Aliaga-Alcalde, N.; Ruiz, E., Mononuclear Single-Molecule Magnets: Tailoring the Magnetic Anisotropy of First-Row Transition-Metal Complexes. *Journal of the American Chemical Society* **2013,** *135* (18), 7010-7018.

71. Lin, P.-H.; Smythe, N. C.; Gorelsky, S. I.; Maguire, S.; Henson, N. J.; Korobkov, I.; Scott, B. L.; Gordon, J. C.; Baker, R. T.; Murugesu, M., Importance of Out-of-State Spin–Orbit Coupling for Slow Magnetic Relaxation in Mononuclear FeII Complexes. *Journal of the American Chemical Society* **2011,** *133* (40), 15806-15809.

72. Atanasov, M.; Aravena, D.; Suturina, E.; Bill, E.; Maganas, D.; Neese, F., First principles approach to the electronic structure, magnetic anisotropy and spin relaxation in mononuclear 3d-transition metal single molecule magnets. *Coordination Chemistry Reviews* **2015,** *289-290*, 177-214.

73. Pinkowicz, D.; Birk, F. J.; Magott, M.; Schulte, K.; Dunbar, K. R., Systematic Study of Open-Shell Trigonal Pyramidal Transition-Metal Complexes with a Rigid-Ligand Scaffold. *Chemistry – A European Journal* **2017,** *23* (15), 3548-3552.

74. Yao, X.-N.; Du, J.-Z.; Zhang, Y.-Q.; Leng, X.-B.; Yang, M.-W.; Jiang, S.-D.; Wang, Z.-X.; Ouyang, Z.-W.; Deng, L.; Wang, B.-W.; Gao, S., Two-Coordinate Co(II) Imido Complexes as Outstanding Single-Molecule Magnets. *Journal of the American Chemical Society* **2017,** *139* (1), 373-380.

75. Mironov, V. S., New approaches to the problem of high-temperature single-molecule magnets. *Dokl Phys Chem* **2006,** *408* (1), 130-136.

76. Qian, K.; Huang, X.-C.; Zhou, C.; You, X.-Z.; Wang, X.-Y.; Dunbar, K. R., A Single-Molecule Magnet Based on Heptacyanomolybdate with the Highest Energy Barrier for a Cyanide Compound. *Journal of the American Chemical Society* **2013,** *135* (36), 13302-13305.

77. Mironov, V. S., Origin of Dissimilar Single-Molecule Magnet Behavior of Three MnII2MoIII Complexes Based on [MoIII(CN)7]4– Heptacyanomolybdate: Interplay of MoIII–CN–MnII Anisotropic Exchange Interactions. *Inorganic Chemistry* **2015,** *54* (23), 11339-11355.

78. Mironov, V. S., Spin Clusters with Orbitally Degenerate Magnetic Centers As Single-Molecule Nanomagnets with High Blocking Temperatures. *Dokl Phys Chem* **2004,** *397* (1), 154-157.

79. Mironov, V. S.; Chibotaru, L. F.; Ceulemans, A., Mechanism of a Strongly Anisotropic MoIII−CN−MnII Spin−Spin Coupling in Molecular Magnets Based on the [Mo(CN)7]4- Heptacyanometalate: A New Strategy for Single-Molecule Magnets with

High Blocking Temperatures. *Journal of the American Chemical Society* **2003,** *125* (32), 9750-9760.

80. Mironov, V. S., Trigonal bipyramidal spin clusters with orbitally degenerate 5d cyano complexes [OsIII(CN)6]3−, prototypes of high-temperature single-molecule magnets. *Dokl Phys Chem* **2007,** *415* (1), 199-204.

81. Mironov, V., Molecular Engineering of High Energy Barrier in Single-Molecule Magnets Based on [MoIII(CN)7]4− and V(II) Complexes. *Inorganics* **2018,** *6* (2), 58.

82. Mironov, V. S.; Chibotaru, L. F.; Ceulemans, A., Exchange interaction in the ${\mathrm{YbCrBr}}_{9}^{3\ensuremath{-}}$ mixed dimer: The origin of a strong ${\mathrm{Yb}}^{3+}\ensuremath{-}{\mathrm{Cr}}^{3+}$ exchange anisotropy. *Physical Review B* **2003,** *67* (1), 014424.

83. Chibotaru, L. F.; Hendrickx, M. F. A.; Clima, S.; Larionova, J.; Ceulemans, A., Magnetic Anisotropy of [Mo(CN)7]4- Anions and Fragments of Cyano-Bridged Magnetic Networks. *The Journal of Physical Chemistry A* **2005,** *109* (32), 7251-7257.

84. Ito, A.; Suenaga, M.; Ôno, K., Mössbauer Study of Soluble Prussian Blue, Insoluble Prussian Blue, and Turnbull's Blue. *The Journal of Chemical Physics* **1968,** *48* (8), 3597-3599.

85. Boxhoorn, G.; Moolhuysen, J.; Coolegem, J. G. F.; van Santen, R. A., Cyanometallates: an underestimated class of molecular sieves. *Journal of the Chemical Society, Chemical Communications* **1985,** (19), 1305-1307.

86. Boudjema, L.; Mamontova, E.; Long, J.; Larionova, J.; Guari, Y.; Trens, P., Prussian Blue Analogues for the Separation of Hydrocarbons in Humid Conditions. *Inorganic Chemistry* **2017,** *56* (14), 7598-7601.

87. Chapman, K. W.; Southon, P. D.; Weeks, C. L.; Kepert, C. J., Reversible hydrogen gas uptake in nanoporous Prussian Blue analogues. *Chemical Communications* **2005,** (26), 3322-3324.

88. Kaye, S. S.; Long, J. R., Hydrogen Storage in the Dehydrated Prussian Blue Analogues M3[Co(CN)6]2 (M = Mn, Fe, Co, Ni, Cu, Zn). *Journal of the American Chemical Society* **2005,** *127* (18), 6506-6507.

89. Asai, M.; Takahashi, A.; Jiang, Y.; Ishizaki, M.; Kurihara, M.; Kawamoto, T., Trace Alcohol Adsorption by Metal Hexacyanocobaltate Nanoparticles and the Adsorption Mechanism. *The Journal of Physical Chemistry C* **2018,** *122* (22), 11918-11925.

90. Takahashi, A.; Tanaka, H.; Parajuli, D.; Nakamura, T.; Minami, K.; Sugiyama, Y.; Hakuta, Y.; Ohkoshi, S.-i.; Kawamoto, T., Historical Pigment Exhibiting Ammonia Gas Capture beyond Standard Adsorbents with Adsorption Sites of Two Kinds. *Journal of the American Chemical Society* **2016,** *138* (20), 6376-6379.

91. Manumpil, M. A.; Leal-Cervantes, C.; Hudson, M. R.; Brown, C. M.; Karunadasa, H. I., Electronic Conductivity in a Porous Vanadyl Prussian Blue Analogue upon Air Exposure. *Inorganic Chemistry* **2017,** *56* (21), 12682-12686.

92. Sato, O.; Iyoda, T.; Fujishima, A.; Hashimoto, K., Photoinduced Magnetization of a Cobalt-Iron Cyanide. *Science* **1996,** *272* (5262), 704-705.

93. Sato, O.; Iyoda, T.; Fujishima, A.; Hashimoto, K., Electrochemically Tunable Magnetic Phase Transition in a High-T_c Chromium Cyanide Thin Film. *Science* **1996,** *271* (5245), 49-51.

94. Long, J.; Asakura, D.; Okubo, M.; Yamada, A.; Guari, Y.; Larionova, J., Electrochemical Li-Ion Intercalation in Octacyanotungstate-Bridged Coordination Polymer with Evidence of Three Magnetic Regimes. *Inorganic Chemistry* **2016,** *55* (15), 7637-7646.

95. Ruiz, E.; Rodríguez-Fortea, A.; Alvarez, S.; Verdaguer, M., Is It Possible To Get High TC Magnets with Prussian Blue Analogues? A Theoretical Prospect. *Chemistry – A European Journal* **2005,** *11* (7), 2135-2144.

96. Rigo, P.; Turco, A., Cyanide phosphine complexes of transition metals. *Coordination Chemistry Reviews* **1974,** *13* (2), 133-172.

97. Nakamoto, K., Infrared and Raman Spectra of Inorganic and Coordination Compounds. **1978**.

98. Shatruk, M.; Avendano, C.; Dunbar, K. R., Cyanide-Bridged Complexes of Transition Metals: A Molecular Magnetism Perspective. In *Progress in Inorganic Chemistry*, Karlin, K. D., Ed. 2009.

99. Pedersen, K. S.; Bendix, J.; Clérac, R., Single-molecule magnet engineering: building-block approaches. *Chemical Communications* **2014,** *50* (34), 4396-4415.

100. Wang, X.-Y.; Avendano, C.; Dunbar, K. R., Molecular magnetic materials based on 4d and 5d transition metals. *Chemical Society Reviews* **2011,** *40* (6), 3213-3238.

101. Beauvais, L. G.; Long, J. R., Cyanide-Limited Complexation of Molybdenum(III): Synthesis of Octahedral [Mo(CN)6]3- and Cyano-Bridged [Mo2(CN)11]5. *Journal of the American Chemical Society* **2002,** *124* (10), 2110-2111.

102. Bennett, M. V.; Long, J. R., New Cyanometalate Building Units: Synthesis and Characterization of [Re(CN)7]3- and [Re(CN)8]3. *Journal of the American Chemical Society* **2003,** *125* (9), 2394-2395.

103. Freedman, D. E.; Jenkins, D. M.; Iavarone, A. T.; Long, J. R., A Redox-Switchable Single-Molecule Magnet Incorporating [Re(CN)7]3. *Journal of the American Chemical Society* **2008,** *130* (10), 2884-2885.

104. Zadrozny, J. M.; Freedman, D. E.; Jenkins, D. M.; Harris, T. D.; Iavarone, A. T.; Mathonière, C.; Clérac, R.; Long, J. R., Slow Magnetic Relaxation and Charge-Transfer in Cyano-Bridged Coordination Clusters Incorporating [Re(CN)7]3−/4−. *Inorganic Chemistry* **2010,** *49* (19), 8886-8896.

105. Samsonenko, D. G.; Paulsen, C.; Lhotel, E.; Mironov, V. S.; Vostrikova, K. E., [MnIII(Schiff Base)]3[ReIV(CN)7], Highly Anisotropic 3D Coordination Framework:

Synthesis, Crystal Structure, Magnetic Investigations, and Theoretical Analysis. *Inorganic Chemistry* **2014,** *53* (19), 10217-10231.

106. Sukhikh, T.; Vostrikova, K., Assembly of Mn(III) Schiff Base Complexes with Heptacyanorhenate (IV). *Inorganics* **2017,** *5* (3), 59.

107. Harris, T. D.; Bennett, M. V.; Clérac, R.; Long, J. R., [ReCl4(CN)2]2−: A High Magnetic Anisotropy Building Unit Giving Rise to the Single-Chain Magnets (DMF)4MReCl4(CN)2 (M = Mn, Fe, Co, Ni). *Journal of the American Chemical Society* **2010,** *132* (11), 3980-3988.

108. Harris, T. D.; Coulon, C.; Clérac, R.; Long, J. R., Record Ferromagnetic Exchange through Cyanide and Elucidation of the Magnetic Phase Diagram for a CuIIReIV(CN)2 Chain Compound. *Journal of the American Chemical Society* **2011,** *133* (1), 123-130.

109. Hilfiger, M. G.; Shatruk, M.; Prosvirin, A.; Dunbar, K. R., Hexacyanoosmate(iii) chemistry: preparation and magnetic properties of a pentanuclear cluster and a Prussian blue analogue with Ni(ii). *Chemical Communications* **2008,** (44), 5752-5754.

110. Palii, A. V.; Reu, O. S.; Ostrovsky, S. M.; Klokishner, S. I.; Tsukerblat, B. S.; Hilfiger, M.; Shatruk, M.; Prosvirin, A.; Dunbar, K. R., Highly Anisotropic Exchange Interactions in a Trigonal Bipyramidal Cyanide-Bridged NiII3OsIII2 Cluster. *The Journal of Physical Chemistry A* **2009,** *113* (25), 6886-6890.

111. Hilfiger, M. G.; Chen, M.; Brinzari, T. V.; Nocera, T. M.; Shatruk, M.; Petasis, D. T.; Musfeldt, J. L.; Achim, C.; Dunbar, K. R., An Unprecedented Charge Transfer Induced Spin Transition in an Fe–Os Cluster. *Angewandte Chemie International Edition* **2010,** *49* (8), 1410-1413.

112. Avendano, C.; Hilfiger, M. G.; Prosvirin, A.; Sanders, C.; Stepien, D.; Dunbar, K. R., Temperature and Light Induced Bistability in a Co3[Os(CN)6]2 6H2O Prussian Blue Analog. *Journal of the American Chemical Society* **2010,** *132* (38), 13123-13125.

113. Pedersen, K. S.; Schau-Magnussen, M.; Bendix, J.; Weihe, H.; Palii, A. V.; Klokishner, S. I.; Ostrovsky, S.; Reu, O. S.; Mutka, H.; Tregenna-Piggott, P. L. W., Enhancing the Blocking Temperature in Single-Molecule Magnets by Incorporating 3d–5d Exchange Interactions. *Chemistry – A European Journal* **2010,** *16* (45), 13458-13464.

114. Pinkowicz, D.; Southerland, H. I.; Avendaño, C.; Prosvirin, A.; Sanders, C.; Wernsdorfer, W.; Pedersen, K. S.; Dreiser, J.; Clérac, R.; Nehrkorn, J.; Simeoni, G. G.; Schnegg, A.; Holldack, K.; Dunbar, K. R., Cyanide Single-Molecule Magnets Exhibiting Solvent Dependent Reversible “On” and “Off” Exchange Bias Behavior. *Journal of the American Chemical Society* **2015,** *137* (45), 14406-14422.

115. Hoeke, V.; Stammler, A.; Bögge, H.; Schnack, J.; Glaser, T., Strong and Anisotropic Superexchange in the Single-Molecule Magnet (SMM) [MnIII6OsIII]3+: Promoting SMM Behavior through 3d–5d Transition Metal Substitution. *Inorganic Chemistry* **2014,** *53* (1), 257-268.

116. Peresypkina, E. V.; Majcher, A. M.; Rams, M.; Vostrikova, K. E., A single chain magnet involving hexacyanoosmate. *Chemical Communications* **2014,** *50* (54), 7150-7153.

117. Peresypkina, E.; Gavriluta, A.; Vostrikova, K., The First Homoleptic Complex of Seven-Coordinated Osmium: Synthesis and Crystallographical Evidence of Pentagonal Bipyramidal Polyhedron of Heptacyanoosmate(IV). *Crystals* **2016,** *6* (9), 102.

118. Young, R. C., A COMPLEX CYANIDE OF TRIVALENT MOLYBDENUM. *Journal of the American Chemical Society* **1932,** *54* (4), 1402-1405.

119. Larionova, J.; Sanchiz, J.; Kahn, O.; Gohlen, S.; Ouahab, L., Crystal structure, ferromagnetic ordering and magnetic anisotropy for two cyano-bridged bimetallic compounds of formula Mn2(H2O)5Mo(CN)7·nH2O. *Chemical Communications* **1998,** (9), 953-954.

120. Larionova, J.; Clérac, R.; Sanchiz, J.; Kahn, O.; Golhen, S.; Ouahab, L., Ferromagnetic Ordering, Anisotropy, and Spin Reorientation for the Cyano-Bridged Bimetallic Compound Mn2(H2O)5Mo(CN)7·4H2O (α Phase). *Journal of the American Chemical Society* **1998,** *120* (50), 13088-13095.

121. Kaur Sra, A.; Andruh, M.; Kahn, O.; Golhen, S.; Ouahab, L.; Yakhmi, J. V., A Mixed-Valence and Mixed-Spin Molecular Magnetic Material: [MnIIL]6[MoIII(CN)7][MoIV(CN)8]2·19.5 H2O. *Angewandte Chemie International Edition* **1999,** *38* (17), 2606-2609.

122. Larionova, J.; Kahn, O.; Bartolome, J.; Burriel, R.; Castro, M.; Ksenofontov, V.; Gütlich, P., Heat Capacity, Alternating Current Magnetic Susceptibilities, and Pressure Effect for the Cyano-Bridged Bimetallic Ferromagnet Mn2(H2O)5Mo(CN)7·4H2O (α Phase). *Chemistry of Materials* **1999,** *11* (11), 3400-3405.

123. Kahn, O.; Larionova, J.; Ouahab, L., Magnetic anisotropy in cyano-bridged bimetallic ferromagnets synthesized from the [Mo(CN)7]4- precursor. *Chemical Communications* **1999,** (11), 945-952.

124. Gillon, B.; Goujon, A.; Willemin, S.; Larionova, J.; Desplanches, C.; Ruiz, E.; André, G.; Stride, J. A.; Guérin, C., Neutron Diffraction and Theoretical DFT Studies of Two Dimensional Molecular-Based Magnet K2[Mn(H2O)2]3[Mo(CN)7]2·6H2O. *Inorganic Chemistry* **2007,** *46* (4), 1090-1099.

125. Tomono, K.; Tsunobuchi, Y.; Nakabayashi, K.; Ohkoshi, S.-i., Vanadium(II) Heptacyanomolybdate(III)-Based Magnet Exhibiting a High Curie Temperature of 110 K. *Inorganic Chemistry* **2010,** *49* (4), 1298-1300.

126. Wei, X.-Q.; Pi, Q.; Shen, F.-X.; Shao, D.; Wei, H.-Y.; Wang, X.-Y., Syntheses, structures, and magnetic properties of three new MnII–[MoIII(CN)7]4− molecular magnets. *Dalton Transactions* **2018,** *47* (34), 11873-11881.

127. Wei, X.-Q.; Qian, K.; Wei, H.-Y.; Wang, X.-Y., A One-Dimensional Magnet Based on [MoIII(CN)7]4–. *Inorganic Chemistry* **2016,** *55* (11), 5107-5109.

128. Wang, K.; Xia, B.; Wang, Q.-L.; Ma, Y.; Liao, D.-Z.; Tang, J., Slow magnetic relaxation based on the anisotropic Ising-type magnetic coupling between the MoIII and MnII centers. *Dalton Transactions* **2017,** *46* (4), 1042-1046.

129. Wu, D.-Q.; Kempe, D.; Zhou, Y.; Deng, L.-D.; Shao, D.; Wei, X.-Q.; Shi, L.; Dunbar, K. R.; Wang, X.-Y., Three-Dimensional FeII–[MoIII(CN)7]4– Magnets with Ordering below 65 K and Distinct Topologies Induced by Cation Identity. *Inorganic Chemistry* **2017,** *56* (12), 7182-7189.

130. Wang, X.-Y.; Prosvirin, A. V.; Dunbar, K. R., A Docosanuclear {Mo8Mn14} Cluster Based on [Mo(CN)7]4−. *Angewandte Chemie International Edition* **2010,** *49* (30), 5081-5084.

131. Wang, Q. L.; Southerland, H.; Li, J. R.; Prosvirin, A. V.; Zhao, H.; Dunbar, K. R., Crystal-to-Crystal Transformation of Magnets Based on Heptacyanomolybdate(III) Involving Dramatic Changes in Coordination Mode and Ordering Temperature. *Angewandte Chemie International Edition* **2012,** *51* (37), 9321-9324.

132. Wu, D.-Q.; Shao, D.; Wei, X.-Q.; Shen, F.-X.; Shi, L.; Kempe, D.; Zhang, Y.-Z.; Dunbar, K. R.; Wang, X.-Y., Reversible On–Off Switching of a Single-Molecule Magnet via a Crystal-to-Crystal Chemical Transformation. *Journal of the American Chemical Society* **2017,** *139* (34), 11714-11717.

133. Freedman, D. E.; Jenkins, D. M.; Long, J. R., Strong magnetic exchange coupling in the cyano-bridged coordination clusters [(PY5Me2)4V4M(CN)6]5+ (M = Cr, Mo). *Chemical Communications* **2009,** *0* (32), 4829-4831.

134. Wang, X.-Y.; Hilfiger, M. G.; Prosvirin, A.; Dunbar, K. R., Trigonal bipyramidal magnetic molecules based on [MoIII(CN)6]3−. *Chemical Communications* **2010,** *46* (25), 4484-4486.

135. Pinkowicz, D.; Southerland, H.; Wang, X.-Y.; Dunbar, K. R., Record Antiferromagnetic Coupling for a 3d/4d Cyanide-Bridged Compound. *Journal of the American Chemical Society* **2014,** *136* (28), 9922-9924.

136. Pinkowicz, D.; Podgajny, R.; Nowicka, B.; Chorazy, S.; Reczynski, M.; Sieklucka, B., Magnetic clusters based on octacyanidometallates. *Inorganic Chemistry Frontiers* **2015,** *2* (1), 10-27.

137. Pinkowicz, D.; Podgajny, R.; Nowicka, B.; Chorazy, S.; Reczyński, M.; Sieklucka, B., Magnetic clusters based on octacyanidometallates. *Inorganic Chemistry Frontiers* **2015,** *2* (1), 10-27.

138. Wang, Q.-L.; Zhang, Y.-Z.; Southerland, H.; Prosvirin, A. V.; Zhao, H.; Dunbar, K. R., Variations in topology and magnetic properties of hepta- and octacyanometallates of molybdenum with manganese(ii). *Dalton Transactions* **2014,** *43* (18), 6802-6810.

139. Nowicka, B.; Korzeniak, T.; Stefańczyk, O.; Pinkowicz, D.; Chorąży, S.; Podgajny, R.; Sieklucka, B., The impact of ligands upon topology and functionality of

octacyanidometallate-based assemblies. *Coordination Chemistry Reviews* **2012,** *256* (17), 1946-1971.

140. Nowicka, B.; Stadnicka, K.; Nitek, W.; Rams, M.; Sieklucka, B., Geometrical isomerism in pentadecanuclear high-spin Ni9W6 clusters with symmetrical bidentate ligands detected. *CrystEngComm* **2012,** *14* (20), 6559-6564.

141. Song, Y.; Zhang, P.; Ren, X.-M.; Shen, X.-F.; Li, Y.-Z.; You, X.-Z., Octacyanometallate-Based Single-Molecule Magnets: CoII9MV6 (M = W, Mo). *Journal of the American Chemical Society* **2005,** *127* (11), 3708-3709.

142. Hilfiger, M. G.; Zhao, H.; Prosvirin, A.; Wernsdorfer, W.; Dunbar, K. R., Molecules based on M(v) (M = Mo, W) and Ni(ii) ions: a new class of trigonal bipyramidal cluster and confirmation of SMM behavior for the pentadecanuclear molecule {NiII[NiII(tmphen)(MeOH)]6[Ni(H2O)3]2[μ-CN]30[WV(CN)3]6}. *Dalton Transactions* **2009,** (26), 5155-5163.

143. Wang, Z.-X.; LiLi; Wang, T.-W.; Li, Y.-Z.; Ohkoshi, S.-i.; Hashimoto, K.; Song, Y.; You, X.-Z., Octacyanotungstate(V)-Based Magnetic Complex Consisting of Dimeric Mn2 and Tetrameric Mn2W2. *Inorganic Chemistry* **2007,** *46* (26), 10990-10995.

144. Sieklucka, B.; Szklarzewicz, J.; Kemp, T. J.; Errington, W., X-ray Evidence of CN Bridging in Bimetallic Complexes Based on [M(CN)8]4- (M = Mo, W). The Crystal Structure of {[Mn(bpy)2]2(μ-NC)2[Mo(CN)6]2(μ-CN)2[Mn(bpy)2]2}·8H2O. *Inorganic Chemistry* **2000,** *39* (22), 5156-5158.

145. Arczyński, M.; Rams, M.; Stanek, J.; Fitta, M.; Sieklucka, B.; Dunbar, K. R.; Pinkowicz, D., A Family of Octahedral Magnetic Molecules Based on [NbIV(CN)8]4–. *Inorganic Chemistry* **2017,** *56* (7), 4021-4027.

146. Korzeniak, T.; Jankowski, R.; Kozieł, M.; Pinkowicz, D.; Sieklucka, B., Reversible Single-Crystal-to-Single-Crystal Transformation in Photomagnetic Cyanido-Bridged Cd4M2 Octahedral Molecules. *Inorganic Chemistry* **2017,** *56* (21), 12914-12919.

147. Alexandru, M.-G.; Visinescu, D.; Madalan, A. M.; Lloret, F.; Julve, M.; Andruh, M., [W(bipy)(CN)6]−: A Suitable Metalloligand in the Design of Heterotrimetallic Complexes. The First CuIILnIIIWV Trinuclear Complexes. *Inorganic Chemistry* **2012,** *51* (9), 4906-4908.

148. Alexandru, M.-G.; Visinescu, D.; Shova, S.; Lloret, F.; Julve, M.; Andruh, M., Two-Dimensional Coordination Polymers Constructed by [NiIILnIII] Nodes and [WIV(bpy)(CN)6]2– Spacers: A Network of [NiIIDyIII] Single Molecule Magnets. *Inorganic Chemistry* **2013,** *52* (19), 11627-11637.

149. Lee, J. W.; Lim, K. S.; Ryu, D. W.; Koh, E. K.; Yoon, S. W.; Suh, B. J.; Hong, C. S., Cyanide-Bridged WVMnIII Bimetallic Chains Composed of a Blocked W Hexacyanide Precursor: Geometry-Related Magnetic Couplings and Magnetostructural Correlation. *Inorganic Chemistry* **2013,** *52* (15), 8677-8684.

150. Alexandru, M.-G.; Visinescu, D.; Shova, S.; Andruh, M.; Lloret, F.; Julve, M., Magnetism in Heterobimetallic and Heterotrimetallic Chains Based on the Use of [WV(bipy)(CN)6]– as a Metalloligand. *European Journal of Inorganic Chemistry* **2018,** *2018* (3-4), 360-369.

151. Kahn, O., Magnetic anisotropy in molecule–based magnets. *Philosophical Transactions of the Royal Society of London A: Mathematical, Physical and Engineering Sciences* **1999,** *357* (1762), 3005-3023.

152. Mironov, V. S., Spin Clusters with Orbitally Degenerate Magnetic Centers As Single-Molecule Nanomagnets with High Blocking Temperatures. *Dokl Phys Chem* **2004,** *397* (1-3), 154-157.

153. Towns, R. L. R.; Levenson, R. A., Structure of the seven-coordinate cyano complex of vanadium(III). *Journal of the American Chemical Society* **1972,** *94* (12), 4345-4346.

154. Sieklucka, B.; Podgajny, R.; Korzeniak, T.; Nowicka, B.; Pinkowicz, D.; Kozieł, M., A Decade of Octacyanides in Polynuclear Molecular Materials. *European Journal of Inorganic Chemistry* **2011,** *2011* (3), 305-326.

155. Kiernan, P. M.; Griffith, W. P., Transition metal cyano complexes. I. Octacyanoniobates(III), -niobates(IV), -molybdates(V), and -tungstates(V). *J. Chem. Soc., Dalton Trans.* **1975,** (23), 2489-94.

156. Yoo, J. S.; Griswold, E.; Kleinberg, J., Reactions of Some Transition Metal Cyano Complexes with Molecular Hydrogen at Elevated Temperatures. *Inorganic Chemistry* **1965,** *4* (3), 365-368.

157. Fowler, J. R.; Kleinberg, J., Reactions of nitrosyl chloride with some transition metal-cyano complexes in selected nonaqueous media. *Inorganic Chemistry* **1970,** *9* (5), 1005-1009.

158. Soares, A. M.; Kiernan, P. M.; Cole-Hamilton, D. J.; Griffith, W. P., The first eight-co-ordinate cyanide hydride, K4[W(CN)7H].2H2O and a new heptacyano-complex, K5[W(CN)7].H2O. *Journal of the Chemical Society, Chemical Communications* **1981,** (3), 84-85.

159. Karunadasa, H. I.; Long, J. R., Synthesis and Redox-Induced Structural Isomerization of the Pentagonal Bipyramidal Complexes [W(CN)5(CO)2]3− and [W(CN)5(CO)2]2−. *Angewandte Chemie International Edition* **2009,** *48* (4), 738-741.

160. Bok, L. D. C.; Leipoldt, J. G.; Basson, S. S., The preparation of Cs3Mo(CN)8·2H2O and Cs3W(CN)8·2H2O. *Zeitschrift für anorganische und allgemeine Chemie* **1975,** *415* (1), 81-83.

161. Connelly, N. G.; Geiger, W. E., Chemical Redox Agents for Organometallic Chemistry. *Chemical Reviews* **1996,** *96* (2), 877-910.

162. Viculis, L. M.; Mack, J. J.; Mayer, O. M.; Hahn, H. T.; Kaner, R. B., Intercalation and exfoliation routes to graphite nanoplatelets. *Journal of Materials Chemistry* **2005,** *15* (9), 974-978.

163. AXS, B. *APEX2 v2014.11-0*, Madison, WI, 2014.

164. Sheldrick, G. M., Program for Empirical Absorption Correction of Area Detector Data. *SADABS* **1996**.

165. Sheldrick, G., A short history of SHELX. *Acta Crystallographica Section A* **2008,** *64* (1), 112-122.

166. Hubschle, C. B.; Sheldrick, G. M.; Dittrich, B., ShelXle: a Qt graphical user interface for SHELXL. *Journal of Applied Crystallography* **2011,** *44* (6), 1281-1284.

167. Pennington, W. T., DIAMOND- Visual Crystal StructureInformation System. *Journal of Applied Crystallography* **1999,** *32*, 1028.

168. Bain, G. A.; Berry, J. F., Diamagnetic Corrections and Pascal's Constants. *Journal of Chemical Education* **2008,** *85* (4), 532.

169. Takao, O.; Hiroyoshi, T., Ring-opening Polymerization of Norbornene and Its Derivatives by MoCl5, WCl6 and ReCl5 Catalysts. *Bulletin of the Chemical Society of Japan* **1968,** *41* (1), 211-217.

170. Junk, P. C.; Atwood, J. L., HYDROGEN-BONDED TETRAMETHYLETHYLENEDIAMMONIUM AND TRIPHENYLPHOSPHONIUM

COMPLEXES DERIVED FROM LIQUID CLATHRATE MEDIA. *Journal of Coordination Chemistry* **1999,** *46* (4), 505-518.

171. Okamura, A. T.-a.; Omi, Y.; Fujii, M.; Tatsumi, M.; Onitsuka, K., Significant differences of monooxotungsten(iv) and dioxotungsten(vi) benzenedithiolates containing two intramolecular NH···S hydrogen bonds from molybdenum analogues. *Dalton Transactions* **2015,** *44* (41), 18090-18100.

172. Rossman, G. R.; Tsay, F. D.; Gray, H. B., Spectroscopic and magnetic properties of heptacyanomolybdate(III). Evidence for pentagonal-bipyramidal and monocapped trigonal-prismatic structures. *Inorganic Chemistry* **1973,** *12* (4), 824-829.

173. Bok, L. D. C.; Leipoldt, J. G.; Basson, S. S., A second configuration for the octacyanide group. The crystal structure of Na3W(CN)8.4H2O. *Acta Crystallographica Section B* **1970,** *26* (6), 684-692.

174. Hoard, J. L.; Hamor, T. A.; Glick, M. D., Stereochemistry of discrete eight-coordination. V. Octacyanomolybdate(IV) ion. *Journal of the American Chemical Society* **1968,** *90* (12), 3177-3184.

175. Hursthouse, M. B.; Malik, K. M. A.; Soares, A. M.; Gibson, J. F.; Griffith, W. P., The x-ray crystal structure of NaK3[Mo(CN)7]· 2H2O and the structure of its anion in aqueous solution. *Inorganica Chimica Acta* **1980,** *45,* L81-L82.

176. Birk, F. J.; Pinkowicz, D.; Dunbar, K. R., The Heptacyanotungstate(IV) Anion: A New 5 d Transition-Metal Member of the Rare Heptacyanometallate Family of Anions. *Angewandte Chemie International Edition* **2016,** *55* (38), 11368-11371.

177. Gutmann, V.; Gritzner, G.; Danksagmuller, K., Solvent effects on the redox potential of hexacyanoferrate(III)-Hexacyanoferrate(II). *Inorganica Chimica Acta* **1976,** *17*, 81-86.

178. Campion, R. J.; Purdie, N.; Sutin, N., The Kinetics of Some Related Electron-Transfer Reactions. *Inorganic Chemistry* **1964,** *3* (8), 1091-1094.

179. Goodenow, E. L.; Garner, C. S., The Exchange Reaction between Octacyanotungstate(IV) and Octacyanotungstate(V) Ions1. *Journal of the American Chemical Society* **1955,** *77* (20), 5272-5274.

180. Wolfgang, R. L., The Charge Transfer Reaction between Molybdo- and Molybdioctacyanides1. *Journal of the American Chemical Society* **1952,** *74* (23), 6144-6145.

181. Williams, A. F., A Theoretical Approach to Inorganic Chemistry. *Springer-Verlag Berlin Heidelberg* **1979**.

182. Chilton, N. F.; Anderson, R. P.; Turner, L. D.; Soncini, A.; Murray, K. S., PHI: A powerful new program for the analysis of anisotropic monomeric and exchange-coupled polynuclear d- and f-block complexes. *Journal of Computational Chemistry* **2013,** *34* (13), 1164-1175.

183. Manakin, Y. V.; Mironov, V. S.; Bazhenova, T. A.; Lyssenko, K. A.; Gilmutdinov, I. F.; Bikbaev, K. S.; Masitov, A. A.; Yagubskii, E. B., (Et4N)[MoIII(DAPBH)Cl2], the first pentagonal-bipyramidal Mo(iii) complex with a N3O2-type Schiff-base ligand: manifestation of unquenched orbital momentum and Ising-type magnetic anisotropy. *Chemical Communications* **2018,** *54* (72), 10084-10087.

184. Bechlars, B.; D'Alessandro, D. M.; Jenkins, D. M.; Iavarone, A. T.; Glover, S. D.; Kubiak, C. P.; Long, J. R., High-spin ground states via electron delocalization in mixed-valence imidazolate-bridged divanadium complexes. *Nature Chemistry* **2010,** *2,* 362.

185. Dolomanov, O. V.; Bourhis, L. J.; Gildea, R. J.; Howard, J. A. K.; Puschmann, H., OLEX2: a complete structure solution, refinement and analysis program. *Journal of Applied Crystallography* **2009,** *42* (2), 339-341.

186. Rana, S.; Dey, A.; Maiti, D., Mechanistic elucidation of C–H oxidation by electron rich non-heme iron(iv)–oxo at room temperature. *Chemical Communications* **2015,** *51* (77), 14469-14472.

187. Xiang, J.; Li, H.; Wu, J.-S., Synthesis, Characterization, and Catalytic Activity of Iron(II) and Nickel(II) Complexes Containing the Rigid Pentadentate Ligand PY5Me2. *Zeitschrift für anorganische und allgemeine Chemie* **2014,** *640* (8-9), 1670-1674.

188. Lo, W. K. C.; McAdam, C. J.; Blackman, A. G.; Crowley, J. D.; McMorran, D. A., The pentadentate ligands 2PyN2Q and N4Py, and their Cu(II) and Zn(II) complexes:

A synthetic, spectroscopic and crystallographic structural study. *Inorganica Chimica Acta* **2015,** *426*, 183-194.

189. Zhao, H.; Shatruk, M.; Prosvirin, A. V.; Dunbar, K. R., Variation of Heterometallic Structural Motifs Based on [W(CN)8]3− Anions and MnII Ions as a Function of Synthetic Conditions. *Chemistry – A European Journal* **2007,** *13* (23), 6573-6589.

190. Qian, S.-Y.; Zhou, H.; Yuan, A.-H.; Song, Y., Syntheses, Structures, and Magnetic Properties of Five Novel Octacyanometallate-Based Lanthanide Complexes with Helical Chains. *Crystal Growth & Design* **2011,** *11* (12), 5676-5681.

191. Przychodzeń, P.; Pełka, R.; Lewiński, K.; Supel, J.; Rams, M.; Tomala, K.; Sieklucka, B., Tuning of Magnetic Properties of Polynuclear Lanthanide(III)−Octacyanotungstate(V) Systems: Determination of Ligand-Field Parameters and Exchange Interaction. *Inorganic Chemistry* **2007,** *46* (21), 8924-8938.

192. Shiga, T.; Takeo, M.; Iijima, F.; Newton, G. N.; Oshio, H., Syntheses, structures and magnetic properties of two-dimensional chiral coordination polymers based on a tetradentate chiral ligand. *New Journal of Chemistry* **2014,** *38* (5), 1946-1949.

193. Venkatakrishnan, T. S.; Imaz, I.; Sutter, J.-P., Octanuclear {Co6W2} aggregate versus mixed valence {Co}3 cluster in the assembling of Co(phen)2Cl2 (phen=1,10-phenanthroline) with octacyano metallates: A case of non-isostructurality between {W(CN)8}4− and {Nb(CN)8}4−. *Inorganica Chimica Acta* **2008,** *361* (12), 3710-3713.

194. Zhang, W.; Wang, Z.-Q.; Sato, O.; Xiong, R.-G., A Secondary Reagent-Assisted Synthesis of A Novel NiII−MoIV Chiral Coordination Polymer. *Crystal Growth & Design* **2009,** *9* (5), 2050-2053.

195. Withers, J. R.; Ruschman, C.; Parkin, S.; Holmes, S. M., One- and three-dimensional octacyanometalate(IV) networks constructed via a building block approach: {[trans-NiII(tn)2(OH2)][trans-NiII(μ-NC)2(tn)2][(μ-NC)3MIV(CN)5]·6H2O} (MIV=Mo, W) and Cs4[CuII(OH2)4]2[CuII(NH3)]4[MoIV(CN)8]4·2H2O. *Polyhedron* **2005,** *24* (14), 1845-1854.

196. Yoshida, M.; Kondo, M.; Okamura, M.; Kanaike, M.; Haesuwannakij, S.; Sakurai, H.; Masaoka, S., Fe, Ru, and Os complexes with the same molecular framework: comparison of structures, properties and catalytic activities. *Faraday Discussions* **2017,** *198* (0), 181-196.

197. Yu, F.; Li, A.-h.; Hu, S.-q.; Li, B., Structure and magnetism of heptanuclear complex encapsulated the octacyanomolybdate(IV) core. *Inorganic Chemistry Communications* **2013,** *35*, 58-60.

198. Korzeniak, T.; Desplanches, C.; Podgajny, R.; Giménez-Saiz, C.; Stadnicka, K.; Rams, M.; Sieklucka, B., Magnetostructural Correlations in CuII−NC−WV Linkage: The Case of [CuII(diimine)]2+−[WV(CN)8]3− 0D Assemblies. *Inorganic Chemistry* **2009,** *48* (7), 2865-2872.

199. Kou, H.-Z.; Zhou, Bei C.; Si, S.-F.; Wang, R.-J., Cyano-Bridged Dimetallic Polynuclear Cu6Cr, Cu6Cr6, Cu2W, and CuW Arrays: Synthesis, Crystal Structure, and Magnetism. *European Journal of Inorganic Chemistry* **2004,** *2004* (2), 401-408.

200. Trofimenko, S., Boron-Pyrazole Chemistry. *Journal of the American Chemical Society* **1966,** *88* (8), 1842-1844.

201. Trofimenko, S., *Scorpionates*. IMPERIAL COLLEGE PRESS: 1999; p 292.

202. Pettinari, C., *Scorpionates II: Chelating Borate Ligands*. PUBLISHED BY IMPERIAL COLLEGE PRESS AND DISTRIBUTED BY WORLD SCIENTIFIC PUBLISHING CO.: 2008; p 572.

203. Philip, J. F.; Stephen, M. H., Pyrazolylborate Cyanometalate Single-Molecule Magnets. *Current Inorganic Chemistry* **2013,** *3* (2), 172-193.

204. Jiang, L.; Choi, H. J.; Feng, X.-L.; Lu, T.-B.; Long, J. R., Syntheses, Structures, and Magnetic Properties of the Face-Centered Cubic Clusters [Tp8(H2O)12M6Fe8(CN)24]4+ (M = Co, Ni). *Inorganic Chemistry* **2007,** *46* (6), 2181-2186.

205. Gu, Z.-G.; Liu, W.; Yang, Q.-F.; Zhou, X.-H.; Zuo, J.-L.; You, X.-Z., Cyano-Bridged FeIII2CuII3 and FeIII4NiII4 Complexes: Syntheses, Structures, and Magnetic Properties. *Inorganic Chemistry* **2007,** *46* (8), 3236-3244.

206. Gu, Z.-G.; Xu, Y.-F.; Kang, L.-C.; Li, Y.-Z.; Zuo, J.-L.; You, X.-Z., A Family of Polynuclear Clusters Containing Cyano-Bridged T-Shaped FeIII3MII (M = Cu, Co, Mn)

Metal Cores: Syntheses, Structures, and Magnetic Properties. *Inorganic Chemistry* **2009,** *48* (12), 5073-5080.

207. Yao, M.-X.; Wei, Z.-Y.; Gu, Z.-G.; Zheng, Q.; Xu, Y.; Zuo, J.-L., Syntheses, Structures, and Magnetic Properties of Low-Dimensional Heterometallic Complexes Based on the Versatile Building Block [(Tp)Cr(CN)3]−. *Inorganic Chemistry* **2011,** *50* (17), 8636-8644.

208. Wang, C.-F.; Zuo, J.-L.; Bartlett, B. M.; Song, Y.; Long, J. R.; You, X.-Z., Symmetry-Based Magnetic Anisotropy in the Trigonal Bipyramidal Cluster [Tp2(Me3tacn)3Cu3Fe2(CN)6]4+. *Journal of the American Chemical Society* **2006,** *128* (22), 7162-7163.

209. Zhang, Y.-Z.; Mallik, U. P.; Rath, N. P.; Clérac, R.; Holmes, S. M., Pyrazolylborates and Their Importance in Tuning Single-Molecule Magnet Properties of {FeIII2NiII} Complexes. *Inorganic Chemistry* **2011,** *50* (21), 10537-10539.

210. Wen, H.-R.; Wang, C.-F.; Song, Y.; Gao, S.; Zuo, J.-L.; You, X.-Z., Synthesis, Crystal Structures, and Magnetic Properties of Cyano-Bridged Heterobimetallic Chains Based on [(Tp)Fe(CN)3]. *Inorganic Chemistry* **2006,** *45* (22), 8942-8949.

211. Wang, S.; Zuo, J.-L.; Zhou, H.-C.; Choi, H. J.; Ke, Y.; Long, J. R.; You, X.-Z., [(Tp)8(H2O)6CuII6FeIII8(CN)24]4+: A Cyanide-Bridged Face-Centered-Cubic Cluster with Single-Molecule-Magnet Behavior. *Angewandte Chemie International Edition* **2004,** *43* (44), 5940-5943.

212. Brown, A.; Saber, M.; Van den Heuvel, W.; Schulte, K.; Soncini, A.; Dunbar, K. R., Titanium(III) Member of the Family of Trigonal Building Blocks with Scorpionate and Cyanide Ligands. *Inorganic Chemistry* **2017,** *56* (3), 1031-1035.

213. Millar, M.; Lincoln, S.; Koch, S. A., Stable monomeric complexes of molybdenum(III) and tungsten(III). *Journal of the American Chemical Society* **1982,** *104* (1), 288-289.

214. Eagle, A. A.; Young, C. G.; Tiekink, E. R. T., Tp*W<emph type="7">IV</emph>O(S<emph type="8">2</emph>CNEt<emph type="8">2</emph>): the Missing Member of the Series. *Australian Journal of Chemistry* **2004,** *57* (3), 269-271.

215. Mashima, K.; Oshiki, T.; Tani, K., Tp*Sn(Cl)Bu2 as a Convenient Reagent for the Preparation of Hydrotris(3,5-dimethylpyrazolyl)borate Complexes of Niobium, Tantalum, and Zirconium. *Organometallics* **1997,** *16* (13), 2760-2762.

216. Schelter, E. J.; Bera, J. K.; Bacsa, J.; Galán-Mascarós, J. R.; Dunbar, K. R., New Paramagnetic Re(II) Compounds with Nitrile and Cyanide Ligands Prepared by Homolytic Scission of Dirhenium Complexes. *Inorganic Chemistry* **2003,** *42* (14), 4256-4258.

217. Schelter, E. J.; Karadas, F.; Avendano, C.; Prosvirin, A. V.; Wernsdorfer, W.; Dunbar, K. R., A Family of Mixed-Metal Cyanide Cubes with Alternating Octahedral and Tetrahedral Corners Exhibiting a Variety of Magnetic Behaviors Including Single

Molecule Magnetism. *Journal of the American Chemical Society* **2007,** *129* (26), 8139-8149.

218. Saber, M. R.; Dunbar, K. R., Trigonal bipyramidal 5d-4f molecules with SMM behavior. *Chemical Communications* **2014,** *50* (17), 2177-2179.

219. Dilworth, J. R.; Zubieta, J.; George, T. A.; Smith, J., Trichlorotris(Tetrahydrofuran)-Molybdenum(III). In *Inorganic Syntheses*, John Wiley & Sons, Inc.: 2007; pp 193-194.

220. Manxzer, L. E. D., Joe ; Sharp, Paul; Schrock ,R. R., 31. Tetragtdrfuran Complexes of Selected Early Transition Metals. In *Inorganic Syntheses*, Fackler, J. P., Ed. 1982.

221. Trofimenko, S., Long, J. R., Nappier, T. and Shore, S. G., Poly(1-pyrazolyl)borates, Their Transition-Metal Complexes, and Pyrazaboles. In *Inorganic Syntheses*, Parry, R. W., Ed. 2007.

222. Heersche, H. B.; de Groot, Z.; Folk, J. A.; van der Zant, H. S. J.; Romeike, C.; Wegewijs, M. R.; Zobbi, L.; Barreca, D.; Tondello, E.; Cornia, A., Electron Transport through Single ${\mathrm{Mn}}_{12}$ Molecular Magnets. *Physical Review Letters* **2006,** *96* (20), 206801.

223. del Carmen Giménez-López, M.; Moro, F.; La Torre, A.; Gómez-García, C. J.; Brown, P. D.; van Slageren, J.; Khlobystov, A. N., Encapsulation of single-molecule magnets in carbon nanotubes. *Nature Communications* **2011,** *2*, 407.

224. Li, J.-J.; Bai, M.-L.; Chen, Z.-B.; Zhou, X.-S.; Shi, Z.; Zhang, M.; Ding, S.-Y.; Hou, S.-M.; Schwarzacher, W.; Nichols, R. J.; Mao, B.-W., Giant Single-Molecule Anisotropic Magnetoresistance at Room Temperature. *Journal of the American Chemical Society* **2015,** *137* (18), 5923-5929.

225. Heinrich, B. W.; Braun, L.; Pascual, J. I.; Franke, K. J., Tuning the Magnetic Anisotropy of Single Molecules. *Nano Letters* **2015,** *15* (6), 4024-4028.

226. Xie, H.; Xu, F.; Jiao, H.; Wang, Q.; Liang, J. Q., Efficient spin-current injection in single-molecule magnet junctions. *AIP Advances* **2018,** *8* (1), 015131.